

# Recent Advances in Multiple Access for 5G-enabled IoT

Lead Guest Editor: Xingwang Li

Guest Editors: Khaled Rabie, Lingwei Xu, and Thomas Aaron Gulliver





---

# **Recent Advances in Multiple Access for 5G-enabled IoT**

Security and Communication Networks

---

## **Recent Advances in Multiple Access for 5G-enabled IoT**

Lead Guest Editor: Xingwang Li

Guest Editors: Khaled Rabie, Lingwei Xu, and  
Thomas Aaron Gulliver



---




Copyright © 2021 Hindawi Limited. All rights reserved.

This is a special issue published in "Security and Communication Networks." All articles are open access articles distributed under the Creative Commons Attribution License, which permits unrestricted use, distribution, and reproduction in any medium, provided the original work is properly cited.

# Chief Editor

Roberto Di Pietro, Saudi Arabia

## Associate Editors

Jiankun Hu , Australia  
Emanuele Maiorana , Italy  
David Megias , Spain  
Zheng Yan , China

## Academic Editors

Saed Saleh Al Rabae , United Arab Emirates  
Shadab Alam, Saudi Arabia  
Goutham Reddy Alavalapati , USA  
Jehad Ali , Republic of Korea  
Jehad Ali, Saint Vincent and the Grenadines  
Benjamin Aziz , United Kingdom  
Taimur Bakhshi , United Kingdom  
Spiridon Bakiras , Qatar  
Musa Balta, Turkey  
Jin Wook Byun , Republic of Korea  
Bruno Carpentieri , Italy  
Luigi Catuogno , Italy  
Ricardo Chaves , Portugal  
Chien-Ming Chen , China  
Tom Chen , United Kingdom  
Stelvio Cimato , Italy  
Vincenzo Conti , Italy  
Luigi Coppolino , Italy  
Salvatore D'Antonio , Italy  
Juhriyansyah Dalle, Indonesia  
Alfredo De Santis, Italy  
Angel M. Del Rey , Spain  
Roberto Di Pietro , France  
Wenxiu Ding , China  
Nicola Dragoni , Denmark  
Wei Feng , China  
Carmen Fernandez-Gago, Spain  
AnMin Fu , China  
Clemente Galdi , Italy  
Dimitrios Geneiatakis , Italy  
Muhammad A. Gondal , Oman  
Francesco Gringoli , Italy  
Biao Han , China  
Jinguang Han , China  
Khizar Hayat, Oman  
Azeem Irshad, Pakistan

M.A. Jabbar , India  
Minho Jo , Republic of Korea  
Arijit Karati , Taiwan  
ASM Kayes , Australia  
Farrukh Aslam Khan , Saudi Arabia  
Fazlullah Khan , Pakistan  
Kiseon Kim , Republic of Korea  
Mehmet Zeki Konyar, Turkey  
Sanjeev Kumar, USA  
Hyun Kwon, Republic of Korea  
Maryline Laurent , France  
Jegatha Deborah Lazarus , India  
Huaizhi Li , USA  
Jiguo Li , China  
Xueqin Liang, Finland  
Zhe Liu, Canada  
Guangchi Liu , USA  
Flavio Lombardi , Italy  
Yang Lu, China  
Vincente Martin, Spain  
Weizhi Meng , Denmark  
Andrea Michienzi , Italy  
Laura Mongioi , Italy  
Raul Monroy , Mexico  
Naghme Moradpoor , United Kingdom  
Leonardo Mostarda , Italy  
Mohamed Nassar , Lebanon  
Qiang Ni, United Kingdom  
Mahmood Niazi , Saudi Arabia  
Vincent O. Nyangaresi, Kenya  
Lu Ou , China  
Hyun-A Park, Republic of Korea  
A. Peinado , Spain  
Gerardo Pelosi , Italy  
Gregorio Martinez Perez , Spain  
Pedro Peris-Lopez , Spain  
Carla Ràfols, Germany  
Francesco Regazzoni, Switzerland  
Abdalhossein Rezai , Iran  
Helena Rifà-Pous , Spain  
Arun Kumar Sangaiah, India  
Nadeem Sarwar, Pakistan  
Neetesh Saxena, United Kingdom  
Savio Sciancalepore , The Netherlands




De Rosal Ignatius Moses Setiadi ,  
Indonesia  
Wenbo Shi, China  
Ghanshyam Singh , South Africa  
Vasco Soares, Portugal  
Salvatore Sorce , Italy  
Abdulhamit Subasi, Saudi Arabia  
Zhiyuan Tan , United Kingdom  
Keke Tang , China  
Je Sen Teh , Australia  
Bohui Wang, China  
Guojun Wang, China  
Jinwei Wang , China  
Qichun Wang , China  
Hu Xiong , China  
Chang Xu , China  
Xuehu Yan , China  
Anjia Yang , China  
Jiachen Yang , China  
Yu Yao , China  
Yinghui Ye, China  
Kuo-Hui Yeh , Taiwan  
Yong Yu , China  
Xiaohui Yuan , USA  
Sherali Zeadally, USA  
Leo Y. Zhang, Australia  
Tao Zhang, China  
Youwen Zhu , China  
Zhengyu Zhu , China

# Contents

## **Multiple-Symbol Detection Scheme for IEEE 802.15.4c MPSK Receivers over Slow Rayleigh Fading Channels**

Gaoyuan Zhang , Haiqiong Li , Congzheng Han , Congyu Shi , Hong Wen, and Dan Wang  
Research Article (19 pages), Article ID 6641192, Volume 2021 (2021)



## **Spectral Efficiency of the Multiway Massive System over Rician Fading Channels**

Junyi He , Junnan Zhang , Cheng Song , and Mengxiang Wu   
Research Article (8 pages), Article ID 6618363, Volume 2021 (2021)





## **Two-Dimensional DOA Estimation of MIMO Radar Coherent Source Based on Toeplitz Matrix Set Reconstruction**

Fei Zhang , Aisuo Jin, and Yin Hu  
Research Article (9 pages), Article ID 6631196, Volume 2021 (2021)


## **Secure and Efficient Image Compression-Encryption Scheme Using New Chaotic Structure and Compressive Sensing**

Yongli Tang, Mingjie Zhao , and Lixiang Li   
Research Article (15 pages), Article ID 6665702, Volume 2020 (2020)



## **Enabling Sector Scheduling for 5G-CPE Dense Networks**

Jie Yang , Li Feng , Tong Jin, Hong Liang , Fangxin Xu , and Liwei Tian  
Research Article (18 pages), Article ID 6684681, Volume 2020 (2020)

## **Energy Management Strategy Using Equivalent Consumption Minimization Strategy for Hybrid Electric Vehicles**

Fazhan Tao, Longlong Zhu, Baofeng Ji, Pengju Si, and Zhumu Fu   
Research Article (8 pages), Article ID 6642304, Volume 2020 (2020)

## **On Enhancing TCP to Deal with High Latency and Transmission Errors in Geostationary Satellite Network for 5G-IoT**

Liang Zong , Yong Bai, Chenglin Zhao, Gaofeng Luo, Zeyu Zhang, and Huawei Ma   
Research Article (7 pages), Article ID 6693094, Volume 2020 (2020)

## **On the Detection of a Non-Cooperative Beam Signal Based on Wireless Sensor Networks**

Guofeng Wei , Bangning Zhang , Guoru Ding , Bing Zhao , Kefeng Guo , and Daoxing Guo   
Research Article (12 pages), Article ID 8830092, Volume 2020 (2020)

## **Secrecy Analysis of Cognitive Radio Networks over Generalized Fading Channels**

Jiangfeng Sun, Zhisong Bie , Hongxia Bie, Pengfei He, and Machao Jin  
Research Article (9 pages), Article ID 8842012, Volume 2020 (2020)

## Research Article

# Multiple-Symbol Detection Scheme for IEEE 802.15.4c MPSK Receivers over Slow Rayleigh Fading Channels

Gaoyuan Zhang <sup>1,2,3</sup>, Haiqiong Li <sup>1</sup>, Congzheng Han <sup>2</sup>, Congyu Shi <sup>1</sup>, Hong Wen,<sup>3</sup>  
and Dan Wang<sup>1</sup>

<sup>1</sup>School of Information Engineering, Henan University of Science and Technology, Luoyang 471023, China

<sup>2</sup>Key Laboratory of Middle Atmosphere and Global Environment Observation, Institute of Atmospheric Physics, Chinese Academy of Sciences, Beijing 100029, China

<sup>3</sup>School of Aeronautics and Astronautics, University of Electronic Science and Technology of China, Chengdu 610054, China

Correspondence should be addressed to Gaoyuan Zhang; zhanggaoyuan407@163.com and Congzheng Han; c.han@mail.iap.ac.cn

Received 14 October 2020; Revised 9 November 2020; Accepted 3 May 2021; Published 20 May 2021

Academic Editor: Savio Sciancalepore

Copyright © 2021 Gaoyuan Zhang et al. This is an open access article distributed under the Creative Commons Attribution License, which permits unrestricted use, distribution, and reproduction in any medium, provided the original work is properly cited.

Although the full multiple-symbol detection (MSD) for IEEE 802.15.4c multiple phase shift keying (MPSK) receivers gives much better performance than the symbol-by-symbol detection (SBSD), its implementation complexity is extremely heavy. We propose a simple MSD scheme based on two implementation-friendly but powerful strategies. First, we find the best and second-best decisions in each symbol position with the standard SBSB procedure, and the global best decision is frozen. Second, for the remaining symbol positions, only the best and second-best symbol decisions, not all the candidates, are jointly searched by the standard MSD procedure. The simulation results indicate that the packet error rate (PER) performance of the simplified MSD scheme is almost the same as that of the full scheme. In particular, at PER of  $1 \times 10^{-3}$ , no more than 0.2 dB performance gap is observed if we just increase the observation window length  $N$  to 2. However, the number of decision metrics needed to be calculated is reduced from 256 to 2. Thus, much balance gain between implementation complexity and detection performance is achieved.

## 1. Introduction

With the widespread application of new information and communication technologies such as the Internet of Things (IoT), cloud computing, and big data, smart cities have developed rapidly in recent years. They have penetrated into all aspects of people's lives and greatly meet the modern people's pursuit of convenient, fast, and high-quality life [1–7]. Reliable and effective transmission of the sensing data is obviously important for the construction of the new smart city [8]. The IEEE 802.15.4c protocol provides the physical layer specification of the low-power short-distance IoT for China [9, 10]. The multiple phase shift keying (MPSK) is provided in IEEE 802.15.4c. This mainly follows from the fact that MPSK modulation is the most able to provide high reliability as well as data rate for sensing data transmission.

Therefore, it is important to study robust detection technology of MPSK signal in line with the characteristics of wireless IoT. This paper focuses on the multiple-symbol detection (MSD) of IEEE 802.15.4c MPSK receiver.

Although the MSD scheme has excellent detection performance, its implementation complexity increases exponentially with the increase of the observation window length [11, 12]. In recent years, many concentrations have been achieved on complexity reduction of MSD. Stephen *et al.* studied the maximum likelihood detection (MLD) based on information symbol blocks. The corresponding block signal is used to limit only a part of the possible signal decisions, which will reduce the complexity of the receiver. However, there is a partial performance loss [13]. LoRici proposed a suboptimal receiver based on Viterbi algorithm. The complexity of the receiver increases in polynomial form



of  $M$ . However, the performance of the algorithm is related to the memory length  $L$  of continuous phase modulation signal. For continuous-phase frequency-shift keying (CPFSK) signal ( $L = 1$ ), its detection performance is seriously degraded [14, 15]. Several low-complexity MSD algorithms are also proposed by Fischer and Wang Xin, but their performance is far behind that of the traditional MSD algorithm [16, 17].

In this work, we propose a simple MSD scheme for IEEE 802.15.4c MPSK receivers. Unlike the traditional receivers that were equipped with full MSD scheme with high complexity to achieve the best possible reliability, we pay our full attention to the simple design to balance the complexity and reliability. We summarize our main contributions as follows:

- (i) The optimal MSD scheme for IEEE 802.15.4c MPSK receivers based on the maximum likelihood criterion can give excellent results in the case of both slow fading and pure additive white Gaussian noise (AWGN) channels. However, the implementation is relatively complex and unachievable for IEEE 802.15.4c MPSK receivers. As an implementation achievable benchmark, a full MSD scheme based on compensation is proposed.
- (ii) As for the proposed full MSD scheme, more than two-hundred-decision statistic should be calculated before making final decision even if we set the observation window length  $N$  to 2. Thus, we propose a new MSD algorithm, which greatly simplifies the full scheme.
- (iii) In order to verify the desirable properties we obtained from this simple scheme, the characteristics of the receiver are studied from many aspects with extensive simulations.

The rest of this paper is organized as follows: Section 2 focuses on the signal model under the slow fading Rayleigh channel. Section 3 describes the full MSD scheme, and Section 4 introduces the proposed simplified MSD scheme. Section 5 concentrates on frequency offset estimation. The simulation results are discussed in Section 6. Finally, some conclusions and future work are provided in Section 7.

## 2. System Model

According to the IEEE 802.15.4c protocol [18], the specific data modulation process for the MPSK physical layer is shown in Figure 1. From the binary data of the physical layer protocol data unit (PPDU), in each symbol period, four information bits form a symbol, which is used to select one of 16 orthogonal spreading sequences. The chips in the sequence are MPSK-modulated onto the carrier. For more details on the mapping rules, please refer to Table 1 in [19].

Ideal carrier synchronization is assumed at the receiver. Specifically, for the  $x$ th symbol  $E[x]$ , the received complex baseband chip sequence can be expressed as

$$r_{x,m} = h_{x,m} s_{y,m} e^{j(\omega_{x,m} m T_c + \theta_{x,m})} + \eta_{x,m}, \quad 1 \leq m \leq M, \quad (1)$$

where  $h_{x,m}$  represents multiplicative fading,  $s_{y,m}$  is the  $m$ th chip of the  $y$ th pseudorandom (PN) sequence  $\mathbf{s}_y$ , and Table 1

shows the detailed correspondence.  $\omega_{x,m} = 2\pi f_{x,m}$  represents the carrier frequency offset (CFO) in radians, and  $f_{x,m}$  represents the residual CFO in Hz.  $\theta_{x,m}$  represents the carrier phase offset (CPO) in radians, and  $T_c$  represents the spreading chip period.  $\eta_{x,m}$  is a discrete, cyclic symmetric, complex Gaussian random variable with zero mean and variance  $\sigma_{x,m}^2$ , and  $M = 16$  represents the length of the PN sequence [18].

We assume that a piecewise constant approximation is made to the multiplicative fading, CFO, and CPO [20]. That is,  $h_{x,m} = h$ ,  $\omega_{x,m} = \omega$ , and  $\theta_{x,m} = \theta$ . In addition, the receiver does not have any prior information about the CPO; that is to say, the uniform distribution in the interval  $(-\pi, \pi)$  is assigned to  $\theta$ . The normalized complex Gaussian process  $h$  follows Rayleigh distribution; that is, the mean  $\bar{h} = 0$ . The CFO  $f$  follows a symmetrical triangular distribution.

## 3. The Full MSD Scheme

Following the idea in [21], we can easily develop the optimal MSD scheme for IEEE 802.15.4c MPSK receivers based on MLD. However, the implementation complexity is extremely heavy as shown in [22], which limits its application in smart cities. Here, we consider a heuristic configuration. The specific detection process is as follows.

First, the baseband chip sample after carrier frequency offset effect (CFOE) compensation can be expressed as

$$r'_{x,m} = r_{x,m} e^{-jm\hat{\varphi}}, \quad (2)$$

where  $\hat{\varphi} = \widehat{\omega T_c}$  denotes the estimated CFOE. The estimation of CFOE should be carefully developed and will be described in detail in Section 5. Please note that we assume that the effect of redundant parameter  $\omega T_c$  on  $r_{x,m}$  is completely eliminated after compensation. In addition, the information is embedded in the carrier phase but not in the carrier amplitude. Therefore, there is no need to estimate and compensate for the multiplicative fading  $h$  even if serious fading of the received signal strength may be exhibited.

Secondly, we divide the whole compensated chip sequence into block, and each block contains  $N$  symbols. The detection metric for the  $i$ th block can be then expressed as [23]

$$U_x = \left| \sum_{x=(i-1)N+1}^{iN} \sum_{m=1}^{16} r'_{x,m} s_{y,m}^* \right|^2, \quad i \geq 1, 1 \leq y \leq 16, \quad (3)$$

where

$$U_x = \{U_{(i-1)N+1,1}, U_{(i-1)N+1,2}, \dots, U_{(i-1)N+1,16}, U_{(i-1)N+2,1}, \\ U_{(i-1)N+2,2}, \dots, U_{(i-1)N+2,16}, \dots, U_{iN,1}, U_{iN,2}, \dots, U_{iN,16}\} \quad (4)$$

and  $*$  represents complex conjugate operation. Note that, for  $N = 1$ , (3) reduces to the symbol-by-symbol detection (SBSD) scheme. From (3), we can also see that the multiplicative fading  $h$  has no effect on the final decision, and there is no need to estimate and compensate for the fading coefficient  $h$ .

Finally, the decision rule can be expressed as follows:

$$\hat{U}[\mathbf{x}] = \arg \max\{U_x\}. \quad (5)$$

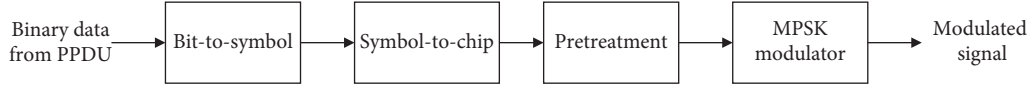


FIGURE 1: Data transmission process for MPSK physical layer in IEEE 802.15.4c.

After demapping, we can obtain the final detection result. This detection scheme is based on [23] but is different from [23]. The signal model in [23] only considers phase offset. In this work, we further considered CPO, spread spectrum, and slow Rayleigh channel. Therefore, we summarize the detailed process of the complete MSD program.

As shown in (3), based on an exhaustive search, 256 detection metrics need to be calculated for the full MSD even if we set the observation window length  $N$  to 2. This is clearly complexity-heavy. In order to make MSD easy for hardware implementation, we consider two simple strategies, which parallels Wilson's approach in [15]. First, we find the best and second-best decisions in each symbol position with the standard SBSB procedure characterized by (3) and freeze the global best decision. Second, for the remaining symbol position, only the best and second-best symbol decisions, not all the candidates, are jointly searched by the standard MSD procedure. Here, a qualitative explanation for this configuration is as follows. Apparently, the detection metric given in (3) can partly reflect the reliability of the decision result in each symbol position. Therefore, it is reasonable that the global best decision with the standard SBSB procedure characterized by (3) is the most reliable and can be frozen especially for high signal-to-noise ratio (SNR). Moreover, under high SNR, only searching the best and second-best symbol decision for the remaining symbol

position is also feasible. In Section 6, we will further verify its rationality through quantitative simulations.

#### 4. The Proposed Detection Scheme

For each symbol position, with the standard SBSB procedure characterized by (3), we can easily obtain two local metrics, that is, the best metric and second-best metric. Then, we froze the decision result corresponding to the most reliable symbol position, which is achieved by searching all the local best metric. For the remaining symbol position, the number of symbols to be searched is truncated. That is to say, only the symbols corresponding to the local best and second-best metrics are considered as the candidates. In this context, for observation window length  $N = 2$ , we have reduced the number of the metrics given in (3) to be calculated from 256 to 2. However, the simulation results in Section 6 show that the performance loss is very small. The specific implementation process is detailed as follows.

For the  $i$ th block, the decision metric for each symbol position is first calculated as

$$V_{x,y} = |w_{x,y}|^2, \quad 1 \leq y \leq 16. \quad (6)$$

Here,  $w_{x,y} = \sum_{m=1}^{16} r'_{x,m} s_{y,m}^*$ , which is the complex cross-correlation function.

Secondly, the best and the second-best metrics for the  $n$ th symbol in the  $i$ th block can be given as follows:

$$\begin{aligned} V_{N(i-1)+n,\hat{y}_1} &= \arg \max_{1 \leq \hat{y}_1 \leq 16} \{V_{N(i-1)+n,\hat{y}_1}\}, \quad i \geq 1, n = 1, 2, \dots, N, \\ V_{N(i-1)+n,\hat{y}_2} &= \arg \max_{1 \leq \hat{y}_2 \leq 16, \hat{y}_2 \neq \hat{y}_1} \{V_{N(i-1)+n,\hat{y}_2}\}, \quad i \geq 1, n = 1, 2, \dots, N, \end{aligned} \quad (7)$$

where  $\hat{y}_1$  and  $\hat{y}_2$ , respectively, represent the estimated value of the index for the PN sequence corresponding to the best and second-best metrics of the  $n$ th symbol. For example, we can see that, as shown in Figure 2, a compensated baseband chip sequence  $r'_{1,m}$  passes through decision block 1 to generate decision set  $\{V_{1,1}, V_{1,2}, \dots, V_{1,16}\}$ , and the best and second-best metrics in the decision set are recorded as  $V_{1,\hat{y}_1}$  and  $V_{1,\hat{y}_2}$ , respectively.

Furthermore, find the global best metric, and freeze the detection result:

$$\text{find } \hat{n} \text{ and } s_{\hat{y}_1} \text{ if } V_{N(i-1)+\hat{n},\hat{y}_1} \text{ is maximum,} \quad (8)$$

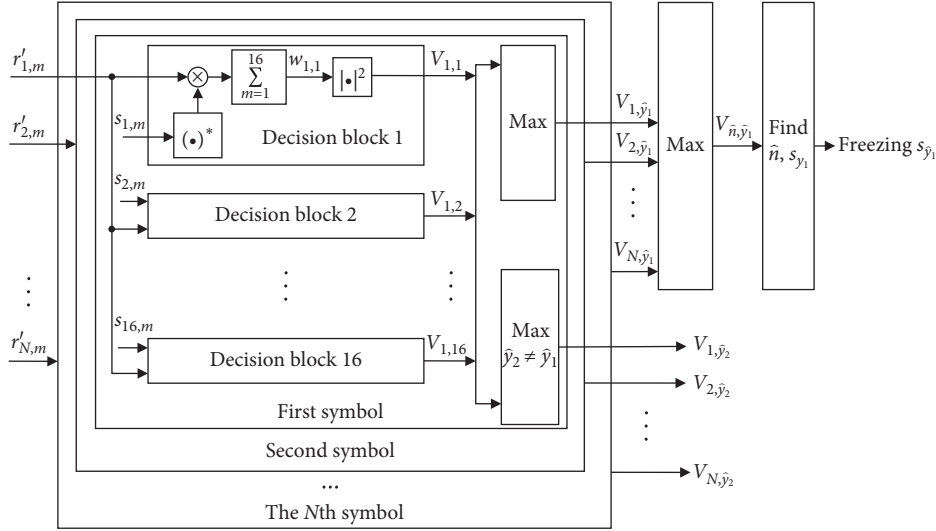
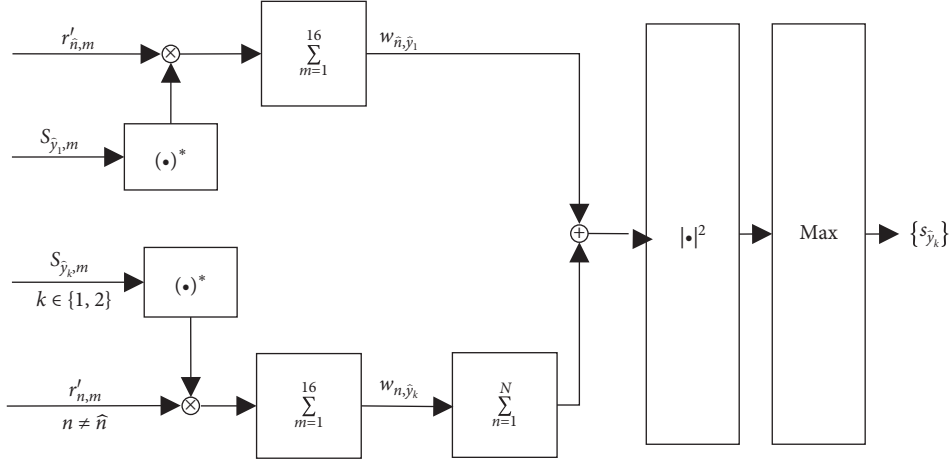
that is, let the detection result of the  $\hat{n}$ th symbol be  $s_{\hat{y}_1}$ . Figure 2 gives the implementation structure.

Finally, the data in the remaining  $N - 1$  symbol periods are jointly determined as follows:

$$\text{find } \{s_{\hat{y}_k}\} \text{ for } n \neq \hat{n} \text{ if } \left| w_{N(i-1)+\hat{n},\hat{y}_1} + \sum_{n \neq \hat{n}} w_{N(i-1)+n,\hat{y}_k} \right|^2, \quad k \in \{1, 2\} \text{ is maximum.} \quad (9)$$

TABLE 1: Symbol-to-chip mapping rule for IEEE 802.15.4c MPSK physical layer.

$S_{y^5 y^m}$	$S_{y,1}$	$S_{y,2}$	$S_{y,3}$	$S_{y,4}$	$S_{y,5}$	$S_{y,6}$	$S_{y,7}$	$S_{y,8}$	$S_{y,9}$	$S_{y,10}$	$S_{y,11}$	$S_{y,12}$	$S_{y,13}$	$S_{y,14}$	$S_{y,15}$	$S_{y,16}$
$S_1$	$e^0$	$e^{j(\pi/4)}$	$e^{j(\pi/16)}$	$e^{j(9\pi/16)}$	$e^\pi$	$e^{-j(7\pi/16)}$	$e^{j(\pi/4)}$	$e^{-j(15\pi/16)}$	$e^0$	$e^{-j(15\pi/16)}$	$e^{j(\pi/4)}$	$e^{-j(7\pi/16)}$	$e^\pi$	$e^{j(9\pi/16)}$	$e^{j(\pi/4)}$	$e^{j(\pi/16)}$
$S_2$	$e^{j(\pi/4)}$	$e^0$	$e^{j(\pi/4)}$	$e^{j(\pi/16)}$	$e^{j(9\pi/16)}$	$e^\pi$	$e^{-j(7\pi/16)}$	$e^{j(\pi/4)}$	$e^{-j(15\pi/16)}$	$e^0$	$e^{-j(15\pi/16)}$	$e^{j(\pi/4)}$	$e^{-j(7\pi/16)}$	$e^\pi$	$e^{j(9\pi/16)}$	$e^{j(\pi/4)}$
$S_3$	$e^{j(9\pi/16)}$	$e^{j(\pi/4)}$	$e^0$	$e^{j(\pi/4)}$	$e^{j(\pi/16)}$	$e^{j(9\pi/16)}$	$e^\pi$	$e^{-j(7\pi/16)}$	$e^{j(\pi/4)}$	$e^{-j(15\pi/16)}$	$e^0$	$e^{-j(15\pi/16)}$	$e^{j(\pi/4)}$	$e^{-j(7\pi/16)}$	$e^\pi$	$e^{j(9\pi/16)}$
$S_4$	$e^{j(9\pi/16)}$	$e^{j(9\pi/16)}$	$e^{j(\pi/16)}$	$e^{j(\pi/4)}$	$e^0$	$e^{j(\pi/4)}$	$e^{j(9\pi/16)}$	$e^{j(9\pi/16)}$	$e^\pi$	$e^{-j(7\pi/16)}$	$e^{-j(15\pi/16)}$	$e^{j(\pi/4)}$	$e^{-j(15\pi/16)}$	$e^{j(\pi/4)}$	$e^{-j(7\pi/16)}$	$e^\pi$
$S_5$	$e^\pi$	$e^{j(9\pi/16)}$	$e^{j(\pi/4)}$	$e^{j(\pi/16)}$	$e^{j(\pi/4)}$	$e^0$	$e^{j(\pi/4)}$	$e^{j(9\pi/16)}$	$e^\pi$	$e^{-j(7\pi/16)}$	$e^{-j(15\pi/16)}$	$e^{j(\pi/4)}$	$e^{-j(15\pi/16)}$	$e^{j(\pi/4)}$	$e^{-j(7\pi/16)}$	$e^\pi$
$S_6$	$e^{-j(7\pi/16)}$	$e^\pi$	$e^{j(9\pi/16)}$	$e^{j(\pi/16)}$	$e^{j(\pi/4)}$	$e^0$	$e^{j(\pi/4)}$	$e^{j(9\pi/16)}$	$e^\pi$	$e^{-j(7\pi/16)}$	$e^{-j(15\pi/16)}$	$e^{j(\pi/4)}$	$e^{-j(15\pi/16)}$	$e^{j(\pi/4)}$	$e^{-j(7\pi/16)}$	$e^\pi$
$S_7$	$e^{-j(15\pi/16)}$	$e^{-j(7\pi/16)}$	$e^\pi$	$e^{j(9\pi/16)}$	$e^{j(\pi/4)}$	$e^{j(\pi/16)}$	$e^0$	$e^{j(\pi/4)}$	$e^{j(9\pi/16)}$	$e^{j(\pi/4)}$	$e^\pi$	$e^{-j(7\pi/16)}$	$e^{-j(15\pi/16)}$	$e^0$	$e^{-j(15\pi/16)}$	$e^{-j(7\pi/16)}$
$S_8$	$e^0$	$e^{-j(15\pi/16)}$	$e^{j(\pi/4)}$	$e^{-j(7\pi/16)}$	$e^\pi$	$e^{j(9\pi/16)}$	$e^{j(\pi/16)}$	$e^0$	$e^{j(\pi/4)}$	$e^{j(\pi/4)}$	$e^{j(9\pi/16)}$	$e^{j(\pi/16)}$	$e^\pi$	$e^{-j(7\pi/16)}$	$e^{-j(15\pi/16)}$	$e^0$
$S_9$	$e^{-j(15\pi/16)}$	$e^{-j(15\pi/16)}$	$e^{j(\pi/4)}$	$e^{-j(7\pi/16)}$	$e^{-j(7\pi/16)}$	$e^{j(9\pi/16)}$	$e^{j(\pi/16)}$	$e^{j(\pi/4)}$	$e^0$	$e^{j(\pi/4)}$	$e^{j(\pi/4)}$	$e^{j(9\pi/16)}$	$e^{j(\pi/16)}$	$e^\pi$	$e^{-j(7\pi/16)}$	$e^{-j(15\pi/16)}$
$S_{10}$	$e^{-j(7\pi/16)}$	$e^0$	$e^{-j(15\pi/16)}$	$e^{j(\pi/4)}$	$e^{-j(7\pi/16)}$	$e^\pi$	$e^{j(9\pi/16)}$	$e^{j(\pi/16)}$	$e^{j(\pi/4)}$	$e^{j(\pi/4)}$	$e^0$	$e^{j(\pi/4)}$	$e^{j(9\pi/16)}$	$e^{j(\pi/16)}$	$e^\pi$	$e^{-j(15\pi/16)}$
$S_{11}$	$e^{-j(7\pi/16)}$	$e^{j(\pi/4)}$	$e^0$	$e^{-j(15\pi/16)}$	$e^{j(\pi/4)}$	$e^{-j(7\pi/16)}$	$e^\pi$	$e^{j(9\pi/16)}$	$e^{j(\pi/16)}$	$e^{j(\pi/4)}$	$e^0$	$e^{j(\pi/4)}$	$e^{j(9\pi/16)}$	$e^{j(\pi/16)}$	$e^\pi$	$e^{-j(15\pi/16)}$
$S_{12}$	$e^\pi$	$e^{-j(7\pi/16)}$	$e^{j(\pi/4)}$	$e^{-j(15\pi/16)}$	$e^0$	$e^{-j(15\pi/16)}$	$e^\pi$	$e^{j(9\pi/16)}$	$e^{j(\pi/16)}$	$e^{j(\pi/4)}$	$e^0$	$e^{j(\pi/4)}$	$e^{j(9\pi/16)}$	$e^{j(\pi/16)}$	$e^\pi$	$e^{-j(15\pi/16)}$
$S_{13}$	$e^{j(9\pi/16)}$	$e^\pi$	$e^{-j(7\pi/16)}$	$e^{j(\pi/4)}$	$e^{-j(15\pi/16)}$	$e^0$	$e^{-j(15\pi/16)}$	$e^\pi$	$e^{j(9\pi/16)}$	$e^{j(\pi/16)}$	$e^{j(\pi/4)}$	$e^0$	$e^{j(\pi/4)}$	$e^{j(9\pi/16)}$	$e^{j(\pi/16)}$	$e^\pi$
$S_{14}$	$e^{j(\pi/16)}$	$e^{j(9\pi/16)}$	$e^\pi$	$e^{-j(7\pi/16)}$	$e^{j(\pi/4)}$	$e^{-j(15\pi/16)}$	$e^0$	$e^{-j(15\pi/16)}$	$e^{j(\pi/4)}$	$e^{-j(7\pi/16)}$	$e^\pi$	$e^{j(\pi/4)}$	$e^{j(9\pi/16)}$	$e^{j(\pi/16)}$	$e^{j(\pi/4)}$	$e^{j(\pi/16)}$
$S_{15}$	$e^{j(\pi/4)}$	$e^{j(\pi/16)}$	$e^\pi$	$e^{-j(7\pi/16)}$	$e^{j(\pi/4)}$	$e^{-j(15\pi/16)}$	$e^0$	$e^{-j(15\pi/16)}$	$e^{j(\pi/4)}$	$e^{-j(7\pi/16)}$	$e^\pi$	$e^{j(\pi/4)}$	$e^{j(9\pi/16)}$	$e^{j(\pi/16)}$	$e^0$	$e^{j(\pi/4)}$
$S_{16}$	$e^{j(\pi/4)}$	$e^{j(\pi/16)}$	$e^{j(\pi/16)}$	$e^\pi$	$e^{-j(7\pi/16)}$	$e^{j(\pi/4)}$	$e^{-j(15\pi/16)}$	$e^0$	$e^{-j(15\pi/16)}$	$e^{j(\pi/4)}$	$e^{-j(7\pi/16)}$	$e^\pi$	$e^{j(\pi/4)}$	$e^{j(9\pi/16)}$	$e^{j(\pi/16)}$	$e^0$


 FIGURE 2: The structure of the first decision, where  $i = 1$ , and the observation window length is  $N$ .

 FIGURE 3: The structure of the joint decision, where  $i = 1$ , and the observation window length is  $N$ .

where  $\hat{n}$  and  $\hat{y}_1$  are given by (8). Figure 3 is a structural diagram of this joint decision.

Algorithm 1 introduces the detailed implementation step of proposed MSD scheme. For simple implementation, we only selected the most and second-most reliable symbols here. More metrics can also be involved, which, however, are complexity-intensive and not suitable for our purposes. In essence, when 16 metrics are selected, we arrive at the full MSD. Furthermore, the simulation results in Section 6.2

show that excellent performance has been exhibited even if we only equip the MSD scheme with the most and second-most reliable metrics.

## 5. Estimation Scheme

Clearly, the chip sample  $r_{x,m}$  in (1) is dependent on the transmitted chip symbol  $s_{x,m}$ , but this dependence can be eliminated if we follow the property  $s_{x,m}s_{x,m}^* = 1$ :

$$Gr_{x,m} \triangleq r_{x,m}s_{x,m}^* = he^{j(m\omega T_c + \theta)} + \eta_{x,m}s_{x,m}^*, \quad 1 \leq x \leq P_1, 1 \leq m \leq M, \quad (10)$$

where  $P_1$  is the length of the preamble,  $1 \leq P_1 \leq P$ , and  $P = 8$  is the maximum length.  $\eta_{x,m}s_{x,m}^*$  is statistically equivalent to  $\eta_{x,m}$ . In this context, our purpose is to estimate  $\omega T_c$  based on the sample observations given in (10).

Within  $N$  symbol intervals, the normalized autocorrelation function of samples is as follows:

$$Z(n) = \frac{1}{(P_1 - n)L_1} \sum_{x=1}^{P_1} \sum_{m=2}^{L_1} (Gr_{x,m}Gr_{x,m-n}^*) = |h|^2 e^{j\omega n T_c} + \eta_n, \quad (11)$$

where  $L_1$  is the sample number of the preamble, and  $2 \leq L_1 \leq M$ .  $\eta_n$  represents the integrated noise.  $n$  denotes the

Input:  
 $r_{x,m}$ : baseband samples of the  $x$ th bit  $E[x]$   
 $J$ : PPDU payload length  
 $L_1$ : sample number of the  $x$ th symbol in the preamble  
 $M$ : length of the PN sequence  
 $K$ : the maximum chip delay number  
 $N$ : observation window length  
 $P_1$ : preamble length  
 In order to simplify the detection process,  $K$  is set 4 in this algorithm.

Output:  
 $\hat{s}_{y_1}$  and  $\{\hat{s}_{y_k}\}$ : detect the spread spectrum sequence of the actual data.

- (1) initial  $J = 44, M = 16, K = 4, Z(n) = 0, Q = 0$
- (2)  $r_{x,m}$  to eliminate the influence of  $s_{x,m}$
- (3) for  $x = 1; x \leq P_1; x++$  for
- (4) for  $m = 2; m \leq M; m++$  for
- (5)  $Gr_{x,m} \leftarrow r_{x,m} s_{x,m}^*$
- (6) end for
- (7) end for
- (8) for  $n = 1; n \leq K; n++$  do
- (9) for  $x = 1; x \leq P_1; x++$  do
- (10) for  $m = 2; m \leq L_1; m++$  do
- (11)  $Z(n) \leftarrow Z(n) + Gr_{x,m} Gr_{x,m-n}^*$
- (12) end for
- (13) end for
- (14)  $Z(n) \leftarrow Z(n) L_1 (P_1 - n)$
- (15)  $Q \leftarrow Q + Z(n)$
- (16) end for
- (17) The quantization function of frequency offset estimator  $g(Q) \leftarrow (2/K + 1) \arg(Q)$ , where  $\hat{\varphi} \triangleq \omega T_c = g(Q)$
- (18) for  $x = 1; x \leq P + (J/4); x++$
- (19) for  $y = 1; y \leq 16; y++$
- (20) for  $m = 1; m \leq 16; m++$
- (21)  $r_{x,m} \leftarrow r_{x,m} e^{-jm\hat{\varphi}}$
- (22)  $w_{x,y} \leftarrow w_{x,y} + r_{x,m} s_{y,m}^*$
- (23) end for
- (24)  $V_{x,y} \leftarrow |w_{x,y}|^2$
- (25) end for
- (26) end for
- (27) for  $i = 1; i \leq L/4N; i++$
- (28) for  $n = 1; n \leq N; n++$
- (29) for  $\hat{y}_1 = 1; \hat{y}_1 \leq 16; \hat{y}_1++$
- (30) for  $\hat{y}_2 = 1; \hat{y}_2 \leq 16; \hat{y}_2++$
- (31)  $V_{N(i-1)+n,\hat{y}_1} \leftarrow \arg \max_{1 \leq \hat{y}_1 \leq 16} \{V_{N(i-1)+n,\hat{y}_1}\}$
- (32)  $V_{N(i-1)+n,\hat{y}_2} \leftarrow \arg \max_{1 \leq \hat{y}_2 \leq 16, \hat{y}_2 \neq \hat{y}_1} \{V_{N(i-1)+n,\hat{y}_2}\}$
- (33) end for
- (34) end for
- (35) end for
- (36) end for
- (37) find  $\hat{n}$  and  $\hat{s}_{y_1}$  if  $V_{N(i-1)+n,\hat{y}_1}$  is maximum, let the judgment result of the  $\hat{n}$ th symbol be  $\hat{s}_{y_1}$
- (38) find  $\{\hat{s}_{y_k}\}$  for  $n \neq \hat{n}$  if  $|w_{N(i-1)+n,\hat{y}_1} + \sum_{n \neq \hat{n}} w_{N(i-1)+n,\hat{y}_k}|^2, k \in \{1, 2\}$  is maximum
- (39) return  $\hat{s}_{y_1}$  and  $\{\hat{s}_{y_k}\}$

ALGORITHM 1: The proposed detection algorithm.

number of chip delays, and  $1 \leq n \leq K$ .  $K$  represents the maximum chip-delay number.

Following the idea in [24], a simple estimation scheme without phase unwrapping can be expressed as follows:

$$\hat{\varphi} = \widehat{\omega T_c} = g(Q), \quad (12)$$

where the quantization function  $g(Q)$  is

$$g(Q) = \frac{2}{K+1} \arg(Q), \quad (13)$$

where  $Q = \sum_{n=1}^K Z(n)$ . The structure of this estimator is shown in Figure 4.

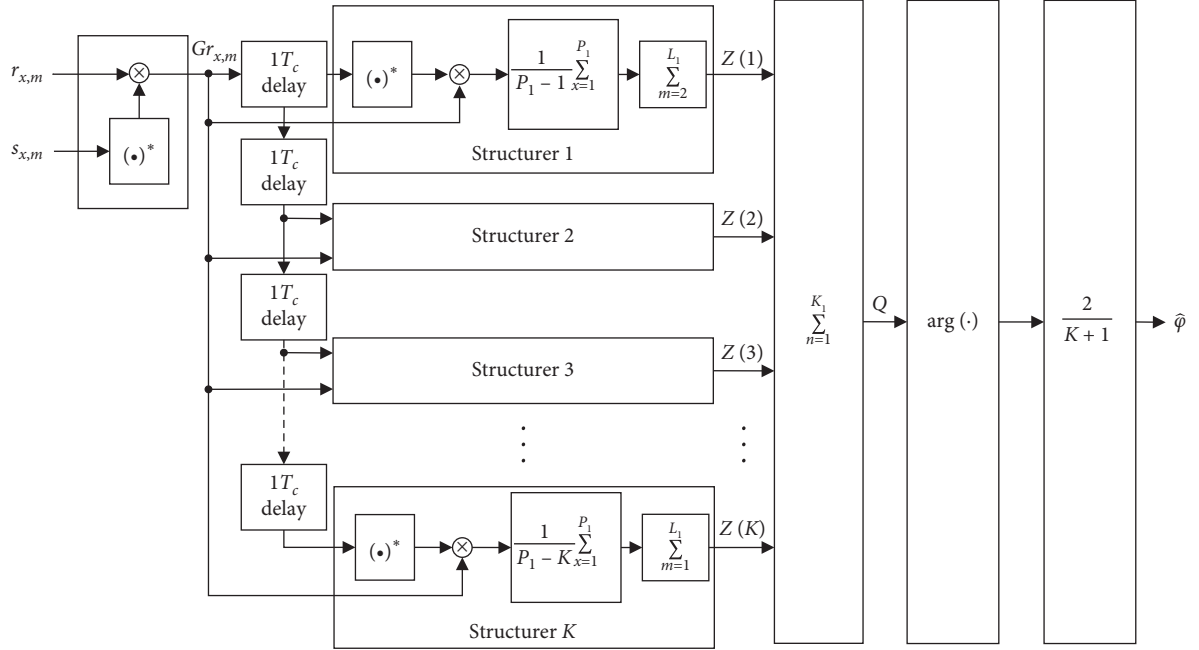
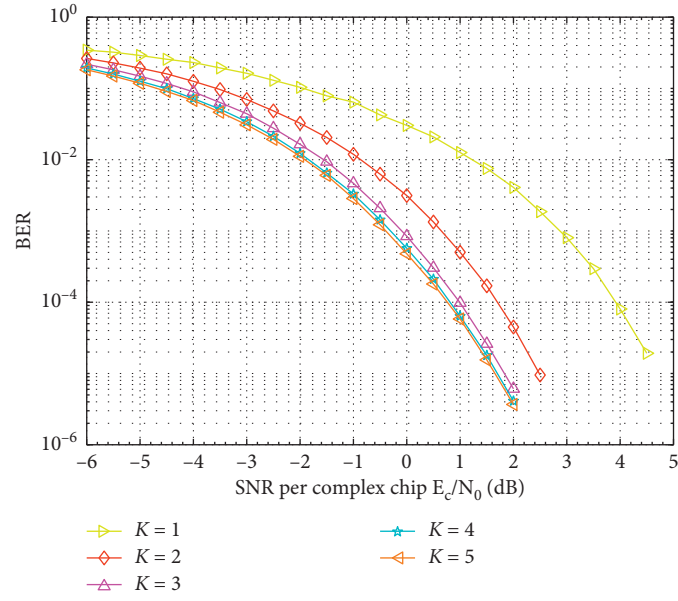


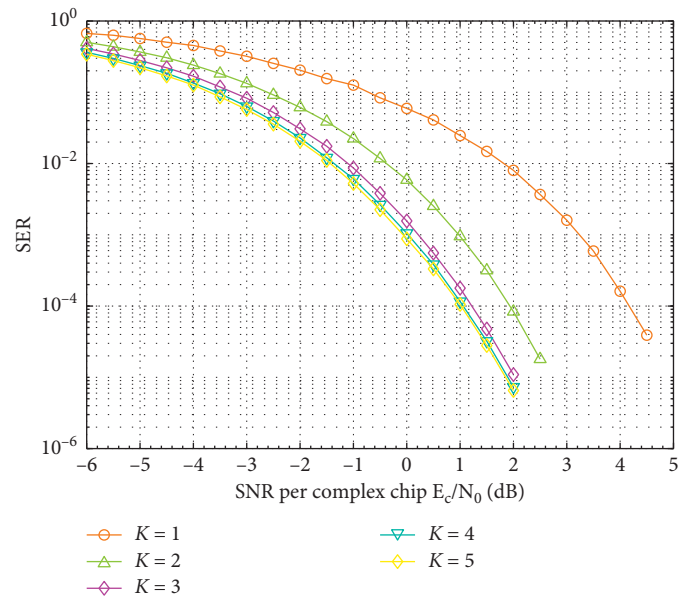
FIGURE 4: The structure diagram of frequency offset estimator.

TABLE 2: Parameters used in simulations.

Parameter	Detailed description
Channel condition	Slow fading or pure AWGN
Power of the complex AWGN	1/SNR
Power of Rayleigh fading channel	Normalized
Detection scheme	MSD
Compensation scheme	Precompensation
Timing synchronization	Perfect
Data modulation	MPSK
Symbols	16-ary orthogonal
PPDU payload length (bits)	176
Spreading factor	16
Chip rate (Mchip/s)	1
Binary data rate (kb/s)	250
Carrier frequency (MHz)	786
CFO $f$ (ppm)	Symmetrical triangular distribution in $(-80, 80)$
CPO $\theta$ (rads)	Uniform distribution in $(-\pi, \pi)$
PN length $M$	16
Preamble length $P_1$	8
Sample number $L_1$	16



(a)



(b)

FIGURE 5: Continued.

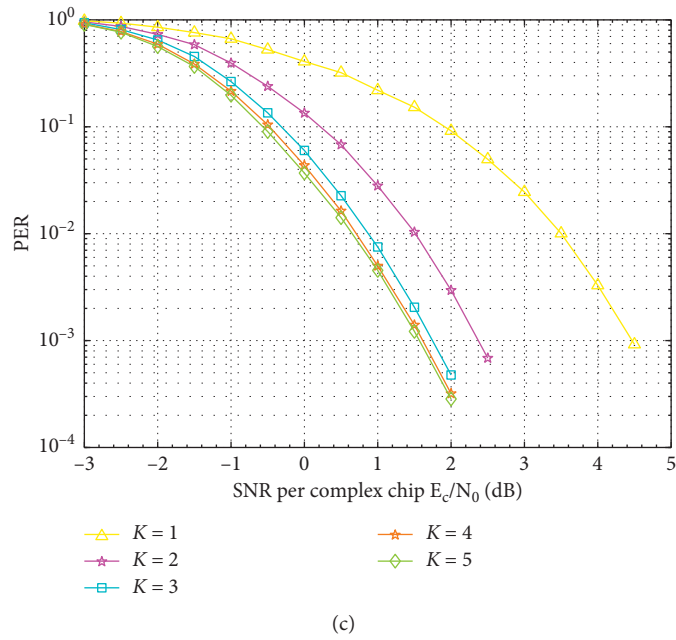


FIGURE 5: In a pure AWGN channel, the effect of parameter  $K$  on the performance of the full estimator in (16),  $N = 2$ . (a) BER performance; (b) SER performance; (c) PER performance.

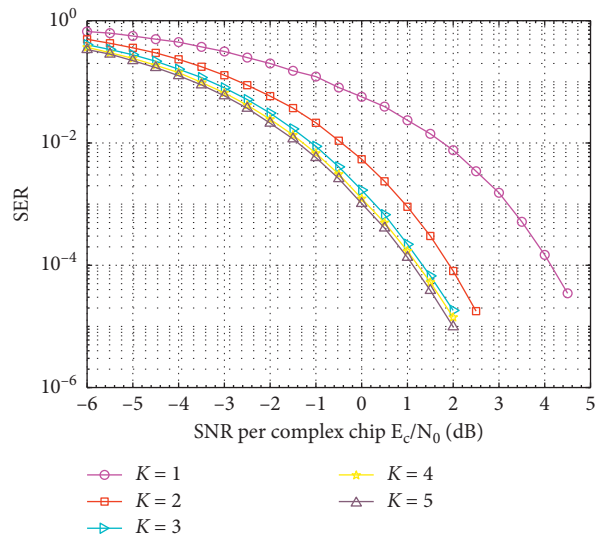
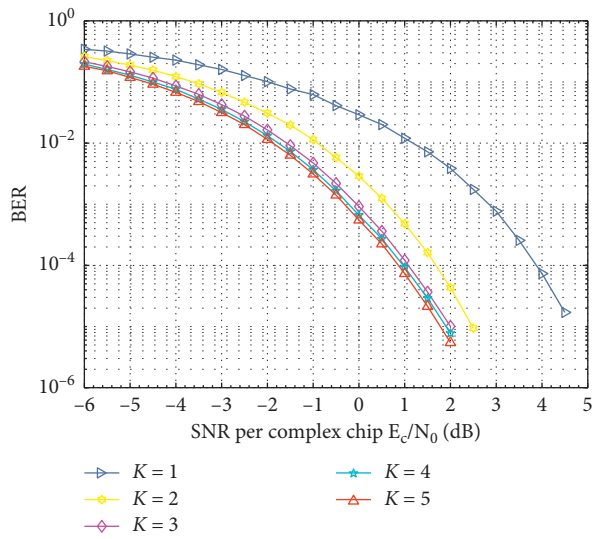
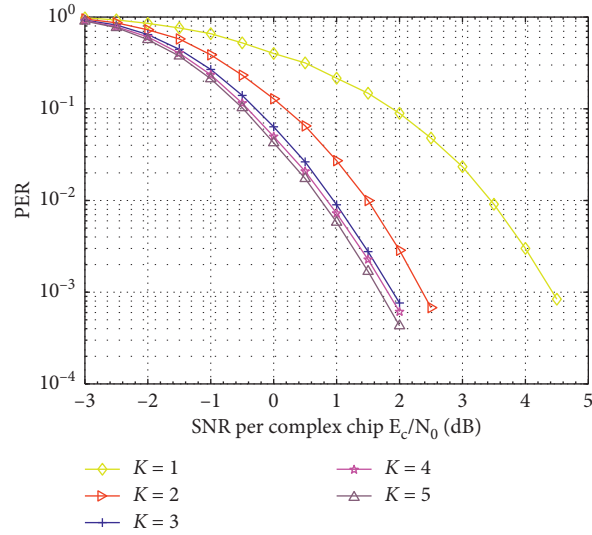


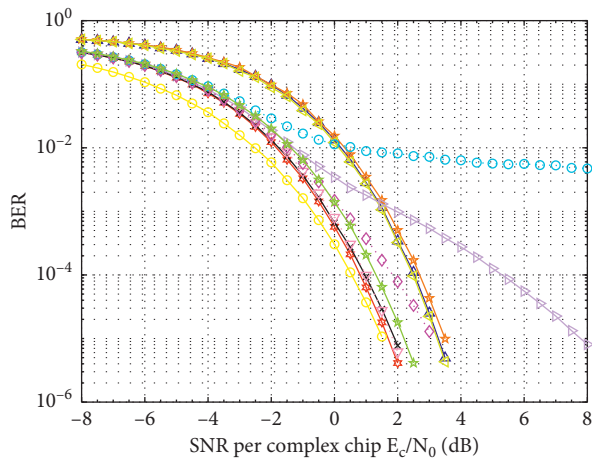
FIGURE 6: Continued.





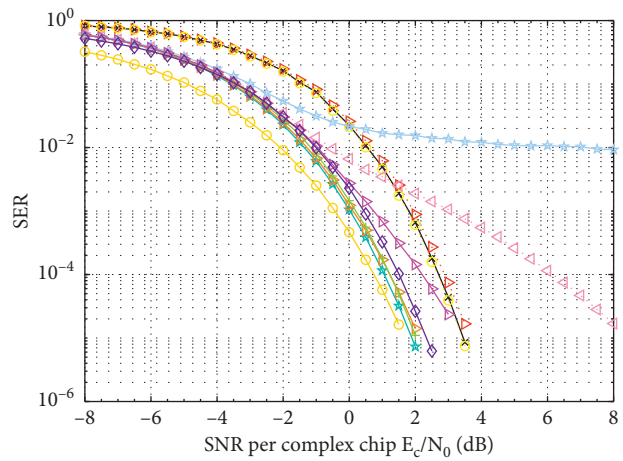
(c)

FIGURE 6: In a pure AWGN channel, the effect of parameter  $K$  on the performance of the simplified estimator in (15),  $N = 2$ . (a) BER performance; (b) SER performance; (c) PER performance.



- SBSBD, estimator in (16)
- ★— SBSBD, estimator in (14)
- ▲— SBSBD, estimator in (15)
- ✱—  $N = 2$ , proposed, estimator in (16)
- ▽—  $N = 2$ , proposed, estimator in (14)
- ✱—  $N = 2$ , proposed, estimator in (15)
- ▽—  $N = 3$ , proposed, estimator in (16)
- $N = 3$ , proposed, estimator in (14)
- ◇—  $N = 3$ , proposed, estimator in (15)
- ★— Optimal noncoherent scheme
- Optimal coherent scheme

(a)



- ✱— SBSBD, estimator in (16)
- ▷— SBSBD, estimator in (14)
- SBSBD, estimator in (15)
- ★—  $N = 2$ , proposed, estimator in (16)
- ▷—  $N = 2$ , proposed, estimator in (14)
- ▷—  $N = 2$ , proposed, estimator in (15)
- ★—  $N = 3$ , proposed, estimator in (16)
- ★—  $N = 3$ , proposed, estimator in (14)
- ▷—  $N = 3$ , proposed, estimator in (15)
- ★— Optimal noncoherent scheme
- Optimal coherent scheme

(b)

FIGURE 7: Continued.

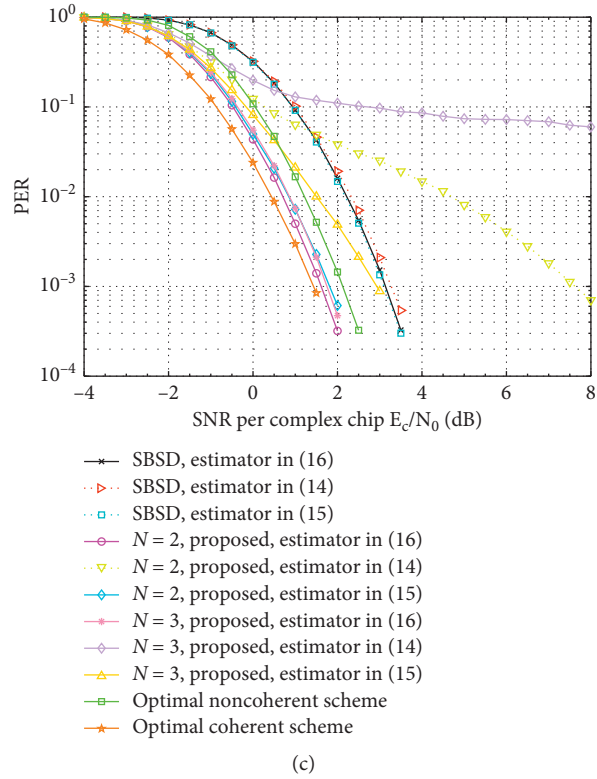
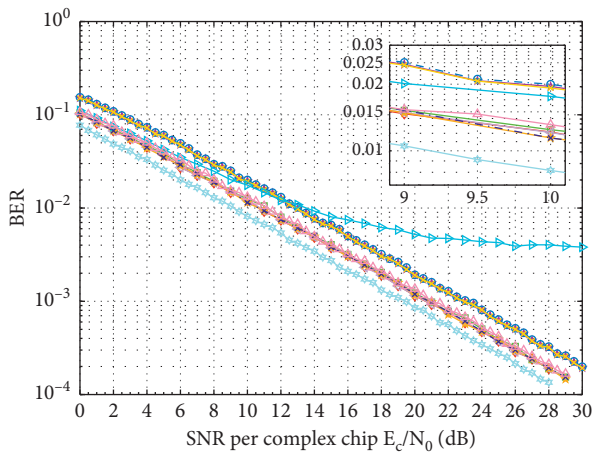
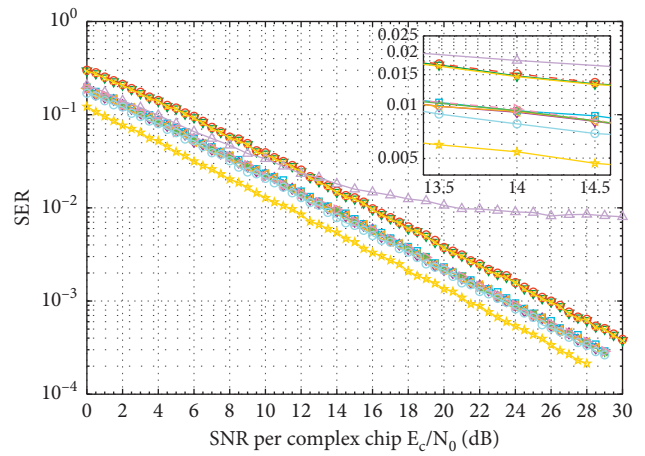


FIGURE 7: Performance comparison of different receivers in pure AWGN channel. (a) BER performance; (b) SER performance; (c) PER performance.



- \*— SBSBD, estimator in (16)
- o— SBSBD, estimator in (14)
- x— SBSBD, estimator in (15)
- ◇—  $N = 2$ , proposed, estimator in (16)
- $N = 2$ , proposed, estimator in (14)
- ▽—  $N = 2$ , proposed, estimator in (15)
- ★—  $N = 3$ , proposed, estimator in (16)
- ▶—  $N = 3$ , proposed, estimator in (14)
- \*—  $N = 3$ , proposed, estimator in (15)
- △— Optimal noncoherent scheme
- ◇— Optimal coherent scheme

(a)



- ▽— SBSBD, estimator in (16)
- o— SBSBD, estimator in (14)
- x— SBSBD, estimator in (15)
- ◇—  $N = 2$ , proposed, estimator in (16)
- $N = 2$ , proposed, estimator in (14)
- ▽—  $N = 2$ , proposed, estimator in (15)
- ★—  $N = 3$ , proposed, estimator in (16)
- ▶—  $N = 3$ , proposed, estimator in (14)
- \*—  $N = 3$ , proposed, estimator in (15)
- △— Optimal noncoherent scheme
- ◇— Optimal coherent scheme

(b)

FIGURE 8: Continued.

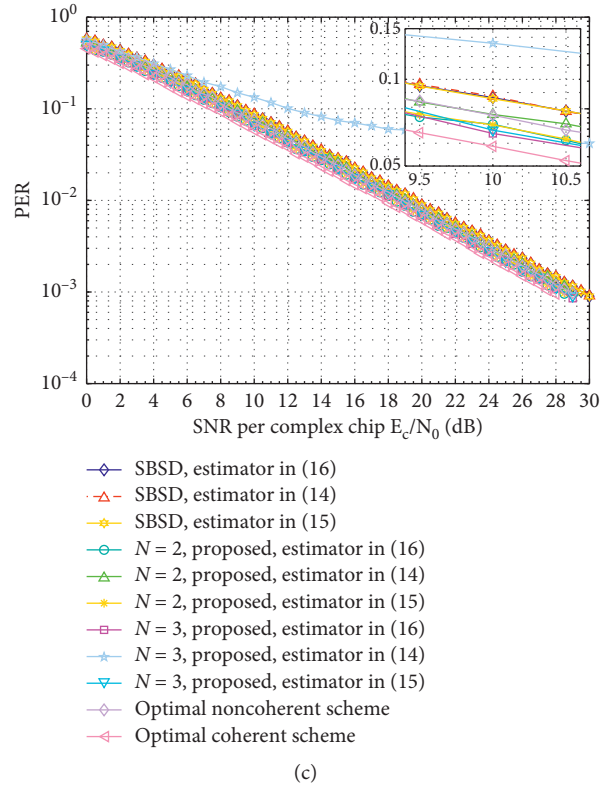


FIGURE 8: Performance comparison of different receivers in slow fading Rayleigh channel. (a) BER performance; (b) SER performance; (c) PER performance.

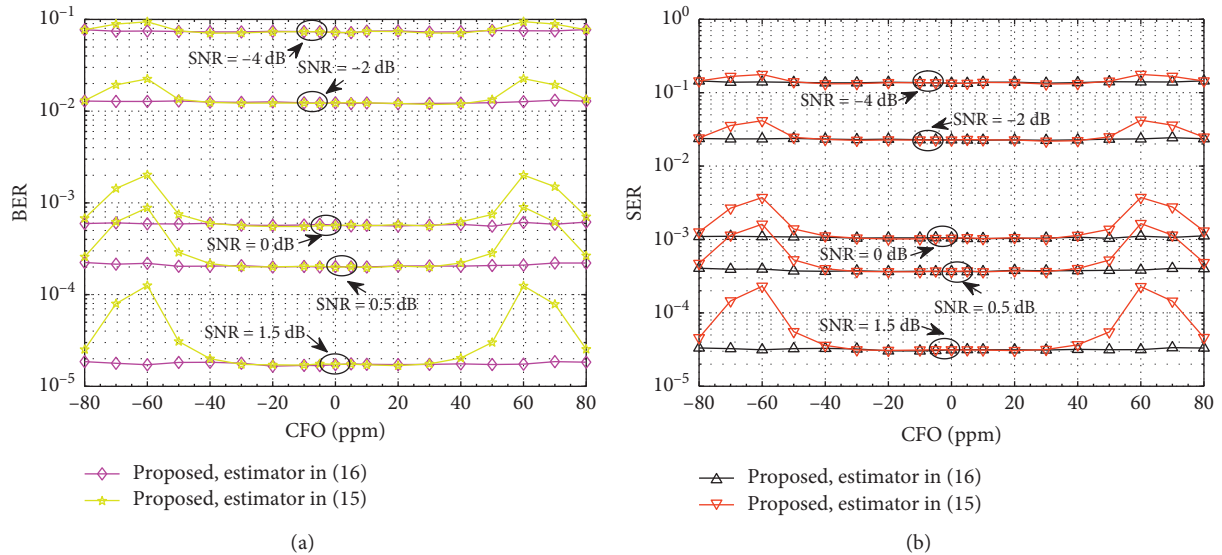


FIGURE 9: Continued.

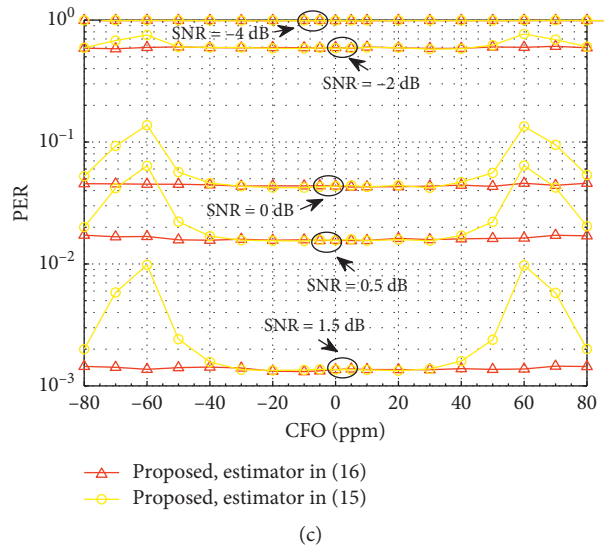


FIGURE 9: Detection performance comparisons of the proposed scheme under various estimators versus CFO over pure AWGN channel,  $N = 2$ . (a) BER performance; (b) SER performance; (c) PER performance.

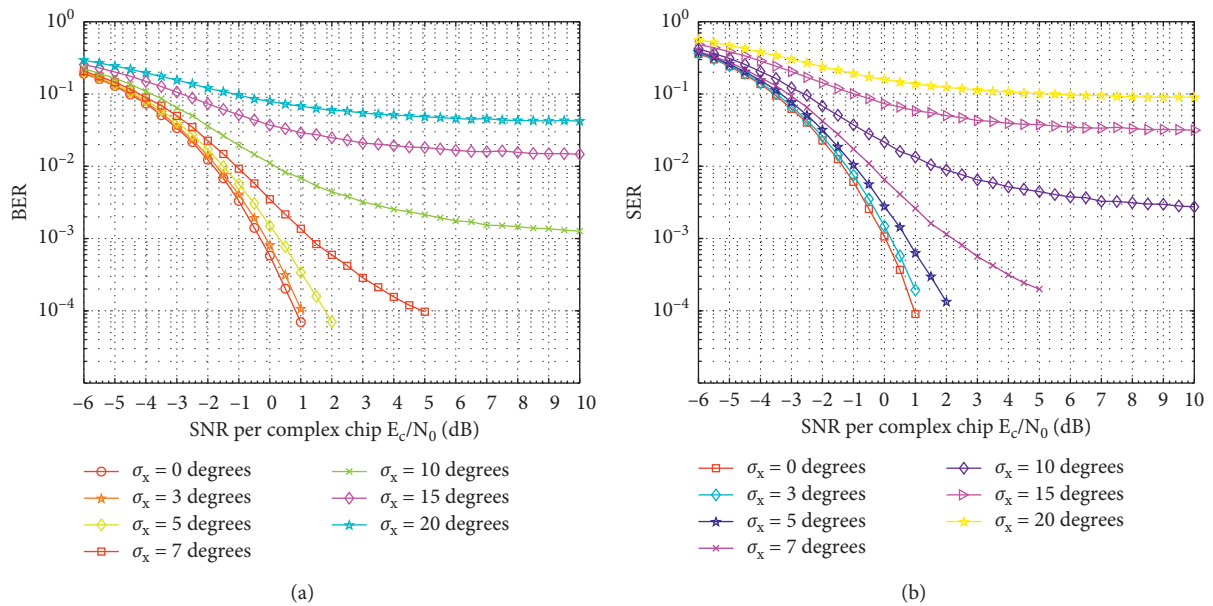
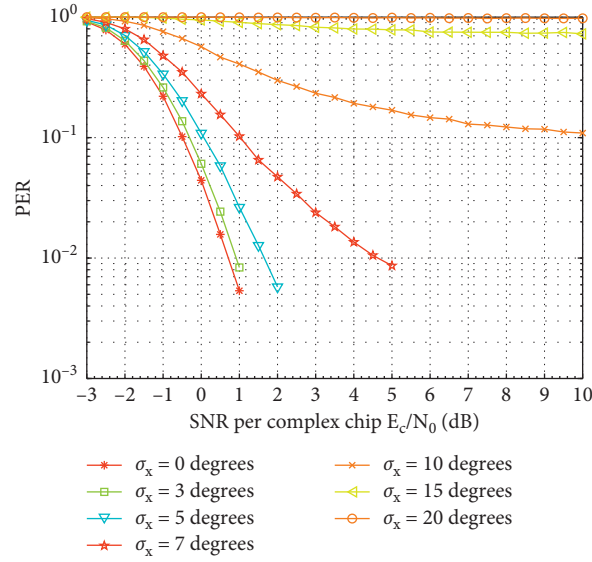
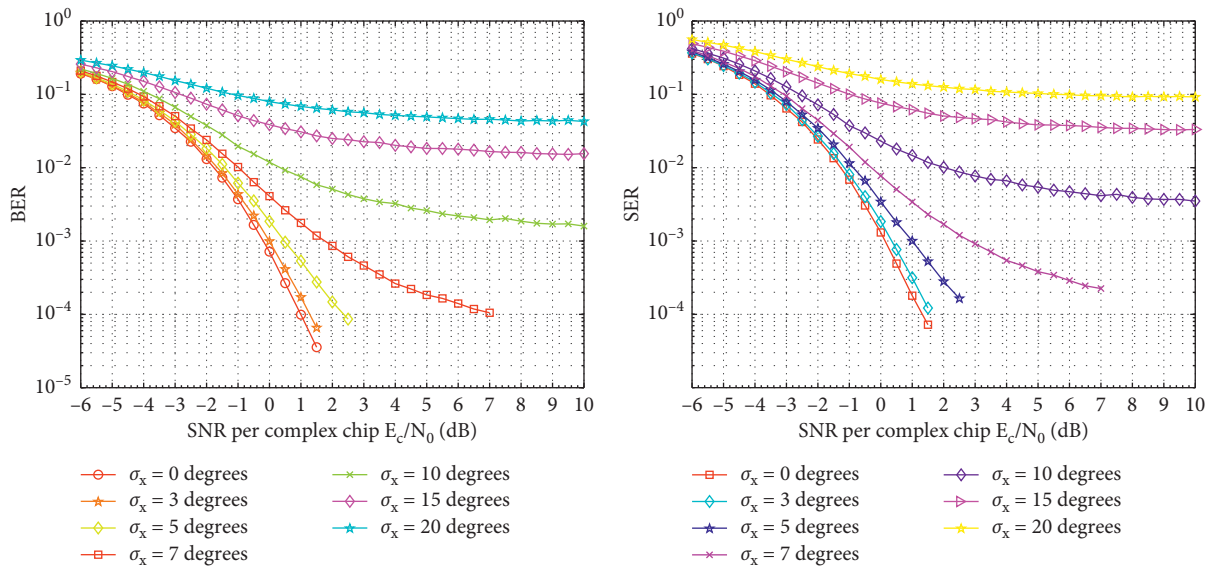


FIGURE 10: Continued.



(c)

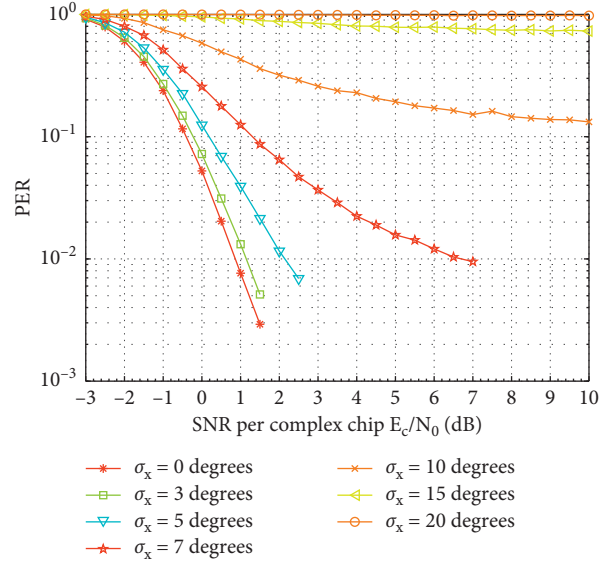
FIGURE 10: In the pure AWGN channel, the proposed scheme is compared with the detection performance of dynamic CPO under the full estimator in (16);  $N = 2$ . (a) BER performance; (b) SER performance; (c) PER performance.



(a)

(b)

FIGURE 11: Continued.



(c)

FIGURE 11: In the pure AWGN channel, the proposed scheme is compared with the detection performance of dynamic CPO under simplified estimator in (15);  $N = 2$ . (a) BER performance; (b) SER performance; (c) PER performance.

It is apparent from (13) and Figure 4 that the estimation process involves complex inverse tangent operation.

According to our previous work [21, 25–27], two simplified estimation schemes can be obtained:

$$\hat{\varphi} \approx \begin{cases} \frac{2}{K+1} \frac{\text{Im}(Q)}{\text{Re}(Q)}, & \text{if } \text{Re}(Q) > 0 \text{ and } |\text{Re}(Q)| \geq |\text{Im}(Q)|, \\ \frac{2}{K+1} \left( \frac{\pi}{2} - \frac{\text{Re}(Q)}{\text{Im}(Q)} \right), & \text{if } \text{Im}(Q) > 0 \text{ and } |\text{Re}(Q)| < |\text{Im}(Q)|, \\ \frac{2}{K+1} \left( -\pi + \frac{\text{Im}(Q)}{\text{Re}(Q)} \right), & \text{if } \text{Re}(Q) < 0 \text{ and } |\text{Re}(Q)| \geq |\text{Im}(Q)|, \\ \frac{2}{K+1} \left( -\frac{\pi}{2} - \frac{\text{Re}(Q)}{\text{Im}(Q)} \right), & \text{if } \text{Im}(Q) < 0 \text{ and } |\text{Re}(Q)| < |\text{Im}(Q)|, \end{cases} \quad (14)$$

$$\hat{\varphi} \approx \begin{cases} \frac{2}{K+1} \frac{\text{Im}(Q)}{\sqrt{\text{Re}^2(Q) + \text{Im}^2(Q)}}, & \text{if } \text{Re}(Q) > 0 \text{ and } |\text{Re}(Q)| \geq |\text{Im}(Q)|, \\ \frac{2}{K+1} \left( \frac{\pi}{2} - \frac{\text{Re}(Q)}{\sqrt{\text{Re}^2(Q) + \text{Im}^2(Q)}} \right), & \text{if } \text{Im}(Q) > 0 \text{ and } |\text{Re}(Q)| < |\text{Im}(Q)|, \\ \frac{2}{K+1} \left( -\pi - \frac{\text{Im}(Q)}{\sqrt{\text{Re}^2(Q) + \text{Im}^2(Q)}} \right), & \text{if } \text{Re}(Q) < 0 \text{ and } |\text{Re}(Q)| \geq |\text{Im}(Q)|, \\ \frac{2}{K+1} \left( -\frac{\pi}{2} + \frac{\text{Re}(Q)}{\sqrt{\text{Re}^2(Q) + \text{Im}^2(Q)}} \right), & \text{if } \text{Im}(Q) < 0 \text{ and } |\text{Re}(Q)| < |\text{Im}(Q)|. \end{cases} \quad (15)$$

TABLE 3: On the pure AWGN channel, the implementation complexity of the proposed receiver and the full form receiver and  $N = 2$ .

Scheme	$(\cdot)(\cdot)^*$	$(\cdot) + (\cdot)$	$ \cdot ^2$
Proposed	576	573	34
Full complexity	8192	8064	256

For integrity of this work, we also give the full estimation scheme here.

$$\hat{\varphi} = \begin{cases} \frac{2}{K+1} \tan^{-1} \left( \frac{\text{Im}(Q)}{\text{Re}(Q)} \right), & \text{if } \text{Re}(Q) > 0 \text{ and } |\text{Re}(Q)| \geq |\text{Im}(Q)|, \\ \frac{2}{K+1} \left( \frac{\pi}{2} - \tan^{-1} \left( \frac{\text{Re}(Q)}{\text{Im}(Q)} \right) \right), & \text{if } \text{Im}(Q) > 0 \text{ and } |\text{Re}(Q)| < |\text{Im}(Q)|, \\ \frac{2}{K+1} \left( -\pi + \tan^{-1} \left( \frac{\text{Im}(Q)}{\text{Re}(Q)} \right) \right), & \text{if } \text{Re}(Q) < 0 \text{ and } |\text{Re}(Q)| \geq |\text{Im}(Q)|, \\ \frac{2}{K+1} \left( -\frac{\pi}{2} - \tan^{-1} \left( \frac{\text{Re}(Q)}{\text{Im}(Q)} \right) \right), & \text{if } \text{Im}(Q) < 0 \text{ and } |\text{Re}(Q)| < |\text{Im}(Q)|. \end{cases} \quad (16)$$

A data-aided detection scheme is considered for simple implementation. However, the non-data-aided detection method can also be applied. This follows from the fact that the modulated data within the sample chip can be easily wiped out with the aid of any PN code using cross-correlation operation. Then, the CFOE can be easily estimated and compensated. At present, there are many other CFO estimation schemes [28–31]. These schemes involve complex mathematical operations, such as the logarithmic operation, the exponential operation, and the trigonometric operation. Our scheme further simplifies these complex operations, as shown in (14) and (15).

## 6. Simulation Result

In this section, we evaluate the bit error rate (BER), symbol error rate (SER), and packet error rate (PER) performance of various detection schemes. Note that, in the simulation, the PPDU payload length is set to 22 bytes. We choose the maximum in 780 MHz frequency band as the carrier frequency, that is, 786 MHz. The detailed simulation parameters are shown in Table 2.

*6.1. Influence of Maximum Chip-Delay Number  $K$  on Detection Performance.* The performance of IEEE 802.15.4c MPSK receiver can be improved by introducing a compatible maximum chip-delay number  $K$ . In slow fading Rayleigh channel and the pure AWGN channel with different  $K$ , we compared the BER, SER, and PER of our

proposed MSD scheme with the full estimator in (16) and the simplified estimator in (15).

It can be seen from Figures 5 and 6 that when the maximum chip-delay number  $K$  increases from 1 to 5, the BER, SER, and PER performance can improved under the pure AWGN channel. In particular, as depicted in Figure 5(c), when  $\text{PER} = 1 \times 10^{-3}$ , as  $K$  increases from 1 to 2, the SNR gain is approximately 2.2 dB; when  $K$  increases from 2 to 3, the SNR gain is about 0.5 dB; when  $K$  increases from 3 to 4, the SNR gain is about 0.1 dB. Furthermore,  $K = 3$  is sufficient to meet the performance requirements of the receiver in pure AWGN channel [9]. Also, the improvement is so small when the maximum chip-delay number ranges from 4 to 5, so we set the maximum chip-delay number to be 4, that is,  $K = 4$ .

*6.2. Detection Performance Comparison.* The BER, SER, and PER results for various detection schemes under pure AWGN channel and slow fading Rayleigh channel are, respectively, shown in Figures 7 and 8. In theory, the full MSD scheme is extremely close to the optimal coherent detection with the increase of the observation window length  $N$ . The implementation of the full MSD scheme is too complex. For the convenience of comparison, we use the optimal coherent detection to replace the simulation results of the full MSD scheme. We take the optimal coherent detection as the lowest bound.

As shown in Figure 7, when  $N = 2$ , the simplified estimation in (14) would lead to serious error floor. This is

caused by the continuous accumulation of larger estimation errors in (3). However, when the full estimation in (16) and the simplified estimation in (15) are used, the detection performance is excellent. There is a little gap between those and the optimal coherent detection, especially at high SNR. Furthermore, when we have  $1 \times 10^{-3}$ , compared with the SBSD method, the proposed scheme can achieve gain about 1.6 dB.

When  $N$  is increased from 2 to 3, the performance of the proposed detection schemes decreases. This is because when  $N = 3$ , the error caused by the estimation scheme introduces a large accumulation in (3), and a mismatch is then observed between the estimator and the detector. In conclusion, the estimation scheme in this paper is especially suitable for the detection scheme, wherein the observation window length  $N$  is set to be 2. Moreover, when  $N = 2$ , the performance gap between our proposed scheme and the optimal coherent detection is so small, and there is almost no more room for improvement. Therefore, we choose  $N$  as 2 in the subsequent simulations. In addition, as shown in Figure 8, we can draw similar conclusions under slow fading Rayleigh channel, which, however, is not illustrated here.

**6.3. Frequency Offset Robustness of the Proposed Scheme in Pure AWGN Channel.** In the pure AWGN channel, we show the BER, SER, and PER performance results with different estimation schemes in Figure 9. CFO  $f$  obeys a symmetry triangular distribution at  $(-80, +80)$  ppm. The results of the full estimation in (16) are used as a benchmark. As shown in Figure 9, for the simplified estimation in (15), the detection performance is good for CFO between  $+60$  and  $-60$  ppm. However, the performance fluctuates when the CFO is greater than  $+60$  ppm or less than  $-60$  ppm. In addition, the performance fluctuation increases with the increase of SNR. However, according to the CFO probability distribution characteristic, the probability that the absolute value of CFO exceeds 60 is 0.0625, which is very small. Thus, the proposed detection scheme is not sensitive to frequency offset.

**6.4. CPO Robustness under Pure AWGN Channel.** In this part, we study the detection performance of the proposed receiver in pure AWGN channel with changing carrier phase, where  $N = 2$ . In Figures 10 and 11, the proposed scheme is robust to dynamic phase jitter. The phase  $\theta$  is modeled as a Wiener process, wherein its initial value is uniformly chosen from  $(-\pi, \pi)$ . As shown in Figures 10 and 11, the proposed scheme is robust to dynamic phase jitter. The performance of the proposed receiver does not significantly degrade if we increase the standard deviation of jitter from  $0^\circ$  to  $3^\circ$ . In addition, an irreducible error floor is observed for the estimators given in (15) and (16) with the increase of SNR.

**6.5. Complexity Analysis.** We compare the implementation complexity of various detection schemes in pure AWGN channels. It is assumed that the full MSD and the proposed detection scheme are equipped with the same estimator. The

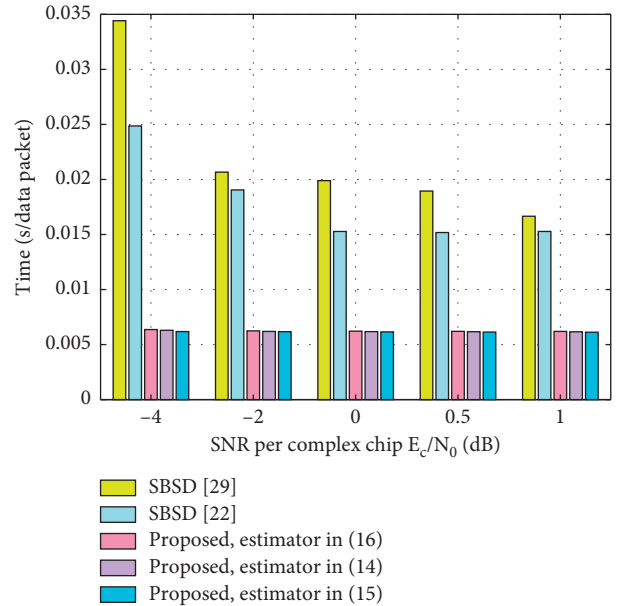


FIGURE 12: Average running time for different detection schemes in pure AWGN channel;  $N = 2$ .

discrepancy in receiver implementation complexity is determined by the metrics given in (3), (5), and (9). Note that we set  $J$ ,  $L_1$ , and  $P_1$  to the maximum, *that is*,  $J = 44$ ,  $L_1 = 16$ , and  $P_1 = 8$ . The structure block diagram of multiplication operation is shown in Figure 3 of [32]. Complex addition is the addition of two complex numbers. It is assumed that a comparison operation is equivalent to an addition operation. As shown in Table 3, our proposed detection scheme only requires 576 complex multiplications, 573 complex additions, and 34 modular squaring operations. The full MSD given in Section 3 requires 8192 complex multiplications, 8064 complex additions, and 256 modular squaring operations. Obviously, compared with the full MSD, the complexity of our scheme is extremely reduced.

In addition, the average running time can also partly reflect the implementation complexity. Specifically, for different detection schemes, we develop various simulations by running enough number of transmission frames. In fact,  $10^5$  frames of data are implemented, and the average running time is achieved. Surprisingly, as shown in Figure 12, when the SNR is  $-4$  dB, the average running time for the traditional SBSD developed from [23] is 4 times as much as that of our proposed MSD scheme. Furthermore, as for the SBSD developed from [33], the average running time is 5.5 times as much as that of our MSD scheme.

## 7. Conclusions

In this paper, a simple but reliable MSD scheme for IEEE 802.15.4c MPSK receiver has been proposed, wherein the CFO has been estimated and compensated by using preamble assisted method. Experimental results showed that our detection performance can meet the requirements of WSN with only four maximum chip delays. In addition, when the standard deviation of the phase jitter is as high as



$3^\circ$ , the performance does not significantly decrease. Finally, compared with the full MSD scheme, our improved scheme is more attractive in terms of complexity. Therefore, the research results of this paper have a positive role in promoting the engineering application of the IoT in the field of new smart city.

In order to avoid the channel and CFO estimation, double-differential modulation is famously used as shown in [34–37]. This idea can be directly borrowed and implemented in our detection scheme for further complexity reduction. Note, however, that more performance loss is exhibited in this case.

## Data Availability

All of the underlying data in this manuscript are available from the corresponding author upon request.

## Conflicts of Interest

The authors declare that there are no conflicts of interest.

## Acknowledgments

This work was partially supported by the National Natural Science Foundation of China (61701172, 41605122, 61701059, 61701062, 61801170, and 61772175), the Key Laboratory of Middle Atmosphere and Global Environment Observation (LAGEO-2021-04), the Natural Science Foundation of Henan Province (162300410097 and 162300410096), the Scientific and Technological Innovation Team of Colleges and Universities in Henan Province (20IRTSTHN018), Postdoctoral Science Foundation of University of Electronic Science and Technology of China (Y02006023601721), the Program for Everest Scholar Talents Development in Tibet University, and the Program for Science and Technology Innovation Talents in the University of Henan Province (Educational Committee) (17HASTIT025).

## References

- [1] M.-D. González-Zamar, E. Abad-Segura, E. Vázquez-Cano, and E. López-Meneses, "IoT technology applications-based smart cities: research analysis," *Electronics*, vol. 9, no. 8, p. 36, 2020.
- [2] H. Habibzadeh, T. Soyata, B. Kantarci, A. Boukerche, and C. Kaptan, "Sensing, communication and security planes: a new challenge for a smart city system design," *Computer Networks*, vol. 144, pp. 163–200, 2018.
- [3] G. Zhang, H. Wen, J. Pu, and J. Tang, "Build-in wiretap channel I with feedback and LDPC codes by soft decision decoding," *IET Communications*, vol. 11, no. 11, pp. 1808–1814, 2017.
- [4] X. Li, M. Zhao, Y. Liu et al., "Secrecy analysis of ambient backscatter NOMA systems under I/Q imbalance," *IEEE Transactions on Vehicular Technology*, vol. 69, no. 10, pp. 12286–12290, 2020.
- [5] X. Li, Q. Wang, Y. Liu, T. A. Tsiftsis, Z. Ding, and A. Nallanathan, "Uav-aided multi-way NOMA networks with residual hardware impairments," *IEEE Wireless Communications Letters*, vol. 9, no. 9, pp. 1538–1542, 2020.
- [6] X. Li, Q. Wang, M. Liu et al., "Cooperative wireless-powered NOMA relaying for B5G IoT networks with hardware impairments and channel estimation errors," *IEEE Internet of Things Journal*, vol. 8, 2020.
- [7] M. Zhan, J. Wu, H. Wen, and P. Zhang, "A novel error correction mechanism for energy-efficient cyber-physical systems in smart building," *IEEE Access*, vol. 6, pp. 39037–39045, 2018.
- [8] M. Zhan, Z. Pang, D. Dzung, and M. Xiao, "Channel coding for high performance wireless control in critical applications: survey and analysis," *IEEE Access*, vol. 6, pp. 29648–29664, 2018.
- [9] IEEE, *IEEE 802.15.4-2015 Standard, IEEE Standard for Low-Rate Wireless Networks*, IEEE Press, New York, NY, USA, 2016.
- [10] IEEE, *Information Technology-Telecommunications and Information Exchange between Systems-Local and Metropolitan Area Networks-specific Requirements-Part 15-4: Wireless Medium Access Control (MAC) and Physical Layer (PHY) Specifications for Low-Rate Wireless Personal Area Networks (WPANs)*, IEEE Press, New York, NY, USA, 2018.
- [11] T. Suzuki and T. Mizuno, "Multiple-symbol differential detection scheme for differential amplitude modulation," *International Zurich Seminar on Digital Communications: Mobile Communications: Advanced Systems Components*, Springer-Verlag, Berlin, Germany, 1994.
- [12] C. Xu, S. X. Ng, and L. Hanzo, "Multiple-symbol differential sphere detection and decision-feedback differential detection conceived for differential QAM," *IEEE Transactions on Vehicular Technology*, vol. 65, no. 10, pp. 8345–8360, 2015.
- [13] S. G. Wilson, J. Freebersyser, and C. Marshall, "Multi-symbol Detection of M-DPSK," *1989 IEEE Global Telecommunications Conference and Exhibition "Communications Technology for the 1990s and beyond"*, Dallas, TX, USA, 1989.
- [14] V. Lottici and Z. Tian, "Multiple symbol differential detection for UWB communications," *IEEE Transactions on Wireless Communications*, vol. 7, no. 5, pp. 1656–1666, 2008.
- [15] J. Jalden and B. Ottersten, "On the complexity of sphere decoding in digital communications," *IEEE Transactions on Signal Processing*, vol. 53, no. 4, pp. 1474–1484, 2005.
- [16] A. Schenk and R. F. H. Fischer, "Compressed-sensing (decision-feedback) differential detection in impulse-radio ultra-wideband systems," *IEEE Transactions on Communications*, vol. 59, no. 6, pp. 121–125, 2011.
- [17] Y. Li, J. Wei, X. Wang, and Q. Yu, "Multiple symbol differential detection based on sphere decoding for unitary space-time modulation," *Science in China Series F: Information Sciences*, vol. 52, no. 1, pp. 126–137, 2009.
- [18] IEEE, *ISO/IEC/IEEE 802.15.4-2018 Standard, Information Technology-Telecommunications and Information Exchange between Systems-Local and Metropolitan Area Networks-specific Requirements-Part 15-4: Wireless Medium Access Control (MAC) and Physical Layer (PHY) Specifications for Low-Rate Wireless Personal Area Networks (WPANs)*, IEEE Press, New York, NY, USA, 2018.
- [19] K.-H. Lin, W.-H. Chiu, and J.-D. Tseng, "Low-complexity architecture of carrier frequency offset estimation and compensation for body area network systems," *Computers & Mathematics with Applications*, vol. 64, no. 5, pp. 1400–1408, 2012.
- [20] H. J. Jeon, T. Demeetchai, W. G. Lee et al., "IEEE 802.15.4 BPSK receiver architecture based on a new efficient detection scheme," *IEEE Transactions on Signal Processing*, vol. 58, no. 9, pp. 4711–4719, 2010.

- [21] G. Zhang, H. Wen, L. Wang, L. Song, J. Tang, and R. Liao, "Simple and robust near-optimal single differential detection scheme for IEEE 802.15.4 BPSK receivers," *IET Communications*, vol. 13, no. 2, pp. 186–197, 2019.
- [22] J. L. Buetefer and W. G. Cowley, "Frequency offset insensitive multiple symbol detection of MPSK," in *Proceedings of the 2000 IEEE International Conference on Acoustics, Speech, and Signal Processing*, Istanbul, Turkey, June 2000.
- [23] S. Kay and P. Hall, "Fundamentals of statistical signal processing, volume ii: detection theory," *Technometrics*, vol. 37, no. 4, pp. 465–466, 1993.
- [24] M. Luise and R. Reggiannini, "Carrier frequency recovery in all-digital modems for burst-mode transmissions," *IEEE Transactions on Communications*, vol. 43, no. 2/3/4, pp. 1169–1178, 1995.
- [25] G. Zhang, D. Wang, L. Song et al., "Simple non-coherent detection scheme for IEEE 802.15.4 BPSK receivers," *Electronics Letters*, vol. 53, no. 9, pp. 628–629, 2017.
- [26] G. Zhang, H. Wen, L. Wang et al., "Multiple symbol differential detection scheme for IEEE 802.15.4 BPSK receivers," *IEICE Transactions on Fundamentals of Electronics, Communications and Computer Sciences*, vol. E101.A, no. 11, pp. 1975–1979, 2018.
- [27] G. Zhang, C. Shi, C. Han et al., "Implementation-friendly and energy-efficient symbol-by-symbol detection scheme for IEEE 802.15.4 O-QPSK receivers," *IEEE Access*, vol. 8, pp. 158402–158415, 2020.
- [28] M. R. Bhatnagar, R. Vishwanath, M. K. Arti, and V. Bhatnagar, "A new iterative decoder of space-time data in time selective mimo channels," *Wireless Personal Communications*, vol. 42, no. 1, pp. 131–142, 2007.
- [29] M. R. Bhatnagar, R. Vishwanath, and V. Bhatnagar, "Performance analysis of space-time block codes in flat fading mimo channels with offsets," *EURASIP Journal on Wireless Communications and Networking*, vol. 2007, no. 1, p. 7, 2007.
- [30] M. R. Bhatnagar, R. Vishwanath, and M. K. Arti, "On blind estimation of frequency offsets in time varying MIMO channels," in *Proceedings of the 2006 IFIP International Conference on Wireless and Optical Communications Networks*, Bangalore, India, April 2006.
- [31] M. R. Bhatnagar and R. Vishwanath, "A new semiblind scheme based on second and fourth order statistics for decoding of space-time data in time selective MIMO channels," *Wireless Personal Communications*, vol. 47, no. 2, pp. 193–205, 2008.
- [32] D. Park, C. S. Park, and K. Lee, "Simple design of detector in the presence of frequency offset for IEEE 802.15.4 LR-WPANs," *IEEE Transactions on Circuits and Systems II: Express Briefs*, vol. 56, no. 4, pp. 330–334, 2009.
- [33] J. H. Do, J. S. Han, H. J. Choi et al., "A Coherent Detection-Based Symbol Detector Algorithm for 2.45GHz LR-WPAN Receiver," in *Proceedings of the Tencon 2005-2005 IEEE Region 10 Conference*, Melbourne, Australia, November 2005.
- [34] M. R. Bhatnagar and A. Hjørungnes, "SER Expressions for Double Differential Modulation," in *Proceedings of the 2007 IEEE Information Theory Workshop on Information Theory for Wireless Networks*, Bergen, Norway, January 2007.
- [35] M. R. Bhatnagar, A. Hjørungnes, and L. Song, "Cooperative communications over flat fading channels with carrier offsets: a double-differential modulation approach," *Eurasip Journal on Advances in Signal Processing*, vol. 2008, no. 1, p. 11, 2008.
- [36] M. Bhatnagar, A. Hjørungnes, and L. Song, "Double-differential orthogonal space-time block codes for arbitrarily correlated Rayleigh channels with carrier offsets," *IEEE Transactions on Wireless Communications*, vol. 9, no. 1, pp. 145–155, 2010.
- [37] M. R. Bhatnagar and O. Tirkkonen, "PI decoding in double differential modulation based decode-and-forward cooperative system," *IEEE Communications Letters*, vol. 17, no. 5, pp. 860–863, 2013.

## Research Article

# Spectral Efficiency of the Multiway Massive System over Rician Fading Channels

Junyi He , Junnan Zhang , Cheng Song , and Mengxiang Wu 

College of Computer Science and Technology, Henan Polytechnic University, 454000 Jiaozuo, Henan, China

Correspondence should be addressed to Junyi He; hejunyi@hpu.edu.cn

Received 15 October 2020; Revised 20 December 2020; Accepted 25 January 2021; Published 25 February 2021

Academic Editor: Khaled Maaiuf Rabie

Copyright © 2021 Junyi He et al. This is an open access article distributed under the Creative Commons Attribution License, which permits unrestricted use, distribution, and reproduction in any medium, provided the original work is properly cited.

In this study, we consider a multiway massive multi-input multi-output (MIMO) relay network over Rician fading channels, where all users intend to share their information with the other users via amplify-and-forward (AF) relays equipped with a great number of antennas. More practical, the imperfect channel state information (CSI) is taken into account. To evaluate the performance of the considered networks, we derived an analytical approximation expression for the spectral efficiency with zero-forcing (ZF) receivers in a closed form. To obtain more insights, the asymptotic analysis as the number of relay antenna approaching infinity is carried out. Finally, the power scaling law is analyzed for two scenarios. The results reveal that (1) massive MIMO is capable of compensating the loss caused by Rician fading, (2) the sum spectral efficiency increases with the increase of the Rician factor, and (3) deploying large-scale antenna is effective to save cost and keep performance.

## 1. Introduction

Massive multiple-input multiple-output in mobile communication technology networks has greatly improved the fluency and stability of communication and provides users with a better experience, which has been defined as a core technology of the fifth generation mobile [1, 2]. Massive MIMO technology is first setup by Marzetta [3] who releases the multicell multiuser noncooperative system, and now, it has got attention on both industry and academic. By deploying tens or hundreds of antennas at the base station (BS) and servicing many users, massive MIMO has an advantage capability to increase the spectral efficiency and energy efficiency by orders of magnitude [4] and, to some extent, preclude the interuser interference (IUI) with low-complexity linear precoding/detecting schemes such as maximal-ratio combining (MRC), maximal-ratio transmission (MRT), zero-forcing, and minimum mean square error (MMSE) [5, 6].

At the same time, multiway relay networks have a significant role on practical application scenarios, e.g., data transmission in multimedia conference call and exchanging information occurring in sensor nodes and data centres in

wireless communication [7, 8]. Thanks to the multiplexing gain, multiway relay networks have become an upgrading technology to further push the performance of spectral efficiency of relay networks [9, 10].

In order to obtain the advantages of massive MIMO and multiple relays, the combination of the two technologies has sparked a great interest [11–15]. In [11], the authors investigated the performance of the multiway relay networks, which figures out the transmit power of each user and relay stays in an increasing trend as the number of relay antennas decreases. Moreover, authors in [12] derive multiway massive MIMO relay networks in wireless communication and the technology of power transfer at the same time. It is shown in [13] that the transmit powers at user and relay nodes can be reduced with large antenna array and keep a fixed quality of service in the multiway massive MIMO networks. In [14], the authors study the performance of multiway relay networks and release that the pairwise multiway relay network achieves the maximum multiplexing gain whenever the number of participating sources is limited to two. In [15], the asymptotic performance of MWRNs with massive MIMO by modelling the channels is investigated, and it concludes that the transmitting power of the user node

is inversely proportional to the number of antennas when the channel is aging. However, the common of the above works has the assumption that all communication are accomplished under the conditions of Rayleigh fading channels [16], which is not practical in some scenarios of line of sights (LoS) environments, such as television broadcasting, satellite communication, and radio relay communication [17, 18].

Motivated by the above discussion, we consider a multiway massive MIMO relay network over Rician fading channels with ZF processing in this study. More practical, we suppose that the channel is not perfect, which can be estimated by the massive MIMO relay with MMSE. Specifically, by utilizing the ZFR/ZFT algorithm, we obtain an approximate analytical evaluation for the spectral efficiency of considered multiway massive MIMO relay networks in close. To obtain more insights, the power scaling law is explored as the amount of relay antennas grows to infinity. The main contributions of the study are shown as follows:

- (1) With fixing the value of the Rician factor and comparing the trend of the sum spectral efficiency, we find out that massive MIMO can compensate the loss caused by Rician fading;
- (2) The sum spectral efficiency grows logarithmic when the Rician fading factor  $K$  grows, and moreover, the spectral efficiency presents highlight when  $K=0$ ;
- (3) Using the estimated amount obtained, the closed form for the spectral efficiency with ZF processing is obtained. Furthermore, the power scale laws are involved in two parts. And in the first case,  $M \rightarrow \infty$ ; we find that the spectral efficiency increases as the antennas increases. As for the other case that the transmit power of users reduces with  $M$  growing, the effects of estimate error and interpair interference can be ignored.

The rest of this study is organized as follows: in Section 2, we introduce the network model and give the channel model, channel estimation, and information transmission. In Section 3, we analyze the spectral efficiency. The power scaling law is considered in Section 4, and the numerical results are shown in Section 5. The last section concludes the study.

Notations: superscript  $(A)^T$  is the transpose of the matrix  $A$ ,  $(A)^*$  is the conjugate of the matrix, and  $(A)^H$  represents the Hermitian of the matrix  $A$ . While,  $\mathbb{E}\{|\cdot|\}$  and  $\mathbb{V}\text{ar}\{|\cdot|\}$  represent the expectation and the variance operators, respectively.  $A_k$  and  $a_k$  are the  $k^{\text{th}}$  columns of matrix  $A$ . The notation  $A \sim \text{CN}(0, 1)$  denotes that  $A$  is a circularly symmetric Gaussian distributed random variable.

## 2. Network Model

We consider a multiway massive MIMO AF relay network as shown in Figure 1, which includes one  $M$  antenna relay and  $N$  single antenna users. Each user with one antenna tries to exchange their information with the other  $N-1$  users with the aid of the AF relay station, which is equipped with  $M$  antennas ( $M \gg N$ ). We suppose that the direct link cannot

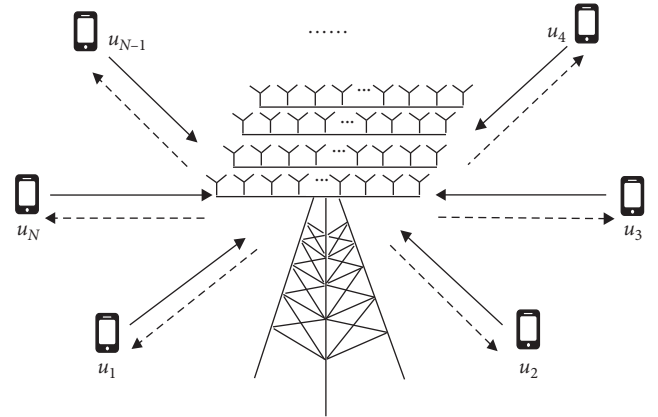


FIGURE 1: System model.

be achieved caused by high path loss and/or severe shadowing.

**2.1. Channels Model.** Let  $G \in \mathbb{C}^{M \times N}$  be the channel matrix from the  $N$  users to the relay, which contains the small-scale and/or the large-scale fading, and it can be written as

$$G = HD^{(1/2)}, \quad (1)$$

where  $D \in \mathbb{C}^{N \times N}$  is a diagonal matrix which contains large-scale fading coefficients, with the restrain by  $\beta_n$  in the  $N^{\text{th}}$  diagonal element. Contrast to [19], due to the channel is in Rician fading, it can be written as [20]

$$H = \sqrt{\frac{K_n}{K_n + 1}} \bar{H} + \sqrt{\frac{1}{K_n + 1}} \tilde{H}, \quad X \in \{A, B\}. \quad (2)$$

In the above formula,  $K_n$  is the Rician  $K$ -factor coefficient which combines the  $N-1$  user pair and the relay, while  $\tilde{H}$  is the random part of the Rician fading channels with the communication of the  $N-1$  user to relay, and all elements in both are independent and identically distributed (i.i.d.)  $\text{CN}(0, 1)$  random variables [21].  $\bar{H}$  is the deterministic part of Rician fading channels with the restrain of the  $N-1$  user pair, which is an arbitrary rank  $[\bar{H}]_{mn} = e^{-j(m-1)(2\pi d/\lambda)\sin(\theta_n)}$ , where  $\lambda$  is the wavelength,  $d$  is the antenna spacing, and  $\theta_n$  stands for the arrival angle of the  $N^{\text{th}}$  user.

Under the time division duplex (TDD) operations, the transmission protocol can be described when the information exchange is totally finished among all  $N$  users. When using TDD operation, there are three parts in each coherence interval: channel estimation, multiple access phase, and broadcasting phase.

**2.2. Channel Estimation.** In a wireless communication system, it is a challenge to obtain perfect CSI, especially in massive MIMO systems which equipped with the large number of antenna array at BS. As in [21], we assume that the deterministic component and Rician factor are known during transmission. We define that  $T$  is the length of coherent interval, and  $\tau$  stands for the training duration in each coherent interval, and set  $T > \tau$ . In the training phase, we

assume that all users send their pilot sequences to the relay at the same time, where the pilot sequences are mutually orthogonal. In this situation, we require  $\tau \geq N$ . Then,  $\widehat{G}$  can be written as [19]

$$\widehat{G} = \overline{G}[\Omega(\Omega + I_N)^{-1}]^{(1/2)} + \widehat{G}_w[(\Omega + I_N)^{-1}]^{(1/2)}, \quad (3)$$

where  $\overline{G}$  is the deterministic component with  $\overline{G} = \overline{H}D^{(1/2)}$ , and  $\widehat{G}_w$  is the estimate channel of random component.

During the training step, orthogonal pilot sequences realize the matrix  $\sqrt{P_p}\Phi \in \mathbb{C}^{\tau \times N}$  ( $\tau \geq N$ ), constraint with  $F^H F = I_N$ , where  $F \triangleq \Phi[\Omega(\Omega + I_N)^{-1}]^{(1/2)}$ , and  $p_p = \tau P_u$  is the transmitted pilot power. The pilot matrix with noise received by the base station can be represented as

$$Y_p = \sqrt{P_p}G\Phi^T + N, \quad (4)$$

where  $N \sim \text{CN}(0, I_M)$  is the AWGN vector at the relay. And the remaining term of the receive matrix is

$$Y_{p,w} = \sqrt{P_p}G_w[(\Omega + I_N)^{-1}]^{(1/2)}\Phi^T + N. \quad (5)$$

Then, using MMSE, we can get the estimate of random component  $G_w$  as follows:

$$\widehat{G}_w = \frac{1}{\sqrt{P_p}}Y_p F^* D, \quad (6)$$

where  $D \triangleq ((1/p_p)D^{-1} + I_N)$ .

With the formula (5), we have

$$\widehat{G}_w = \left( G_w + \frac{1}{p_p} Z \right) D, \quad (7)$$

where  $Z \triangleq N F^*$ ,  $Z \sim \text{CN}(0, I_M)$  is the AWGN vector, and  $\widehat{G}_w \sim \text{CN}(0, \widehat{D}_w)$ , and  $[\widehat{D}_w]_{mm} = (\tau P_p \beta_n^2 / \tau P_p \beta_n + 1)$ .

Substituting (7) to (3), the channel estimate matrix of  $G$  can be obtained as [22]

$$\widehat{G} = G - E, \quad (8)$$

where  $\widehat{G}$  and  $E$  are independent with each other, and  $E$  presents the estimation error matrix. In addition,  $\widehat{G} \sim \text{CN}(0, \widehat{D})$  and  $E \sim \text{CN}(0, D_E)$ , where  $\widehat{D}$  and  $D_E$  are the diagonal matrices, and its diagonal elements are  $[\widehat{D}]_{mm} = \sigma_n^2 = (K_n/K_n + 1)\sqrt{(\tau P_p \beta_n^2 / \tau P_p \beta_n + 1) + (\tau P_p \beta_n^2 / \tau P_p \beta_n + 1)}\sqrt{1/(K_n + 1)}$  and  $[D_E]_{mm} = \sigma_{e,n}^2 = \beta_n - \sigma_n^2$ , respectively.

### 2.3. Information Transmission

**2.3.1. Multiple Access Phase.** Based on the estimated channels, data are sent to the relay simultaneously by all users. Let  $x_k$  be the transmitted signal from  $k^{\text{th}}$  user with  $\mathbb{E}\{|x_k|^2\} = 1$ . Thus, at the relay, the received signal is

$$y_R = \sqrt{P_u}Gx + n_r. \quad (9)$$

In above formula,  $x \triangleq [x_1, \dots, x_K]^T$ , and  $n_r \sim \text{CN}(0, I_M)$  indicates the AWGN vector at the relay. With the aid of the

estimated channel and ZF processing technique, the relay combines the received signals from all  $M$  antennas as

$$\tilde{y}_R = W^T y_R, \quad (10)$$

where  $W^T$  is the ZF receiver and can be obtained from [23]

$$W^T = \left( \widehat{G}^H \widehat{G} \right)^{-1} \widehat{G}^H. \quad (11)$$

**2.3.2. Broadcasting Phase.** In this state, it takes  $K-1$  time slots to send signal to all users with the help of the relay. The relay tries to send  $x_{k+1}$  to user  $k$ , when the  $t^{\text{th}}$  time slot comes. Thus, at the relay, for the  $t^{\text{th}}$  time slots, the transmitted signal vector can be written as [9]

$$S_R^{(t)} = \sqrt{\alpha^{(t)} P_u} B^{(t)} x + \sqrt{\alpha^{(t)} C^{(t)}} n_r, \quad (12)$$

where  $B^{(t)} \triangleq A \Pi^{(t)} W^T G$  and  $C^{(t)} \triangleq A \Pi^{(t)} W^T$ , and  $\alpha^{(t)}$  is chosen to satisfy the power constraint at the relay. And  $\Pi^{(t)} \in \mathbb{C}^{N \times N}$  is the permutation matrix at the  $t^{\text{th}}$  time slot as in [8].  $A$ , which represents the ZF precoding matrix, can be written as

$$A = \widehat{G}^* \left( \widehat{G}^T \widehat{G}^* \right)^{-1}, \quad (13)$$

$$\mathbb{E}\left\{ \|S_R^{(t)}\|^2 \right\} = P_r. \quad (14)$$

Substituting (12) into (14), we can have

$$\alpha^{(t)} = \frac{P_r}{P_u Q_1^{(t)} + P_u Q_2^{(t)} + Q_3^{(t)}}, \quad (15)$$

where

$$Q_1^{(t)} \triangleq \mathbb{E}\left\{ \text{Tr}\left[ \left( A \Pi^{(t)} W^T \widehat{G} \right) \left( A \Pi^{(t)} W^T \widehat{G} \right)^H \right] \right\}, \quad (16)$$

$$Q_2^{(t)} \triangleq \mathbb{E}\left\{ \text{Tr}\left[ \left( A \Pi^{(t)} W^T E \right) \left( A \Pi^{(t)} W^T E \right)^H \right] \right\}, \quad (17)$$

$$Q_3^{(t)} \triangleq \mathbb{E}\left\{ \text{Tr}\left[ \left( A \Pi^{(t)} W^T \right) \left( A \Pi^{(t)} W^T \right)^H \right] \right\}.$$

From (12), the transmitted signal can be obtained, and the  $K$  users meet

$$y_u^{(t)} = G^T S_R^{(t)} + n_u^{(t)} = \sqrt{\alpha^{(t)} P_u} G^T B^{(t)} x + \sqrt{\alpha^{(t)} G^T C^{(t)}} n_r + n_u^{(t)}, \quad (18)$$

where  $n_u \sim \text{CN}(0, I_N)$  is the AWGN vector in the end.

## 3. Spectral Efficiency Analysis

In this section, we derive a closed-form expression for the spectral efficiency of massive MIMO multirelay systems over Rician fading channels. In terms of the other time slots, the same analysis can meet the requirement. Depending on the effort of [24], the received signal at the  $n^{\text{th}}$  user  $y_{u,n}^{(1)}$  can be shown as

$$y_{u,n}^{(1)} = \sqrt{\alpha^{(1)} P_u} \mathbb{E}\{g_n^T b_{n+1}^{(1)}\} x_{n+1} + \tilde{N}_n^{(1)}, \quad (19)$$

where

$$\begin{aligned} \tilde{N}_n^{(1)} &\triangleq \sqrt{\alpha^{(1)} P_u} (g_n^T b_{n+1}^{(1)} - \mathbb{E}\{g_n^T b_{n+1}^{(1)}\} x_{n+1}) \\ &+ \sqrt{\alpha^{(1)} P_u} \sum_{i=1}^N g_n^T b_i^{(1)} x_i + \sqrt{\alpha^{(1)} g_n^T C^{(1)} n_r + n_{u,n}^{(1)}}. \end{aligned} \quad (20)$$

For the  $k^{\text{th}}$  user, the worst-case Gaussian noise will produce reachable spectral efficiency, and the formula is

$$\text{SE}_n^{(1)} = \left(\frac{T-\tau}{T}\right) \left(\frac{N-1}{N}\right) \log_2 \left(1 + \frac{\alpha^{(1)} P_u |\mathbb{E}\{g_n^T b_{n+1}^{(1)}\}|^2}{\text{Var}(\tilde{N}_n^{(1)})}\right). \quad (21)$$

To obtain the closed form of the spectral efficiency, we need to calculate  $\mathbb{E}\{g_n^T b_{n+1}^{(1)}\}$  and  $\text{Var}(\tilde{N}_n^{(1)})$ . Due to the independence relationship of  $G$  and  $E$ , we can obtain

$$\mathbb{E}\{g_n^T b_{n+1}^{(1)}\} = \mathbb{E}\{\tilde{g}_n^T A \Pi^{(1)} W^T \tilde{g}_{n+1}\} = 1. \quad (22)$$

Because  $\tilde{N}_n^{(1)}$  has a complex form, which cannot be calculated, and also, it is difficult to get the exact form of  $\text{Var}(\tilde{N}_n^{(1)})$ . However, by using the law of Large Numbers [9], we can have the following approximation.

**Theorem 1.** *With  $M \rightarrow \infty$ , the spectral efficiency can be evaluated as*

$$\text{SE}_n^{(1)} \rightarrow \left(\frac{T-\tau}{T}\right) \left(\frac{N-1}{N}\right) \times \log_2 \left(1 + \frac{\alpha^{(1)} P_u}{\alpha^{(1)} P_u \sum_{i=1}^N I_{n,i} + \alpha^{(1)} \zeta_n + 1}\right), \quad (23)$$

where

$$\alpha^{(1)} \triangleq \frac{M(M-N)P_r}{MP_u \sum_{n=1}^N (1/\sigma_n^2) + P_u \sum_{n=1}^N \sigma_{e,n}^2 \sigma + \sigma}, \quad (24)$$

$$I_{n,i} \triangleq \frac{M\sigma_{i-1}^2 \sigma_{e,i}^2 + M\sigma_{n+1}^2 \sigma_{e,k}^2 + \sigma_{n+1}^2 \sigma_{i-1}^2 \sigma_{e,k}^2 \sigma_{e,i}^2 \sigma}{M(M-N)\sigma_{i-1}^2 \sigma_{n+1}^2},$$

$$\zeta_n \triangleq \frac{M + \sigma_{n+1}^2 \sigma_{e,k}^2 \sigma}{M(M-N)\sigma_{n+1}^2}, \quad (25)$$

$$\sigma \triangleq \sum_{n'=1}^N \frac{1}{\sigma_{n'}^2 \sigma_{n'+1}^2}.$$

*Proof.* See Appendix.  $\square$

#### 4. Power Scaling Laws

In this part, the power scaling law is studied for the considered networks. We mainly focus on these two cases: (1) fix

$P_u, P_r$ , and set  $p_p = (E_p/M^{\alpha_p})$  with the restrain of  $\alpha_p > 0$ ; (2) fix  $E_u, E_r$ , and  $P_p$ , and set  $p_u = (E_u/M^{\alpha_u})$  and  $p_r = (E_r/M^{\alpha_r})$ , with the restrain of  $\alpha_u > 0, \alpha_r > 0$ .

First case: the power scaling laws can be calculated as below when  $M$  has a trend to infinity.

**Theorem 2.** *Fix  $P_u, P_r$ , and  $E_p$ ; set  $p_p = (E_p/M^{\alpha_p})$ , with the restrain of  $\alpha_p$ , we have*

$$\begin{aligned} \text{SE}_n^{(1)} &\rightarrow \left(\frac{T-\tau}{T}\right) \left(\frac{N-1}{N}\right) \\ &\times \log_2 \left(1 + \frac{\alpha^{(1)} P_u}{\hat{\alpha}^{(1)} P_u \sum_{i=1}^N \hat{I}_{n,i} + \hat{\alpha}^{(1)} \hat{\zeta}_n + 1}\right), \end{aligned} \quad (26)$$

where

$$\hat{\alpha}^{(1)} \triangleq \frac{M(M-N)P_r}{MP_u \sum_{n=1}^N (1/\sigma_n^2) + P_u \sum_{n=1}^N \sigma_{e,n}^2 \sigma + \sigma},$$

$$\hat{I}_{n,i} \triangleq \frac{M\sigma_{i-1}^2 \sigma_{e,i}^2 + M\sigma_{n+1}^2 \sigma_{e,k}^2 + \sigma_{n+1}^2 \sigma_{i-1}^2 \sigma_{e,k}^2 \sigma_{e,i}^2 \sigma}{M(M-N)\sigma_{i-1}^2 \sigma_{n+1}^2}$$

$$\hat{\zeta}_n \triangleq \frac{M + \sigma_{n+1}^2 \sigma_{e,k}^2 \sigma}{M(M-N)\sigma_{n+1}^2},$$

$$\sigma^2 \triangleq \frac{K_n}{K_n + 1} \sqrt{\frac{\tau E_p \beta_n^2}{\tau E_p \beta_n + M^{\alpha_p}} + \frac{\tau E_p \beta_n^2}{\tau E_p \beta_n + M^{\alpha_p}} \sqrt{\frac{1}{K_n + 1}}}. \quad (27)$$

*Proof.* By substituting  $P_p = (E_p/M^{\alpha_p})$  and making  $M$  into infinity.

Note 1: Theorem 2 shows that the sum spectral efficiency is not relevant to  $\alpha_p$ , due to the reason that the estimation error becomes a regular number when  $P_p \rightarrow 0$ . Furthermore, with the antennas having a trend of growth, the spectral efficiency increases.

Second case: the users transmit power reduces when the number of antenna  $M$  increases.  $\square$

**Theorem 3.** *Fix  $E_u, E_r$ , and  $P_p$ , when  $P_u = (E_u/M^{\alpha_u})$  and  $P_r = (E_r/M^{\alpha_r})$ , with the restrain  $\alpha_u > 0, \alpha_r > 0$ .*

*Proof.* By substituting  $P_u = (E_u/M^{\alpha_u})$ ,  $P_r = (E_r/M^{\alpha_r})$  and taking  $M$  into infinity.

Note 2: it is shown that the effects of estimate error and interpair interference can be ignored when  $M$  climbs to infinity. When meeting the condition that  $0 < \alpha_u, \alpha_r < 1$ , the spectral efficiency of the user grows in an unlimited trend. When  $\alpha_u = \alpha_r = 1$ , the spectral efficiency of the user is fixed. When  $\alpha_u > 1, \alpha_r > 1$ , the spectral efficiency drops to zero as  $M \rightarrow \infty$ .  $\square$

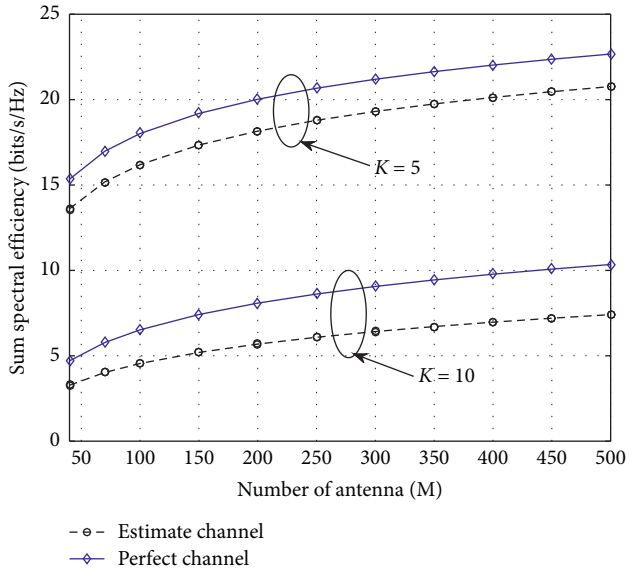


FIGURE 2: Sum spectral efficiency via number of antennas with  $K = 10, 5$ .

## 5. Numerical Results

The sum spectral efficiency is taken as our performance indicator. The sum spectral efficiency can be rewritten follows:

$$SE_{\text{sum}} = \sum_{n=1}^N SE_n^{(1)} \text{ bit/s/Hz.} \quad (28)$$

Figure 2 shows the sum spectral efficiency in a multiway massive MIMO system with ZF processing versus number of antennas with different values of  $K$ . The diamond dotted represents the Monte Carlo results of the spectral efficiency of the multichannel massive MIMO relay, while the dotted circle line represents the analysis result of Part 3. In this figure, we fix  $P_u = 10$  dB,  $N = 8$ ,  $P_p = P_u$ , and  $P_r = 2NP_u$ . In this figure, we can find that the simulation value is in agreement with the Monte Carlo result. Furthermore, we can easily conclude that the ZF processing has a slow growth when the antenna increases heavily.

Figure 3 shows the sum spectral efficiency of the considered system with ZF versus SNR when  $K$  is set to 10 and 5. As can be seen from Figure 3, spectral efficiency grows larger with the increase of SNR. We can learn that the ZF processing has a better performance with SNR growing in a multiway massive MIMO system. In addition, the spectral efficiency decreases with  $K$  growing, which means the performance of the considered system is limited by the Rician factor.

Figure 4 investigates the sum spectral efficiency with different values of  $K$ . As shown in figure, with the increase of  $K$ , the sum spectral efficiency can get an apparent decline,

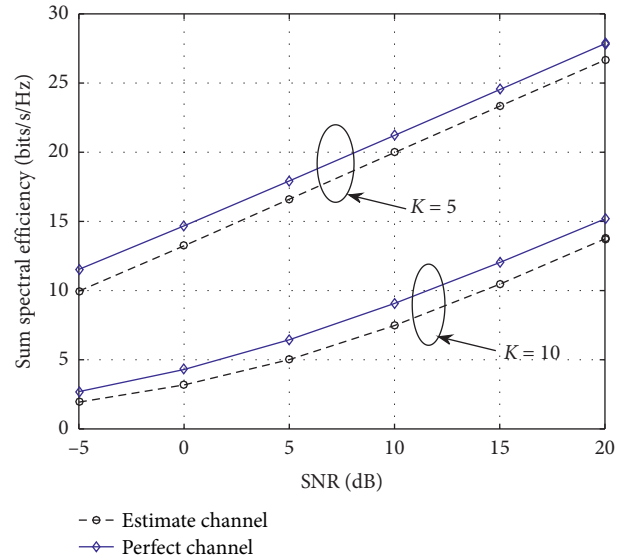


FIGURE 3: Sum spectral efficiency via SNR with  $K = 10, 5$ .

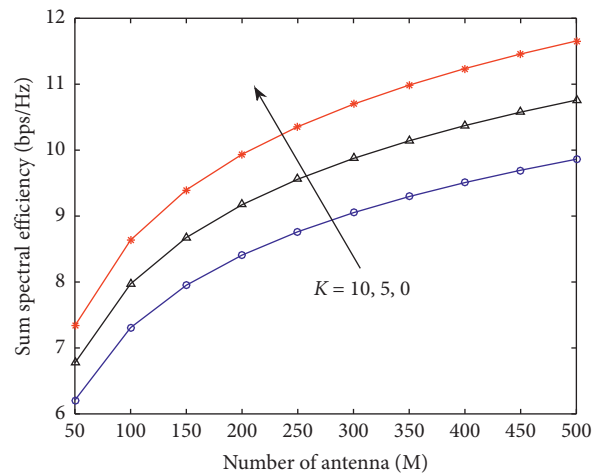
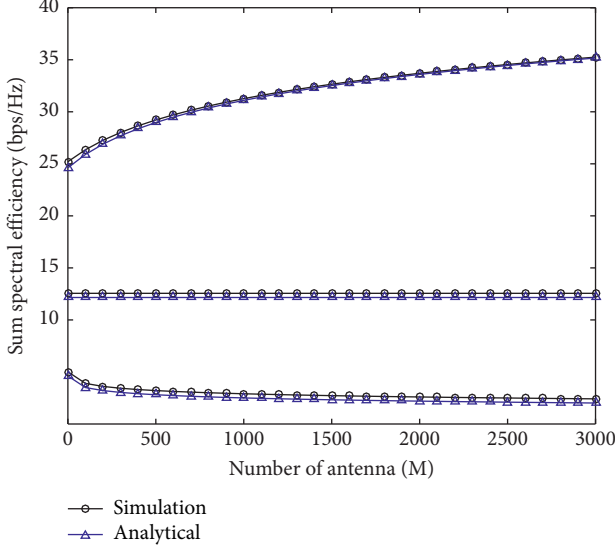


FIGURE 4: Sum spectral efficiency via the Rician fading factor.

which is going to say, the sum spectral efficiency descends with the Rician factor  $K$  rising.

Figure 5 shows the power scaling law versus  $M$  for the transmit power of each user  $P_u = (E_u/M^{\alpha_u})$  and the relay  $p_r = (E_r/M^{\alpha_r})$  of the considered system. In this figure, we set  $N = 8$ ,  $E_u = 10$  dB,  $E_r = 20$  dB,  $P_p = 10$  dB,  $K = 10$  dB, and  $T = 200$ . As we can see that when  $\alpha_u, \alpha_r > 1$ , the sum spectral efficiency reduces to zero, which can get that when the transmit power is reduced too much on each user and relay, the sum spectral efficiency will be greatly reduced. When  $\alpha_u, \alpha_r < 1$ , the sum spectral efficiency grows with the number of antenna  $M$  increasing. When  $\alpha_u = \alpha_r = 1$ , the sum spectral efficiency becomes a constant, which shows that we cannot promote the sum spectral efficiency by making the number of antenna increase.

FIGURE 5: Sum spectral efficiency via  $M$ .

## 6. Conclusions

In this study, we summarized the influence of the Rician factor on the performance of the multiway massive MIMO relay network with ZF processing. We deduced an approximate expression for the spectral efficiency in a closed form. Also, the relationship between the Rician factor and the sum spectral efficiency is obtained. And massive MIMO have an ability to compensate the loss caused by Rician fading. Moreover, we show that ZF processing offers a higher spectral efficiency in most circumstances.

## Appendix

1

**Lemma 1.** Let  $X \in \mathbb{C}^{M \times N}$ ,  $M > N$ . Each row of  $X$  is  $CN(0, D)$ , where  $D$  is a diagonal matrix. Furthermore, let  $\hat{D} \in \mathbb{C}^{N \times N}$  be another diagonal matrix. Then, we have

$$\mathbb{E}\left\{\text{Tr}\left[\hat{D}(X^H X)^{-1}\right]\right\} = \frac{1}{M-N} \sum_{n=1}^N \frac{[\hat{D}]_{nn}}{[D]_{nn}}. \quad (\text{A.1})$$

*Proof.* By expressing  $\text{Tr}[\hat{D}(X^H X)^{-1}] = \sum_{n=1}^N ([\hat{D}]_{nn} / [D]_{nn}) [W^{-1}]_{NN}$ , where  $W$  is a  $K \times K$  central Wishart matrix of  $M$  degrees of freedom, and using [10], Lemma 2.10 is obtained.  $\square$

2

**Lemma 2.** Let  $A \in \mathbb{C}^{M \times M}$ , and  $X \sim CN(0, I_M)$ . Then,

$$\mathbb{E}\left\{|X^T A X|^2\right\} = \text{Tr}(A A^H) + \text{Tr}(A A^*). \quad (\text{A.2})$$

3

Proof of Theorem 1

- (1) Derivation of  $\alpha^{(1)}$ : from (10), to compute  $\alpha^{(1)}$ , we need to compute  $Q_1^{(1)}$ ,  $Q_2^{(1)}$ , and  $Q_3^{(1)}$ . Substituting (5) and (7) into (11) yields

$$Q_1^{(1)} = \mathbb{E}\left\{\text{Tr}\left(\hat{G}^T \hat{G}^*\right)^{-1}\right\} = \frac{1}{M-N} \sum_{n=1}^N (1/\sigma_n^2). \quad (\text{A.3})$$

Where in the last equality, we have used Lemma 1. To compute  $Q_2^{(1)}$ , we substitute (5) and (7) into (12) to obtain

$$Q_2^{(1)} = \sum_{n=1}^N \sigma_{e,n}^2 \mathbb{E}\left\{\text{Tr}\left[\Pi^{(1)} \hat{G}^H \hat{G}^*\right]^{-1} (\Pi^{(1)})^H (\hat{G}^T \hat{G}^*)^{-1}\right\}. \quad (\text{A.4})$$

From the law of large numbers, we have that  $\hat{G}^H \hat{G} \rightarrow M \hat{D}$ , and hence,  $Q_2^{(1)}$  can be approximated as

$$\begin{aligned} Q_2^{(1)} &\rightarrow \sum_{n=1}^N \sigma_{e,n}^2 \mathbb{E}\left\{\text{Tr}\left[\Pi^{(1)} \hat{G}^H \hat{G}^*\right]^{-1} (\Pi^{(1)})^H (\hat{G}^T \hat{G}^*)^{-1}\right\} \\ &= \frac{\varrho}{M(M-N)} \sum_{n=1}^N \sigma_{e,n}^2. \end{aligned} \quad (\text{A.5})$$

Where again, we have used Lemma 1 to obtain the last equality.

Similarly, we obtain

$$Q_3^{(1)} \rightarrow \frac{\varrho}{M(M-N)}. \quad (\text{A.6})$$

Substituting (A.4), (A.5), and (A.6) into (16), we obtain (24).

- (2) Derivation of  $\text{Var}(\tilde{N}_n^{(1)})$ : from (20), we have

$$\begin{aligned} \text{Var}\left(\tilde{N}_n^{(1)}\right) &= \alpha^{(1)} P_u \text{Var}\left(g_n^T b_{n+1}^{(1)}\right) + \alpha^{(1)} P_u \mathbb{E}\left\{|g_n^T b_n^{(1)}|^2\right\} \\ &\quad + \alpha^{(1)} P_u \sum_{i=1, i \neq (n, n+1)}^N \mathbb{E}\left\{|g_n^T b_i^{(1)}|^2\right\} \\ &\quad + \alpha^{(1)} \mathbb{E}\left\{\|g_n^T C^{(1)}\|^2\right\} + 1. \end{aligned} \quad (\text{A.7})$$

- (a) Compute  $\text{Var}(g_n^T b_{n+1}^{(1)})$ , we have

$$\text{Var}\left(g_n^T b_{n+1}^{(1)}\right) = V_1 + V_2 + V_3. \quad (\text{A.8})$$

Where

$$\begin{aligned} V_1 &\triangleq \mathbb{E}\left\{|\hat{g}_n^T A \Pi^{(1)} W^T e_{n+1}|^2\right\}, \\ V_2 &\triangleq \mathbb{E}\left\{|e_n^T A \Pi^{(1)} W^T \hat{g}_{n+1}|^2\right\}, \\ V_3 &\triangleq \mathbb{E}\left\{|e_n^T A \Pi^{(1)} W^T e_{n+1}|^2\right\}. \end{aligned} \quad (\text{A.9})$$



The term  $V_1$  can be calculated as

$$\begin{aligned} V_1 &= \sigma_{e,n+1}^2 \mathbb{E} \left\{ \hat{g}_n^T \mathbf{A} \Pi^{(1)} W^{T2} \right\} \\ &= \sigma_{e,n+1}^2 \mathbb{E} \left\{ \left[ \left( \hat{G}^H \hat{G} \right)^{-1} \right]_{n+1,n+1} \right\} = \frac{\sigma_{e,n+1}^2}{(M-N)\sigma_{n+1}^2}. \end{aligned} \quad (\text{A.10})$$

Similarly, we obtain  $V_2 = (\sigma_{e,n}^2 / (M-K)\sigma_n^2)$ , and  $V_3 = (\sigma_{e,n}^2 \sigma_{e,n+1}^2 / M(M-N)\rho)$ . Therefore,

$$\text{Var} \left( g_n^T b_{n+1}^{(1)} \right) = I_{n,n+1}. \quad (\text{A.11})$$

(b) Compute  $\mathbb{E} \left\{ |g_n^T b_n^{(1)}|^2 \right\}$ , we get

$$\mathbb{E} \left\{ |g_n^T b_n^{(1)}|^2 \right\} = \mathbb{E} \left\{ |I_1 + I_2 + I_3|^2 \right\}. \quad (\text{A.12})$$

Where  $I_1 \triangleq \hat{g}_n^T \mathbf{A} \Pi^{(1)} W^T e_n$ ,  $I_2 \triangleq \hat{e}_n^T \mathbf{A} \Pi^{(1)} W^T \hat{g}_n$ , and  $I_3 \triangleq \hat{e}_n^T \mathbf{A} \Pi^{(1)} W^T e_n$ . We obtain

$$\mathbb{E} \left\{ |g_n^T b_n^{(1)}|^2 \right\} = \mathbb{E} \left\{ |I_1|^2 \right\} + \mathbb{E} \left\{ |I_2|^2 \right\} + \mathbb{E} \left\{ |I_3|^2 \right\}. \quad (\text{A.13})$$

Similarly, we have

$$\mathbb{E} \left\{ |I_1|^2 \right\} = \frac{\beta_n - \sigma_n^2}{(M-K)\sigma_{n+1}^2}, \quad (\text{A.14})$$

$$\mathbb{E} \left\{ |I_2|^2 \right\} = \frac{\beta_n - \sigma_n^2}{(M-N)\sigma_{n-1}^2}. \quad (\text{A.15})$$

Next, we compute  $\mathbb{E} \left\{ |I_3|^2 \right\}$ . We obtain

$$\begin{aligned} \mathbb{E} \left\{ |I_3|^2 \right\} &= \sigma_{e,k}^4 \mathbb{E} \left\{ \text{Tr} \left[ \Pi^{(1)} \hat{G}^H \hat{G}^* \right]^{-1} \left( \Pi^{(1)} \right)^H \left( \hat{G}^T \hat{G}^* \right)^{-1} \right\} \\ &+ \sigma_{e,k}^4 \mathbb{E} \left\{ \text{Tr} \left[ \Pi^{(1)} \hat{G}^H \hat{G}^* \right]^{-1} \left( \Pi^{(1)} \right)^H \left( \hat{G}^T \hat{G}^* \right)^{-1} \right\} \\ &\longrightarrow \frac{\sigma_{e,n}^4 \rho}{M(M-N)}. \end{aligned} \quad (\text{A.16})$$

Substituting (A.15) and (A.16) into (A.13), we get

$$\mathbb{E} \left\{ |g_n^T b_n^{(1)}|^2 \right\} \longrightarrow I_{n,n}. \quad (\text{A.17})$$

(c) Compute  $\mathbb{E} \left\{ |g_n^T b_n^{(1)}|^2 \right\}$ , we obtain

$$\mathbb{E} \left\{ |g_n^T b_n^{(1)}|^2 \right\} \longrightarrow I_{n,i}. \quad (\text{A.18})$$

(d) Compute  $\mathbb{E} \left\{ \|g_n^T C^{(1)}\|^2 \right\}$ , we obtain

$$\mathbb{E} \left\{ \|g_n^T C^{(1)}\|^2 \right\} = \frac{M + \sigma_{n+1}^2 \sigma_{e,n}^2 \rho}{M(M-N)\sigma_{n+1}^2}. \quad (\text{A.19})$$

Substituting (A.11), (A.16), (A.18), and (A.19) into (A.7) yields (23).  $\square$

## Data Availability

The (software code) data used to support the findings of this study are available from the corresponding author upon request.

## Conflicts of Interest

The authors declare that there are no conflicts of interest.

## Acknowledgments

This work was supported in part by Key Scientific and Technological Projects in Henan Province, China (no. 192102210123), Key Research Fund for University in Henan Province, China (no. 20A520015), and Programs for Science and Technology Development in Henan Province, China (no. 212102210092).

## References

- [1] T. L. Marzetta, "Massive MIMO: an introduction," *Bell Labs Technical Journal*, vol. 20, pp. 11–22, 2015.
- [2] X. Li, Q. Wang, Y. Liu, T. A. Tsiftsis, Z. Ding, and A. Nallanathan, "UAV-aided multi-way NOMA networks with residual hardware impairments," *IEEE Wireless Communications Letters*, vol. 9, 2020.
- [3] T. L. Marzetta, "Noncooperative cellular wireless with unlimited numbers of base station antennas," *IEEE Transactions on Wireless Communications*, vol. 9, no. 11, pp. 3590–3600, 2010.
- [4] C. D. Ho, "How to scale up the spectral efficiency of multi-way massive MIMO relaying?" *IEEE International Conference on Communications IEEE*, vol. 9, 2018.
- [5] E. G. Larsson, O. Edfors, F. Tufvesson, and T. L. Marzetta, "Massive MIMO for next generation wireless systems," *IEEE Communications Magazine*, vol. 52, no. 2, pp. 186–195, 2014.
- [6] X. Li, L. Li, F. Wen, J. Wang, and C. Deng, "Sum rate analysis of MU-MIMO with a 3D MIMO base station exploiting elevation features," *International Journal of Antennas and Propagation*, vol. 2015, p. 9, Article ID 318123, 2015.
- [7] E. Björnson, E. G. Larsson, and T. L. Marzetta, "Massive MIMO: ten myths and one critical question," *IEEE Communication*, vol. 54, no. 2, pp. 114–123, 2016.
- [8] G. Amarasuriya, C. Tellambura, and M. Ardakani, "Multi-way MIMO amplify-and-forward relay networks with zero-forcing transmission," *IEEE Transactions on Communications*, vol. 61, no. 12, pp. 4847–4863, 2013.
- [9] C. D. Ho, H. Q. Ngo, M. Matthaiou, and T. Q. Duong, "On the performance of zero-forcing processing in multi-way massive MIMO relay networks," *IEEE Communications Letters*, vol. 21, no. 4, pp. 849–852, 2017.
- [10] S. Silva, G. A. A. Baduge, M. Ardakani, and C. Tellambura, "NOMA-aided multi-way massive MIMO relay networks," *IEEE Transactions on Communications*, vol. 68, no. 7, pp. 4050–4062, 2019.
- [11] G. Amarasuriya and H. V. Poor, "Multi-way amplify-and-forward relay networks with massive MIMO," 2015.
- [12] G. Amarasuriya, E. G. Larsson, and H. V. Poor, "Wireless information and power transfer in multiway massive MIMO relay networks," *IEEE Transactions on Wireless Communications*, vol. 15, no. 6, pp. 3837–3855, 2016.

- [13] C. D. Ho, H. Q. Ngo, M. Matthaiou, and T. Q. Duong, "Multi-way massive MIMO relay networks with maximum-ratio processing," in *Proceedings of the 2017 International Conference on Recent Advances in Signal Processing, Telecommunications & Computing (SigTelCom)*, IEEE, Da Nang, Vietnam, February 2017.
- [14] G. Amarasuriya, C. Tellambura, and M. Ardakani, "Performance analysis of pairwise amplify-and-forward multi-way relay networks," *IEEE Wireless Communications Letters*, vol. 1, no. 5, pp. 524–527, 2012.
- [15] G. Amarasuriya and H. V. Poor, "Impact of channel aging in multi-way relay networks with massive MIMO," *IEEE Access*, vol. 2015, 2015.
- [16] F. Tan, "Energy-efficient power allocation for massive MIMO-enabled multi-way AF relay networks with channel aging," *EURASIP Journal on Wireless Communications and Networking*, vol. 9, 2018.
- [17] S. Silva, G. A. A. Baduge, M. Ardakani, and C. Tellambura, "NOMA-aided multi-way massive MIMO relaying," *IEEE Transactions on Communications*, vol. 68, no. 7, pp. 4050–4062, 2020.
- [18] F. Tan, T. Lv, and P. Huang, "Global energy efficiency optimization for wireless-powered massive MIMO aided multiway AF relay networks," *IEEE Transactions on Signal Processing*, vol. 66, no. 9, pp. 2384–2398, 2018.
- [19] Q. Zhang, S. Jin, K.-K. Wong, H. Zhu, and M. Matthaiou, "Power scaling of uplink massive MIMO systems with arbitrary-rank channel means," *IEEE Journal of Selected Topics in Signal Processing*, vol. 8, no. 5, pp. 966–981, 2014.
- [20] X. Li, J. Li, L. Li, L. Du, J. Jin, and D. Zhang, "Performance analysis of cooperative small cell systems under correlated Rician/Gamma fading channels," *IET Signal Processing*, vol. 12, no. 1, pp. 64–73, 2018.
- [21] X. Li, M. Matthaiou, Y. Liu et al., "Multi-pair two-way massive MIMO relaying with hardware impairments over rician fading channels," *IEEE Global Communication Conference*, vol. 9, no. 13, pp. 1–6, 2018.
- [22] C. D. Ho, "Multi-way massive MIMO with maximum-ratio processing and imperfect CSI," 2016.
- [23] H. Q. Ngo, E. G. Larsson, and T. L. Marzetta, "Energy and spectral efficiency of very large multiuser MIMO systems," *IEEE Transactions on Communications*, vol. 61, no. 4, pp. 1436–1449, 2013.
- [24] H. Q. Ngo, H. A. Suraweera, M. Matthaiou, and E. G. Larsson, "Multipair full-duplex relaying with massive arrays and linear processing," *IEEE Journal on Selected Areas in Communications*, vol. 32, no. 9, pp. 1721–1737, 2014.

## Research Article

# Two-Dimensional DOA Estimation of MIMO Radar Coherent Source Based on Toeplitz Matrix Set Reconstruction

Fei Zhang , Aisuo Jin, and Yin Hu

School of Electronic Information, Jiangsu University of Science and Technology, Zhenjiang, Jiangsu 212000, China

Correspondence should be addressed to Fei Zhang; [zjzf@just.edu.cn](mailto:zjzf@just.edu.cn)

Received 14 October 2020; Revised 23 November 2020; Accepted 30 December 2020; Published 4 February 2021

Academic Editor: Xingwang Li

Copyright © 2021 Fei Zhang et al. This is an open access article distributed under the Creative Commons Attribution License, which permits unrestricted use, distribution, and reproduction in any medium, provided the original work is properly cited.

In order to realize the high-precision direction of arrival (DOA) estimation of the coherent source of two-dimensional multiple-input and multiple-output (MIMO) radar, a solution is given by combining Toeplitz matrix set reconstruction. MIMO radar obtains a larger aperture with fewer arrays. Traditional two-dimensional reconstruction Toeplitz-like algorithms use part of the information in the construction of two correlation matrices or covariance matrices to construct the Toeplitz matrix when performing two-dimensional coherent source DOA estimation, which makes the information utilization incomplete and requires additional denoising processing. To solve the above problems, this paper proposes an improved Toeplitz matrix set reconstruction algorithm based on the two-dimensional reconstruction Toeplitz class algorithm. The complete array element receiving signal vector is used to construct two Toeplitz matrix sets containing complete information, and then their conjugate transposes. Multiply and sum to correct the matrix to obtain a full-rank matrix, so as to achieve the purpose of decoherence and combine the traditional ESPRIT algorithm to perform two one-dimensional reconstruction processing through rotation invariance and then perform angle matching to achieve two-dimensional coherent signal angle estimation, while avoiding additional denoising processing. Finally, the simulation results of the cross array and the *L*-shaped array verify the effectiveness of the algorithm in this paper and further extend it to the two-dimensional MIMO radar array model and compare it with the traditional ESPRIT-like algorithm and the REC-FBSS-ESPRIT algorithm. In comparison, the algorithm in this paper has better performance under the conditions of successful resolution, DOA estimation accuracy, and low signal-to-noise ratio.

## 1. Introduction

The multiple-input and multiple-output (MIMO) radar system is a new radar system proposed in recent years. MIMO technology has brought a new breakthrough to the application performance of the radar system. Compared with the traditional radar, MIMO radar has potential advantages in parameter target estimation, target parameter detection, estimation performance analysis, space-time adaptive processing suppression, radar interference waveform design, and so forth. The direction of arrival (DOA) [1] estimation problem is one of the important research directions in the signal processing of sensor arrays [2, 3], and it is widely used in radar [4–6]. High-precision DOA estimation based on subspace has become the focus of research [7–9]; for example, multiple signal classification (MUSIC)

and estimation of signal parameters via rotational invariance techniques (ESPRIT) [10] can provide higher resolution to estimate the direction of arrival of uncorrelated and partially related signals [11–13]. But in practice, there are a large number of coherent sources due to multipath propagation and cofrequency interference [14]. When the signals are coherent, the rank of the covariance matrix accepted by the array will be deficient, so that the signal will be diffused to the noise, and the performance of the DOA estimation will be degraded [15, 16]. The methods of decoherence include spatial smoothing algorithms, such as forward smoothing, backward smoothing, and forward and backward smoothing, but they are usually only applicable to isometric uniform linear arrays, and the corrected dimension is lower than the original matrix dimension; that is, decoherence is in exchange for lower degrees of freedom [6, 14].

Another problem to solve rank deficit is to construct an algorithm based on vector and matrix reconstruction [14]. This algorithm rearranges the elements by covariance processing of the vector of the received signal and then constructs a Toeplitz matrix so that its rank is only the direction of arrival is related without being affected by signal correlation, so as to achieve the purpose of decoherence. Reference [17] proposed the ESPRIT-like algorithm by constructing a special antenna array model to reconstruct a Toeplitz matrix with the covariance matrix of the received signal matrix and using rotation invariance to achieve decoherence, but this method only works for the center array of the covariance matrix. When the center row of the covariance matrix is selected for reconstruction, the noise term is only a scalar quantity; otherwise, the denoising process still needs to be used to estimate the DOA using the ESPRIT algorithm. Because only one line of covariance is used, its information utilization is incomplete and affects DOA estimation performance. Reference [6] extended [17] to the two-dimensional DOA estimation of coherent sources. Reference [18] proposed the REC-FBSS-ESPRIT algorithm for reconstructing a covariant matrix, using the forward and backward spatial smoothing method as a preprocessing method to solve the problem of rank deficiency, and constructed an L-shaped matrix for two-dimensional DOA estimation, but the signal is still affected by noise and requires denoising. Reference [14] proposed an improved algorithm based on Toeplitz matrix reconstruction, by constructing a Toeplitz matrix set on the signal matrix, processing the Toeplitz matrix and the signal matrix, and then multiplying and summing by the conjugate transposed matrix. The matrix is corrected to obtain a full-rank matrix to achieve decoherence, and no additional denoising is required, but it is only suitable for one-dimensional DOA estimation.

Based on the literature [14], this paper proposes an improved Toeplitz matrix set reconstruction algorithm based on the two-dimensional reconstruction of the Toeplitz-like algorithms and uses cross arrays and  $L$ -shaped arrays for the two-dimensional DOA estimation [19], further extending to MIMO radar two-dimensional DOA estimation, using the characteristics of MIMO radar, with fewer array antennas to obtain higher DOA measurement accuracy. The algorithm uses two even linear arrays of mutually orthogonal array elements, through two permutation matrices and the relationship between the signal subspace and

the direction vector, using rotation invariance, through two one-dimensional processing and then angle matching. Thus, DOA estimation of two-dimensional coherent signals is realized. Finally, simulation experiments verify the universality of the proposed algorithm for two-dimensional DOA estimation. Compared with the traditional ESPRIT-like algorithm and the REC-FBSS-ESPRIT algorithm in [18], the successful resolution probability and DOA estimation accuracy of the algorithm in this paper have better performance in the case of low signal-to-noise ratio, does not require spectrum peak search, and the amount of calculation is small.

## 2. Materials and Methods

**2.1. Cross Array.** A cross-shaped array as shown in Figure 1 supposes the intersection of the cross-shaped array is the origin of the coordinates, the array elements are evenly distributed on the  $x$ -axis and  $y$ -axis, and the number of array elements on the  $x$ -axis and  $y$ -axis is  $N=2M+1$ . The total number of array elements is  $4M+1$ . The array element spacing is  $d=(\lambda/2)$ , where  $\lambda$  is the wavelength. Assuming that  $P$  signals are incident on the antenna, the two-dimensional arrival angles of the  $i$ th signal are  $\theta_i, \phi_i$  ( $i=1, 2, \dots, P$ ), and  $\theta_i$  and  $\phi_i$  are the azimuth angle and the pitch angle, respectively.

Then, the received signals of  $x$ -axis and  $y$ -axis are

$$\begin{cases} X = A_x s + N_x, \\ Y = A_y s + N_y, \end{cases} \quad (1)$$

where  $A_x = [a_x(\theta_1), a_x(\theta_2), \dots, a_x(\theta_p)]$  and  $A_y = [a_y(\theta_1), a_y(\theta_2), \dots, a_y(\theta_p)]$  are the  $x$ -axis and  $y$ -axis direction matrices, respectively; the dimension is  $(2M+1) \times P$ , and  $a_x(\theta_p) = [e^{-j2\pi M d \sin \theta_p \sin \phi_p / \lambda}, \dots, 1, \dots, e^{j2\pi M d \sin \theta_p \sin \phi_p / \lambda}]$ ,  $a_y(\theta_p) = [e^{-j2\pi M d \sin \theta_p \sin \phi_p / \lambda}, \dots, 1, \dots, e^{j2\pi M d \sin \theta_p \sin \phi_p / \lambda}]$ ;  $s = [s_1, s_2, \dots, s_p]$  is  $P \times 1$  dimension incident signal vector;  $P$  signals can be independent, correlated, or coherent;  $N_x$  and  $N_y$  are the additive Gaussian noise of the  $x$ -axis and  $y$ -axis receiving models, respectively; the dimensions are  $2M+1$ ; and they are not related to the source.

First, construct the Toeplitz matrices and of the received signal. As can be seen from [14], Toeplitz matrices  $B_x(t)$  and  $B_y(t)$  can be expressed as follows:

$$\begin{cases} B_x(t) = \begin{bmatrix} X_0(t) & X_1(t) & \cdots & X_M(t) \\ X_{-1}(t) & X_0(t) & \cdots & X_{M-1}(t) \\ \vdots & \vdots & \ddots & \vdots \\ X_{-M}(t) & X_{-M+1}(t) & \cdots & X_0(t) \end{bmatrix} = A_{rx} S A_{rx}^H + B_{N_x}(t), \\ B_y(t) = \begin{bmatrix} Y_0(t) & Y_1(t) & \cdots & Y_M(t) \\ Y_{-1}(t) & Y_0(t) & \cdots & Y_{M-1}(t) \\ \vdots & \vdots & \ddots & \vdots \\ Y_{-M}(t) & Y_{-M+1}(t) & \cdots & Y_0(t) \end{bmatrix} = A_{ry} S A_{ry}^H + B_{N_y}(t), \end{cases} \quad (2)$$

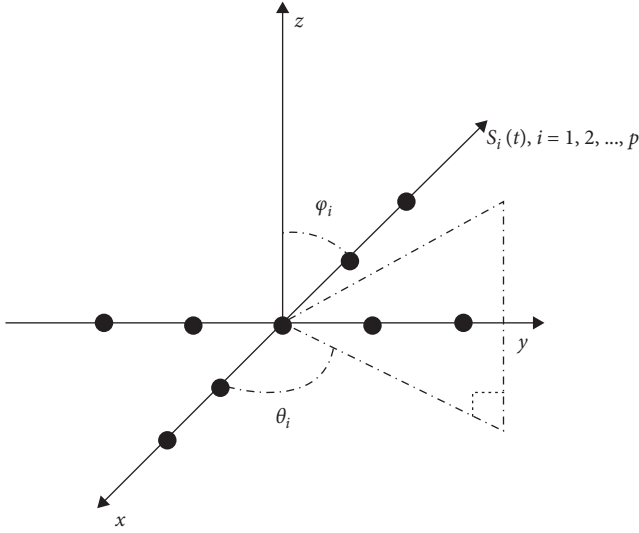


FIGURE 1: Cross array.

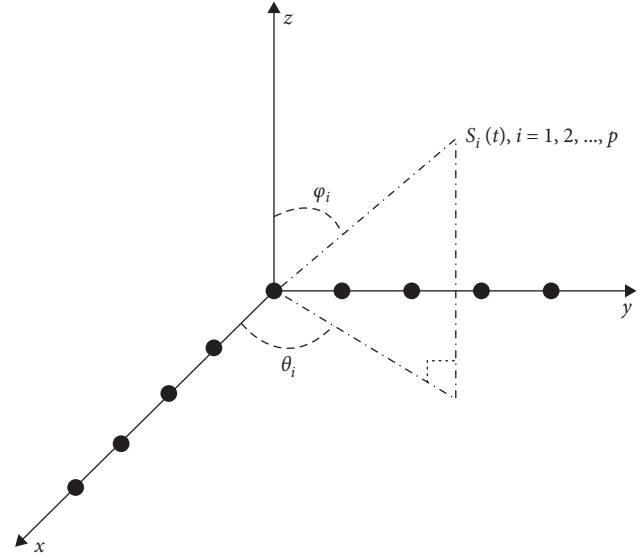


FIGURE 2: L-shaped array.

where  $A_{rx} = [a_{rx}(\theta_1), a_{rx}(\theta_2), \dots, a_{rx}(\theta_p)]$ ,  $a_{rx}(\theta_p) = [1, e^{-j2\pi d \sin \theta_p \sin \phi_p / \lambda}, \dots, e^{-j2\pi d \sin \theta_p \sin \phi_p / \lambda}]$ , and  $a_{ry}(\theta_p) = [1, e^{-j2\pi d \cos \theta_p \sin \phi_p / \lambda}, \dots, e^{-j2\pi d \cos \theta_p \sin \phi_p / \lambda}]$  in the same way;  $S = \text{diag}\{s_1, s_2, \dots, s_p\}$  which means that  $S$  is a full-rank diagonal matrix. In other words, the rank of  $S$  is independent of the coherence between signals, and the decorrelation can be achieved.  $B_{Nx}(t)$  and  $B_{Ny}(t)$  are Toeplitz matrices composed of noise vectors.

**2.2. L-Shaped Array.** L-shaped array is shown in Figure 2: let the coordinate origin of the L-shaped array be the reference array element. The array elements are evenly distributed on the  $x$ -axis and the  $y$ -axis. The numbers of array elements on the  $x$ -axis and the  $y$ -axis are both  $N = 2M + 1$  and the total number of array elements is  $4M + 1$ . The array element spacing is  $d = (\lambda/2)$ , where  $\lambda$  is the wavelength. Assuming that  $P$  signals are incident on the antenna, the two-

dimensional arrival angles of the  $i$ th signal are  $\theta_i, \phi_i$  ( $i = 1, 2, \dots, P$ ), and  $\theta_i$  and  $\phi_i$  are the azimuth angle and the pitch angle, respectively.

Similarly, the received signals of the  $x$ -axis and  $y$ -axis are

$$\begin{cases} X = A_x s + N_x \\ Y = A_y s + N_y \end{cases} \quad (3)$$

In the same way, where  $A_x$  and  $A_y$  are the direction matrix of the  $x$ -axis and  $y$ -axis, respectively, the dimension is  $(2M + 1) \times P$ , where  $a_x(\theta_p) = [1, e^{(j2\pi d \sin \theta_p \sin \phi_p / \lambda)}, \dots, e^{(j2\pi d \sin \theta_p \sin \phi_p / \lambda)}]$ ;  $a_y(\theta_p) = [1, e^{(j2\pi d \cos \theta_p \sin \phi_p / \lambda)}, \dots, e^{(j2\pi d \cos \theta_p \sin \phi_p / \lambda)}]$ ; and  $S$  and  $N$  are the same as the cross array.

The Toeplitz matrices  $B_x(t)$  and  $B_y(t)$  are constructed as follows:

$$\left\{ \begin{array}{l} B_x(t) = \begin{bmatrix} X_M(t) & X_{M+1}(t) & \cdots & X_{2M}(t) \\ X_{M-1}(t) & X_M(t) & \cdots & X_{2M-1}(t) \\ \vdots & \vdots & \ddots & \vdots \\ X_0(t) & X_1(t) & \cdots & X_M(t) \end{bmatrix} \\ B_y(t) = \begin{bmatrix} Y_M(t) & Y_{M+1}(t) & \cdots & Y_{2M}(t) \\ Y_{M-1}(t) & Y_M(t) & \cdots & Y_{2M-1}(t) \\ \vdots & \vdots & \ddots & \vdots \\ Y_0(t) & Y_1(t) & \cdots & Y_M(t) \end{bmatrix} \end{array} \right. = \begin{cases} C_1 A_{rx} S A_{rx}^H + B_{Nx}(t), \\ C_2 A_{ry} S A_{ry}^H + B_{Ny}(t). \end{cases} \quad (4)$$

Among them,  $C_1$  and  $C_2$  are constants; since  $S$  is a diagonal matrix, the correlation matrix is not affected by the constants. If  $S = CS$ , then  $B_x(t)$  and  $B_y(t)$  are the same.

**2.3. MIMO Array.** The single-static MIMO array is shown in Figure 3; set the number of transmitting array elements as  $1 \times M$  and the number of receiving array elements as  $N \times 1$ ;

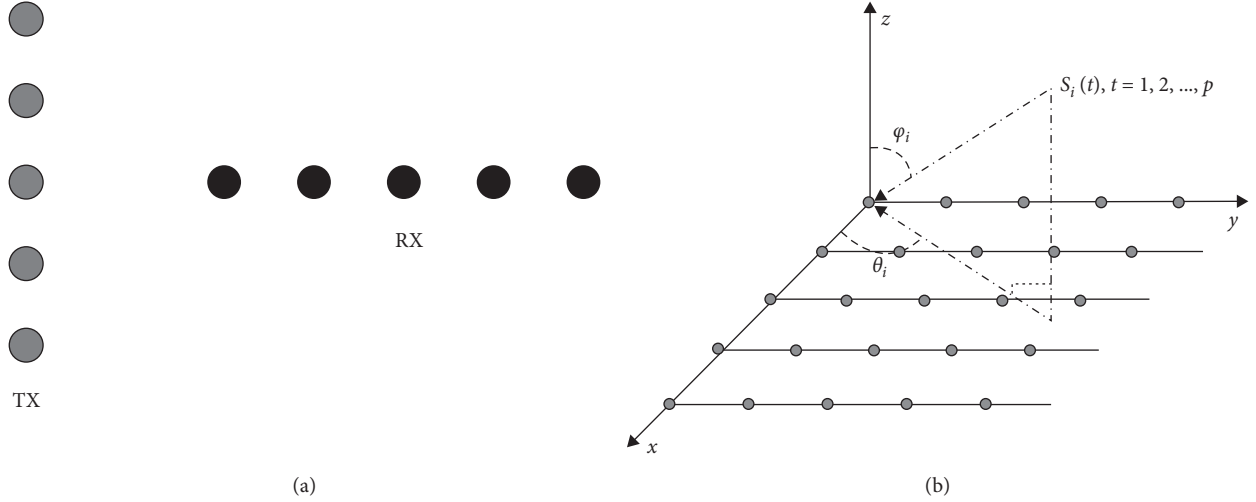


FIGURE 3: MIMO array. (a) Transmitting and receiving array model. (b) Virtual array model.

that is, the total number of array elements is  $M + N$ . Due to the nature of the MIMO array model, it can be virtualized. The number of arrays is  $M \times N$ , and the array elements are uniformly distributed on the  $x$ -axis and  $y$ -axis, respectively, and the total number of array elements is  $M \times N$ . The element spacing is  $d = (\lambda/2)$ , where  $\lambda$  is the wavelength. Assuming that  $P$  signals are incident on the antenna, the two-dimensional arrival angles of the  $i$ th signal are  $\theta_i, \phi_i$  ( $i = 1, 2, \dots, P$ ), and  $\theta_i$  and  $\phi_i$  are the azimuth and elevation angles, respectively.

Then, the output is

$$x(l) = [a_t(\theta_1, \phi_1) \otimes a_r(\theta_1, \phi_1), a_t(\theta_2, \phi_2) \otimes a_r(\theta_2, \phi_2), \dots, a_t(\theta_k, \phi_k) \otimes a_r(\theta_k, \phi_k)]S(l) + n(l), \quad (5)$$

where  $\theta_k, \phi_k$  are the elevation and azimuth angles corresponding to the  $k$ th target;  $n(l)$  is the  $MN \times 1$  Gaussian white noise vector, the mean is 0, and the covariance is  $\sigma^2 I_{MN}$ ; and  $a_t(\theta_k, \phi_k) = a_{ty}(\theta_k, \phi_k) \otimes a_{tx}(\theta_k, \phi_k)$  and  $a_r(\theta_k, \phi_k) = a_{ry}(\theta_k, \phi_k) \otimes a_{rx}(\theta_k, \phi_k)$ , where  $a_{ty}(\theta_k, \phi_k)$  and  $a_{tx}(\theta_k, \phi_k)$  are the antenna steering vectors along the  $y$ -axis and  $x$ -axis of the transmitting array (corresponding to the  $k$ th target) and  $a_{ry}(\theta_k, \phi_k)$  and  $a_{rx}(\theta_k, \phi_k)$  are the same. So, there are the following relations

$$\begin{cases} a_{ty}(\theta_k, \phi_k) = [1, 1, \dots, 1], \\ a_{tx}(\theta_k, \phi_k) = [1, e^{-j\pi \sin \theta_k \cos \phi_k}, \dots, e^{-jM\pi \sin \theta_k \cos \phi_k}], \\ a_{ry}(\theta_k, \phi_k) = [1, e^{-j\pi \sin \theta_k \sin \phi_k}, \dots, e^{-jN\pi \sin \theta_k \sin \phi_k}], \\ a_{rx}(\theta_k, \phi_k) = [1, 1, \dots, 1]. \end{cases} \quad (6)$$

Then, set  $x(l)$  to  $X = A_x s + N_x$ . The same is  $Y = A_y s + N_y$ .

Correlation calculation of  $B_x(t)$  and  $B_y(t)$  with the corresponding received signals  $X_i(t)$  and  $Y_i(t)$  of the  $i$ th array element:

$$\begin{cases} R_{X_i} = E[B_x(t)X_i^*(t)] = A_{rx} E[Sx_i^*(t)]A_{rx}^H + \sigma_n^2 I_{x,(M+1),i} \\ = R_{x_i} + \sigma_n^2 I_{x,(M+1),i}, \\ R_{Y_i} = E[B_y(t)Y_i^*(t)] = A_{ry} E[Sy_i^*(t)]A_{ry}^H + \sigma_n^2 I_{y,(M+1),i} \\ = R_{y_i} + \sigma_n^2 I_{y,(M+1),i}. \end{cases} \quad (7)$$

Let  $E[Sx_i^*(t)] = S_{x_i}$  and  $E[Sy_i^*(t)] = S_{y_i}$ , where  $R_{x_i}$  and  $R_{y_i}$  are correlation operations without noise;  $I_{M+1,i}$  is the  $(M+1) \times (M+1)$ -dimensional matrix whose  $i$ th diagonal is 1. When  $i=0$ ,  $I_{M+1,0} = I_{M+1}$  is the  $M+1$  dimension identity matrix;  $E[\bullet]$  represents mathematical expectation.

It can be obtained from equation (7) that, for the ESPRIT-like algorithm in [17], the method is to use an optional set of Toeplitz matrices  $R_{X_i}$  and  $R_{Y_i}$  to achieve the purpose of decoherence of coherent source signals. If  $i=0$  is selected as the central array element to construct  $R_{X_i}$  and  $R_{Y_i}$ , then  $I_{M+1,i}$  is an identity matrix, and after that the relationship between the signal subspace and the direction vector can be used to directly perform feature decomposition on  $R_{X_i}$  and  $R_{Y_i}$  to find the final DOA information, but when  $i \neq 0$  is the central array element,  $I_{M+1,i}$  is not an identity matrix, so denoising is still required. And ESPRIT-like only constructs one  $R_{X_i}$  and  $R_{Y_i}$ , so the complete information of the array is not fully utilized. To solve the above problems, all  $R_{X_i}$ ,  $R_{Y_i}$  and their corresponding  $R_{X_i}^H, R_{Y_i}^H$  are multiplied and summed:

Cross array:

$$\begin{cases} R_{X\Sigma} = A_{rx} \sum_{k=0}^M D_{xk} \left( \sum_{i=-M}^M C_{x_i} + 2\sigma_n^2 R_s \right) D_{xk}^H A_{rx}^H \\ + (M+1)\sigma_n^4 I_{x,M+1,0}, \\ R_{Y\Sigma} = A_{ry} \sum_{k=0}^M D_{yk} \left( \sum_{i=-M}^M C_{y_i} + 2\sigma_n^2 R_s \right) D_{yk}^H A_{ry}^H \\ + (M+1)\sigma_n^4 I_{y,M+1,0}. \end{cases} \quad (8)$$

$L$ -shaped array:

$$\left\{ \begin{array}{l} R_{X\Sigma} = A_{rx} \sum_{k=0}^M D_{xk} \left( \sum_{i=0}^{2M} C_{xi} + 2\sigma_n^2 R_s \right) D_{xk}^H A_{rx}^H \\ \quad + (M+1)\sigma_n^4 I_{x,M+1,0}, \\ R_{Y\Sigma} = A_{ry} \sum_{k=0}^M D_{yk} \left( \sum_{i=0}^{2M} C_{yi} + 2\sigma_n^2 R_s \right) D_{yk}^H A_{ry}^H \\ \quad + (M+1)\sigma_n^4 I_{y,M+1,0}. \end{array} \right. \quad (9)$$

The same is for the MIMO array.

$R_{X\Sigma}$  and  $R_{Y\Sigma}$  obviously have a joint diagonalization structure and span the same range of space of  $A_{rx}$  and  $A_{ry}$ , where  $R_s = E[SS^H]$  is the signal covariance matrix. For  $D_{xk}$ ,  $D_{yk}$ ,  $C_{xi}$ , and  $C_{yi}$ , see literature [14].

From equations (8) and (9), it can be seen that the reconstructed equivalent covariance matrix is a positive definite matrix with rank  $P$ . The rank is not affected by signal correlation, but only related to the number of signals [14]. To further improve accuracy,  $R_{X\Sigma}$  and  $R_{Y\Sigma}$  are revised

$$\left\{ \begin{array}{l} R_x = \frac{1}{2} \left( R_{X\Sigma} + J R_x^* \sum J \right), \\ R_y = \frac{1}{2} \left( R_{Y\Sigma} + J R_y^* \sum J \right), \end{array} \right. \quad (10)$$

where  $J$  is a permutation matrix with an antidiagonal of 1. Since  $A_{rx}$  and  $A_{ry}$  are Vandermonde matrices and  $\theta_i \neq \theta_j$ ,  $A_{rx}$  and  $A_{ry}$  are full ranks, and because  $\sum_{k=0}^M D_x^k \left( \sum_{i=0}^M C_x + 2\sigma_n^2 R_s \right) (D_x^k)^H$  and  $\sum_{k=0}^M D_y^k \left( \sum_{i=0}^{2M} C_y + 2\sigma_n^2 R_s \right) (D_y^k)^H$  are diagonal matrices, their feature decomposition can obtain  $P$  large eigenvalues and  $M+1-P$  small eigenvalues, where the eigenvectors corresponding to large eigenvalues constitute the signal subspace  $\Phi_s = \text{span}\{v_1, v_2, \dots, v_p\}$  and the eigenvectors corresponding to the small eigenvalues constitute the noise subspace  $\Phi_n = \text{span}\{v_{1+p}, v_{2+p}, \dots, v_M\}$ .

### 3. Two-Dimensional DOA Estimation of Coherent Sources

Let  $A_{rx} = \begin{bmatrix} a_1 \\ A_{Bx} \end{bmatrix} = \begin{bmatrix} A_{Fx} \\ a_{M+1} \end{bmatrix}$ , where  $a_1$  and  $a_{M+1}$  are the first and last terms of  $A_{rx}$ . Similarly, the signal subspace is decomposed  $\{v_1, v_2, \dots, v_p\} = U_{Sx} = \begin{bmatrix} u_1 \\ U_{Bx} \end{bmatrix} = \begin{bmatrix} U_{Fx} \\ u_{M+1} \end{bmatrix}$ , where  $u_1$  and  $u_{M+1}$  are the first and last columns of  $U_{Sx}$ , respectively. It is easy to get  $A_{Bx} = A_{Fx} \Phi_x$ , where

$$\Phi_x = \text{diag} \left\{ e^{-j2\pi d \sin \theta_1 \sin \phi_1 / \lambda}, e^{-j2\pi d \sin \theta_2 \sin \phi_1 / \lambda}, \dots, e^{-j2\pi d \sin \theta_p \sin \phi_1 / \lambda} \right\}. \quad (11)$$

It is a rotation matrix. Since  $A_{rx}$  and  $U_{Sx}$  are the same signal subspace,  $U_{Fx} = A_{Fx} T$  and  $U_{Bx} = A_{Bx} T$ , in which  $T$  is a full-rank matrix; then,

$$U_{Fx} T^{-1} \Phi_x T = A_{Fx} T T^{-1} \Phi_x T = A_{Fx} \Phi_x T = A_{Bx} T = U_{Bx}. \quad (12)$$

Let  $\Psi_x = T^{-1} \Phi_x T$ ; then,  $U_{Fx} \Psi_x = U_{Bx}$ . We can derive  $e^{-j2\pi d \sin \theta_k \sin \phi_k / \lambda}$ ,  $k = 1, 2, \dots, p$ , by feature decomposition of  $\Psi_x$ . Both  $\sin \theta_k \sin \phi_k$  can be estimated, and  $\cos \theta_k \sin \phi_k$  can be estimated in the same way. The following two-dimensional DOA angle can be estimated:

$$\left\{ \begin{array}{l} \theta_k = \tan^{-1} \left( \frac{\sin \theta_k \sin \phi_k}{\cos \theta_k \sin \phi_k} \right), \\ \phi_k = \sin^{-1} \left( \sqrt{(\sin \theta_k \sin \phi_k)^2 + (\cos \theta_k \sin \phi_k)^2} \right). \end{array} \right. \quad (13)$$

In summary, the steps of the two-dimensional DOA estimation method based on the Toeplitz matrix set proposed in this paper are shown in Table 1.

### 4. Computer Simulation

In order to verify the universality of the proposed algorithm for two-dimensional DOA estimation, the proposed algorithm is compared with the cross-shaped array ESPRIT-like algorithm in [6] and the  $L$ -shaped array REC-FBSS-ESPRIT algorithm in [18]. Perform 100 Monte Carlo simulations on each algorithm and define the root mean square error as

$$\text{RSME} = \frac{1}{K} \sum_{k=1}^K \sqrt{\frac{1}{100} \sum_{n=1}^{100} [(\hat{\theta}_{k,n} - \theta_k)^2 + (\hat{\phi}_{k,n} - \phi_k)^2]}. \quad (14)$$

The DOA of the three sources used in the simulation are  $(35^\circ, 40^\circ)$ ,  $(75^\circ, 70^\circ)$ ,  $(89^\circ, 80^\circ)$ , and sources 1, 3 are related signals. The numbers of array elements on the  $x$ - and  $y$ -axis are both 11, and the array element spacing is half a wavelength.

Figure 4 shows the DOA estimation performance of each algorithm, where Figures 4(a)–4(e) are the cross-shaped ESPRIT-like algorithm,  $L$ -shaped array REC-FBSS-ESPRIT algorithm, MIMO array, and the DOA estimation results of the cross array,  $L$ -type array, and MIMO array using the algorithm of this paper when the signal-to-noise ratio is SNR = 10 and the number of snapshots is 1024. From the figure, it can be seen intuitively that the algorithm of this paper is closer to the actual angle and has better two-dimensional DOA estimated performance.

Figure 5 shows the performance comparison of azimuth estimation using the cross array,  $L$ -shaped array, MMO array, ESPRIT-like algorithm, and REC-FBSS-ESPRIT algorithm using this algorithm and examines the RSME variation of the algorithm under different signal-to-noise ratios (SNR). When the signal-to-noise ratio is 0, the performance of this algorithm is improved by about 40% compared to the ESPRIT-like algorithm and improved by about 25% compared to the REC-FBSS-ESPRIT algorithm. By comparing RSMEs with different signal-to-noise ratios, it is concluded that the proposed algorithm performs better

TABLE 1: Algorithm steps in this paper.

---

Step 1: construct the received data $X$ and $Y$ from different matrix models and construct the Toeplitz matrix from equations (2) and (4)
Step 2: $RXi$ and $RYi$ are obtained from Toeplitz matrix and receiving matrix through formula (7)
Step 3: select all $RXi$ and $RYi$ to get $RX\Sigma$ and $RY\Sigma$ from formulas (8) and (9)
Step 4: $R$ is calculated from the $R = (1/2)(R\Sigma + JR\Sigma^* J)$ formula
Step 5: perform feature decomposition on $R$ to obtain signal subspace $US$
Step 6: get the corresponding $UB$ and $UF$ from $US$ , get the corresponding $\Psi$ , and then perform feature decomposition
Step 7: match by equation (13) to obtain two-dimensional DOA estimation of $P$ signals

---

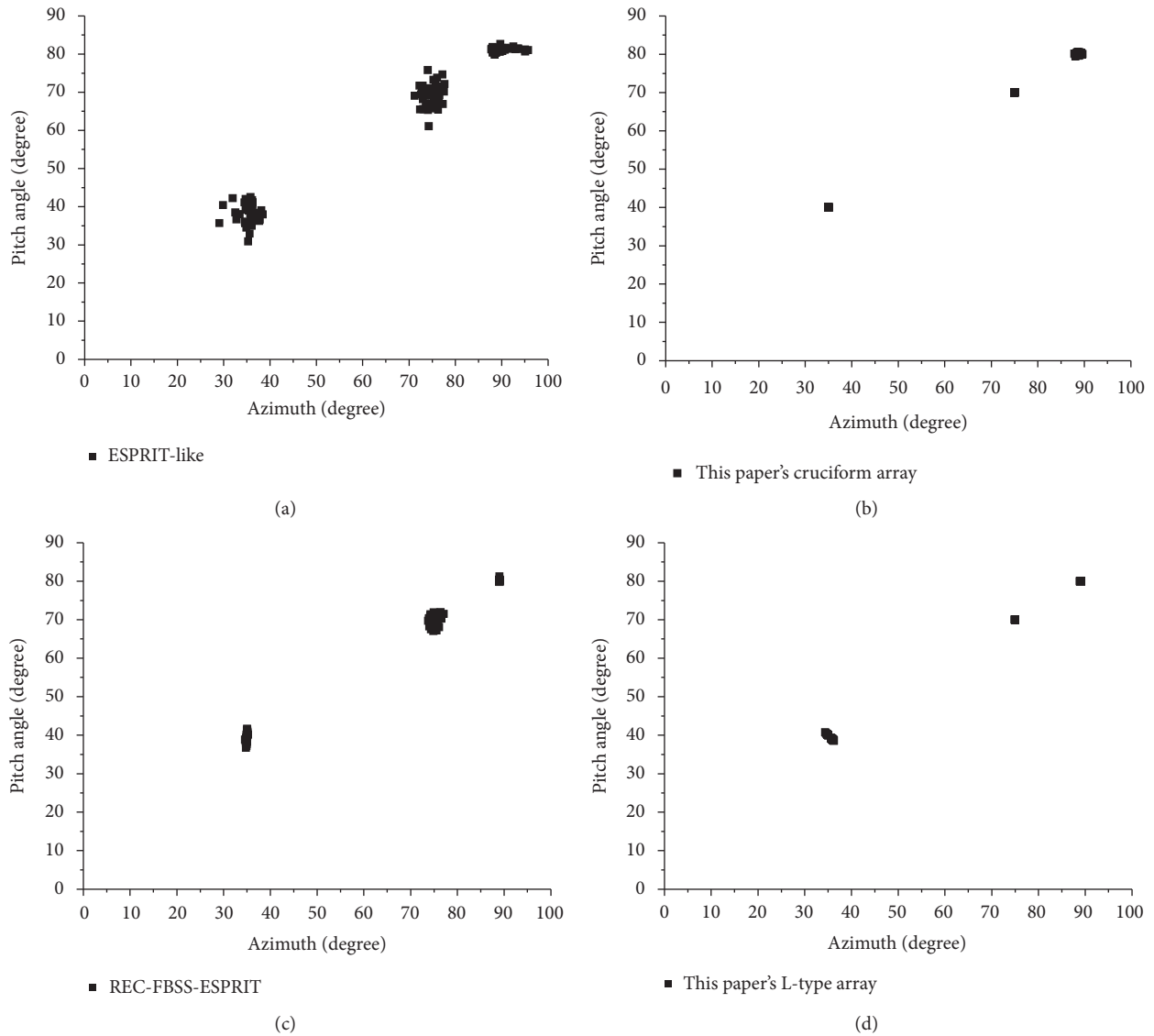


FIGURE 4: Continued.



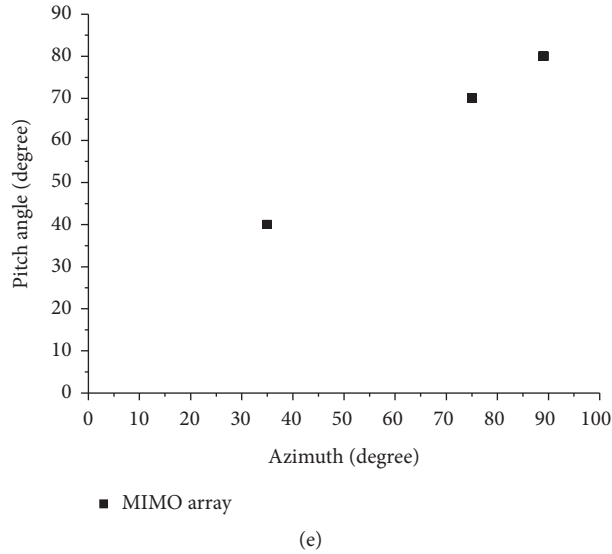


FIGURE 4: DOA estimation performance of each algorithm. (a) ESPRIT-like algorithm DOA estimation performance graph. (b) Performance graph of DOA estimation of cross array in this paper. (c) REC-FBSS-ESPRIT algorithm DOA estimation performance graph. (d) The performance graph of DOA estimation of *L*-type array in this paper. (e) MIMO array DOA estimation performance graph.

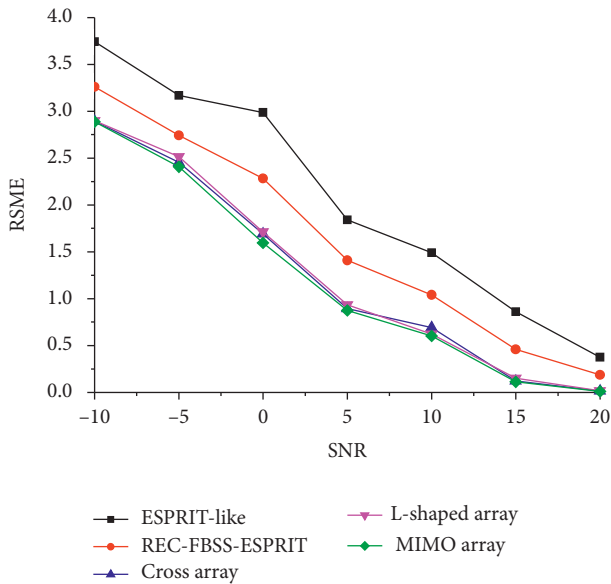


FIGURE 5: Comparison of mean square error under different signal-to-noise ratios.

than the ESPRIT-like algorithm and REC-FBSS-ESPRIT algorithm at low signal-to-noise ratios.

Figure 6 shows the comparison of the resolution probability of the cross array, *L*-shaped array, MIMO array ESPRIT-like algorithm, and REC-FBSS-ESPRIT algorithm using this algorithm. Here, it is defined that if the estimated  $\hat{\theta}_1$  and  $\hat{\theta}_2$  directions of the two sources satisfy  $|\hat{\theta}_1 - \theta_1| + |\hat{\theta}_2 - \theta_2| < |\hat{\theta}_1 - \hat{\theta}_2|$ , it is said that the two sources are correctly resolved. The resolution probability refers to the ratio of the number of correct resolutions to the total number of experiments. The experimental conditions were 10 experiments per group under the condition that the

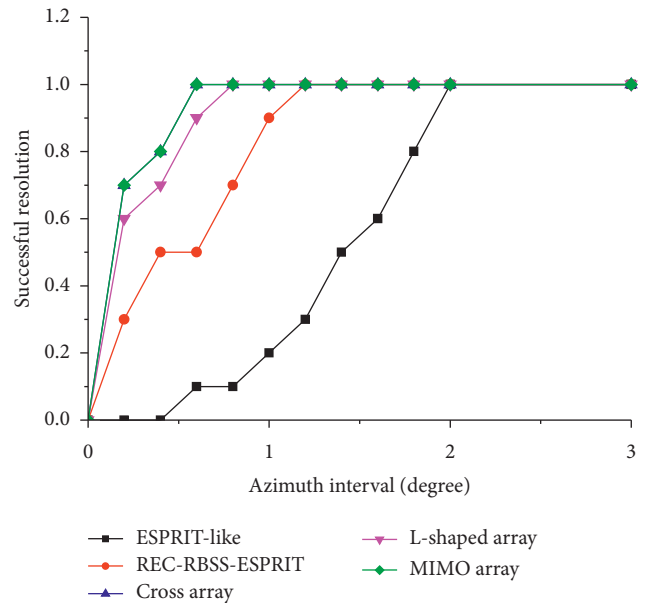


FIGURE 6: Success resolution as a function of azimuth interval.

number of snapshots was 1024 and the signal-to-noise ratio SNR was 20. The experimental results show that the probability of successful resolution of this algorithm under low azimuth interval is higher than that of ESPRIT-like algorithm and REC-FBSS-ESPRIT algorithm, which shows that the accuracy of DOA estimation of this algorithm is higher than the other two algorithms, and, moreover, the cross array, the *L*-shaped array, and the MIMO array all have better successful resolution in the case of low azimuth spacing.

Figure 7 shows the influence of correlation coefficients on the performance of each algorithm. From Figure 7(a), we

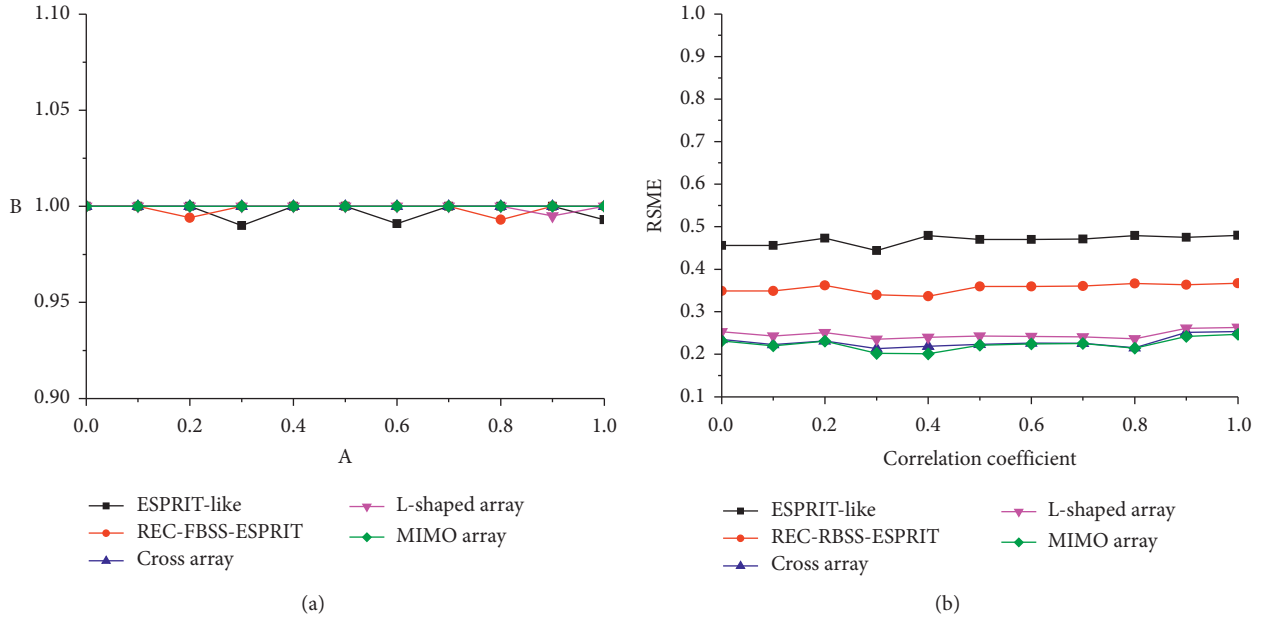


FIGURE 7: Influence of correlation coefficient on performance. (a) Relationship between the successful resolution and correlation coefficient. (b) Relationship between mean square error and correlation coefficient.

TABLE 2: Main performance comparison.

Algorithm	Snapshots: 100; SNR: 0; mean square error	Snapshots: 20; SNR: 20; mean square error	Snapshots: 1000; SNR: 10; correlation coefficient: 0.5, mean square error
Cross array	1.6918	1.0116	0.2335
L-shaped array	1.7132	1.1364	0.2433
MIMO array	1.832	1.2451	0.2719
ESPRIT-like	2.9868	1.5782	0.4712
REC-FBSS-ESPRIT	2.2841	1.2821	0.3594

TABLE 3: DOA estimation time comparison.

Algorithm	100 experiments' simulation time (s)	500 experiments' simulation time (s)	1000 experiments simulation time (s)
Cross array	0.9045	4.1106	7.9423
L-shaped array	0.9769	4.4346	8.5693
MIMO array	1.0746	4.5571	8.7709
ESPRIT-like	0.7741	3.5709	7.0441
REC-FBSS-ESPRIT	7.9567	40.5768	96.7324

can see the successful resolution of the MIMO array using this algorithm when the signal-to-noise ratio SNR is 10 and the number of snapshots is 1024, and with the change of the correlation coefficient, the success resolution is always 100%, and the success rate of the L-shaped array using the algorithm of this paper is only 99% to 100% when the correlation coefficient is 0.9. The success rate of the ESPRIT-like algorithm and the REC-FBSS-ESPRIT algorithm is many times between 99% and 100%. It can be seen from the Figure 7(b) that the two arrays adopting the algorithm of this paper have small changes in RSME when the correlation coefficient changes and slightly rise when the correlation

coefficient is close to 1, while the ESPRIT-like algorithm has both changes when the correlation coefficient changes. The square error is also small, but the performance is lower than the algorithm in this paper. The mean square error of the REC-FBSS-ESPRIT algorithm under the change of the correlation coefficient is lower than the ESPRIT-like algorithm but higher than the algorithm in this paper. The experimental results show that the two-dimensional DOA estimation algorithm in this paper is less affected by the correlation coefficient, and the estimation performance is higher than the ESPRIT-like and REC-FBSS-ESPRIT algorithms.

Table 2 shows the performance comparison of the cross array,  $L$ -shaped array, ESPRIT-like algorithm, and REC-FBSS-ESPRIT algorithm under different parameters using this algorithm. Experiments show that the algorithm in this paper has a low signal-to-noise ratio and a low number of snapshots; the mean square error is lower than the ESPRIT-like algorithm and the REC-FBSS-ESPRIT algorithm.

Table 3 shows the comparison of the time required for different algorithms to perform 100, 500, and 1000 experiments on 3 signals. The results show that the simulation time of the algorithm in this paper is similar to that of the ESPRIT-like algorithm, only slightly slower, but compared to the REC-FBSS-ESPRIT algorithm, it is much faster and has a better real-time performance.

## 5. Conclusions

This paper proposes a modified Toeplitz matrix set reconstruction algorithm based on the two-dimensional reconstruction of Toeplitz-like algorithms, which is based on the incomplete information of traditional reconstruction Toeplitz algorithm and the need for denoising. The Toeplitz matrix set is multiplied and summed with the conjugate transposed matrix to achieve solution coherence, avoiding additional denoising. The simulation experiment gives a comparative analysis of the performance of this algorithm, the ESPRIT algorithm, and REC-FBSS-ESPRIT algorithm and utilizes the special performance of MIMO arrays to simulate more arrays with fewer antennas, universality under the array model.

## Data Availability

The datasets used or analysed during the current study are available from the corresponding author on reasonable request.

## Conflicts of Interest

The authors declare that there are no conflicts of interest regarding the publication of this paper.

## Acknowledgments

This work was supported by the National Natural Science Foundation of China under Grant no. 11574120 and Jiangsu Provincial University Natural Science Fund under Grant no. 14KJD510002.

## References

- [1] L. P. Qiao, C. S. I. Xi, and L. I. Li, "Fast subspace DOA algorithm without eigendecomposition," *Systems Engineering and Electronics*, vol. 32, no. 4, pp. 691–693, 2010.
- [2] F. Mendoza-Montoya, D. H. Covarrubias-Rosales, and C. A. Lopez-Miranda, "DOA estimation in mobile communications system using subspace tracking methods," *IEEE Latin America Transactions*, vol. 6, no. 2, pp. 123–129, 2008.
- [3] N. S. John, A. G. Konstantinos, and S. Katherine, "On the direction of arrival (DOA) estimation for a switched-beam antenna system using neural networks," *IEEE Transactions on Antennas and Propagation*, vol. 57, no. 5, pp. 1399–1411, 2009.
- [4] J. Y. Lu and W. L. Wu, "A novel DOA algorithm for CDMA system," in *Proceedings of the International Conference on Communication Technology, ICCT 2003*, pp. 1164–1168, Beijing, China, 2003.
- [5] J. X. Wu, T. Wang, Z. Y. Suo, and Z. Bao, "DOA estimation for ULA by spectral Capon rooting method," *Electronics Letters*, vol. 45, no. 1, pp. 84–85, 2009.
- [6] J. Yu, W. Y. Chen, and X. F. Zhang, "Two-dimensional DOA blind estimation algorithm for coherent sources," in *Proceedings of the 2009 Annual Conference on Communication Theory and Signal Processing*, pp. 19–24, Quanzhou, China, 2009.
- [7] C. Qian, L. Huang, M. Cao, J. Xie, and H. C. So, "PUMA: an improved realization of MODE for DOA estimation," *IEEE Transactions on Aerospace and Electronic Systems*, vol. 53, no. 5, pp. 2128–2139, 2017.
- [8] G. Hu, H. Zhou, J. Shi et al., "Orthogonal projection method for DOA estimation in low-altitude environment based on signal subspace," *AEU: Archiv fur Elektronik und Ubertragungstechnik: Electronic and Communication*, vol. 83, pp. 317–321, 2018.
- [9] S. F. B. Pinto and R. C. de Lamare, "Multistep knowledge-aided iterative ESPRIT: design and analysis," *IEEE Transactions on Aerospace and Electronic Systems*, vol. 54, no. 5, pp. 2189–2201, 2018.
- [10] S. Li, *Array Multi-Parameter Estimation Algorithm under the Framework of Compressed Sensing Parallel factors*, Nanjing University of Aeronautics and Astronautics, Nanjing, China, 2017.
- [11] R. Schmidt, "Multiple emitter location and signal parameter estimation," *IEEE Transactions on Antennas & Propagation*, vol. 34, no. 5, 1986.
- [12] C. Qian, L. Huang, and H. C. So, "Computationally efficient ESPRIT algorithm for direction-of-arrival estimation based on Nyström method," *Signal Processing*, vol. 94, pp. 74–80, 2014.
- [13] C. Qian, L. Huang, W.-J. Zeng, and H. C. So, "Direction-of-Arrival estimation for coherent signals without knowledge of source number," *IEEE Sensors Journal*, vol. 14, no. 9, pp. 3267–3273, 2014.
- [14] W. Zhang, Y. Han, M. Jin, and X. L. Qiao, "Coherent source DOA estimation based on Toeplitz matrix set reconstruction," *Journal of Jilin University (Engineering Science Edition)*, vol. 50, no. 2, pp. 703–710, 2020.
- [15] J. Luo, G. Zhang, and K. Yu, "An automatically paired two-dimensional direction-of-arrival estimation method for two parallel uniform linear arrays," *AEU-International Journal of Electronics and Communications*, vol. 72, pp. 46–51, 2017.
- [16] J. Zhuang, C. Duan, W. Wang, and Z. Chen, "Joint estimation of azimuth and elevation via manifold separation for arbitrary array structures," *IEEE Transactions on Vehicular Technology*, vol. 67, no. 7, pp. 5585–5596, 2018.
- [17] F. M. Han and X. D. Zhang, "An ESPRIT-like algorithm for coherent DOA estimation," *IEEE Antennas & Wireless Propagation Letters*, vol. 4, pp. 443–446, 2005.
- [18] A. Shahimaeen and M. J. Dehghani, "Two-dimensional DOA estimation for coherent signals using a novel covariance-like matrix," *Transactions on Emerging Telecommunications Technologies*, vol. 30, no. 6, 2019.
- [19] Y. P. Zhang, Y. L. Zhao, and X. Y. Sun, "A coherent stepwise dimension reduction DOA estimation method for  $L$ -shaped arrays," *Journal of Computer Applications*, vol. 33, no. 5, pp. 1477–1480, 2016.

## Research Article

# Secure and Efficient Image Compression-Encryption Scheme Using New Chaotic Structure and Compressive Sensing

Yongli Tang,<sup>1</sup> Mingjie Zhao ,<sup>1</sup> and Lixiang Li <sup>2</sup>

<sup>1</sup>School of Computer Science and Technology, Henan Polytechnic University, Jiaozuo 454003, China

<sup>2</sup>Information Security Center, State Key Laboratory of Networking and Switching Technology, Beijing University of Posts and Telecommunication, Beijing 100876, China

Correspondence should be addressed to Lixiang Li; [lixiang@bupt.edu.cn](mailto:lixiang@bupt.edu.cn)

Received 9 October 2020; Revised 6 November 2020; Accepted 8 December 2020; Published 29 December 2020

Academic Editor: Lingwei Xu

Copyright © 2020 Yongli Tang et al. This is an open access article distributed under the Creative Commons Attribution License, which permits unrestricted use, distribution, and reproduction in any medium, provided the original work is properly cited.

The rapid development of the Internet leads to a surge in the amount of information transmission and brings many security problems. For multimedia information transmission, especially digital images, it is necessary to compress and encrypt at the same time. The emergence of compressive sensing solves this problem. Compressive sensing can compress and encrypt at the same time, which can not only reduce the transmission bandwidth of the network but also improve the security of the system. However, when using compressive sensing encryption, the whole measurement matrix needs to be stored, and the compressive sensing can be combined with a chaotic system, so only the generation parameters of the matrix need to be stored, and the security of the system can be further improved by using the sensitivity of the chaotic system. This paper introduces a secure and efficient image compression-encryption scheme using a new chaotic structure and compressive sensing. The chaotic map used in the scheme is generated by our new and universal chaotic structure, which not only expands the chaotic range of the chaotic system but also improves the performance of the chaotic system. After analyzing the performance comparison of traditional one-dimensional chaotic maps and some existing methods, the image compression-encryption scheme based on a new chaotic structure and compressive sensing has a good encryption effect and large keyspace, which can resist brute force attack and statistical attack.

## 1. Introduction

With the advent of the fifth-generation mobile networks (5G) era, the amount of information transmission is gradually increasing, and the requirements for transmission speed are also increased significantly, which requires more effective compression sampling methods to achieve higher sampling rates and signal processing speeds. Due to the security problems of the network itself, multimedia data are vulnerable to various attacks in the process of storage and secure transmission in the network, so it is particularly important to ensure the security of media information data [1, 2]. In order to carry out multimedia communication more effectively, the original image must be compressed and encrypted at the same time, and the emergence of compressive sensing can solve this problem. In 2006, Donoho [3] and Candès et al. [4] formally proposed the theory of

compressive sensing (CS). Compressive sensing is an improvement on the Nyquist sampling, which can sample sparse signals nonuniformly with the number of samples far less than Nyquist sampling law and recover the original data with the reconstruction performance lower than Nyquist sampling. It is widely used in wireless sensor networks, image encryption, image data hiding, etc.

Due to the use of compressive sensing for encryption, the whole measurement matrix needs to be stored, which requires a large amount of storage space. However, it is possible to use the chaotic system that only needs to store the generation parameters of the measurement matrix, instead of storing the characteristics of the whole measurement matrix to reduce the storage space. Because of their chaotic characteristics, such as sensitivity to initial values and parameters [5, 6], ergodicity [7, 8], and uncertainty [9, 10], chaotic systems have been widely used in encryption fields

[11–13]. Therefore, researchers have designed many image encryption algorithms that combine compressive sensing with chaotic systems [14–16].

Peng et al. [14] proposed a security and energy-saving scheme in wireless body area networks, which can solve both energy-saving and data security problems. Compared with the traditional encryption scheme, which only used one matrix to encrypt, they use any one of Chebyshev map, Logistic map, and Tent map to generate two chaotic matrices to encrypt at the same time, which increased the security and solved the security problem in a wireless volume domain network. Wang et al. [15] proposed a visual security image encryption scheme with parallel compressive sensing and designed a visual security encryption scheme with parallel compressive sensing counter mode and embedding technology. In order to achieve a higher security level, the Logistic-Tent chaotic system and 3D Cat map are introduced to construct the measurement matrix, and Zigzag confusion is used for interference. Chai et al. [16] proposed an image encryption method based on the combination of a magnetically controlled memristive chaotic system and compressive sensing. This scheme uses the technologies of a magnetically controlled memristive chaotic system, Secure Hash Algorithm- (SHA-) 512, and cellular automata. In this scheme, cellular automata are used in the diffusion stage to enhance the security of the encryption system, and SHA-512 is used to calculate the initial value of the chaotic system and further generate a measurement matrix, which makes the measurement matrix used in encrypting different types of data. This scheme can improve the correlation between the original image and the algorithm and resist known plaintext attacks and selected plaintext attacks. Chanil et al. [17] proposed a chaotic structure and applied a Logistic map and Sine map into their structure. In order to verify the performance of the proposed chaotic structure, they proposed a new bit-level color image encryption scheme. Through simulation analyses of the bifurcation diagram and Lyapunov exponent, it was proved that their chaotic structure was correct and the range of chaotic parameters was expanded.

We propose a secure and effective image compression-encryption scheme using the new chaotic structure and compressive sensing. The chaotic map used in the compression-encryption scheme is to apply the commonly used traditional one-dimensional chaotic maps to the new and general chaotic structure proposed by us. In this encryption scheme, compressive sensing is used for sampling, which can reduce storage space and transmission bandwidth. The chaotic system only needs to store matrix generation parameters, which can further reduce transmission bandwidth. Arnold interference technology and the SHA-256 function are also used, and the SHA-256 function makes different original images have different keys. Firstly, the Discrete Wavelet Transform (DWT) is used to sparse the original image, and then Arnold interference is applied to the sparse image. The interference parameters of Arnold interference are generated by the SHA-256 function. Then, compressive sensing is used to compress and sample the interference images. Finally, a chaotic sequence is used to perform row and column cyclic shift interference on the compressed and sampled image. Simulation results show that the compression-

encryption scheme has a large parameter space and keyspace, which can prevent the statistical attack and brute force attack.

The rest of this paper is arranged as follows. Section 2 introduces the related basic knowledge. Section 3 describes the proposed chaotic structure and chaotic map under a new structure. Section 4 describes our encryption and decryption scheme. Section 5 simulates and evaluates our encryption scheme. Section 6 summarizes the research content carried out in this paper.

## 2. Fundamental Knowledge

This section gives a brief introduction to the traditional one-dimensional chaotic maps and compressive sensing.

*2.1. Chaotic Maps.* The commonly used traditional one-dimensional chaotic systems are the Sine map, Logistic map, Chebyshev map, and Tent map.

### (1) Sine map

Sine map is a very simple and commonly used chaotic system [18]. Sine map is denoted as

$$s_{n+1} = r_s \times \sin(\pi \times s_n), \quad (1)$$

where  $r_s$  is the chaotic parameter of the Sine map, and  $s_n \in [0, 1]$  is the Sine chaotic sequence.

The bifurcation diagram and Lyapunov exponent diagram of the traditional Sine map are shown in Figures 1(a) and 2(a). The Lyapunov exponent indicates that the chaotic system must have at least one positive Lyapunov exponent. When the Lyapunov exponent is positive, the chaotic characteristics of the system can be quantified; that is, a chaotic system is sensitive to initial conditions. The larger the Lyapunov exponent is, the more sensitive to initial values the chaotic system is. As can be seen from Figures 1(a) and 2(a), the Sine map has chaotic behaviors when the chaotic parameter  $r_s$  is in the range  $r_s \in [0.867, 1]$ .

### (2) Logistic map

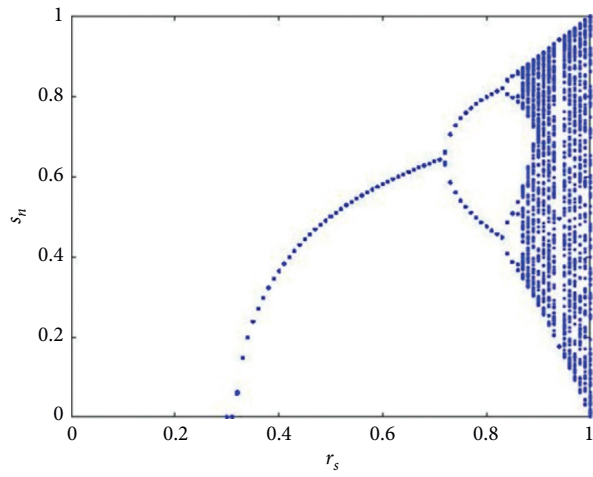
The logistic map is also a very simple but widely used chaotic system [19]. Its performance is similar to that of a Logistic map, and it is defined as

$$l_{n+1} = r_l \times l_n \times (1 - l_n), \quad (2)$$

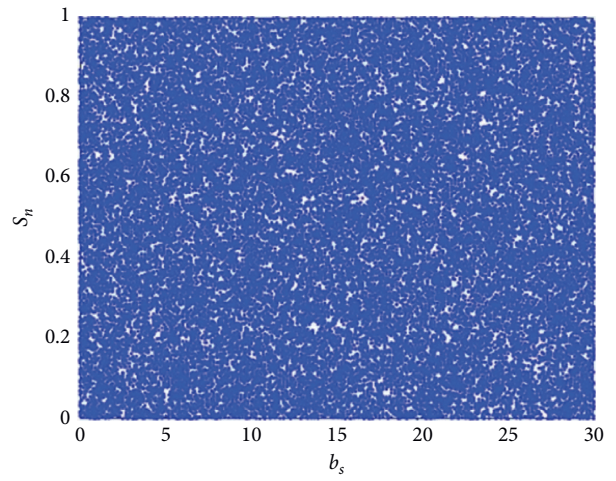
where  $r_l$  is the chaotic parameter of the Logistic map, and  $l_n \in [0, 1]$  is the Logistic chaotic sequence.

The bifurcation diagram and Lyapunov exponent diagram of the traditional Logistic map are shown in Figures 1(c) and 2(c). As can be seen from Figures 1(c) and 2(c), the Logistic map has chaotic behaviors when the control parameter  $r_l$  is in the range  $r_l \in [3.5, 4]$ .

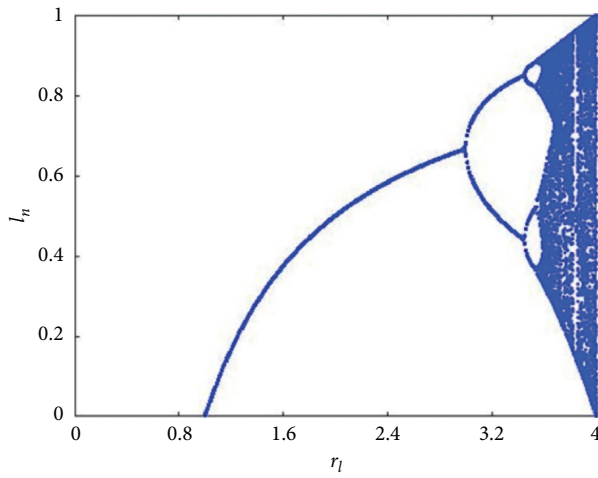
### (3) Chebyshev map



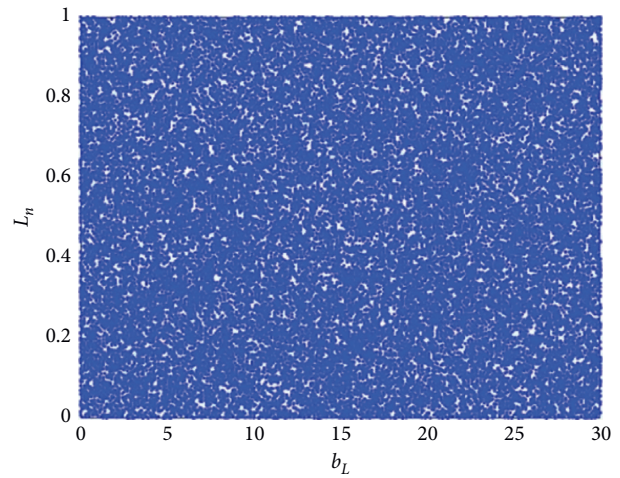
(a)



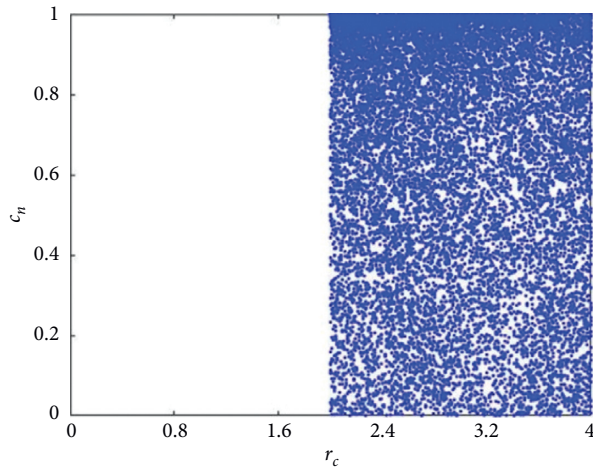
(b)



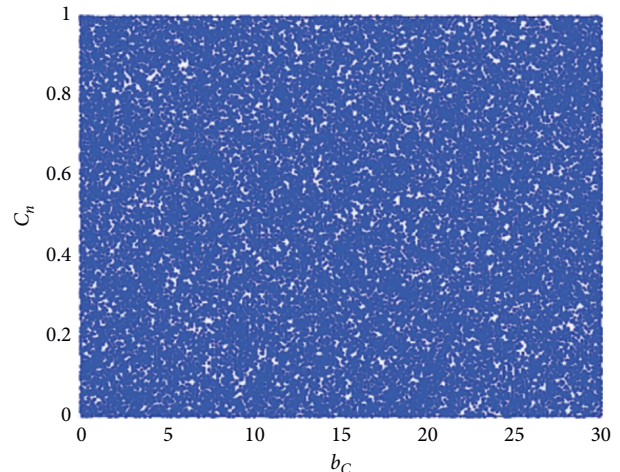
(c)



(d)



(e)



(f)

FIGURE 1: Continued.

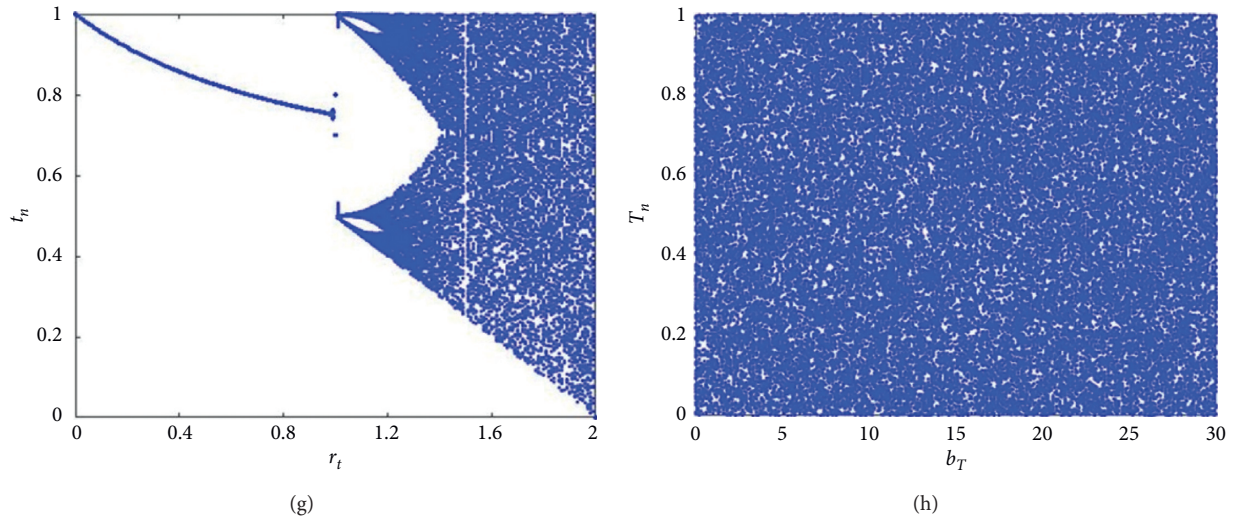


FIGURE 1: Bifurcation diagrams of the traditional one-dimensional chaotic maps and the corresponding new one-dimensional chaotic maps under our chaotic structure: (a) the traditional Sine map, (b) Sine map under our chaotic structure, (c) the traditional Logistic map, (d) Logistic map under our chaotic structure, (e) the traditional Chebyshev map, (f) Chebyshev map under our chaotic structure, (g) the traditional Tent map, and (h) Tent map under our chaotic structure.

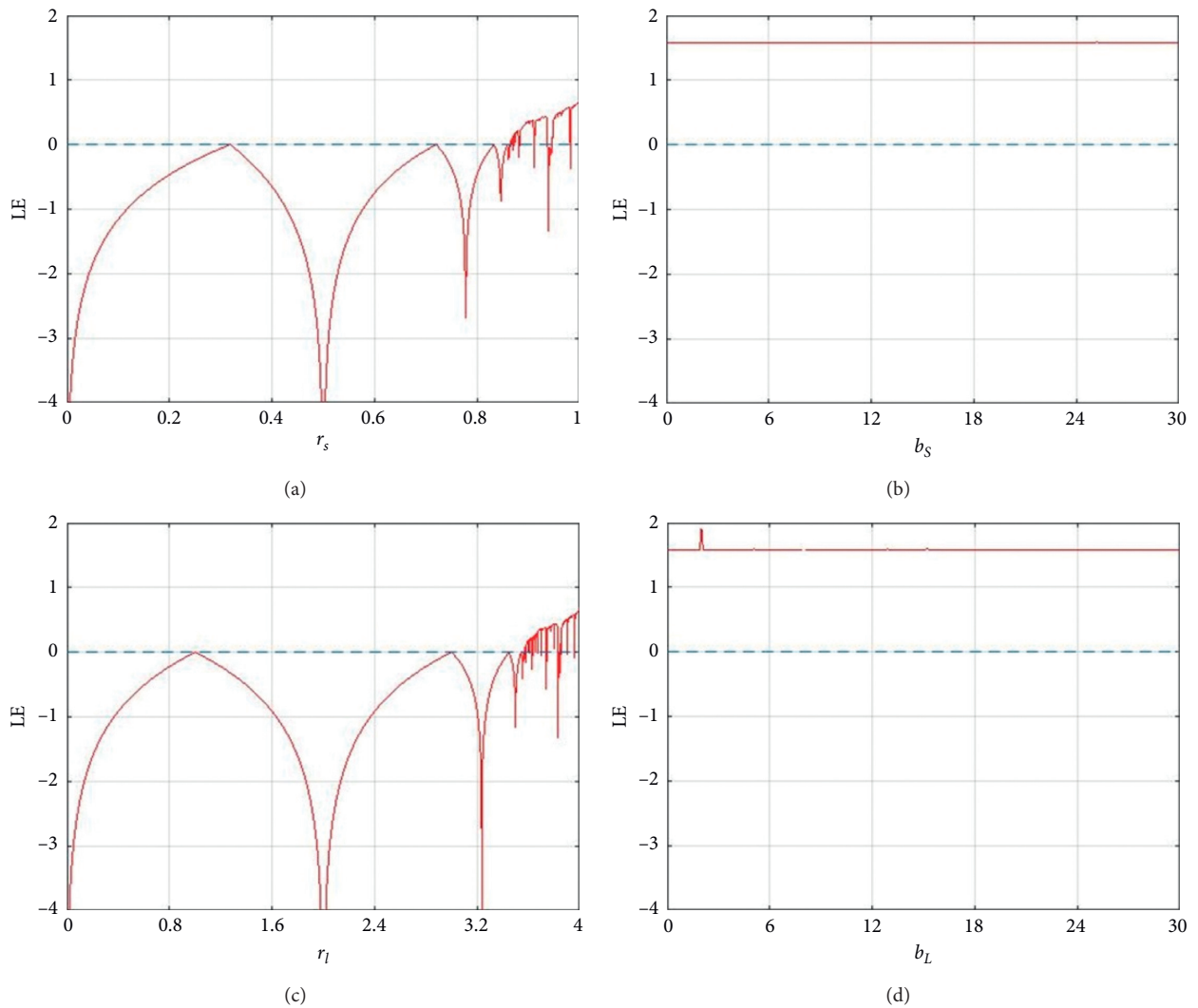


FIGURE 2: Continued.

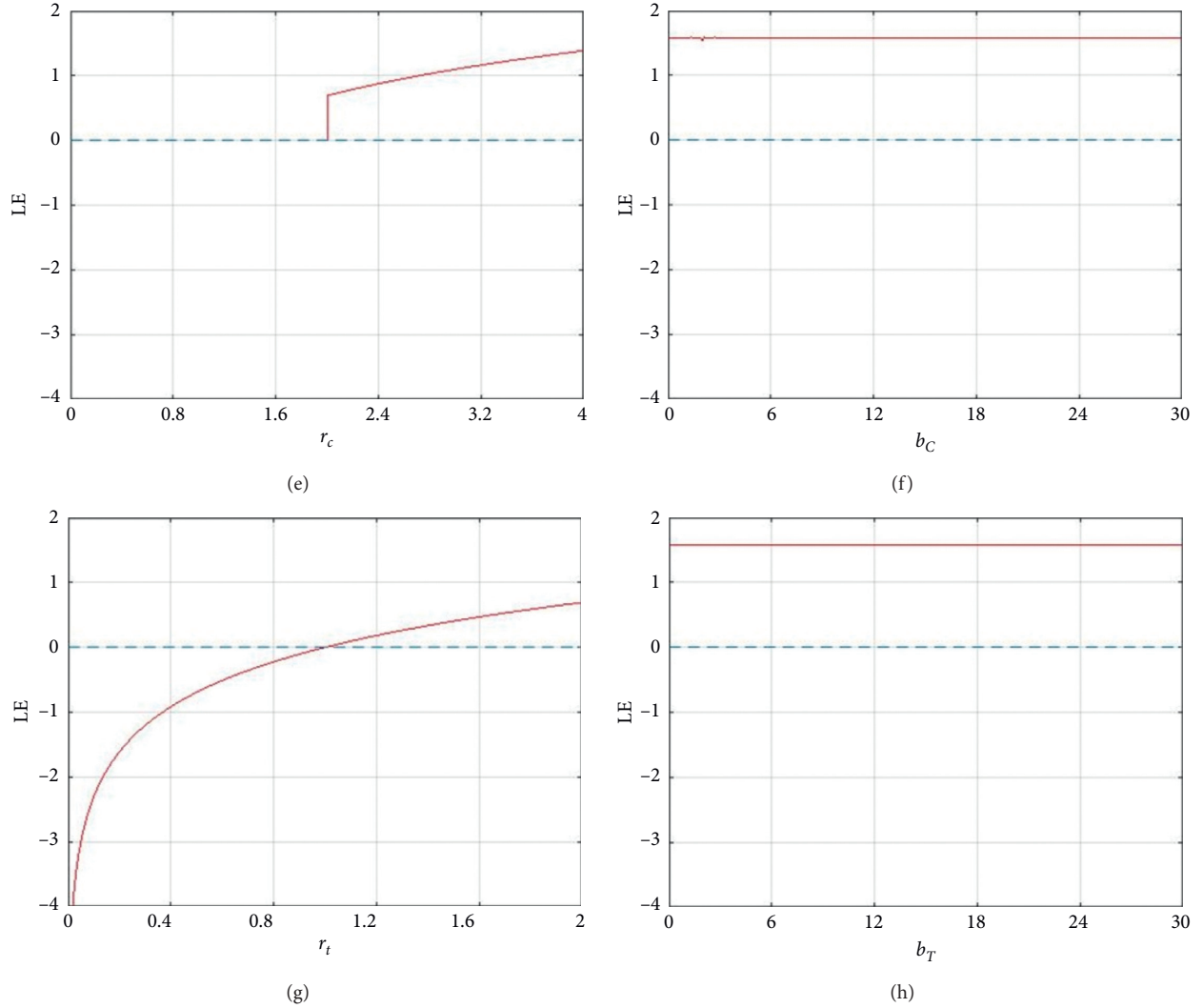


FIGURE 2: Lyapunov exponent diagrams of the traditional one-dimensional chaotic maps and the corresponding new one-dimensional chaotic maps under our chaotic structure: (a) the traditional Sine map, (b) Sine map under our chaotic structure, (c) the traditional Logistic map, (d) Logistic map under our chaotic structure, (e) the traditional Chebyshev map, (f) Chebyshev map under our chaotic structure, (g) the traditional Tent map, and (h) Tent map under our chaotic structure.

Like the Logistic map and Sine map, the Chebyshev map is also a commonly used one-dimensional chaotic map [20], and it is defined as follows:

$$c_{n+1} = \cos(r_c \times \arccos c_n), \quad (3)$$

where  $r_c$  is the chaotic parameter of the Chebyshev map, and  $c_n \in [-1, 1]$  is the Chebyshev chaotic sequence.

The bifurcation diagram and Lyapunov exponent diagram of the traditional Chebyshev map are shown in Figures 1(e) and 2(e). Chebyshev map has chaotic behaviors when the chaotic parameter  $r_c$  takes values in the range  $r_c \in [2, 4]$ .

#### (4) Tent map

Tent map is defined as follows [21]:

$$t_{n+1} = 1 - r_t \times |t_n - 0.5|, \quad (4)$$

where  $r_t$  is the chaotic parameter of the Tent map, and  $t_n \in [0, 1]$  is the chaotic sequence of the Tent map.

The bifurcation diagram and Lyapunov exponent diagram of the traditional Tent map are shown in Figures 1(g) and 2(g). Tent map has chaotic behaviors when the chaotic parameter  $r_t$  is in the range  $r_t \in (1, 2]$ .

**2.2. Compressive Sensing.** Candès et al. [22] proposed that if  $\mathbf{x} \in R^N$  is an unknown vector, which is sparse or compressible on a set of orthogonal bases, the unknown vector  $\mathbf{x}$  can be accurately recovered by fewer random measured values  $\mathbf{y}$ . And this sampling process can be described by a mathematical model as follows:

$$\mathbf{y} = \Phi \mathbf{x}, \quad (5)$$



where  $\Phi$  is the matrix is of size  $M \times N$ ,  $M < N$ , and  $\mathbf{y} \in R^M$  is the sampling value.

This mathematical representation is also a description of the standard framework of compressed perception which is a special case of underdetermined linear equations. Since there are infinitely many solutions in equation (5), the original signal  $\mathbf{x}$  cannot be recovered directly from the sampled value  $\mathbf{y}$ . However, if  $\mathbf{x}$  reflects sparsity in the sparse dictionary  $\Psi$  [23], that is,

$$\mathbf{x} = \Psi \mathbf{a}, \quad (6)$$

where  $\mathbf{a}$  is  $K$ -sparse and is denoted as  $\mathbf{a} \in \Sigma_K$ , so we have

$$\mathbf{y} = \Phi \mathbf{x} = \Phi \Psi \mathbf{a} = \boldsymbol{\theta} \mathbf{a}, \quad (7)$$

where  $\boldsymbol{\theta} = \Phi \Psi$  is the measurement matrix in compressive sensing. So we can recover  $\mathbf{x}$  from  $\mathbf{y}$ .  $\mathbf{a}$  is recovered by

$$\min_{\mathbf{a}} \|\mathbf{a}\|_0, \quad \text{where, } \mathbf{y} = \boldsymbol{\theta} \mathbf{a}. \quad (8)$$

Equation (8) is a  $l_0$  optimization problem. Under certain conditions, the  $l_0$  optimization problem can be transformed into a  $l_1$  optimization problem. The typical conditions include Null Space Property (NSP) and Restricted Isometry Property (RIP). And the equivalent solution can be obtained by [24]

$$\min_{\mathbf{a}} \|\mathbf{a}\|_1, \quad \text{where, } \mathbf{y} = \boldsymbol{\theta} \mathbf{a}. \quad (9)$$

For the measurement matrix, spark property should be satisfied, that is, the minimum number of linear correlation of the columns of the measurement matrix, and the formula is

$$\text{spark}(\boldsymbol{\theta}) = \min_{\mathbf{a} \neq 0} \|\mathbf{a}\|_0, \quad \text{where, } \boldsymbol{\theta} \mathbf{a} = 0. \quad (10)$$

Donoho [25] pointed out that if  $\text{spark}(\boldsymbol{\theta}) > 2K$ , for any vector  $\mathbf{y} \in R^M$ , there is at most one signal  $\mathbf{a} \in \Sigma_K$  that makes  $\mathbf{y} = \boldsymbol{\theta} \mathbf{a}$ .

Because solving a sparse solution is an NP-hard problem, it is impractical to solve the measurement matrix  $\boldsymbol{\theta}$  that satisfies this condition from the perspective of computation [26]. In order to recover sparse signals in reality, Candès et al. [4] introduced the RIP that there is a constant  $\delta_K \in (0, 1)$ . Equation (11) holds true for all  $\mathbf{a} \in \Sigma_K$ .

$$(1 - \delta_K) \|\mathbf{a}\|_2^2 \leq \|\boldsymbol{\theta} \mathbf{a}\|_2^2 \leq (1 + \delta_K) \|\mathbf{a}\|_2^2. \quad (11)$$

Although RIP provides a theoretical guarantee for recovering  $K$ -sparse signals, it is relatively complex to verify that a measurement matrix  $\boldsymbol{\theta}$  meets RIP characteristics. Therefore, in many cases, it is necessary to use the correlation  $\mu(\boldsymbol{\theta})$  of the measurement matrix  $\boldsymbol{\theta}$  to provide a more specific recovery guarantee. Correlation  $\mu(\boldsymbol{\theta})$  refers to the maximum value of the normalized inner product of two columns randomly selected in  $\boldsymbol{\theta}$  [27], namely,

$$\mu(\boldsymbol{\theta}) = \max_{1 \leq i \neq j \leq N} \frac{|\langle \boldsymbol{\theta}_i, \boldsymbol{\theta}_j \rangle|}{\|\boldsymbol{\theta}_i\|_2 \|\boldsymbol{\theta}_j\|_2}, \quad (12)$$

where  $\boldsymbol{\theta}_i$  is the  $i$ -th column of  $\boldsymbol{\theta}$ . For any vector  $\mathbf{y}$ , if  $\mu(\boldsymbol{\theta}) \leq 1/(2K - 1)$ , there is at most one signal  $\mathbf{a} \in \Sigma_K$ , making  $\mathbf{y} = \boldsymbol{\theta} \mathbf{a}$ .

Common recovery algorithms include Matching Pursuit (MP) algorithm [28], Orthogonal Matching Pursuit (OMP) algorithm [29], Orthogonal Matching Pursuit (StOMP) algorithm [30], and Compressive Sampling Matching Pursuit (CoSaMP) algorithm [31].

### 3. New Chaotic Structure

In this section, we firstly describe a new chaotic structure in detail, and secondly, we describe the new chaotic maps generated by applying the Sine map, Logistic map, Chebyshev map, and Tent map to the new chaotic structure.

*3.1. New Chaotic Structure.* The new chaotic structure is given as follows:

$$\mathbf{y}_{n+1} = F(b, \mathbf{y}_n, k) = \text{mod} \left( \left( F_{\text{chaos}}(b, \mathbf{y}_n) - \frac{\mathbf{y}_n}{3} \right) \times 2^k, 1 \right), \quad k \geq 0, \quad (13)$$

where  $F_{\text{chaos}}(b, \mathbf{y}_n)$  is the traditional one-dimensional chaotic map mentioned in Section 2,  $F(b, \mathbf{y}_n, k)$  is a new chaotic map generated under our new chaotic structure,  $\mathbf{y}_n \in [0, 1]$  is the chaotic sequence,  $b$  is the chaotic parameter of the proposed chaotic structure, and  $b$  can take any value.  $\text{mod}$  is a modulus function, which ensures that the values of the generated chaotic sequence are in the range  $[0, 1]$ .  $2^k$  is an adjustment function about the iteration parameter  $k$ , which is iterated through adjustments to eliminate the transient effect. The values of  $b, k$  in this chaotic structure should be specifically analyzed according to the embedded map; that is to say, when different chaotic maps are applied to the proposed chaotic structure, the values of  $b, k$  will have different value ranges.

*3.2. Application and Analysis of Our New Chaotic Structure.* In this subsection, we give the detailed analyses of new chaotic maps generated by our new chaotic structure.

#### (1) New Sine map under our new chaotic structure

The new Sine map under our new structure is defined as follows:

$$S_{n+1} = \text{mod} \left( b_S \times \sin(\pi \times S_n) - \frac{S_n^2}{3} \right) \times 2^{k_S}, 1, \quad (14)$$

where  $S_n \in [0, 1]$  is the new Sine chaotic sequence which is generated by our new chaotic structure, and  $S_0$  is the initial value of the new Sine chaotic sequence.  $b_S$  is the chaotic parameter of this new Sine map, and  $k_S$  is the iterations parameter of the new Sine map.

The bifurcation diagram and Lyapunov exponent diagram of the new Sine map under our new structure are shown in Figures 1(b) and 2(b). It can be seen from Figures 1(b) and 2(b) that the new Sine map under our new structure has a much larger

chaotic parameter range than the traditional Sine map and the Lyapunov exponent that are all positive numbers, which proves the superiority of the proposed Sine map. When  $k_S \in [6, 28]$  and  $b_S \in [0, 30]$ , the state of the new Sine map under our new structure is fully chaotic.

- (2) New Logistic map under our new chaotic structure

The new Logistic map generated by our new chaotic structure is presented as follows:

$$L_{n+1} = \text{mod} \left( b_L \times L_n \times (1 - L_n) - \frac{L_n^2}{3} \times 2^{k_L}, 1 \right), \quad (15)$$

where  $L_n \in [0, 1]$  is the new Logistic chaotic sequence which is generated by our new chaotic structure, and  $L_0$  is the initial value of the new Logistic chaotic sequence.  $b_L$  is the chaotic parameter of the new Logistic map, and  $k_L$  is the iterations parameter of the new Logistic map.

The bifurcation diagram and Lyapunov exponent diagram of the new Logistic map under our new structure are shown in Figures 1(d) and 2(d). Like the new Sine map under our new structure, its chaotic range and performance are much better than the traditional Logistic map. When  $k_L \in [7, 21]$ ,  $b_L \in [0, 30]$ , the Logistic map under our new structure is in a fully chaotic state.

- (3) New Chebyshev map under our new chaotic structure

The new Chebyshev map under our new structure can be expressed as follows:

$$C_{n+1} = \text{mod} \left( \cos(b_C \times \arccos(C_n)) - \frac{C_n^2}{3} \times 2^{k_C}, 1 \right), \quad (16)$$

where  $C_n \in [0, 1]$  is the new Chebyshev chaotic sequence which is generated by our new chaotic structure, and  $C_0$  is the initial value of the new Chebyshev chaotic sequence.  $b_C$  is the chaotic parameter of this new Chebyshev map, and  $k_C$  is the iterations parameter of the new Chebyshev map.

The bifurcation diagram and Lyapunov exponent diagram of the new Chebyshev map under our new structure are shown in Figures 1(f) and 2(f). When  $k_C \in [8, 29]$  and  $b_C \in [0, 30]$ , the state of the Chebyshev map under our new structure is fully chaotic.

- (4) New Tent map under our new chaotic structure

The new Tent map under our new structure is defined as follows:

$$T_{n+1} = \text{mod} \left( \left( (1 - b_T \times |T_n - 0.5|) - \frac{T_n^2}{3} \right) \times 2^{k_T}, 1 \right), \quad (17)$$

where  $T_n \in [0, 1]$  is the new Tent chaotic sequence which is generated by our new chaotic structure, and  $T_0$

is the initial value of the new Tent chaotic sequence.  $b_T$  is the chaotic parameter of the new Tent map, and  $k_T$  is the iterations parameter of the new Tent map.

The bifurcation diagram and Lyapunov exponent diagram of the new Tent map under our new structure are shown in Figures 1(h) and 2(h). The Tent map under our new chaotic structure is fully chaotic when  $k_T \in [5, 21]$ ,  $b_T \in [0, 30]$ .

## 4. The Proposed Compression-Encryption Scheme

In this section, a secure and effective image compression-encryption scheme is proposed by using the new chaotic map under a new structure and compressive sensing.

### 4.1. Key Generation

- (1) The generation of the Arnold interference parameters  $k_1, k_2$  and the interference number  $k_3$ : calculate the 256-bit hash value  $H$  according to the original image  $X$  with SHA-256 function, then divide  $H$  into two blocks, and three initial values  $n_0, \mathbf{a}_0, b_0$  are randomly selected. SHA-256 function can be used to calculate the key according to the original image, and different original images have different Arnold interference effects and different chaotic sequence parameters, so as to achieve different effects of original images and different measurement matrix. The specific formula of SHA-256 function can be expressed as follows:

$$\begin{aligned} H &= h_1, h_2, \dots, h_{31}, h_{32}, \\ k_1 &= n_0 + (h_1 \oplus h_2 \oplus \dots \oplus h_{15} \oplus h_{16}), \\ k_2 &= k_1 + \mathbf{a}_0 \times (h_{17} \oplus h_{18} \oplus \dots \oplus h_{31} \oplus h_{32}), \\ k_3 &= (k_1 \oplus k_2) + b_0. \end{aligned} \quad (18)$$

- (2) The generation of two improved chaotic sequences  $z_0, z_1$ : we use the new chaotic maps proposed in this paper to generate chaotic sequences. Two improved chaotic sequences are generated according to the initial values  $z'_0, z'_1$  and control parameters  $u_0, u_1$ . Take a new Tent map and new Chebyshev map as examples:

$$\begin{aligned} z_0 &= \text{mod} \left( \cos(u_0 \times \arccos(z'_0)) - \frac{z_0^2}{3} \right) \times 2^{16}, 1, \\ z_1 &= \text{mod} \left( (1 - u_1 \times |z'_1 - 0.5|) - \frac{z_1^2}{3} \right) \times 2^{16}, 1. \end{aligned} \quad (19)$$

- (3) Calculate the cyclic sequence bitRow in the row direction. Randomly select the cycle number keyRow of the cyclic shift in the row direction, and generate LogisticRow according to the initial value

LogisticRow' and control parameter  $\omega_0$ . The steps can be expressed as follows:

$$\begin{aligned}
& \text{LogisticRow} = \text{zero}(\text{keyRow}, \text{Rows}), \\
& \text{bitRow} = \text{zero}(\text{keyRow}, \text{Rows}), \\
& \text{for } i = 2: \text{keyRow}: \text{Rows}, \\
& \text{LogisticRow}(i) = \omega_0 \times \text{LogisticRow}(i-1) \\
& \quad \times (1 - \text{LogisticRow}(i-1)), \\
& \text{bitRow}(i) = \text{rem}(\text{round}(\text{LogisticRow}(i) \\
& \quad \times 100,000), \text{Columns}), \\
& \text{end},
\end{aligned} \tag{20}$$

where LogisticRow is the traditional Logistic map which is used to interfere with the sequence in the row direction, Rows is the numbers of rows, and Columns is the numbers of columns. The number of cycles on the row is once per row, so it needs Rows time. The interference in the row direction is performed according to the cycle number keyRow of the cyclic shift in the row direction. Since the number of interference in the row direction will not be greater than the number of Columns, the number of cycles can be set to Columns.

- (4) Calculate the cyclic sequence bitColumn in the column direction. Randomly select the cycle number keyColumn of the cyclic shift in the column direction, and generate LogisticColumn according to the initial value LogisticColumn' and control parameter  $\omega_1$ . The steps can be expressed as follows:

$$\begin{aligned}
& \text{LogisticColumn} = \text{zero}(\text{keyColumn}, \text{Columns}), \\
& \text{bitColumn} = \text{zero}(\text{keyColumn}, \text{Columns}), \\
& \text{for } i = 2: \text{keyColumn}: \text{Columns}, \\
& \text{LogisticColumn}(i) = \omega_1 \times \text{LogisticColumn}(i-1) \\
& \quad \times (1 - \text{LogisticColumn}(i-1)), \\
& \text{bitColumn}(i) = \text{rem}(\text{round}(\text{LogisticColumn}(i) \\
& \quad * 100,000), \text{Rows}), \\
& \text{end},
\end{aligned} \tag{21}$$

where LogisticColumn is the traditional Logistic map which is used to interfere with the sequence in the column direction. Similarly, the number of cycles on the column is one for each column, so it takes Columns time. Interference in the column direction is performed according to the number of cycles keyColumn of cyclic shift in the column direction. Since the number of interference in the column direction will not be greater than the number of Rows, the number of cycles can be set to Rows.

**4.2. Compression-Encryption Scheme.** The chaotic map proposed in this paper is used to construct the measurement matrix for compression and encryption. Specific encryption steps can be described as follows:

Step 1: firstly, an original image  $X$  with the size of  $m \times n$  is obtained.

Step 2: the original image  $X$  is sparse by Discrete Wavelet Transform (DWT), and the sparse image  $X_1$  with the size  $m \times n$  is obtained.

Step 3: Arnold interference is carried out on a sparse image  $X_1$  according to Arnold interference parameters  $k_1, k_2$  and interference number  $k_3$ . The interference image is represented by  $X_2$  with size  $m \times n$ .

Step 4: according to the  $z_0, z_1$  chaotic sequences, two measurement matrices are obtained. One measurement matrix is represented by  $\Phi_1$  and the size is  $p \times q$ .  $p$  is a random number as the number of rows of the measurement matrix. The number of columns of the measurement matrix is the same as the number of rows of the measured image, that is  $q = m$ , which is used for compression and sampling, and the other measurement matrix is represented by  $\Phi_2$ , whose size is  $p \times q$ . The compression and sampling process using compressive sensing is expressed as follows:

$$X_3 = \Phi_1 \times X_2 + \Phi_2, \tag{22}$$

where  $X_3$  is the image after compressed sampling, and its size is  $p \times n$ .

Step 5: then perform cyclic shift encryption in the row direction to obtain the encrypted image  $X_4$  in the row direction, wherein the size is  $p \times n$ , and the encryption steps in the row direction are expressed as follows:

$$\begin{aligned}
& \text{for } r \text{ times} = 1: \text{keyRow}, \\
& \quad \text{for } i = 1: p, \\
& \quad X_4(i, :) = \text{circshift}(X_3(i, :), [0 \quad \text{bitRow} \\
& \quad \quad \quad - (r \text{ times}, i)]), \\
& \quad \text{end}, \\
& \text{end},
\end{aligned} \tag{23}$$

where  $r$  times is the number of bit cycles to be performed in all row directions for the control as a whole. circshif function has two parameters, one to control the row and the other to control the column. Now, as long as the column is operated, circshif function is set to  $[0 \quad \text{bitRow} - (r \text{ times}, i)]$ .

Step 6: then, perform cyclic shift encryption in the column direction to obtain the encrypted image  $Y$  in the column direction with size  $p \times n$ , and the encryption steps in the column direction are expressed as follows:

$$\begin{aligned}
& \text{for } c \text{ times} = 1: \text{keyColumn}, \\
& \quad \text{for } i = 1: q, \\
& \quad Y(i, :) = \text{circshift}(X_4(i, :), [\text{bitColumn} - (c \text{ times}, i) \quad 0]), \\
& \quad \text{end}, \\
& \text{end},
\end{aligned} \tag{24}$$

where  $c$  times is the number of bit cycles to be performed in all column directions for the control as a whole. Now, as long as the row is operated, so the circshift function is set to  $[\text{bitColumn} - (c \text{ times}, i) 0]$ .

**4.3. Decryption Scheme.** The decryption scheme is actually the reverse operation of the encryption scheme, and its principle is the same as that of the encryption scheme. The specific decryption steps can be described as follows:

Step 1: first obtain the encrypted image, which is represented by  $Y'$  and size is  $p \times n$ .

Step 2: according to the cycle number  $\text{keyColumn}$  of the cyclic shift in the column direction sent by the encryption party, a bit cyclic sequence  $\text{bitColumn}$  for decryption in the column direction is constructed.

Step 3: decrypt the encrypted image with a cyclic shift in column direction according to  $\text{keyColumn}$  and  $\text{bitColumn}$  and obtain the cyclic shift in the column direction to decrypt image  $X_{4'}$ , with size  $p \times n$ . The steps are as follows:

```
for c times = 1: keyColumn,
    for i = 1: q,
         $X_{4'}(:, i) = \text{circshift}(Y'(:, i), [p - \text{bitColumn}(c \text{ times}, i) 0]);$ 
    end,
end,
(25)
```

Step 4: according to the cycle number  $\text{keyRow}$  of the cyclic shift in the row direction sent by the encryption party, construct the bit cyclic sequence  $\text{bitRow}$  used for encryption in the row direction.

Step 5: perform cyclic shift decryption on the cyclic shift decrypted image  $X_{4'}$  in the column direction according to the cycle number  $c_0$  of cyclic shift encryption in the row direction sent by the encrypting party to obtain the cyclic shift decrypted image  $X_{3'}$  in the row direction with size  $p \times n$ . The steps are as follows:

```
for r times = 1: keyRow,
    for i = 1: p,
         $X_{3'}(i, :) = \text{circshift}(X_{4'}(i, :), [0 \quad q - \text{bitColumn}(r \text{ times}, i)]);$ 
    end,
end.
(26)
```

Step 6: generate the improved chaotic sequence according to the improved chaotic sequence initial values  $u_0, \omega_0$  sent by the encryption party to construct the random measurement matrix, which is used for decompression sampling. And  $X_{3'}$  is recovered by the OMP algorithm to obtain a decompressed image, which is represented as  $X_{2'}$  with size  $m \times n$ .

Step 7: Arnold inverse interference is performed on  $X_{2'}$  according to Arnold interference parameters  $k_1, k_2$  and interference number  $k_3$  sent by the encryption party, and the image after inverse Arnold interference is represented as  $X_{1'}$  with size  $m \times n$ .

Step 8: image  $X_{1'}$  is subjected to inverse sparsity processing by Inverse Discrete Wavelet Transform (IDWT), and the final decrypted image  $X'$  with size  $m \times n$  is obtained.

This allows the receiver to decrypt the encrypted image and retrieve the original message. The flow chart of encryption and decryption is shown in Figure 3.

## 5. Simulation Result and Discussion

In this section, we simulate and evaluate the safe and effective image compression-encryption scheme, using MATLAB R2018a to simulate. The size of the selected image is  $256 \times 256$ , and the size of the constructed random measurement matrix is  $230 \times 256$ . And  $n_0 = 4, a_0 = 3, b_0 = 2$ , the initial values of all chaotic sequences are set to 0.3, and  $u_0 = 0.3, u_1 = 0.4, \omega_0 = 3.87, \omega_1 = 3.95$ . The cycle number of row cyclic shift encryption is  $\text{keyRow} = 6$ , and the cycle number of column cyclic shift is  $\text{keyColumn} = 5$ . DWT is used to perform the sparse operation, and the OMP algorithm is used for recovery.

**5.1. Encryption Effect.** We select “Lena,” “Boom,” “Moon,” and “Rice” images for encryption to analyze the encryption and decryption effect. We use four new chaotic maps proposed in this paper to perform chaotic encryption. The encryption effect is shown in Figure 4.

It can be seen from Figures 4(a) and 4(c) that the original image becomes disorganized and irregular after encryption, and the data of the original image cannot be identified, which proves that the encryption scheme proposed in this paper has a good encryption effect.

**5.2. Histogram Analysis.** The histogram represents the distribution of the pixel intensity of digital images in a graphical way, which can intuitively show the pixel distribution states of the original image and the encrypted image. When the pixel distribution is not uniform, it may cause the loss of image details. The histogram of the original image is unique and vulnerable to statistical attack. To prevent this attack, the histogram of the encrypted image must be relatively uniform and different from that of the original image.

From Figures 4(b) and 4(d), the histograms of the original images are not uniformly distributed, while the encrypted histograms are uniformly distributed. It can be seen that the proposed chaotic maps applied to the encryption field have a strong resistance to statistical attack.

**5.3. Key Sensitivity Analysis.** We use the proposed Logistic map under our new structure for testing. Firstly, we give a set of encryption keys to encrypt the original image and then decrypt it with the same key. We randomly use a set of keys

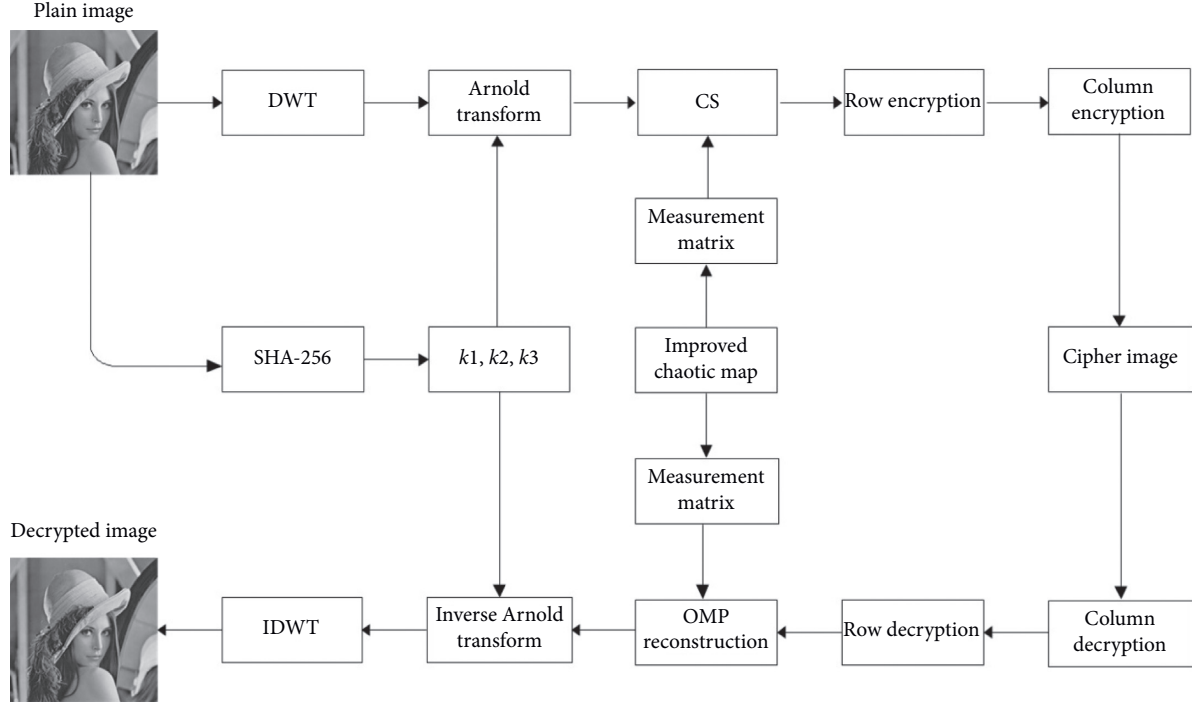


FIGURE 3: Flow chart of encryption and decryption.

$[0.568 \ 0.265 \ 1.25 \ 23.26 \ 456.2 \ 256.2 \ 2 \ 1]$  to encryption. When we use  $[0.568 \ 0.265 \ 1.25 \ 23.26 \ 456.2 \ 256.2 \ 2 \ 1]$  to decrypt, we can get the decrypted image. But when we use  $[0.568 \ 0.265 \ 1.25 \ 23.26 \ 456.2 \ 256.2 \ 2.0000000000000001 \ 1]$  to decrypt, we could not get the decrypted image. As shown in Figure 5, even if the decryption keys differ by  $0.0000000000000001$ , the decrypted image cannot be obtained; thus, the useful information cannot be obtained, which shows that new chaotic maps have high sensitivity.

**5.4. Keyspace Analysis.** A good encryption scheme should make the keyspace greater than  $10^{30}$  in order to resist a brute force attack. There are 14 keys in our encryption scheme, which are  $k, n_0, a_0, b_0, u_0, u_1, z_0, z_1, \omega_0, \omega_1, \text{keyRow}, \text{LogisticRow}', \text{keyColumn}, \text{and LogisticColumn}'$ . If the accuracy is set to  $10^{-14}$ , then the keyspace of our encryption scheme is  $10^{196}$ . This shows that the keyspace of our encryption scheme is large enough to resist a brute force attack.

**5.5. PSNR and SSIM Analysis.** In order to further verify whether the encryption algorithm is safe and reliable, the quality of the images before and after encryption is analyzed. The quality of the restored images can be evaluated using the Peak Signal-to-Noise Ratio (PSNR) and the Structural Similarity Index (SSIM). PSNR can be expressed as

$$\text{PSNR} = 10 \log \frac{255^2}{\left( \frac{1}{N^2} \sum_{i=1}^N \sum_{j=1}^N [P(i, j) - P'(i, j)]^2 \right)}, \quad (27)$$

where  $P(i, j)$  is the pixel value at the  $(i, j)$  position of the original image,  $P'(i, j)$  is the pixel value at the  $(i, j)$  position

of the restored image,  $N$  is the size of the image selected for the experiment, and 255 is the maximum value of the 8-bit representation. Generally, when the value of PSNR is lower than 28, the difference in image quality is greater. The smaller the PSNR, the greater the difference in image quality. The greater the PSNR, the less distortion the original image.

SSIM is used to measure the similarity between the original image and the restored image, which can be expressed as

$$\text{SSIM} = \frac{(2\mu_X\mu_Y + C_1)(2\sigma_{XY} + C_2)}{(\mu_X^2 + \mu_Y^2 + C_1)(\sigma_X^2 + \sigma_Y^2 + C_2)}, \quad (28)$$

where  $C_1 = 0.01 \times (2^8 - 1)$ ,  $C_2 = 0.01 \times (2^8 - 1)$ ,  $\mu_X$  is the mean value of the original image, and  $\mu_Y$  is the mean value of the restored image.  $\sigma_X^2$  is the variance of the original image,  $\sigma_Y^2$  is the variance of the restored image, and  $\sigma_{XY}$  is the covariance of the original image and the restored image. The range of structural similarity is  $[-1, 1]$ . In general, the larger the SSIM values, the better the overall quality of the reconstructed images. When the original image and the restored image are identical, the value of SSIM is 1.

Table 1 lists the analysis results of PSNR and SSIM. It can be seen from Table 1 that the PSNR and SSIM of our encryption scheme are the largest, indicating that the encryption and decryption effect proposed in this paper is good.

**5.6. Information Entropy Analysis.** Information entropy is used to measure the confusion of the image and the distribution of gray values. The larger the entropy of the images is, the more consistent the gray distribution of the images is.

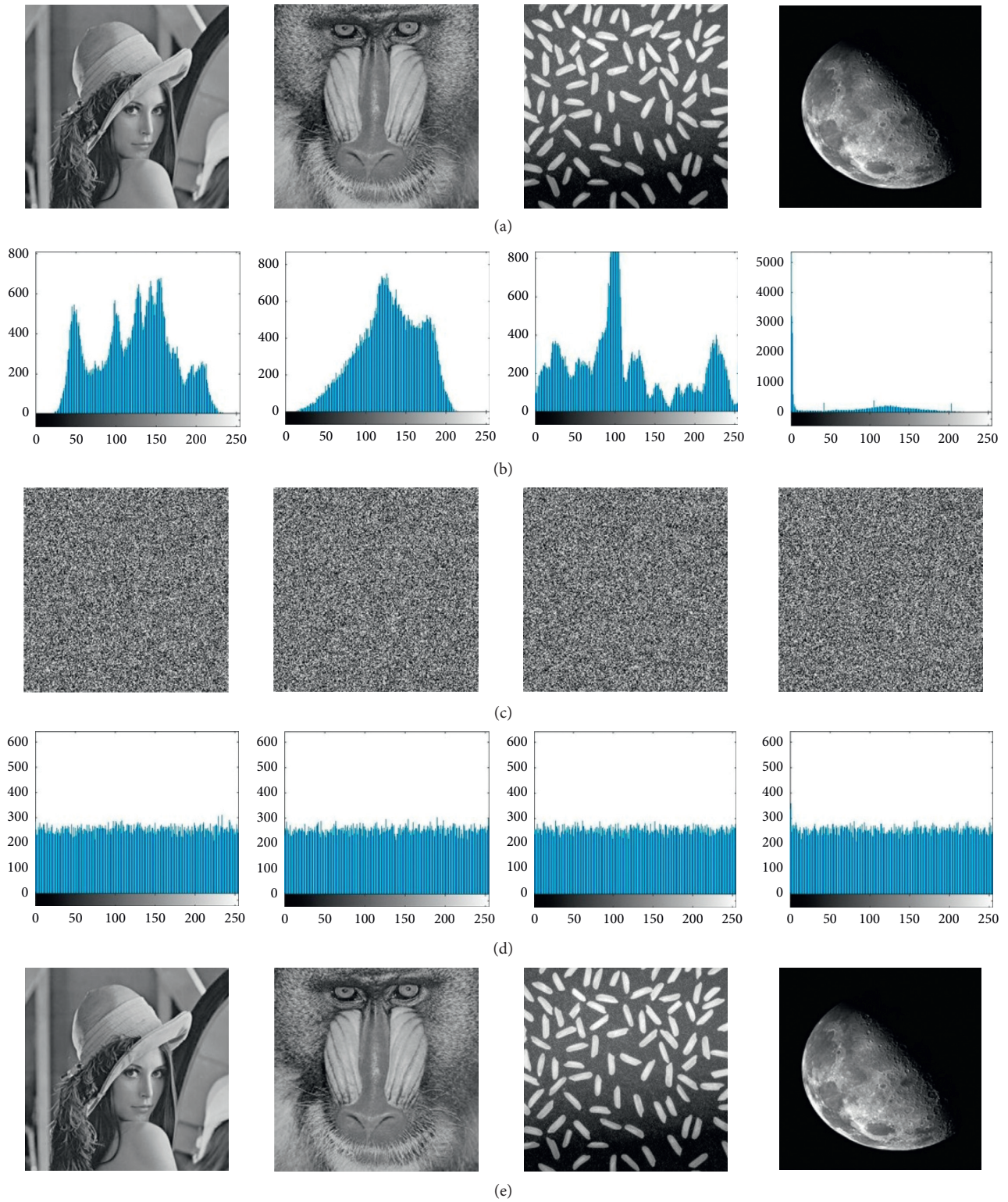


FIGURE 4: (a) Original image, (b) original image histogram, (c) encrypted image, (d) encrypted image histogram, and (e) decrypted image.

For a gray image of size  $256 \times 256$ , the theoretical value of information entropy is 8. An effective encryption algorithm should make the information entropy of the encrypted image close to the theoretical value. The information entropy can be expressed as

$$H(m) = - \sum_{i=1}^{L \times L} P(m_i) \log_2 P(m_i), \quad (29)$$

where  $P(m_i)$  is the probability of the gray value  $m_i$ , and  $L$  is the gray level.

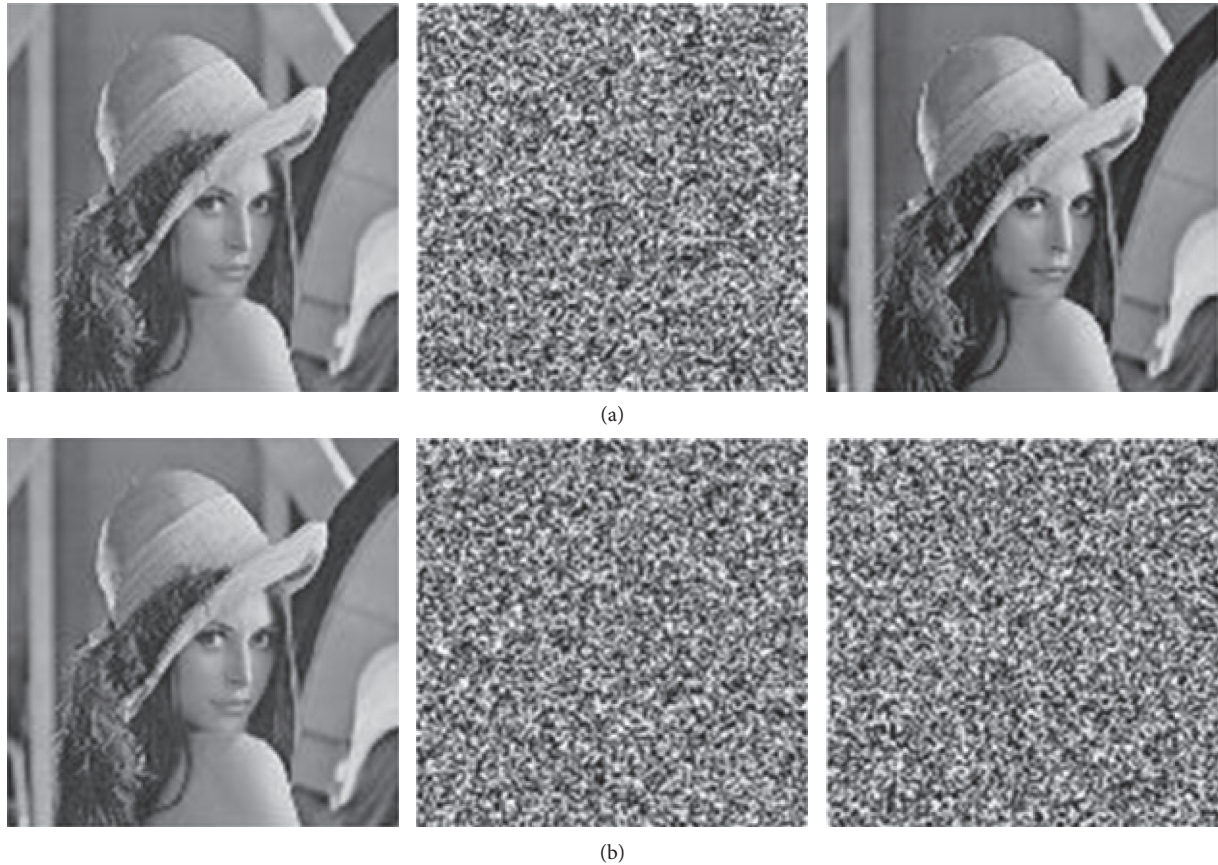


FIGURE 5: Key sensitivity analysis. The encryption key is  $[0.568 \ 0.265 \ 1.25 \ 23.26 \ 456.2 \ 256.2 \ 2 \ 1]$ . (a) decryption key is  $[0.568 \ 0.265 \ 1.25 \ 23.26 \ 456.2 \ 256.2 \ 2 \ 1]$  and (b) decryption key is  $[0.568 \ 0.265 \ 1.25 \ 23.26 \ 456.2 \ 256.2 \ 2.0000000000000001 \ 1]$ .

TABLE 1: PSNR and SSIM analysis.

	Chaotic map	CS scheme [14]			Our scheme		
		Lena	Boom	Average	Lena	Boom	Average
PSNR	Chebyshev + Tent [14]	32.2193	23.3287	<b>27.7740</b>	34.7032	26.9524	<b>30.8278</b>
	Our-Chebyshev + our-Tent	32.3556	23.4894	<b>27.9225</b>	35.4272	27.1717	<b>31.2995</b>
	Sine + Logistic [17]	32.2724	23.0829	<b>27.6777</b>	35.1394	26.5448	<b>30.8421</b>
	Our-Sine + our-Logistic	32.2654	23.5357	<b>27.9006</b>	35.3708	26.9977	<b>31.1843</b>
SSIM	Chebyshev + Tent [14]	0.7517	0.6227	<b>0.6872</b>	0.8118	0.7872	<b>0.7995</b>
	Our-Chebyshev + our-Tent	0.7528	0.6394	<b>0.6961</b>	0.8184	0.7971	<b>0.8078</b>
	Sine + Logistic [17]	0.7538	0.6450	<b>0.6994</b>	0.8164	0.7883	<b>0.8024</b>
	Our-Sine + our-Logistic	0.7512	0.6664	<b>0.7088</b>	0.8194	0.7955	<b>0.8075</b>

Table 2 lists the results of information entropy analysis. As can be seen from Table 2, the information entropy of the encrypted image is higher than that of the original image, which proves that the gray distribution of the encrypted image is more uniform than that of the original image.

*5.7. Correlation Analysis.* Correlation analysis mainly analyzes the correlation between pixels in adjacent locations. The correlation between adjacent pixels of the original image is very high, while the correlation between encrypted cryptographic images after an effective secure encryption system should be

TABLE 2: Information entropy analysis.

	Chaotic map	CS scheme [14]			Our scheme		
		Lena	Boom	Average	Lena	Boom	Average
Information entropy	Chebyshev + Tent [14]	7.2172	7.2735	<b>7.2454</b>	7.6397	7.8880	<b>7.7639</b>
	Our-Chebyshev + our-Tent	7.5729	7.5738	<b>7.5734</b>	7.9820	7.9895	<b>7.9858</b>
	Sine + Logistic [17]	7.2750	7.2735	<b>7.2743</b>	7.6658	7.6945	<b>7.6802</b>
	Our-Sine + our-Logistic	7.5612	7.5940	<b>7.5776</b>	7.9812	7.9840	<b>7.9826</b>

TABLE 3: Correlation analysis.

Image	Direction	Correlation coefficient of plain image	Correlation coefficient of cipher image				
			Chebyshev + Tent [14]	Our- our-Tent	Sine + Logistic [17]	Our- Logistic	
CS scheme [14]	Lena	Horizontal	0.9343	-0.0407	0.0098	-0.0568	-0.0251
		Vertical	0.9715	-0.0549	-0.0324	0.0943	0.0107
		Diagonal	0.9271	0.0343	-0.0047	0.0633	0.0624
	Boom	Horizontal	0.8544	-0.0195	-0.0011	0.0521	0.0372
		Vertical	0.8311	0.0402	0.0287	-0.0149	-0.0236
		Diagonal	0.7576	-0.0608	0.0293	0.0459	-0.0438
	Average	Horizontal	<b>0.8944</b>	<b>-0.0301</b>	<b>0.0044</b>	<b>-0.0024</b>	<b>0.0061</b>
		Vertical	<b>0.9013</b>	<b>-0.0074</b>	<b>-0.0019</b>	<b>0.0397</b>	<b>-0.0065</b>
		Diagonal	<b>0.8424</b>	<b>-0.0133</b>	<b>0.0123</b>	<b>0.0546</b>	<b>0.0093</b>
Our scheme	Lena	Horizontal	0.9278	0.0393	-0.0058	-0.0010	0.0012
		Vertical	0.9688	0.0352	0.0197	0.0428	-0.0306
		Diagonal	0.9031	0.0140	0.0246	-0.0023	-0.0197
	Boom	Horizontal	0.8685	-0.0125	-0.0105	-0.0123	-0.0126
		Vertical	0.8247	-0.0278	-0.0156	-0.0814	0.0181
		Diagonal	0.7623	-0.0173	-0.0149	0.0226	0.0344
	Average	Horizontal	<b>0.8982</b>	<b>0.0134</b>	<b>-0.0082</b>	<b>-0.0067</b>	<b>-0.0057</b>
		Vertical	<b>0.8968</b>	<b>0.0037</b>	<b>0.0021</b>	<b>-0.0193</b>	<b>-0.0063</b>
		Diagonal	<b>0.8327</b>	<b>-0.0017</b>	<b>0.0049</b>	<b>0.0102</b>	<b>0.0074</b>

relatively low, with the correlation coefficient close to 0. The correlation calculation can be expressed as

$$r_{xy} = \frac{\text{cov}(x, y)}{\sqrt{D(x)D(y)}}$$

$$\text{cov}(x, y) = \frac{1}{N} \sum_{i=1}^N [x_i - E(x)][y_i - E(y)],$$

$$D(x) = \frac{1}{N} \sum_{i=1}^N [x_i - E(x)]^2,$$

$$E(x) = \frac{1}{N} \sum_{i=1}^N x_i,$$
(30)

where  $x$  and  $y$  represent the gray values of two adjacent pixels.

Table 3 lists the correlation coefficient analysis results of the safe and effective image encryption scheme. It can be seen from Table 3 that, compared with the correlation coefficient of the original image, the correlation coefficient of the encrypted image is greatly reduced and close to 0, which indicates that the abovementioned security theoretical scheme has a good encryption effect.

## 6. Conclusion

We propose a safe and effective image compression-encryption scheme based on a new chaotic structure and compressive sensing. This scheme uses a new chaotic structure proposed by ourselves and applies the commonly used traditional one-dimensional chaotic maps to the proposed chaotic structure to generate corresponding new one-dimensional chaotic maps. The proposed new chaotic maps not only keep the advantages of simple structure and easy implementation of a traditional one-dimensional chaotic map but also expands the parameter range space of traditional one-dimensional chaotic maps. It is useful whenever chaotic digital sequences are needed. In addition, compressive sensing is used for sampling in this encryption scheme, which can reduce the storage space and transmission bandwidth. The chaotic system only needs to store matrix generation parameters, which can further reduce the bandwidth. Simulation results show that the proposed chaotic structure and chaotic maps have a good chaotic effect and high chaotic intensity, and the output sequence has strong chaos in a very large area of parameter space and can prevent phase space reconstruction. It can be applied to the image encryption scheme in this paper and has a large parameter space and



keyspace, which can prevent brute force attacks and statistical attacks.

## Data Availability

The data used to support the findings of this study are available from the first or corresponding author upon request.

## Conflicts of Interest

The authors declare there are no conflicts of interest regarding the publication of this paper.

## Acknowledgments

This research was fully supported by the National Natural Science Foundation of China (nos. 61972051 and 62032002), the Support Plan of Scientific and Technological Innovation Team in Universities of Henan Province (no. 20IRTSTHN013), the Henan Key Laboratory of Network Cryptography Technology (no. LNCT2019-A04), and the Research Foundation of Young Core Instructor in Henan Province (no. 2018GGJS058).

## References

- [1] Z. Hua and Y. Zhou, "Design of image cipher using block-based scrambling and image filtering," *Information Sciences*, vol. 396, pp. 97–113, 2017.
- [2] J.-x. Chen, Z.-l. Zhu, C. Fu, H. Yu, and L.-b. Zhang, "An efficient image encryption scheme using gray code based permutation approach," *Optics and Lasers in Engineering*, vol. 67, pp. 191–204, 2015.
- [3] D. L. Donoho, "Compressed sensing," *IEEE Transactions on Information Theory*, vol. 52, no. 4, pp. 1289–1306, 2006.
- [4] E. J. Candès, J. Romberg, and T. Tao, "Robust uncertainty principles: exact signal reconstruction from highly incomplete frequency information," *IEEE Transactions on Information Theory*, vol. 52, no. 2, pp. 489–509, 2006.
- [5] D. Wang, B. Zhang, D. Qiu, and F. Xie, "On the Super-Lorenz Chaotic model for the virtual synchronous generator," *IEEE Transactions on Circuits and Systems II: Express Briefs*, vol. 65, no. 4, pp. 511–515, 2018.
- [6] L. Zhang, X. Liao, and X. Wang, "An image encryption approach based on chaotic maps," *Chaos, Solitons & Fractals*, vol. 24, no. 3, pp. 759–765, 2005.
- [7] X. Li, C. Li, and I.-K. Lee, "Chaotic image encryption using pseudo-random masks and pixel mapping," *Signal Processing*, vol. 125, pp. 48–63, 2016.
- [8] K. W. Wong, Q. Lin, and J. Chen, "Simultaneous arithmetic coding and encryption using chaotic maps," *IEEE Transactions on Circuits and Systems II: Express Briefs*, vol. 57, no. 2, pp. 146–150, 2010.
- [9] C. Zhou, W. Hu, L. Wang, and G. Chen, "Turbo trellis-coded differential chaotic modulation," *IEEE Transactions on Circuits and Systems II: Express Briefs*, vol. 65, no. 2, pp. 191–195, 2018.
- [10] S. El Assad and M. Farajallah, "A new chaos-based image encryption system," *Signal Processing: Image Communication*, vol. 41, pp. 144–157, 2016.
- [11] G. Zhou, D. Zhang, Y. Liu, Y. Yuan, and Q. Liu, "A novel image encryption algorithm based on chaos and Line map," *Neurocomputing*, vol. 169, pp. 150–157, 2015.
- [12] K. Cho and T. Miyano, "Chaotic cryptography using augmented Lorenz equations aided by quantum key distribution," *IEEE Transactions on Circuits and Systems I: Regular Papers*, vol. 62, no. 2, pp. 478–487, 2015.
- [13] A. Akhshani, S. Behnia, A. Akhavan, H. A. Hassan, and Z. Hassan, "A novel scheme for image encryption based on 2D piecewise chaotic maps," *Optics Communications*, vol. 283, no. 17, pp. 3259–3266, 2010.
- [14] H. Peng, Y. Tian, J. Kurths, L. Li, Y. Yang, and D. Wang, "Secure and energy-efficient data transmission system based on chaotic compressive sensing in body-to-body networks," *IEEE Transactions on Biomedical Circuits and Systems*, vol. 11, no. 3, pp. 558–573, 2017.
- [15] H. Wang, D. Xiao, M. Li et al., "A visually secure image encryption scheme based on parallel compressive sensing," *Signal Processing*, vol. 155, pp. 218–232, 2017.
- [16] X. Chai, X. Zheng, Z. Gan, D. Han, and Y. Chen, "An image encryption algorithm based on chaotic system and compressive sensing," *Signal Processing*, vol. 148, pp. 124–144, 2018.
- [17] P. Chanil, A. Kwangil, J. Paeksan et al., "A novel bit-level color image encryption using improved 1D chaotic map," *Multimedia Tools and Applications*, vol. 78, no. 9, pp. 12027–12042, 2019.
- [18] R. Lan, J. He, S. Wang, Y. Liu, and X. Luo, "A parameter-selection-based chaotic system," *IEEE Transactions on Circuits and Systems II: Express Briefs*, vol. 66, no. 3, pp. 492–496, 2019.
- [19] Y. Zhou, L. Bao, and C. L. P. Chen, "Image encryption using a new parametric switching chaotic system," *Signal Processing*, vol. 93, no. 11, pp. 3039–3052, 2013.
- [20] X. Li, L. Bao, D. Zhao et al., "The analyses of an improved 2-order Chebyshev chaotic sequence," in *Proceedings of the International Conference on Computer Networks and Inventive Communication Technologies*, pp. 24–26, Harbin, China, 2011.
- [21] R. Ponuma and R. Amutha, "Compressive sensing based image compression-encryption using novel 1D-chaotic map," *Multimedia Tools and Applications*, vol. 77, no. 15, pp. 19209–19234, 2018.
- [22] E. J. Candès and T. Tao, "Near-optimal signal recovery from random projections: universal encoding strategies?" *IEEE Transactions on Information Theory*, vol. 52, no. 12, pp. 5406–5425, 2006.
- [23] K. J. Persohn and R. J. Povinelli, "Analyzing logistic map pseudorandom number generators for periodicity induced by finite precision floating-point representation finite precision floating-point representation," *Chaos, Solitons & Fractals*, vol. 45, no. 3, pp. 238–245, 2012.
- [24] H. Zhang, W. Yin, and L. Cheng, "Necessary and sufficient conditions of solution uniqueness in 1-norm minimization," *Journal of Optimization Theory and Applications*, vol. 164, no. 1, pp. 109–122, 2015.
- [25] D. L. Donoho and M. Elad, "Optimally sparse representation in general (nonorthogonal) dictionaries via  $l_1$  minimization," *Proceedings of the National Academy of Sciences*, vol. 100, no. 5, pp. 2197–2202, 2003.
- [26] M. A. Hanson, H. C. Powell, A. T. Barth et al., "Body area sensor networks: challenges and opportunities," *Computer*, vol. 42, no. 1, pp. 58–65, 2009.
- [27] J. A. Tropp, "Greed is good: algorithmic results for sparse approximation," *IEEE Transactions on Information Theory*, vol. 50, no. 10, pp. 2231–2242, 2004.

- [28] S. G. Mallat and Z. Zhifeng Zhang, "Matching pursuits with time-frequency dictionaries," *IEEE Transactions on Signal Processing*, vol. 41, no. 12, pp. 3397–3415, 1993.
- [29] J. A. Tropp and A. C. Gilbert, "Signal recovery from random measurements via orthogonal matching pursuit," *IEEE Transactions on Information Theory*, vol. 53, no. 12, pp. 4655–4666, 2007.
- [30] D. L. Donoho, Y. Tsaig, I. Drori, and J.-L. Starck, "Sparse solution of underdetermined systems of linear equations by stagewise orthogonal matching pursuit," *IEEE Transactions on Information Theory*, vol. 58, no. 2, pp. 1094–1121, 2012.
- [31] D. Needell and J. A. Tropp, "CoSaMP: iterative signal recovery from incomplete and inaccurate samples," *Applied and Computational Harmonic Analysis*, vol. 26, no. 32, pp. 301–321, 2009.

## Research Article

# Enabling Sector Scheduling for 5G-CPE Dense Networks

Jie Yang , Li Feng , Tong Jin, Hong Liang , Fangxin Xu , and Liwei Tian

Faculty of Information Technology, Macau University of Science and Technology, Taipa, Macau 999078, China

Correspondence should be addressed to Li Feng; [lfeng@must.edu.mo](mailto:lfeng@must.edu.mo)

Received 15 October 2020; Revised 23 November 2020; Accepted 8 December 2020; Published 28 December 2020

Academic Editor: Lingwei Xu

Copyright © 2020 Jie Yang et al. This is an open access article distributed under the Creative Commons Attribution License, which permits unrestricted use, distribution, and reproduction in any medium, provided the original work is properly cited.

5G customer premise equipment (5G-CPE) is an IoT gateway technology that integrates 5G and Wi-Fi and therefore can provide Wi-Fi connection for IoT devices and meanwhile benefit from the advantages of 5G. With the increasing number of IoT devices, transmission collisions and hidden/exposed terminal problems on the Wi-Fi connection side become more and more serious. Conventional mechanisms cannot solve these problems well. In this paper, we propose a Wi-Fi sector (Wi-FiS) design, which is compatible with Wi-Fi, to solve them fundamentally. Wi-FiS divides the whole coverage area of Wi-Fi into multiple sectors and utilizes beamforming technology and sector-based scheduling to improve system performance of Wi-Fi dense networks. For a single-cell network, Wi-FiS differentiates uplink and downlink operations and totally excludes collision in downlink. For a multicell network, Wi-FiS can avoid hidden and exposed terminal problems, while enabling parallel transmissions among multiple cells. We then develop a theoretical model to analyze Wi-FiS's throughput. Extensive simulations verify that our theoretical model is very accurate and Wi-FiS can improve system throughput of Wi-Fi dense networks significantly.

## 1. Introduction

In Industry 4.0, a great many Internet of Things (IoT) devices are widely deployed in multiple factories. In each factory, IoT devices work together to coordinate and monitor progress along assembly lines, under the control of an operation control center. Usually, the operation control center is located in a cloud or an edge server. To achieve real-time control, Industry 4.0 requires a high-speed and low-latency network between the operation control center and these IoT devices.

5G technology is promising to meet the network requirement of Industry 4.0, since it can provide a high speed of 10 Gbps and a low latency of 1 ms–10 ms [1–3]. To apply 5G technology to Industry 4.0, we need to establish a 5G base station which connects these IoT devices and the operation control center, and it is required that these IoT devices are 5G enabled. However, to date, deploying 5G base stations is expensive, and 5G modules, which are large in size and power-consuming, are therefore not suitable to install in resource-limited IoT devices.

To overcome the above problem, we may adopt 5G customer premise equipment (5G-CPE) solution. In this

solution, 5G-CPE, a 5G- and Wi-Fi-enabled node, is introduced to act as a relay between IoT devices and the 5G base station, as shown in Figure 1. The advantages of this solution are twofold. On the one hand, most of IoT devices support Wi-Fi due to low-cost Wi-Fi modules; however, it is generally expensive and difficult to deploy wired network infrastructure such as optical fibers to connect Wi-Fi base stations, due to constraint of factories' geographical locations. Therefore, enabling 5G-CPE to connect IoT devices via Wi-Fi is convenient, economic, and fast. On the other hand, utilizing 5G-CPE to connect the operation control center via 5G may fully take advantage of 5G's high bandwidth and low latency.

*1.1. Motivation.* In this paper, for the 5G-CPE solution, we are concerned with the 5G-CPE network, i.e., the Wi-Fi network where IoT devices communicate with the 5G-CPE. As the number of IoT devices grows, the channel congestion, transmission collision, and hidden/exposed terminal problems of 5G-CPE network will become more and more serious. Usually, there are two methods to solve these problems in large-scale Wi-Fi dense networks; however, the

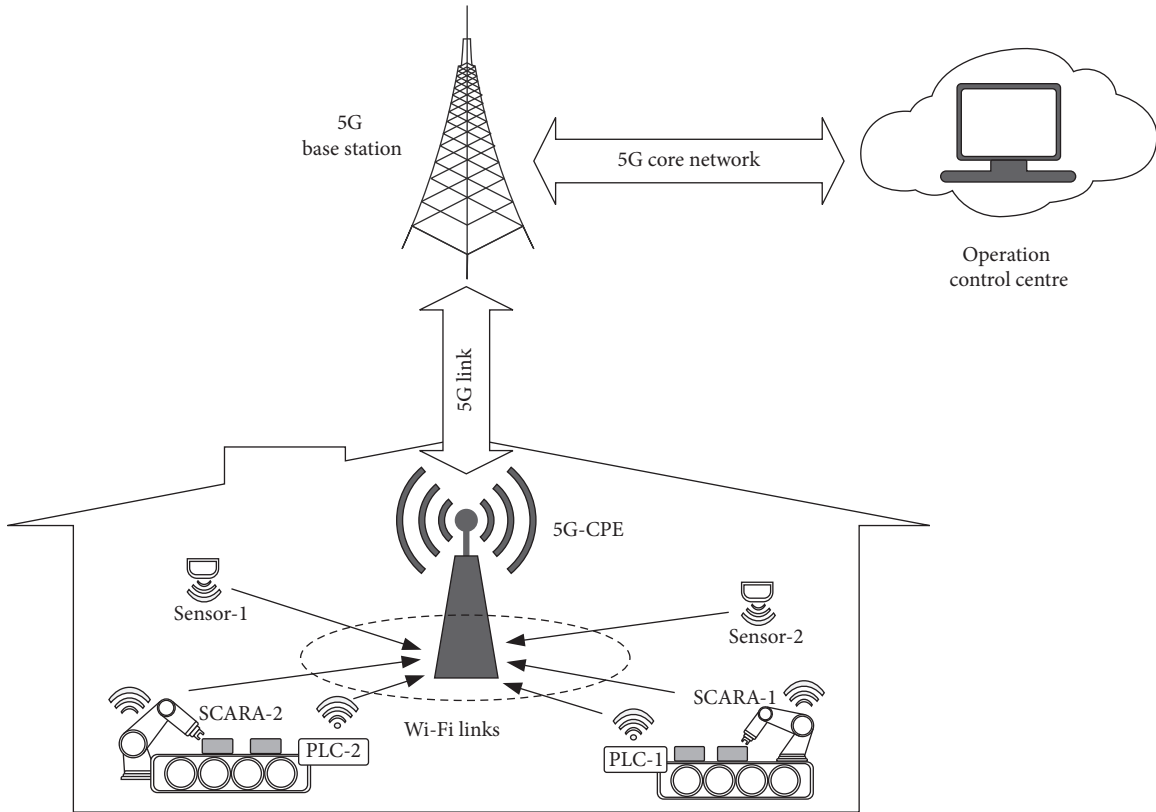


FIGURE 1: 5G-CPE for Industry 4.0.

two methods only achieve limited performance improvement and therefore do not solve these problems fundamentally [4–8].

- (i) The first one is the contention window- (CW-) based adjustment method. In Wi-Fi, each node chooses a random time between 0 and CW as a waiting time before data transmission. In this method, as the number of nodes grows, the CW size increases and therefore the average waiting time of each node will increase. A longer waiting time will help reduce the collision probability. However, a longer waiting time will lead to much time waste in channel contention.
- (ii) The second one is the request-to-send/clear-to-send (RTS/CTS) method. In this method, by sending short RTS frames to reserve channel, nodes can reduce the time waste caused by the collision of large data. However, this method introduces additional transmission times of RTS and CTS frames and a large population of nodes will still lead to serious RTS collision.

In addition, for multicell networks, existing methods cannot well solve the hidden and exposed terminal problems. For example, the RTS/CTS method solves the hidden terminal problem, but it also induces the exposed terminal problem simultaneously [6–8]. These challenges motivate this study.

*1.2. Our Contributions.* In this paper, we propose a Wi-Fi sector (for short, Wi-FiS) design, which is compatible with Wi-Fi, to solve the aforementioned challenges fundamentally. Wi-FiS borrows the hard-disk sector idea [9] to divide the whole coverage area of a 5G-CPE dense network into multiple sectors (as shown in Figure 2), each sector including a small number of nodes. Hereafter, we use the access point (AP) to represent the 5G-CPE for shortening notations. Benefitting beamforming technology and sector-based scheduling, Wi-FiS can improve the system performance of single- and multicell networks significantly. Our contributions are summarized as follows.

- (i) For a single-cell network, Wi-FiS groups contention nodes and performs sector scheduling. With Wi-FiS, the access point (AP) first silences all nodes and then activates each sector sequentially via directional beam. In this way, while keeping compatibility with Wi-Fi, Wi-FiS can reduce contention collision and improve system throughput of dense networks significantly.
- (ii) For a multicell network, Wi-FiS can avoid hidden and exposed terminal problems, while enabling parallel transmissions among multiple cells. With Wi-FiS, once detecting one ongoing transmission in one cell that might lead to a potential hidden/exposed terminal problem, the AP in another cell may

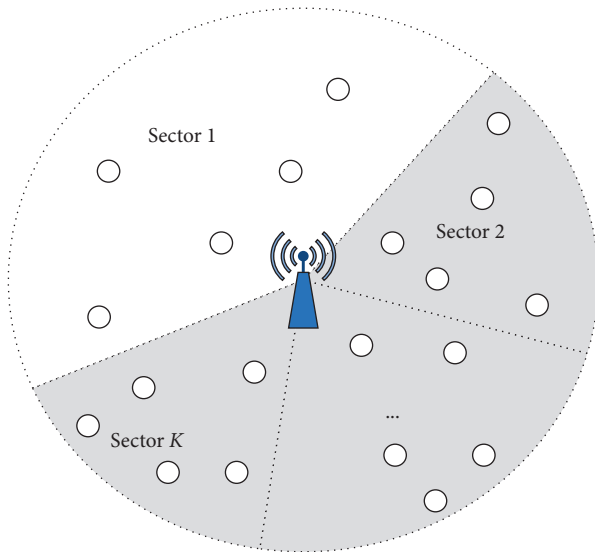


FIGURE 2: Software-defined MAC for sector scheduling.

trigger its directional transmissions without interfering with the ongoing transmission.

- (iii) We run extensive simulations to verify that our Wi-FiS design is very effective and can significantly outperform conventional methods in terms of system throughput.

The rest of the paper is organized as follows. Section 2 summarizes related works. Section 3 presents the Wi-FiS architecture. Sections 4 and 5 present Wi-FiS scheduling for single- and multicell, respectively. Section 6 analyzes Wi-FiS's throughput theoretically. Section 7 evaluates Wi-FiS's performance. Finally, Section 8 concludes this paper.

## 2. Related Works

Currently, there are mainly two types of methods that solve the collision problem of large-scale networks [4–14]: dynamic CW adjustment and RTS/CTS-based methods. These two methods and their shortcomings are briefly described below.

- (i) Dynamic CW adjustment method: this method reduces transmission collision via contention window adjustment.
  - (1) Shahin et al., Deng et al., and Ali et al. [10–12] studied the collision problem in single-cell scenario. Shahin et al. [10] used a channel observation-based mechanism to monitor the real-time collision probability of the channel and implemented dynamic adjustment of the contention window accordingly, avoiding the high delay caused by blindly multiplying the contention window. Deng et al. [11] proposed a bit-error-ratio channel adjustment algorithm to design the contention window under the dense network to obtain higher performance. Ali et al. [12] introduced a reinforcement learning

method to observe the channel state and selected the optimal contention window accordingly. However, these methods still lead to large contention overhead in dense network environments.

- (2) Sen et al. [4, 5] studied the hidden terminal problems in multicell scenario. CSMA/CN [4] solved the hidden terminal problem by detecting collision notification information. Gollakota and Katabi [5] proposed a method to decode the collision packets when a hidden terminal problem occurs. However, these methods can only solve the hidden terminal problem, but cannot combat the exposed terminal problem.
- (ii) RTS/CTS-based methods: this method reduces the collision via RTS/CTS-based channel reservation.
    - (1) Wang et al. [13, 14] proposed a RTS/CTS method to solve the collision problem in single-cell scenario, where nodes will send an RTS frame before its data transmission. This introduces additional control overhead of RTS/CTS.
    - (2) Xiong et al. [6–8] studied the hidden/exposed problems in multicell scenario. Xiong et al. [6] designed a novel S-CTS packet, which can be detected in lower SNR (signal to noise) environments, to combat the hidden terminal problem. Magistretti et al. [7] exploited cross-correlation to detect control frames (such as RTS, CTS, and ACK); this design can tolerate strong interferences in multicell environments. MACA-P [8] utilized RTS/CTS handshakes to schedule the node-pairs' transmission order, which can help avoid the hidden terminal problem and increase transmission concurrency. However, these methods cannot resolve the traditional exposed terminal problem and will lead to a new NAV type exposed terminal problem.

Different from the above two types of research studies, our design adopts beamforming and NAV mechanisms to solve the collision and hidden/exposed terminal problems in an entire network. Particularly, using virtual carrier sense, our design can only activate parts of nodes each time for contention and therefore can reduce the collision probability significantly.

## 3. Wi-FiS Architecture

In this section, we describe the architecture design of Wi-FiS.

We design Wi-FiS based on the standard Wi-Fi framework [15]. Below, we illustrate the MAC design and PHY design of Wi-FiS (as shown in Figure 3):

- (i) Wi-FiS PHY: based on standard Wi-Fi PHY layer, Wi-FiS introduces sector-beam transmission technology. Using this technology, AP can transmit and control specific physical sector areas.

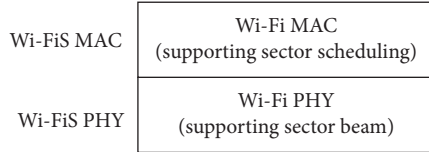


FIGURE 3: Wi-FiS architecture.

- (ii) Wi-FiS MAC: based on standard Wi-Fi MAC layer, Wi-FiS introduces the sector-scheduling technology based on sector. Using this technology, the AP can trigger each sector one by one.

**3.1. PHY Design.** Here, we present the hardware of the AP that supports multiple antennas for directional beamforming.

Based on hardware support, our design can improve the 802.11ac version or newer routing protocols, as shown in Figure 4. 802.11ac routing already supports using up to 8 antennas in a single channel to form beams, so it can provide directional beams. In our design, Wi-FiS can be installed directly on 802.11ac devices (including the 5G-CPE or 802.11ac router) without hardware modification. We assume that AP or STAs have up to 8 antennas, so that they can perform beamforming under a single channel, and these antennas are all omnidirectional antennas. In particular, these 8 antennas can provide beamforming technology in the form of digital precoding according to 802.11 protocol standard to achieve directional scanning.

In this paper, we adopt DOA-based location detection technology and RSSI power detection technology [16–18] for the physical layer, and we assume that the default transmission power of all nodes is the same and known (the power is negotiated in during the association process). DOA and RSSI functionalities can be implemented by updating the firmware of software. Therefore, in our design, AP can get the relative position (including relative angle and distance) of nodes around it via the DOA and RSSI technologies.

**3.2. MAC Design.** In this section, we present MAC design of Wi-FiS. Wi-FiS divides the whole network coverage into sectors and then activates/schedules its sectors sequentially via its PHY and MAC technologies. Below, we first present its PHY design that adopts directional beamforming to activate a specific sector, then its MAC frames that are used to set the duration field for silencing/activating nodes, and finally its MAC protocols for sector scheduling.

The basic idea of Wi-FiS is to divide sectors into time-sharing access, i.e., only allowing nodes in a sector to contend channel each time. This method restricts the number of nodes for channel access and therefore reduces collision probability. The MAC layer protocol of Wi-FiS contains 3 stages: **topology generation**, **sector generation**, and **sector scheduling**.

With the help of Figure 5, we present the above three stages.

- (i) Topology generation: in this stage, the AP will periodically perform background scans to obtain information, i.e., direction angle and basic service set identifiers (BSSIDs), about surrounding nodes so as to calculate the physical location of each node and form a physical topology. To generate the entire topology, we need to obtain basic service set identifier (BSSID) of each node and its corresponding direction of arrival (DOA) through scans.

- (1) Obtaining BSSID: in our design, the AP and nodes work in CSMA/CA and the AP acquires BSSIDs of nodes by scanning background flows in real time during the omnibeam uplink (UL) process. During the scanning, the AP will first extract BSSID field from the MAC header of a node's frame in the flows and then cache the BSSID to a database. However, a random BSSID mechanism affects obtaining a BSSID. To address the problem, we can automatically integrate a random BSSID with a real BSSID through a mechanism of matching RSSI (received signal strength indicator) and CSI (channel state information), reducing the impact of the random BSSID mechanism.
- (2) Obtaining DOA: the AP can estimate DOAs using information extracted from physical headers of frames during the scanning of background flows, since nodes adopt multi-antenna mechanism. This mechanism has been adopted by many wireless related technologies, e.g., [16–18]. When the AP receives a frame, it estimates DOA, associates DOA with BSSID extracted from the frame, and then caches them. Finally, the AP generates the physical topology according to DOA information and then divides the overall network into sectors according to the topology.
- (3) Obtaining distance : during the association phase, the AP assigns the transmit power to all nodes, so the AP knows the transmit power of each packet. After receiving a packet, the AP obtains the receive power and further estimates the distance according to the transmit and receive power and the RSSI channel attenuation model.

- (ii) Sector generation: in this stage, after obtaining the physical topology, the AP will divide the network into several sectors according to a preset restricted number of nodes (i.e.,  $n_k$ ) and the topology information. This sectorization method makes it possible for the AP to later schedule each sector via directional beamforming. Wi-FiS does not adopt equal partitioning method in hard disk. To ensure the network performance of each sector, we set the maximum number of nodes in each sector to  $n_k$ . Usually, we preset  $n_k$  based on the actual network topology, packet size, and the theoretical performance model (mentioned in Section 6). As shown in

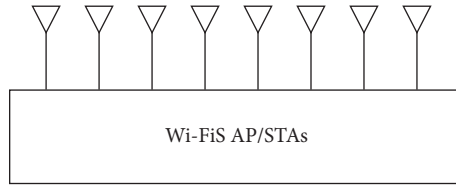


FIGURE 4: Hardware design of a AP/STA adopted in Wi-FiS.

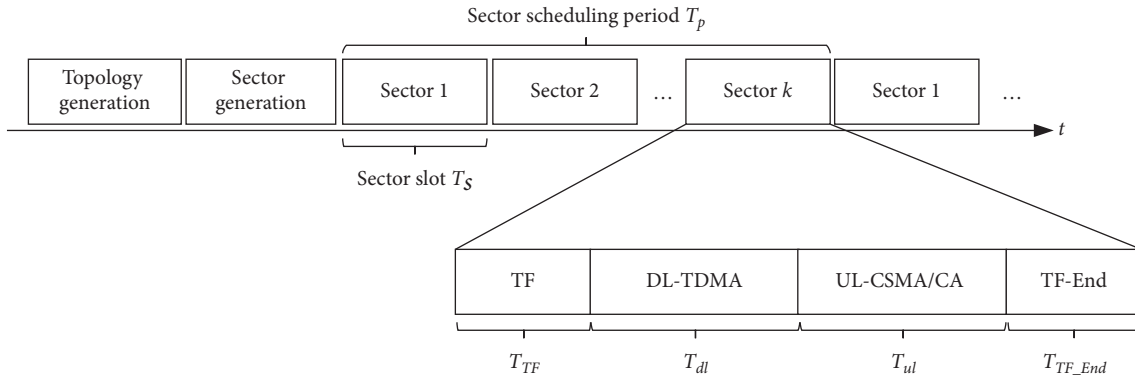


FIGURE 5: MAC protocol overview.

Figure 2, we obtain partitions via the control of arc and set the number of nodes in each sector to a fixed constant value. If the distribution of nodes in a sector is looser, the arc of the sector will be larger, and if the distribution of nodes is tighter, the arc is smaller.

Besides, our sector partition uses an incremental partition strategy, which can be divided into the following two steps.

- (1) *Step 1.* Divide the total number of nodes  $N$  by  $n_k$  and then add 1 to the integer part of the result (i.e., dealing the result through a ceiling function). The integer part of result represents a saturated number of nodes in a sector, which is equal to  $n_k$ .
- (2) *Step 2.* Let the remainder of  $N$  divided by  $n_k$  be the number of nodes for the last sector. Since the number of nodes in this sector is less than those of other sectors, the throughput of this sector will be slightly smaller. In our design, we adopt the same control mechanism for all sectors rather than introducing a specific control mechanism for this sector.

With the above strategy, the AP divides all nodes into sectors. After sectorization, they will enter the channel access stage.

- (iii) *Sector scheduling:* in this stage, after the generation of sectors, the AP will schedule each sector. The AP determines whether there is an overlap between APs by listening to the TF frames of other APs. If yes, there will be no hidden/exposed terminals; otherwise, there possibly exists hidden/exposed terminals. Let  $T_p$  be the scheduling time of all the sectors.

$T_p$  is a total time of  $k$  sectors' operation time, where time for each sector (i.e., sector slot in Figure 5) is  $T_s$ . To schedule one sector, we make use of two control frames, i.e., trigger frame (TF) and TF-End frame. Note that we adopt omnibeam or sector beam for different frame types in this design to achieve scheduling for a specific area. Each sector slot process includes four processes, i.e., TF frame, downlink TDMA access (DL-TDMA), uplink CSMA/CA access (UL-CSMA/CA), and TF-End frame.

For a single-cell network, we may adopt omnibeam to transmit data during the DL-TDMA and UL-CSMA/CA processes. In contrast, for a multicell network, we may adopt sector beam to transmit data during DL-TDMA and UL-CSMA/CA processes to avoid hidden and exposed terminal problems.

**3.3. MAC Frame Settings.** Conventional Wi-Fi has three types of Wi-Fi frames: management, control, and data frames. Here, we present their settings for silencing/activating nodes in Wi-FiS.

In the design of Wi-FiS, NAV parameters are set based on the duration/AID field. In order to implement the sector-based time-sharing contention strategy, we need to control the duration/AID field of the frame sent by AP/STA. In 802.11 standard, the duration/AID field has two different functions. As shown in Figure 6, if the highest bit is set to 0, it is used as the duration filed, and the node will receive a frame including this field and update it to the node's own NAV timer; oppositely, if the highest bit is set to 1, then this field is used as an AID, and the node will not update this field to its NAV timer.

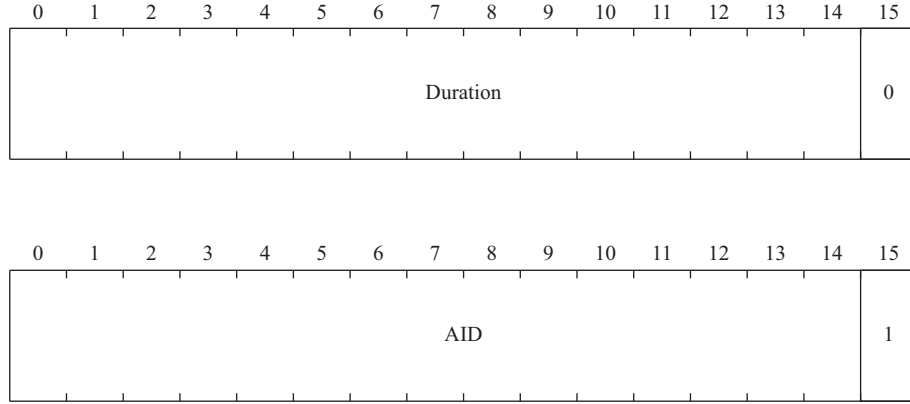


FIGURE 6: Duration/AID field in a 802.11 frame.

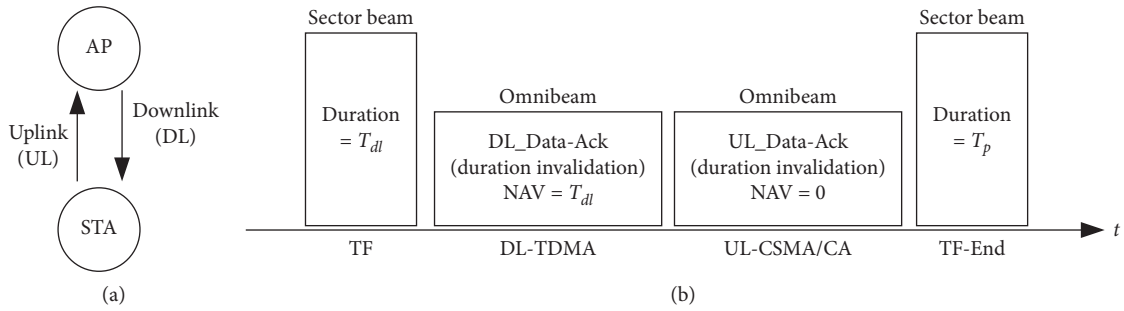


FIGURE 7: An overview of sector scheduling overview.

Therefore, in this design, due to the reason that we need to use APs for global scheduling, we use different types of duration/AID field to set mechanisms for frames of different objects.

(i) Frames sent by AP.

- (1) TF and TF-End frames: the duration/AID field is set as the duration parameter for purpose of implementing partition scheduling.
- (2) Data and control (ACK) frame: control frames include ACK and other different frames, and the data frames can be downlink data. Here, the AP sets the duration/AID field in these frames as the AID parameter. For example, the duration/AID field in both the ACK and downlink data frames can be set to the target AID. In the 802.11 protocol, if the duration/AID field is set to AID, then no AID analysis is performed.

(ii) Frames sent by STA: since nodes are scheduled objects, the duration/AID fields of the management frames (such as probes, association requests, and so on) sent by the node should be set to AID. A node may not have the corresponding AID value when it is not associated with an AP, and thus this value can be filled with 0. The control frame and data frame sent by the node are the same as the control frame and data frame sent by the AP and should be set to the target AID.

#### 4. Wi-FiS Scheduling for Single Cell

Here, we present the Wi-FiS scheduling method in a single cell.

**4.1. Overview.** In the 802.11 protocol, the AP may prohibit nodes from contending for the channel by setting nodes to the NAV state and then manipulate the entire transmission process. In the initial state, the NAV timer of all nodes is set to the maximum value. As mentioned in Section 3.2, the entire scheduling process of each sector includes four processes (as shown in Figure 7), trigger frame (TF) process, downlink TDMA (DL-TDMA) process, uplink CSMA/CA (UL-CSMA/CA) access, and TF-End process. The TF and TF-End processes are used to control NAV settings, while the DL-TDMA and UL-CSMA/CA data transmissions do not affect NAV. Below, we detail each process.

- (i) TF process: at the beginning of each sector switching process, using a TF frame, the AP will schedule a sector  $k$  to operate and set the corresponding competition and transmission parameters for nodes in this sector, where the transmission time of the TF frame is  $T_f$ . After receiving the TF frame, the nodes in the sector  $k$  area will set their NAV to  $T_{dl}$ , which means that the AP will take the next  $T_{dl}$  time for DL-TDMA data transmission.
- (ii) DL-TDMA process: after the TF process, the AP will first perform the downlink data transmission. The



downlink data are transmitted back-to-back in the order of TDMA and the nodes' AIDs, where the time of DL-TDMA is  $T_{dl}$ . The NAV timer of the node in sector  $k$  decreases with time, and when the DL-TDMA transmission process ends, this NAV timer is decreased to zero and therefore the nodes in sector  $k$  can contend for the channel freely.

- (iii) UL-CSMA/CA process: after the DL-TDMA process, nodes in the sector can perform uplink competition, which is based on the CSMA/CA protocol. After a node wins the competition, it can transmit uplink data to the AP, where the time of UL-CSMA/CA is  $T_{ul}$ .
- (iv) TF-End process: after the UL-CSMA/CA process, the AP will deactivate the sector. It will send a TF-End frame to set all nodes in the sector to NAV state, and the sector cannot be activated again until the next sector scheduling period.

In our design, TF and TF-End frames are transmitted in the form of sector beam, which is used to schedule a specific sector. The data transmissions, that is, DL-TDMA and UL-CSMA/CA processes, do not have the scheduling function. Therefore, omnibeam transmission can be performed. As described in Section 3.3, only the duration/AID fields for TF and TF-End frames are set to duration, while the data and ack packets in DL-TDMA and UL-CSMA/CA are set to AID. Therefore, only TF and TF-End affect the NAV settings, while data and ACKs do not.

In these two processes, the duration/AID fields of data and ACK frames are set for AID function, and hence NAV will not be affected. However, to avoid hidden/exposed terminal problems for multicell scenarios, we will change to sector-beam transmission for the data transmission process when these problems happen.

**4.2. TF.** At the beginning of each sector switching process, the AP will send TF frames via sector beam. Here, a TF frame contains the following two fields (as shown in Figure 8):

- (i) Duration/AID field: it silences all nodes by setting them to NAV state.
- (ii) Wi-FiS parameter element field: this field is used to notify and configure the transmission parameters of nodes in one sector, i.e., CW, sector ID,  $T_s$ , and  $T_{dl}$ .
- (iii) CW: this field configures the contention parameter used by the node (similar to EDCA Parameter [19] of 802.11e). In our design, the AP can set the value of CW in the Wi-FiS parameter element field.
- (iv) Sector ID: this field identifies the ID of the current scheduled sector by a TF frame and is used to let other APs know which sector is currently scheduled. Further, it determines whether there are hidden/exposed terminal problems.
- (v)  $T_s$  (sector slot) and  $T_{dl}$  (DL-TDMA): these two fields identify the time of the entire sector scheduling time and the corresponding downlink TDMA scheduling time. They are used to allow other APs to

determine whether there are hidden terminals or exposed terminal problems and the time when the problems occur, since  $T_{ul}$  can be obtained through  $T_s - T_{dl} - T_{TF} - T_{TF\_End}$ , where  $T_{TF}$  and  $T_{TF\_End}$  are constant values.

Remark: usually CW is used in single-cell sector scheduling scenario, while sector ID,  $T_s$ , and  $T_{dl}$  are used in multicell sector scheduling scenario.

**4.3. DL-TDMA.** As soon as TF frame transmission ends, the downlink TDMA transmission starts and will last for  $T_{dl}$  time. In our design, the downlink process adopts TDMA. The reasons are as follows. In downlink, the AP can allocate the access time slice of TDMA to nodes, and therefore there is no need for contention. Further, the AP can optimize the time slice allocation of TDMA according to the local cache information, and therefore TDMA is more efficient.

During this time period, the AP will sequentially send DL-DATA 1 to node 1 (i.e., AID = 1), DL-DATA 2 to node 2, and so on in the order of TDMA. The time interval between DL-DATA is equal to SIFS. The AP will transmit the downlink data of all nodes at one time, and during this process, the nodes will not actively feed back ACK. When the AP sends downlink data, it will record the sending sequence on the local bitmap.

After the downlink data transmission, the AP will broadcast an ACK request (ACK Req.) to request ACK feedback from all nodes. After the nodes receive the ACK Req., each of them will sequentially feed back an ACK to the AP according to corresponding AID sequence of the bitmap in the ACK Req. If the node successfully receives the downlink data, then it will feed back an ACK. If the node fails to receive the data, it needs to feed back a NACK (that is, the ACK indicates that the reception failed). When all nodes finish feeding back ACKs, the DL-TDMA process ends.

In our design,  $T_{dl}$  is set based on the current downlink traffic. In the DL-TDMA process, AP will first determine whether there is a downlink packet toward a node based on its local cache. If yes, the AP sends the packet to the node; otherwise, it checks if there is a downlink packet toward the next node. In this paper, we assume the downlink is saturated. So, the transfer time is equal to  $n_k$  times the round-time of a data-ack transmission. Therefore, it can set the time duration of this transmission,  $T_{dl}$ .

**4.4. UL-CSMA/CA.** After the downlink transmission, the nodes in the current sector can perform uplink contention (i.e., UL-CSMA/CA process), and the time for UL-CSMA/CA is  $T_{ul}$ . In our design, the uplink process adopts CSMA/CA. The reasons are as follows. The uplink transmission should be based on contention, adapting to the change of traffic load, while CSMA/CA is a very successful contention protocol that is widely adopted in conventional 802.11 networks. Further, for uplink, CSMA/CA is more efficient than TDMA, since the AP does not know about the node's uplink traffic information and therefore cannot allocate

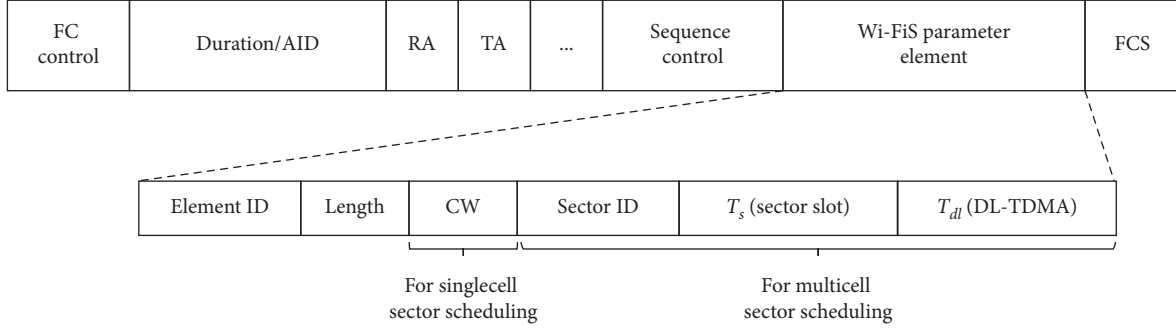


FIGURE 8: Structure of a trigger frame (TF).

access time to each node. As a result, it is better to let nodes contend for data transmission if they have packets. In this process, the  $NAV = 0$  of a node in the sector indicates that the node is activated and can compete for channel freely.  $NAV = T_p$  of the node in other sectors indicates that the node is in the silence state.

The nodes in the sector compete for channel according to the standard backoff process. Each node will first select a random value range from  $[0, CW]$  for its Backoff cOunter (BO). The selected value is stored in the BO. Every time there is an idle slot passing, BO will count down one once. When a node's BO counts down to 0, it means the node wins the channel contention. Hence, the node can send its uplink data to the AP. When the AP receives the data and verifies that it is correct, it will feed back an ACK to the node; otherwise, if the node fails to receive the data, it needs to feed back a NACK [20].

In the UL-CSMA/CA process, the random access-based CSMA/CA mechanism makes it unable to determine the end of this process. However, to set fixed time duration of the UL-CSMA/CA process,  $T_{ul}$ , in our design, we will keep a holding time duration,  $T_h$ , for each end of a UL-CSMA/CA process. Within this time ( $T_h$ ) range, all nodes will be set to the silence state, and they will not perform backoff and data transmission. The setting of  $T_h$  refers to the necessary time required for one minimum complete transmission (including the average backoff time and the time of data transmission and ACK). In order to realize the protection mechanism of the holding time, we need the following settings based on the ACK mechanism.

- (i) If  $T_r \geq T_h$ , the AP can only feed back ACK, which means that the remaining time of the UL-CSMA/CA process is enough for one complete transmission.
- (ii) If  $T_r < T_h$ , after the AP feeds back the ACK, it will send padding frames to occupy the channel, so that the next round of transmission cannot start for the remaining time (because the remaining time is not enough to guarantee one complete transmission). The duration of the padding frame transmission is  $T_r$ . Since the channel is always occupied by the AP, all nodes in the sector will not be able to perform backoff until the next UL-CSMA/CA process of this sector.

Unlike downlink transmission, the AP cannot accurately get the real-time buffering situation of all nodes in uplink access. Therefore, the AP sets uplink UL-CSMA/CA time duration  $T_{ul}$  to a fixed value regardless of nodes' buffering situation.

**4.5. TF-End.** At the end of each sector switching process, the AP will use sector beam to send TF-End frames. In the TF-End frame, the AP will set the duration to  $T_p$  (as shown in Figure 9).

## 5. Wi-FiS Scheduling for Multicell

In the multicell scenario of the wireless network, there are two basic problems: (1) hidden terminal problem and (2) exposed terminal problem. In this section, we take a two-cell topology as an example for discussion, and each cell contains 1 AP and 1 node (namely,  $AP_1$  and  $N_1$  and  $AP_2$  and  $N_2$ , respectively).

**5.1. Overview.** Here, we outline Wi-FiS scheduling method in multicell. In the multicell scenario, the AP of the cell (such as  $AP_1$ ) will actively receive TF frames from APs of other cells (such as  $AP_2$ ). The AP determines if there is an overlap between the two cells by receiving the TF frames of other APs. If yes, there might exist hidden/exposed terminal problems; otherwise, there are no such problems. In order to solve the problem of hidden/exposed terminals on  $AP_x$ , we need to dynamically adjust the  $AP_x$  to perform sector-beam transmission rather than omnidirectional transmission in a single cell (as shown in Figure 10). To achieve this, we need to determine whether the hidden/exposed terminal will happen and how long it will last for. Therefore, we need to know the relative position of the APs in other cells and how long their relative scheduling time is.

- (i) Obtaining relative position of APs in other cells: we can get relative position of APs through DOA and distance measurement-related technologies [16–18]. Further, based on this position information, we can determine whether there will be hidden/exposed terminal problems between  $AP_1$  and  $AP_2$ .

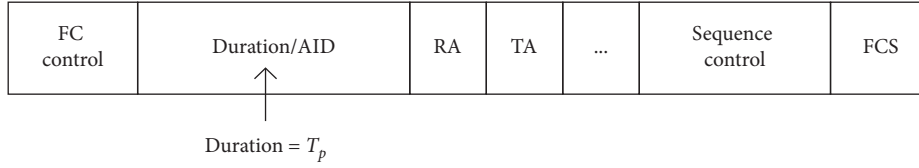


FIGURE 9: The structure of a TF-End frame.

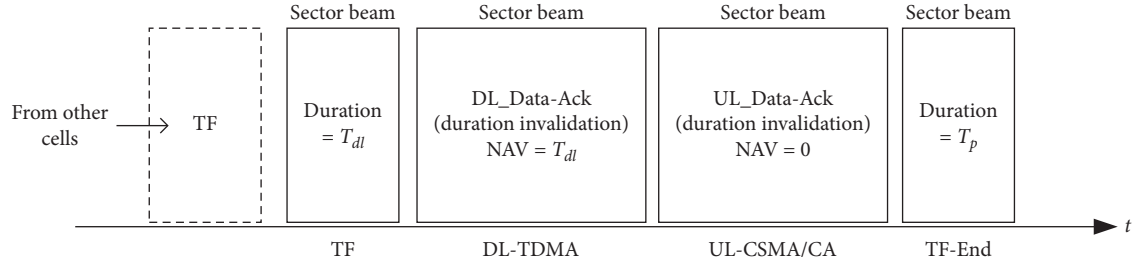


FIGURE 10: Wi-FiS scheduling for multicell scenario.

- (ii) Obtaining sector scheduling time of other cells: since we include the sector ID, the total transmission time  $T_s$  of the sector, and the DL-TDMA time  $T_{dl}$  in the TF frame, we can further deduce the time duration of hidden/exposed terminals.

Based on the above information, in the sector scheduling stage, in addition to the time scheduling relative to single cell (such as  $T_{dl}$  and  $T_{ul}$  time), to avoid hidden terminal and exposed terminal problems, we can use sector beam for data transmission. However, it should be noted that the sector-beam method requires extra overhead for a certain measurement (such as CSI measuring) to operate precoding. Therefore, in a single-cell scenario, or in a scenario where there is no hidden/exposed terminal, we can directly adopt omnibeam transmission. Below, we, respectively, describe the problem of hidden/exposed terminal and its solution.

## 5.2. Hidden Terminal Problem and Solution

**5.2.1. Hidden Terminal Problem.** Taking Figure 11 as an example, since  $AP_1$  is in the coverage of both  $N_1$  and  $AP_2$ , when  $N_1$  uses an omnidirectional antenna to transmit uplink data to  $AP_1$  and  $AP_2$  uses an omnidirectional antenna to transmit downlink data to  $N_2$ ,  $AP_1$  will receive the superimposed signals of  $N_1$  and  $AP_2$  at the same time. Therefore, the signal cannot be demodulated, which causes a collision. Such collision problem is called as hidden terminal problem.

**Solution.**  $\sqrt{(1(1))^{?1}}$ : at the beginning of the network operation,  $AP_1$  will first broadcast a TF (denoted by  $\sqrt{(1(1))^{?1}}$  in the figure), which announces that the network covered by  $AP_1$  will perform uplink transmission.

$\sqrt{(2a(2a))^{?2a}}$ : after  $AP_2$  receives the TF, it will use directional beam transmission when performing

downlink transmission, that is, beam-downlink (denoted by  $\sqrt{(2a(2a))^{?2a}}$  in the figure above).  $\sqrt{(2b(2b))^{?2b}}$ :  $AP_1$  will also allow the local node to perform uplink transmission after transmitting the TF. As shown in the figure,  $N_1$  uses broadcast to perform uplink transmission (denoted by  $\sqrt{(2b(2b))^{?2b}}$  in the figure).

## 5.3. Exposed Terminal Problem and Solution

**5.3.1. Exposed Terminal Problem.** Taking Figure 12 as an example, the network covered by  $AP_2$  includes both  $AP_1$  and  $N_2$ . When  $AP_1$  uses an omnidirectional antenna for downlink transmission,  $AP_2$  will actively receive the transmitted signal by  $AP_1$ . The signal can be either one of the following two frames: (1) a trigger frame (TF) that  $AP_2$  needs to receive; (2) a data frame that  $AP_2$  does not need to receive. Then, if the signal is a data frame from  $AP_1$ , the receiving of the signal causes a waste of channel utilization for  $AP_2$  because the channel used for receiving these data can be used for  $N_2$ 's downlink transmission instead. Such a waste problem is called an exposed terminal problem.

**Solution.**  $\sqrt{(1(1))^{?1}}$ : at the beginning of the network operation,  $AP_1$  will first broadcast a TF (denoted by  $\sqrt{(1(1))^{?1}}$  in the figure), which announces that the network covered by  $AP_1$  will perform directional downlink transmission.

$\sqrt{(2a(2a))^{?2a}}$ : after  $AP_2$  receives the TF, it learns that the  $AP_1$  will perform directional downlink transmission, and the node that is transmitting data is not within the coverage of  $AP_2$ . At this point,  $AP_2$  can perform downlink transmission in form of broadcasting (denoted by  $\sqrt{(2a(2a))^{?2a}}$  in the figure above).

\(\uparrow\)^{2b}\): after AP<sub>1</sub> finishes transmitting the TF frame, it will directly use a directional beam to perform downlink transmission (denoted by \(\uparrow\)^{2b} in the figure) and transmit data to node N<sub>1</sub> directionally.

## 6. Theoretical Analysis

### 6.1. Th(K): Total Throughput

*Assumption 1.* We assume that an AP passively collects topology information, so the topology generation process does not need to spend additional channel time. And because the sector generation process is done locally, it does not need to occupy the channel resource.

*Assumption 2.* Both the uplink and downlink transmissions of the system are saturated.

In this section, we analyze the performance of the proposed Wi-FiS protocol. Under Assumptions 1 and 2, we define the system throughput as follows:

$$Th(K) = \frac{\sum_{k=1}^K (Th_k(n_k) \cdot T_s)}{T_p}, \quad (1)$$

where  $k$  represents the  $k$ -th sector  $k = 1, 2, 3, \dots, K$ ,  $T_p$  is the time of a sector scheduling period,  $T_s$  is the scheduling time of a sector, and  $Th_k(n_k)$  represents the relative throughput of the  $k$ -th sector.

**6.2. Th<sub>k</sub>(n<sub>k</sub>): Throughput of Sector k.** Since our design includes downlink transmission (i.e., DL-TDMA) and uplink contention transmission (i.e., UL-CSMA/CA), we need to calculate the throughput of these two parts separately.

*Assumption 3.* The fixed length of the data frame is  $L_{MPDU}$ .

Let  $Th_{DL_k}(n_k)$  denote the downlink throughput of DL-TDMA and let  $Th_{UL_k}(n_k)$  denote the uplink throughput of UL-CSMA/CA. Therefore, under Assumption 3, the relative throughput of sector  $k$  can be calculated as

$$Th_k(n_k) = \frac{Th_{DL_k}(n_k) \cdot T_{dl} + Th_{UL_k}(n_k) \cdot T_{ul}}{T_s}. \quad (2)$$

**6.3. Th<sub>DL\_k</sub>(n<sub>k</sub>): Downlink (DL-TDMA) Throughput of Sector k.** In this section, we describe the downlink (i.e., DL-TDMA) throughput calculation of sector  $k$ . Referring to Figure 13, the entire downlink transmission time  $T_{dl}$  depends on the maximum number of transmissions  $M$  in this period.

Let  $M$  denote the total number of downlink transmissions in this sector, and the value of  $M$  can be calculated as follows:

$$M = \frac{T_{dl} - (L_{ACK-Req}/R + tT_{SIFS})}{2 * T_{PHY\_Header} + (L_{MPDU} + L_{Ack})/R + T_{SIFS}}, \quad (3)$$

where  $T_{dl}$  is the total time of downlink transmission,  $R$  is the data transmission rate,  $T_{PHY\_Header}$  is the transmission time of the physical layer header,  $L_{MPDU}$  is the size of the entire payload,  $L_{ACK-Req}$  is the size of the ACK request frame,  $L_{Ack}$  is the size of the ACK frame, and  $T_{SIFS}$  is the size of the SIFS time interval.

*Assumption 4.* The total downlink transmission time  $T_{dl}$  is set depending on the number of transmissions  $M$ .

In our design, the total number of downlink transmissions  $M$  is set to the number of nodes in a sector,  $n_k$ , that is,  $M = n_k$ . So, under Assumption 4, the throughput of downlink transmission is as follows:

$$Th_{DL_k}(n_k) = \frac{L_{MPDU} * n_k}{T_{dl}}. \quad (4)$$

**6.4. Th<sub>UL\_k</sub>(n<sub>k</sub>): Uplink (UL-CSMA/CA) Throughput of Sector k.** In this section, we describe the uplink (UL-CSMA/CA) throughput calculation of sector  $k$ . Referring to Figure 14, the CSMA/CA contention mode is adopted in the uplink process. We first calculate the total number of successful uplink transmissions  $M$  with the following formula:

$$M = E_{M_{tr|N}}(n_k) \cdot P_{SUC|N}(1|n_k), \quad \text{when } (n_k \geq 2), \quad (5)$$

where  $E_{M_{tr|N}}(n_k)$  represents the average number of attempts to transmit data packets in sector  $k$  (under the condition of  $N = n_k$ ) and  $P_{SUC|N}(1|n_k)$  represents successful transmission in sector  $k$  (under the condition of  $N = n_k$ ). Thus, we have:

$$\begin{aligned} Th_{UL_k}(n_k) &= \frac{L_{MPDU} * M}{T_{ul}} \\ &= \frac{L_{MPDU} * E_{M_{tr|N}}(n_k) \cdot P_{SUC|N}(1|n_k)}{T_{ul}}. \end{aligned} \quad (6)$$

Below we need to calculate  $E_{M_{tr|N}}(n_k)$  and  $P_{SUC|N}(1|n_k)$ .

$$P_{SUC|N}(1|n_k). \quad (7)$$

Based on the standard Bianchi model, we can calculate the collision probability  $p$  and the transmission probability  $\tau$ :

$$\begin{aligned} p &= 1 - (1 - \tau)^{n_k - 1}, \\ \tau &= \frac{E[R]}{E[B] + E[R]}, \end{aligned} \quad (8)$$

where  $E[R]$  and  $E[B]$  can be calculated as follows:

$$\begin{aligned}
E[R] &= \sum_{r=1}^{R_{\max}-1} r(1-p)p^{r-1} + R_{\max}p^{R_{\max}-1} = \sum_{r=1}^{R_{\max}} p^{r-1}, \\
E[B] &= \frac{1}{2} \sum_{r=1}^{R_{\max}-1} \min\{2^{r-1}CW_{\min}, CW_{\max}\} (1-p)p^{r-1} \\
&\quad + \frac{1}{2} \min\{2^{R_{\max}-1}CW_{\min}, CW_{\max}\} p^{R_{\max}-1} \\
&= \frac{1}{2} \sum_{r=1}^{R_{\max}} \min\{2^{r-1}CW_{\min}, CW_{\max}\} p^{r-1}.
\end{aligned} \tag{9}$$

In the above formulas,  $R_{\max}$  is the maximum number of transmission attempts. Under normal circumstances, we can set it to 5, which means that after the seventh transmission failure of a node, the packet loss will occur directly.

By solving  $p$  and  $\tau$  simultaneously using the above equations, we can calculate the probability of successful transmission  $P_{\text{SUC}|N}(1|n_k)$ , namely,

$$P_{\text{SUC}|N}(1|n_k) = \frac{n_k \tau (1 - \tau)^{n_k - 1}}{1 - (1 - \tau)^{n_k}}, \tag{10}$$

$$\mathbf{E}_{M_{\text{tr}}|N}(\mathbf{n}_k),$$

where  $\mathbf{E}_{M_{\text{tr}}|N}(\mathbf{n}_k)$  can be calculated as follows:

$$E_{M_{\text{tr}}|N}(n_k) = \sum_{m_{\text{tr}}=1}^{M_{\text{tr}}\text{-upper}(T_{\text{ul}}-T_h)} m_{\text{tr}} P_{M_{\text{tr}}|N}(m_{\text{tr}}|n_k), \tag{11}$$

where  $M_{\text{tr}}\text{-upper}$  is the upper bound of the number of transmissions in UL-CSMA/CA process,  $T_{\text{ul}}$  is the total uplink access transmission time, and  $T_h$  is a fixed guard time overhead (as shown in Figure 14).

Then, we calculate  $P_{M_{\text{tr}}|N}(m_{\text{tr}}|n_k)$ :

(i) When  $1 \leq m_{\text{tr}} \leq M_{\text{tr}}\text{-upper}(T_{\text{ul}} - T_h)$ ,

$$\begin{aligned}
P_{M_{\text{tr}}|N}(m_{\text{tr}}|n_k) &= \text{Prob}(M_{\text{tr}} \geq m_{\text{tr}}) \\
&\quad - \text{Prob}(M_{\text{tr}} \geq m_{\text{tr}} + 1).
\end{aligned} \tag{12}$$

(ii) When  $M_{\text{tr}} = M_{\text{tr}}\text{-upper}(T_{\text{ul}} - T_h)$ ,

$$P_{M_{\text{tr}}|N}(m_{\text{tr}}|n_k) = \text{Prob}[M_{\text{tr}} \geq M_{\text{tr}}\text{-upper}(T_{\text{ul}} - T_h)], \tag{13}$$

where

$$M_{\text{tr}}\text{-upper}(T_{\text{ul}} - T_h) = \frac{T_{\text{ul}} - T_h}{2 * T_{\text{PHY\_Header}} + (L_{\text{MPDU}} + L_{\text{Ack}})/R + T_{\text{SIFS}}}, \tag{14}$$

where  $R$  is the data transmission rate,  $T_{\text{PHY\_Header}}$  is the transmission time of the physical layer header,  $L_{\text{MPDU}}$  is the size of the entire payload,  $L_{\text{ACK-Req}}$  is the size of the ACK request frame,  $L_{\text{Ack}}$  is the size of the ACK frame, and  $T_{\text{SIFS}}$  is the SIFS time interval.

*Assumption 5.* The smallest unit on the entire timeline is the Wi-FiS slot.

To calculate  $\text{Prob}(M_{\text{tr}} \geq m_{\text{tr}})$ , under Assumption 5, we have

$$\text{Prob}(M_{\text{tr}} \geq m_{\text{tr}}) = \text{Prob}\{T_{b,m_{\text{tr}}} + T_{t,m_{\text{tr}}} \leq T_{\text{ul}} - T_h\}. \tag{15}$$

According to [21], we stipulate that  $T_{b,m_{\text{tr}}}$  is the total backoff time during  $m_{\text{tr}}$  transmission (based on Assumption 4, which is the total number of slots),  $T_{t,m_{\text{tr}}}$  is the total transmission time in the  $m_{\text{tr}}$  transmission process (including the total time of DIFS  $d$ , data packet, SIFS, ACK), and  $\varphi$  is the time of one packet transmission process. Hence, we have the following.

$\text{Prob}(M_{\text{tr}} \geq m_{\text{tr}}) = \sum_{z=m_{\text{tr}}}^{T_{\text{ul}}-T_h} \text{Prob}\{\sum_{j=1}^{m_{\text{tr}}} T_{b,j} = z|n_k\}$ . Let  $q' = 1 - (1 - \tau)^g$ , so this formula can be further simplified as

$$\begin{aligned}
\text{Prob}(M_{\text{tr}} \geq m_{\text{tr}}) &= \text{Prob}(T_{t,m-1} + d + T_{b,m} + 1 \leq T_{\text{ul}} - T_h) \\
&= \sum_{z=m_{\text{tr}}}^{T_{\text{ul}}-T_h-(m-1)(\varphi+d)-d+1} \text{Prob}\left\{\sum_{j=1}^{m_{\text{tr}}} T_{b,j} = z|n_k\right\} \\
&= \sum_{k=0}^{T_{\text{ul}}-T_h-(m-1)\varphi-d-1-m} \binom{k+m-1}{m-1} q'^m (1-q')^k.
\end{aligned} \tag{16}$$

## 7. Performance Evaluation

In this section, we evaluate the performance of Wi-FiS.

*7.1. Simulation Setting.* We write C++ codes to simulate the Wi-FiS protocol, and each simulation lasts for 100 s. We assume that there are at most 100 nodes in the network covered by an AP. All nodes are partitioned according to a fixed number of nodes (i.e.,  $n_k$ ). As the number of nodes continues to increase, the number of partitions should increase accordingly. Since we are mainly concerned with the uplink traffic of the node, we assume the AP has no downlink traffic in Figures 15–20. The simulation parameters are shown in Table 1.

*7.2. Single-Cell Network.* Figure 20 plots the system throughput via the total number of nodes. Its  $x$ -axis denotes the total number of nodes, ranging from 1 to 100, and its  $y$ -axis denotes the throughput in Mbps. In the figure, the blue line is the throughput in CSMA/CA, the red dotted line is the throughput in RTS/CTS, and the purple and yellow lines denote the throughput corresponding to the proposed Wi-FiS in this article.

From a holistic perspective, we can see that the throughput of Wi-FiS is significantly better than that of CSMA/CA and RTS/CTS. From this figure, we have the following observations.

- (i) As the number of nodes increases (within 5 nodes), the throughput of these four methods increases as the number of nodes increases. This is because the increase in the number of nodes will lead to the increase in the transmission probability of the node, and in the meantime, the collision probability still maintains a small value. So, it will not have a major impact on the throughput.
- (ii) When the number of nodes is between 5 and 100, the throughput exhibits different trends for different schemes.
  - (1) The throughput of CSMA/CA drops sharply as the number of nodes increases. This is because the collision probability increases with the number of nodes. In the meantime, since collision overhead is the transmission time of the entire data frame, high overall collision overhead leads to throughput degradation. As the number of nodes increases, the throughput will continue to decline.
  - (2) The throughput of RTS/CTS decreases slowly as the number of nodes increases. Compared with the CSMA/CA mode, although the collision probability is also increased, the collision overhead in the RTS/CTS is less than the transmission time of the data frame. Therefore, RTS/CTS slows down the throughput degradation. We can see that the throughput of RTS/CTS is better than that of CSMA/CA for about 35 nodes.

- (3) The throughput of Wi-FiS (downlink enabled) increases as the number of nodes increases. The reason is that the throughput of Wi-FiS (downlink enabled) is the weighted sum of uplink throughput and downlink throughput. Since there are no collisions in the downlink transmission, the throughput of it increases with the number of nodes, which in turn leads to an upward trend in the overall throughput of Wi-FiS.
- (4) The throughput of Wi-FiS (downlink disabled) stays almost unchanged as the number of nodes increases (in fact, it decreases slowly). This is because we control the network through sector partition scheduling so that collisions among large-scale nodes contentions caused by simultaneous contention can be avoided. We set up to 5 nodes for each sector. Compared with the CSMA/CA, since we have reduced the number of nodes which perform contention for each unit of sector time (i.e.,  $T_s$ ), the collision probability is controlled within a limited range to ensure high throughput. Compared with the RTS/CTS mode, our transmission management overhead is for each unit of sector time (i.e.,  $T_s$ ), which requires 2 management frames (i.e., TF and action frames) and 2 SIFS, which is relatively smaller than RTS/CTS (each transmission requires a handshake). Therefore, the throughput will be higher than that in the RTS/CTS mode.

In the figure, we can also see that with about 5 nodes (namely,  $n_k$ ), the Wi-FiS throughput will suddenly drop once and then gradually rise again. This is because we adopt an incremental partitioning strategy. For example, when there are 11 nodes, we will divide all nodes into 3 sectors, which are 2 sectors with 5 fixed nodes and a sector with 1 node. In the channel access process, time-sharing access is performed in accordance with 3 sectors, which will result in a decrease in the throughput of the sector with only one node, and finally weighted to a decrease in the overall throughput. However, as the number of nodes in this area increases, its throughput gradually rises. When the number of nodes continues to increase, the throughput will periodically drop due to the newly added sectors.

Figure 15 plots the theoretical and simulation throughput of the UL-CSMA/CA process as the number of total nodes varies from 1 to 100, where the number of nodes in each sector,  $n_k$ , is 5 and 20, respectively. The red solid line represents the theoretical throughput while the black dashed line is for the simulation throughput. From this figure, we have the following observations.

- (1) The overall throughput when  $n_k = 5$  is higher than the overall throughput when  $n_k = 20$ . The reason is that when the number of nodes in each

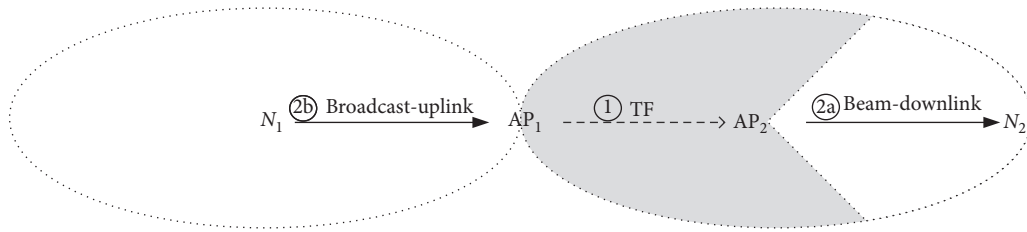


FIGURE 11: An example of hidden terminal problem and solution.

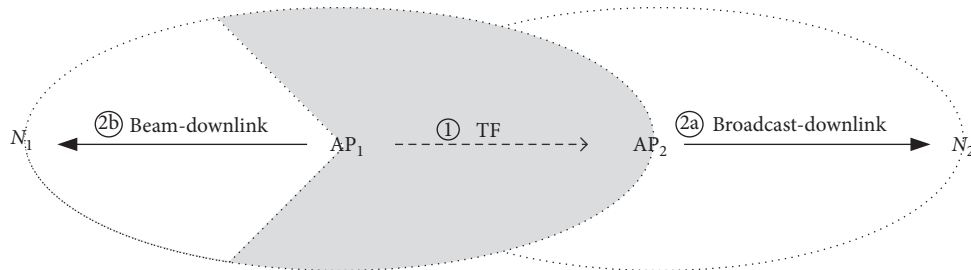


FIGURE 12: An example of exposed terminal problem and solution.

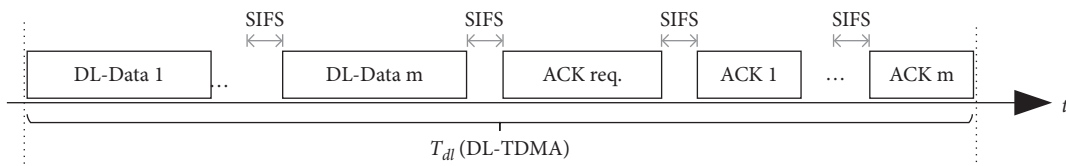


FIGURE 13: The downlink TDMA transmission (DL-TDMA) process.

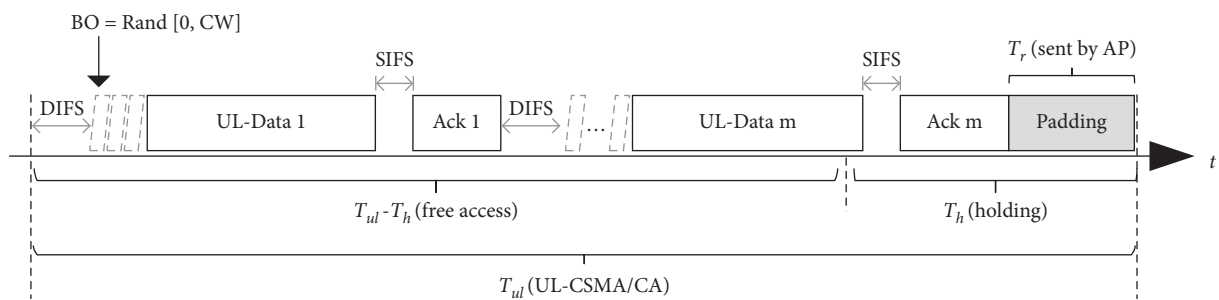


FIGURE 14: The uplink CSMA/CA (UL-CSMA/CA) transmission process.

sector is bigger, the collision probability for each sector will be higher, which decreases the throughput.

- (2) For  $n_k = 20$ , periodically the throughput first increases rapidly, then decreases slowly, and drops suddenly. The reason can be explained as follows. The throughput increases since the number of nodes increases and then decreases because the collision probability increases with

node number increasing, which decreases the throughput. Following the same deduction, the reason for sudden throughput drop can be explained for  $n_k = 5$ .

Figure 16 shows the throughput of the UL-CSMA/CA process as the number of nodes varies from 1 to 100, where the holding time  $T_h$  is  $500 \mu s$  and  $2000 \mu s$ , respectively. It can be observed from this figure that the overall throughput when  $T_h =$

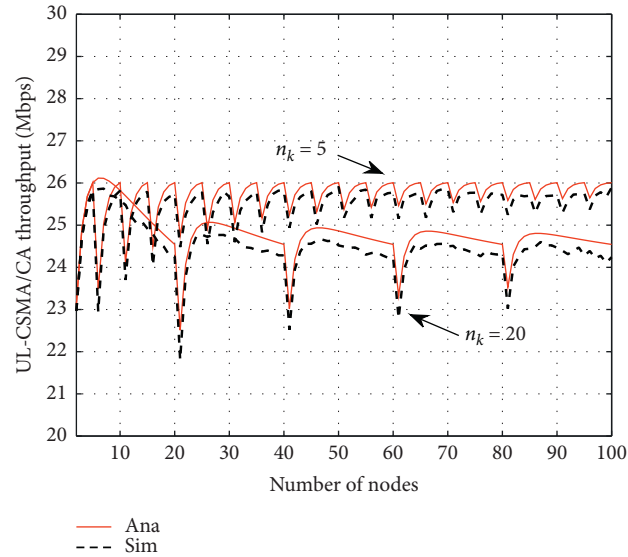


FIGURE 15: UL-CSMA/CA throughput vs. number of nodes,  $N$ , when  $n_k = 5, 20$ .

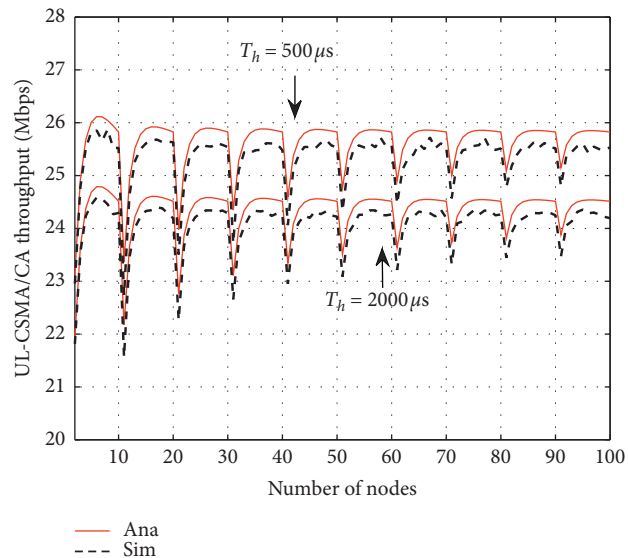


FIGURE 16: UL-CSMA/CA throughput vs. number of nodes,  $N$ , when  $T_h = 500$  and  $T_h = 2000$ .

500 is higher than that when  $T_h = 2000$ . It is because the longer the holding time is, the more the time that can be used for transmission is wasted. Besides, following the same deduction of Figure 15, we can explain the sudden drop in the throughput.

Figure 17 plots the throughput of the UL-CSMA/CA process as the number of nodes varies from 1 to 100, where the uplink transmission time  $T_{ul}$  is set to  $10000 \mu s$  and  $30000 \mu s$ , respectively. In this simulation, we set the holding time  $T_h$  to a fixed value of

$500 \mu s$ . It can be seen from this figure that the throughput when  $T_{ul} = 30000$  is higher than that when  $T_{ul} = 10000$ . The reason is that the longer the time for the uplink transmission is, the more the data transmission there is and therefore the higher the throughput is.

Figure 18 plots the throughput of the UL-CSMA/CA process as the payload length varies from 200 to 2000 bytes, where the number of each sector,  $n_k$ , is 5 and 20, respectively. From this figure, we have the following observations.



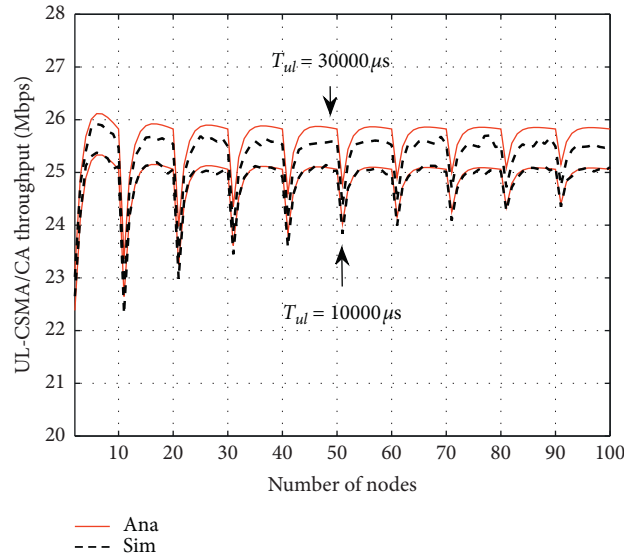


FIGURE 17: UL-CSMA/CA throughput vs. number of nodes,  $N$ , when  $T_{ul} = 10000$  and  $T_{ul} = 30000$ .

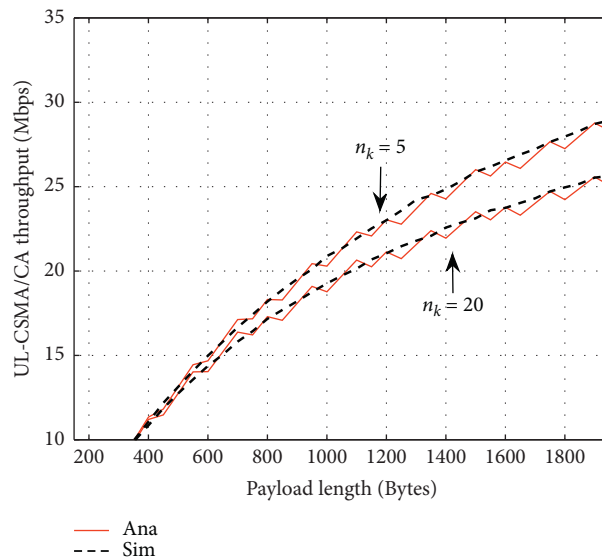


FIGURE 18: UL-CSMA/CA throughput vs. payload length, when  $n_k = 5$  and  $n_k = 20$ .

- (1) The throughput increases as the payload length increases. The reason is intuitive. A key factor that affects the throughput is how many bytes of frames are transmitted. Therefore, the longer the frame is transmitted, the higher the total throughput is.
- (2) The overall throughput when  $n_k = 5$  is higher than that when  $n_k = 20$ . The larger the number of nodes, the higher the collision probability in each sector. With collision probability increasing, the throughput is decreased.

Figure 19 plots the throughput of UL-CSMA/CA as the physical data rate varies from 10 Mbps to 100 Mbps, where the number of each sector,  $n_k$ , is 5

and 20, respectively. From this figure, we have the following observations.

- (1) The simulation curves closely match the corresponding theoretical curves, which manifests that our model is very accurate.
- (2) The throughput increases as the physical data rate increases. This is because the higher physical data rate can make more transmissions finished in the same time.
- (3) The overall throughput when  $n_k = 5$  is higher than that when  $n_k = 20$ . This indicates that sector with a smaller number of nodes usually has a lower collision probability, which in turn leads to a higher throughput.

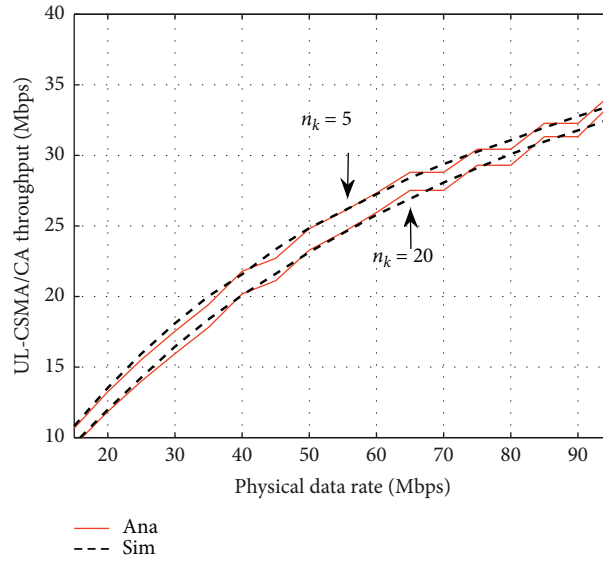


FIGURE 19: UL-CSMA/CA throughput vs. physical data rate, when  $n_k = 5$  and  $n_k = 20$ .

TABLE 1: Simulation settings.

$N$	100	$T_{\text{PHY\_Header}}$	$20 \mu\text{s}$	$T_{\text{SIFS}}$	$10 (\mu\text{s})$
$n_k$	5, 20	R	54 Mbps	$T_{\text{SLOT}}$	20
$K$	20, 5	$L_{\text{MPDU}}$	1528 Bytes	$T_{\text{DIFS}}$	50
$T_s$	$49600 \mu\text{s}$	$L_{\text{ACK-Req.}}$	14 Bytes	$T_{\text{ACK-Req.}}$	22
$T_{\text{dl}}$	$19525 \mu\text{s}$	$L_{\text{ACK}}$	14 Bytes	$T_{\text{ACK}}$	22
$T_{\text{ul}}$	$30000 \mu\text{s}$	$L_{\text{TF}}$	124 Bytes	$T_{\text{TF}}$	38
$T_h$	$500 \mu\text{s}$	$L_{\text{TF-END}}$	124 Bytes	$T_{\text{TF-END}}$	38

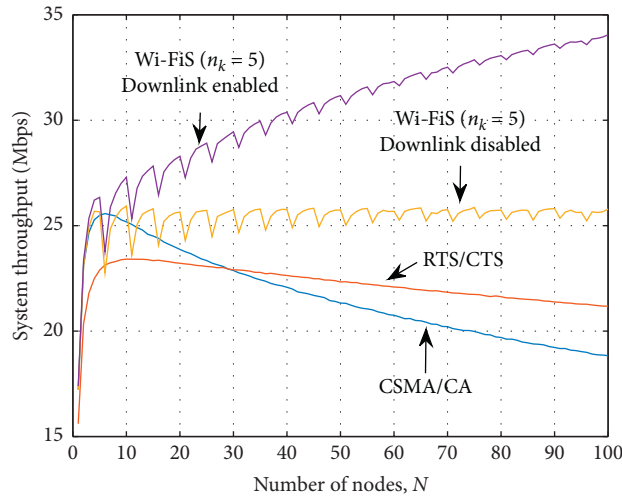


FIGURE 20: Comparison of system throughput among Wi-FiS, RTS/CTS, and CSMA/CA.

**7.3. Multicell Network.** We run simulations for hidden/exposed terminal problems with corresponding settings of Figures 11 and 12, respectively.

Figure 21 plots the throughput of CSMA/CA and Wi-FiS when there are hidden terminals. In this figure, we can see that, for CSMA/CA, hidden terminals cannot monitor each

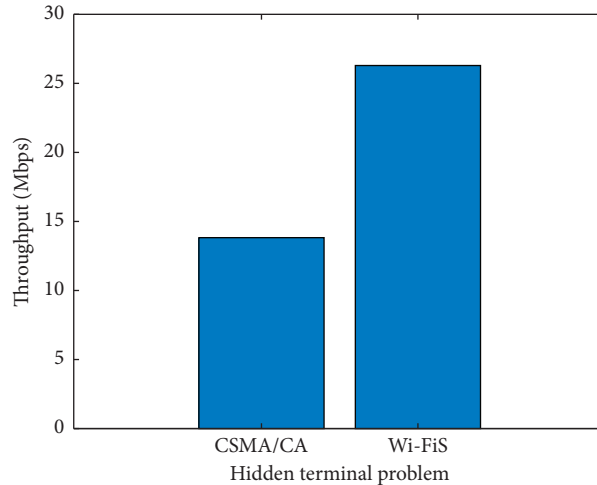


FIGURE 21: Comparison of throughput between Wi-FiS and CSMA/CA for hidden terminal scenario.

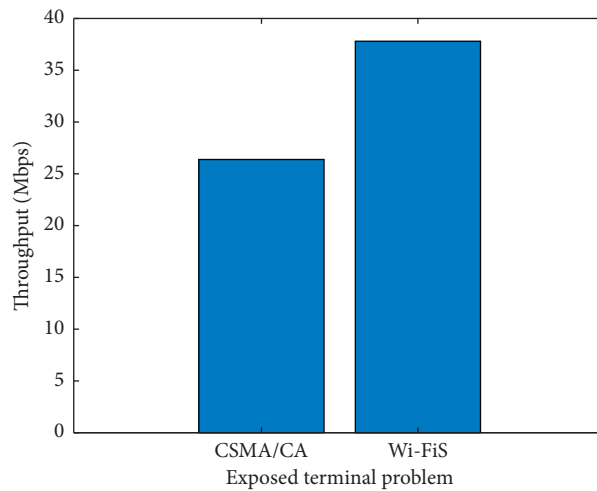


FIGURE 22: Comparison of throughput between Wi-FiS and CSMA/CA for exposed terminal scenario.

other's existence, so they will transmit at the same time when they cannot transmit data, which will lead to collisions at the receiving node. Therefore, the throughput of CSMA/CA is low. Our protocol uses a partitioned method to allow nodes to perform directional transmission for solving the collision problem caused by hidden terminals, thereby increasing the throughput.

Figure 22 plots the throughput of CSMA/CA and Wi-FiS when there are exposed terminals. In this figure, we can see that, for CSMA/CA, because the exposed terminals have monitored each other's existence, they may needlessly defer transmitting when they can transmit data, which will lead to channel resource wastage problem, thereby reducing throughput. Therefore, our protocol uses a directional beam to make AP perform downlink transmission to solve the problem of low channel utilization caused by exposed terminals, thereby effectively improving throughput.

In summary, it can be seen that the Wi-FiS is significantly better than the traditional protocol, and as the number of nodes increases, the throughput of Wi-FiS will not fluctuate significantly and is relatively stable. It shows that our protocol has good adaptability in large-scale and high-density Wi-Fi networks, which can ensure overall throughput and improve network performance.

## 8. Conclusions

5G-CPE integrates 5G and Wi-Fi protocols and is one of the key technologies that bring 5G to Industry 4.0. In order to solve the collision and hidden/exposed problems in large-scale 5G-CPE Wi-Fi networks, this paper designs a new wireless access protocol called Wi-FiS. Wi-FiS divides a dense network into different sectors and performs sector scheduling and therefore significantly reduces transmission

collision. For multicell networks, utilizing directional beam, Wi-FiS can avoid hidden and exposed terminal problems, while enabling parallel transmissions among multiple cells. A salient feature of Wi-FiS is that it effectively utilizes (rather than modifying) the virtual carrier sense mechanism of conventional Wi-Fi protocols for sector scheduling and therefore has good compatibility with conventional Wi-Fi protocols. We then theoretically analyze Wi-FiS's throughput. Extensive simulations show that the proposed model is very accurate, and the proposed design greatly outperforms related designs and can make a dense network achieve high throughput.

### Data Availability

The data used to support the findings of this study are available from the corresponding author upon request.

### Conflicts of Interest

The authors declare that there are no conflicts of interest regarding the publication of this paper.

### Acknowledgments

This study was funded in part by the National Natural Science Foundation of China (61872451 and 61872452), in part by the Science and Technology Development Fund, Macau SAR (0098/2018/A3, 0076/2019/A2, and 0037/2020/A1), and in part by the Dongguan Social Science and Technology Development (General) Project (2020507154645).

### References

- [1] International Telecommunications Union Radio Communication Sector (ITU-R), "Minimum requirements related to technical performance for IMT-2020 radio interface(s)," Report ITU-R M.2410-0 (11/2017), International Telecommunications Union Radio Communication Sector (ITU-R), Geneva, Switzerland, 2017, <https://www.itu.int/%20pub/R-REP-M.2410-2017>.
- [2] 5G Alliance for Connected Industries and Automation (5G ACIA), "5G for connected industries and automation white paper," 2019, [https://www.5g-acia.org/fileadmin/5G-ACIA/Publikationen/Whitepaper\\_5G\\_for\\_Connected\\_Industries\\_and\\_Automation/WP\\_5G\\_for\\_Connected\\_Industries\\_and\\_Automation\\_Download\\_19.03.19.pdf](https://www.5g-acia.org/fileadmin/5G-ACIA/Publikationen/Whitepaper_5G_for_Connected_Industries_and_Automation/WP_5G_for_Connected_Industries_and_Automation_Download_19.03.19.pdf).
- [3] M. Simsek, A. Aijaz, M. Dohler, J. Sachs, and G. Fettweis, "5G-enabled tactile internet," *IEEE Journal on Selected Areas in Communications*, vol. 34, no. 3, pp. 460–473, 2016.
- [4] S. Sen, R. R. Choudhury, and S. Nelakuditi, "CSMA/CN: carrier sense multiple access with collision notification," in *Proceedings of the ACM 16th Annual International Conference on Mobile Computing and Networking*, pp. 25–36, Chicago, IL, USA, September 2010.
- [5] S. Gollakota and D. Katabi, "Zigzag decoding," *ACM SIGCOMM Computer Communication Review*, vol. 38, no. 4, pp. 159–170, 2008.
- [6] T. Xiong, J. Zhang, J. Yao, and W. Lou, "Symbol-level detection: a new approach to silencing hidden terminals," in *Proceedings of the 2006 IEEE International Conference on Network Protocols*, pp. 1–10, Austin, TX, USA, October 2012.
- [7] E. Magistretti, O. Gurewitz, and E. W. Knightly, "802.11ec: collision avoidance without control messages," in *Proceedings of the 18th annual international conference on Mobile computing and networking*, pp. 65–76, Istanbul, Turkey, August 2012.
- [8] A. Acharya, A. Misra, and S. Bansal, "Design and analysis of a cooperative medium access scheme for wireless mesh networks," in *Proceedings of the 2004 IEEE International Conference on Broadband Networks*, San Jose, CA, USA, October 2004.
- [9] T. Yamaguchi, K. Shishida, H. Hirai, K. Tsuneta, and M. Sato, "Improvement of servo robustness for digital sector servo system (hard disk drives)," *IEEE Transactions on Magnetics*, vol. 28, no. 5, pp. 2910–2912, 1992.
- [10] N. Shahin, R. Ali, S. W. Kim, and Y.-T. Kim, "Cognitive backoff mechanism for IEEE802.11ax high-efficiency WLANs," *Journal of Communications and Networks*, vol. 21, no. 2, pp. 158–167, 2019.
- [11] D.-J. Deng, C.-H. Ke, H.-H. Chen, and Y.-M. Huang, "Contention window optimization for IEEE 802.11 DCF access control," *IEEE Transactions on Wireless Communications*, vol. 7, no. 12, pp. 5129–5135, 2008.
- [12] R. Ali, N. Shahin, Y. B. Zikria, B.-S. Kim, and S. W. Kim, "Deep reinforcement learning paradigm for performance optimization of channel observation-based MAC protocols in dense WLANs," *IEEE Access*, vol. 7, pp. 3500–3511, 2018.
- [13] L. Wang, K. Wu, and M. Hamdi, "Attached-RTS: eliminating an exposed terminal problem in wireless networks," *IEEE Transactions on Parallel and Distributed Systems*, vol. 24, no. 7, pp. 1289–1299, 2012.
- [14] Y.-H. Lee and W.-R. Wu, "A WLAN uplink collision-resolving scheme using multi-user beamforming technique," *IEEE Transactions on Vehicular Technology*, vol. 69, no. 10, pp. 11042–11054, 2020.
- [15] IEEE 802.11, "Wireless LAN medium access control (MAC) and physical layer (PHY) specifications," *ANSI/IEEE Std 802.11*, 2016.
- [16] A. Gaber and A. Omar, "A study of wireless indoor positioning based on joint TDOA and DOA estimation using 2-D matrix pencil algorithms and IEEE 802.11ac," *IEEE Transactions on Wireless Communications*, vol. 14, no. 5, pp. 2440–2454, 2015.
- [17] A. Neri, A. Di Nepi, and A. M. Vegni, "DOA and TOA based localization services protocol in IEEE 802.11 networks," *Wireless Personal Communications*, vol. 54, no. 1, pp. 155–168, 2010.
- [18] F. Wen and C. Liang, "An indoor AOA estimation algorithm for IEEE 802.11ac Wi-Fi signal using single access point 2014.11ac Wi-Fi signal using single access point," *IEEE Communications Letters*, vol. 18, no. 12, pp. 2197–2200, 2014.
- [19] IEEE 802.11-TGe, "Wireless LAN medium access control (MAC) and physical layer (PHY) specifications, specification-amendment 8: medium access control (MAC) quality of service enhancements," *ANSI/IEEE Std 802.11*, 2005.
- [20] N. M. Sabah and A. Hocanin, "The use of negative acknowledgement control packets (NACKs) to improve throughput and delay in IEEE 802.11 networks," in *Proceedings of the 2010 2nd International Conference on Computer Technology and Development*, pp. 136–140, Cairo, Egypt, November 2010.
- [21] L. Zheng, M. Ni, L. Cai, J. Pan, C. Ghosh, and K. Doppler, "Performance analysis of group-synchronized DCF for dense IEEE 802.11 networks," *IEEE Transactions on Wireless Communications*, vol. 13, no. 11, pp. 6180–6192, 2014.

## Research Article

# Energy Management Strategy Using Equivalent Consumption Minimization Strategy for Hybrid Electric Vehicles

Fazhan Tao,<sup>1,2</sup> Longlong Zhu,<sup>1</sup> Baofeng Ji,<sup>1,2</sup> Pengju Si,<sup>1,2</sup> and Zhumu Fu <sup>1,2</sup>

<sup>1</sup>School of Information Engineering, Henan University of Science and Technology, Luoyang 471000, China

<sup>2</sup>Henan Key Laboratory of Robot and Intelligent Systems, Henan University of Science and Technology, Luoyang 471000, China

Correspondence should be addressed to Zhumu Fu; fuzhumu@haust.edu.cn

Received 13 October 2020; Revised 24 November 2020; Accepted 7 December 2020; Published 18 December 2020

Academic Editor: Xingwang Li

Copyright © 2020 Fazhan Tao et al. This is an open access article distributed under the Creative Commons Attribution License, which permits unrestricted use, distribution, and reproduction in any medium, provided the original work is properly cited.

In this paper, an energy management strategy for electric vehicles equipped with fuel cell (FC), battery (BAT), and supercapacitor (SC) is considered, aiming at improving the whole performance under a framework of vehicle to network application. In detail, based on wavelet transform and equivalent consumption minimization strategy (ECMS), the demand power of vehicles is optimized to enhance the lifespan of fuel cell, fuel economy, and dynamic performance of electric vehicles. The wavelet transform is used to separate the high-frequency power in order to provide a peak power and recycle the braking energy. The equivalent consumption minimization strategy is used to distribute the low-frequency power to fuel cell and battery for minimizing the hydrogen consumption. Obtained results are studied using an advanced vehicle simulator, and its effectiveness of the strategy is confirmed, which provides a fundamental control method for the IOV application.

## 1. Introduction

As the development of automobile industry has reached a certain level [1–4], it also leads to some issues, such as environmental pollution, global warming, energy crisis, and the growing number of traffic congestion and accidents. Many further aspirations are emerging to make the vehicle safer, more eco-friendly, and more intelligent. Meantime, since the technology of Internet of vehicles has achieved many developments rapidly [5–13], it provides a better way to optimize a control strategy for HEVs by sharing a package of data consisting of relevant information related to the vehicle status and the road condition.

As for the energy management strategy for hybrid electric vehicles equipped with FC, BAT, and SC (FCHEV), it has an important role in the performance of hybrid electric system, which can be roughly classified into rule-based EMS and optimization-based EMS from the optimization aspects [14–23]. Rule-based energy strategies are developed based on rules or maps extracted from the designed splitting

methods [13, 19, 20]. In order to solve the cruising range of three-energy plug-in HEV, Zhang et al. [19] proposed a rule-based fuzzy control strategy to realize a hierarchical control based on driving pattern recognition, whose results show that the proposed method can effectively extend the PHEV cruising range and the energy management efficiency. In [20], dual-energy (FC + BAT) and triple-energy (FC + BAT + SC) management strategies are considered using the fuzzy control method, achieving the energy distribution between the required power and multiple energy sources for four standard driving cycles and compared with the original power tracking strategy in ADVISOR. A double-fuzzy logic controller is proposed [14] to decouple power of the vehicle and to ensure the economy of fuel consumption of the vehicle. Considering rule-based EMSs cannot achieve optimal power distribution, it is constrained to a certain extent.

Therefore, the optimization-based EMS has been proposed. The optimization-based EMS includes global optimal strategies and real-time optimal strategies, which has been studied by researchers and engineers, including

dynamic programming, genetic algorithm, model control prediction, and Pontryagin's minimum principle [17, 18, 20, 21]. In [21], a novel real-time energy management strategy based on ECMS is proposed, and the equivalent factor is adaptive to the drive conditions to catch energy-saving opportunities during the trip, which improves the fuel economy. Zhang et al. proposed a minimum hydrogen consumption equivalent strategy, adding an energy storage system to the original FC system for compensating peak demand power and recycling braking energy to improve the economy of hydrogen consumption [22]. In [23], in order to improve fuel economy and adaptability of various driving conditions for online energy management, a hierarchical model predictive control strategy is proposed, the upper controller realizes optimal torque distribution, and the lower controller ensures the tracking performance of engine output torque for the distributed torque from the upper controller.

As for the aforementioned results, most of them focus on HEVs and existing high burden on computation for online application. As for the considered FCHEV in this paper, FC regarded as the main energy source cannot recover braking energy and needs to be combined with energy storage system. Consider a high energy density of BAT and higher power density of SC, and both of them are combined as an energy storage system. Meantime, considering the different characteristic of the existing three power sources, how to design one low burden computation and an effective EMS is important for the IOV application. Wavelet transform (WT) is a very efficient signal processing method, and it can effectively separate the low-frequency and high-frequency parts of the required power signal, which is supposed to significantly protect the fuel cell from required power fluctuations, and can be implemented online easily. In this paper, in order to tackle unreasonable energy distribution and low energy utilization rate among various energy sources, energy management strategy based on wavelet transform and equivalent consumption minimization strategy is proposed for the FCHEV.

The rest of the paper is organized as follows: the models of the main component's description and the topology and mathematical models of FCHEV are stated in Section 2. Main results on EMS are addressed based on wavelet transform and ECMS in Section 3. In Section 4, simulation results are furnished to verify the effectiveness of the proposed strategy. Finally, Section 5 draws the conclusion of this paper.

## 2. Modelling for FCHEVs

In FCHEV, fuel cell as a primary power source through the unidirectional DC/DC converter delivers power to motor, and a battery is used as a direct energy source to directly transmit power to motor and recycle braking power. When the vehicle accelerates suddenly, supercapacitor provides peak power through bidirectional DC/DC while absorbing the braking energy of the vehicle. The model of vehicles is shown in Figure 1.

The power of a hybrid electric vehicle is provided by fuel cell, battery, and supercapacitor, and the power demand can be calculated as follows:

$$P_{\text{req}} = \lambda_1 P_{\text{fc}} + P_{\text{bat}} + \lambda_2 P_{\text{sc}}, \quad (1)$$

where  $P_{\text{req}}$ ,  $P_{\text{fc}}$ ,  $P_{\text{bat}}$ , and  $P_{\text{sc}}$  represent the demand power of vehicle and the power provided by fuel cell, battery, and supercapacitor, respectively.  $\lambda_1$  indicates the efficiency of fuel cell, and  $\lambda_2$  indicates the efficiency of the supercapacitor.

Fuel cell converts chemical energy into electrical energy by consuming hydrogen to provide energy for vehicles.  $P_{\text{fc}}$  can be expressed as follows:

$$P_{\text{fc}} = \eta_{\text{fc}} \times \int_0^t \frac{m_{H_2}(t) \times 1.4 \times 10^8}{3600} dt, \quad (2)$$

where  $m_{H_2}$  indicates the mass of  $H_2$ ,  $1.4 \times 10^8$  indicates the heating value of  $H_2$  combustion, and  $\eta_{\text{fc}}$  indicates the efficiency of hydrogen combustion into power.

As for battery,  $P_{\text{bat}}$  can be expressed by equation (4). In this paper, the internal resistance of the battery is ignored:

$$P_{\text{bat}} = u \int_0^t i(t) dt, \quad (3)$$

where  $u$  indicates the voltage of battery and  $i(t)$  indicates the instantaneous current of battery.

In order to prevent the battery from working excessively thereby reducing its lifetime, the SOC of battery should be kept within the operable range. The SOC of battery ( $\text{SOC}_{\text{bat}}$ ) is given as follows:

$$\text{SOC}_{\text{bat}} = \text{SOC}_0 - \int_0^t \frac{i(t)}{Q_{\text{bat}}} dt, \quad (4)$$

where  $\text{SOC}_0$  indicates the initial SOC of the battery and  $Q_{\text{bat}}$  is the maximum charge of the battery.

The output voltage of the supercapacitor consists of two parts: one part is the energy released by the supercapacitor and the other part is caused by the internal resistance of the supercapacitor. The supercapacitor SOC ( $\text{SOC}_{\text{sc}}$ ) can be expressed by the following equation:

$$\text{SOC}_{\text{sc}} = \text{SOC}_1 - \frac{Q_0 - \int_0^t u(t)/R_i dt}{Q_{\text{sc\_max}}}, \quad (5)$$

where  $\text{SOC}_1$  indicates the initial SOC of supercapacitor,  $Q_0$  indicates the initial charge of supercapacitor,  $Q_{\text{sc\_max}}$  indicates the maximum charge of supercapacitor.  $u(t)$  indicates the instantaneous voltage of supercapacitor, and  $R_i$  indicates the internal resistance of supercapacitor.

## 3. Energy Management Strategy for FCHEV

Considering different characteristics of power sources of FCHEV, the supercapacitor suits to supply high-frequency components of  $P_{\text{req}}$ , and the fuel cell and battery are suitable to supply low-frequency components of  $P_{\text{req}}$ . Therefore, an EMS is proposed in this paper, as shown in Figure 2. Firstly, the wavelet transform is utilized for decoupling  $P_{\text{req}}$ ,  $P_{\text{high}}$  (high-frequency components of  $P_{\text{req}}$ ) will be assigned

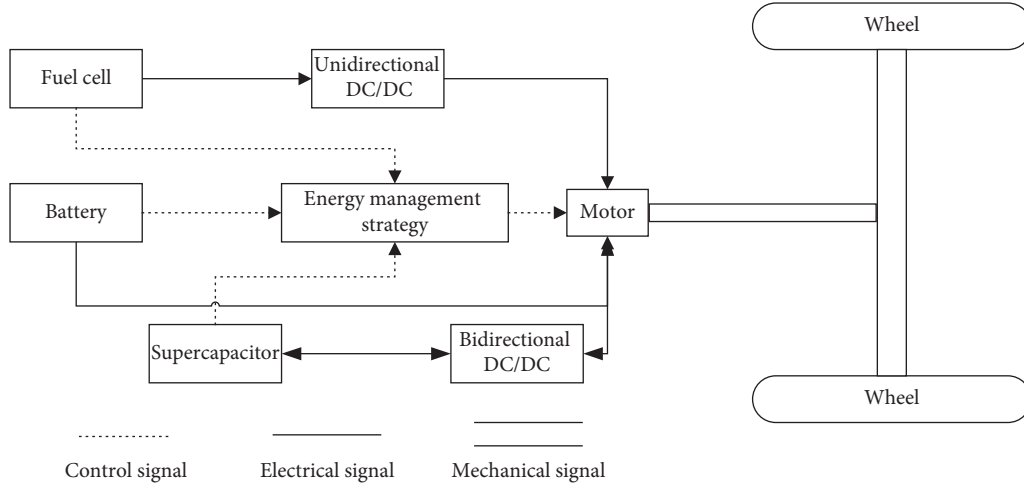


FIGURE 1: Power structure of HEV.

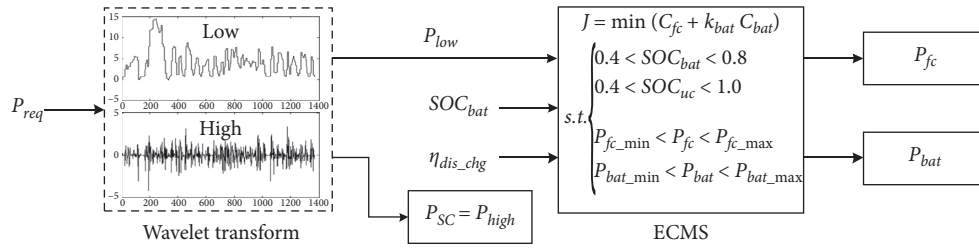


FIGURE 2: The structure of the proposed EMS.

to supercapacitor, and  $P_{low}$  (low-frequency components of  $P_{req}$ ) will be assigned to fuel cell and battery. Secondly, ECMS method is used to distribute  $P_{low}$  to fuel cell and battery for minimizing the hydrogen consumption and to maintain battery in a predefined range.

Wavelet transform and inverse wavelet transform are adopted as follows:

$$W(\lambda, u) = \int s(t) \frac{1}{\sqrt{\lambda}} \Psi\left(\frac{t-u}{\lambda}\right) dt, \quad (6)$$

$$\lambda = 2^j,$$

$$u = k2^j,$$

$$k \in Z,$$

$$s(t) = \sum_{j=Z} \sum_{k=Z} W(j, k) \Psi_{(j,k)}(t), \quad (7)$$

where  $s(t)$  is the original signal,  $\lambda$  is the scale parameter,  $u$  is the position parameter,  $\Psi$  is the mother wavelet, and  $W$  is the wavelet coefficient.

Inspired by [24, 25], the energy distribution process of FCHEV is regarded as the one stationary process and, therefore, is chosen as the other wavelet to relax calculation burden on the real-time application for IOV. Hence, in this paper, Harr wavelet is chosen as follows, and the three-level

Haar wavelet decomposition and reconstruction are shown in Figure 3:

$$\Psi(t) = \begin{cases} 1, & 0 \leq t \leq 0.5, \\ 1, & 0.5 < t \leq 1, \\ 0, & \text{otherwise.} \end{cases} \quad (8)$$

From Figure 3, by  $l_0(z)$  (low-pass filter) and  $h_0(z)$  (high-pass filter),  $s(n)$  (original signal) is reconstructed with very slight errors based on the reconstruction filter bank. Based on the proposed method,  $P_{req}$  can be obtained as follows:

$$\begin{cases} P_{low} = s_0(n) = P_{fc} + P_{bat}, \\ P_{high} = s_1(n) + s_2(n) + s_3(n) = P_{sc}, \end{cases} \quad (9)$$

where  $s_0(n)$  is the reference signal.

After the WT process, the low component of the required power needs to be further processed to determine the power distribution ratio between the fuel cell and battery. The essence of the strategy of minimum equivalent consumption is to convert the BAT and SC power into equal fuel consumption and then optimize equivalent hydrogen consumption of FCHEV. Therefore, the total hydrogen consumption of FCHEV including the three power sources is shown as follows:

$$C_m = \min(C_{fc} + k_{bat} C_{bat}), \quad (10)$$

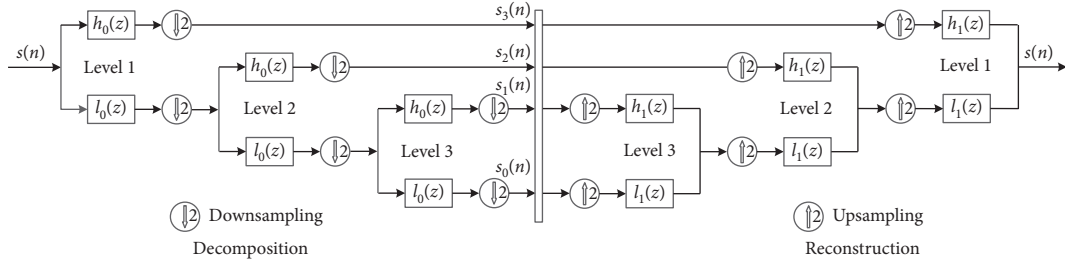


FIGURE 3: Three-level Haar wavelet decomposition and reconstruction.

where  $C_m$ ,  $C_{fc}$ , and  $C_{bat}$  represent the minimum hydrogen consumption of vehicles and hydrogen consumption of FC and BAT and  $k_{bat}$  represents equivalent factor of the equivalent hydrogen consumption of BAT and SC. The hydrogen consumption of the fuel cell is shown as follows:

$$C_{fc} = \int_0^t \frac{i_{fc}(t)}{NA \times e} dt, \quad (11)$$

where  $i_{fc}(t)$  represents the current generated by the fuel cell consuming hydrogen, NA represents the Avogadro constant  $6.02 \times 10^{23} \text{ mol}^{-1}$ , and  $e$  means the electric quantity of electrons is  $1.6 \times 10^{-19} \text{ C}$ .

The hydrogen consumption of the battery is shown as follows:

$$C_{bat} = \int_0^t \frac{i_{fc}(t) \times P_{bat}}{NA \times e \times P_{fc} \times \eta_{dis\_chg}} dt, \quad (12)$$

where  $\eta_{dis\_chg}$  indicates the charging and discharging efficiency of the battery.

The equivalent factor of the equivalent hydrogen consumption of the battery is related to SOC of battery. When the battery work in a safety range,  $K_{bat}$  can be expressed as follows:

$$K_{bat} = 1 - \mu \frac{SOC - 0.5(SOC_{bat\_max} - SOC_{bat\_min})}{SOC_{bat\_max} - SOC_{bat\_min}}, \quad (13)$$

where  $SOC_{bat\_max}$  and  $SOC_{bat\_min}$  represent the maximum and minimum SOC values of the battery.

Considering influence of the charging and discharging state of the battery and working range of the fuel cell on service life of the battery and fuel cell, the charging and discharging state of the battery and working range of the fuel cell are taken as constraints as follows:

$$\begin{cases} 0.4 < SOC_{bat} < 0.8, \\ 0.4 < SOC_{uc} < 1.0, \\ P_{fc\_min} < P_{fc} < P_{fc\_max}, \\ P_{bat\_min} < P_{bat} < P_{bat\_max}, \end{cases} \quad (14)$$

where  $P_{fc\_min}$  and  $P_{fc\_max}$  represent the minimum and maximum power allowed for fuel cell operation, respectively, and  $P_{bat\_min}$  and  $P_{bat\_max}$  indicate the minimum and maximum power allowed for fuel cell operation, respectively.

## 4. Simulation Results

In this section, the advanced vehicle simulator is employed to confirm the effectiveness of the proposed method. Firstly, New European Drive Cycle (NEDC), Highway Fuel Economy Test (HWFET), and Urban Dynamometer Driving Schedule (UDDS) drive cycle are the typical road conditions representing suburbs, highway, and city, respectively. Thus, the combined drive cycle (NEDC + HWFET + UDDS) is used to test the effectiveness of the proposed EMS in reducing hydrogen consumption and extending fuel cell lifespan by using MATLAB/Simulink. Vehicle speed and required power under combined drive cycle is shown in Figure 4. Main parameters and component models of FCHEV are listed in Table 1. Then, power distribution of fuel cell, battery, and supercapacitor, fuel cell power fluctuation, SOC of battery and supercapacitor, and fuel cell efficiency are given in Figures 5–8, respectively.

The power distribution of fuel cell, battery, and supercapacitor under combined drive cycle (NEDC + HWFET + UDDS) is shown in Figure 5. It is obvious from Figure 5 that the fuel cell and battery provide steady-state part of the required power, and supercapacitor supplies/absorbs the peak power rapidly when FCHEV accelerates and brakes. Thus, it is supposed to significantly improve fuel cell and battery lifespan by the proposed EMS. Meanwhile, battery and supercapacitor recycle all braking energy when the HEV brakes. From the simulation results, the proposed EMS can effectively improve the energy efficiency of the whole vehicle and extend the vehicle mileage.

In order to show the effectiveness and advantages of the proposed EMS in reducing fuel cell output power fluctuation in detail, fuel cell power fluctuation (variation in fuel cell output power per second) is shown in Figure 6. It can be seen that, with the proposed EMS, the maximum fuel cell output power fluctuation is limited within  $\pm 250 \text{ W/s}$  and almost fuel cell output power fluctuation is concentrated in the range of  $-100 \text{ W/s}$  to  $100 \text{ W/s}$ . With smooth output of fuel cell, its lifespan is effectively extended.

Figure 7 shows the SOC variations in battery and supercapacitor under the combined drive cycle. From Figure 7, it is clear that the proposed EMS can maintain the SOC of battery and supercapacitor in a limited range, and the battery charges and discharges with a high efficiency in this range. The proposed EMS guarantees the battery and supercapacitor always have enough power for accelerating the vehicle.



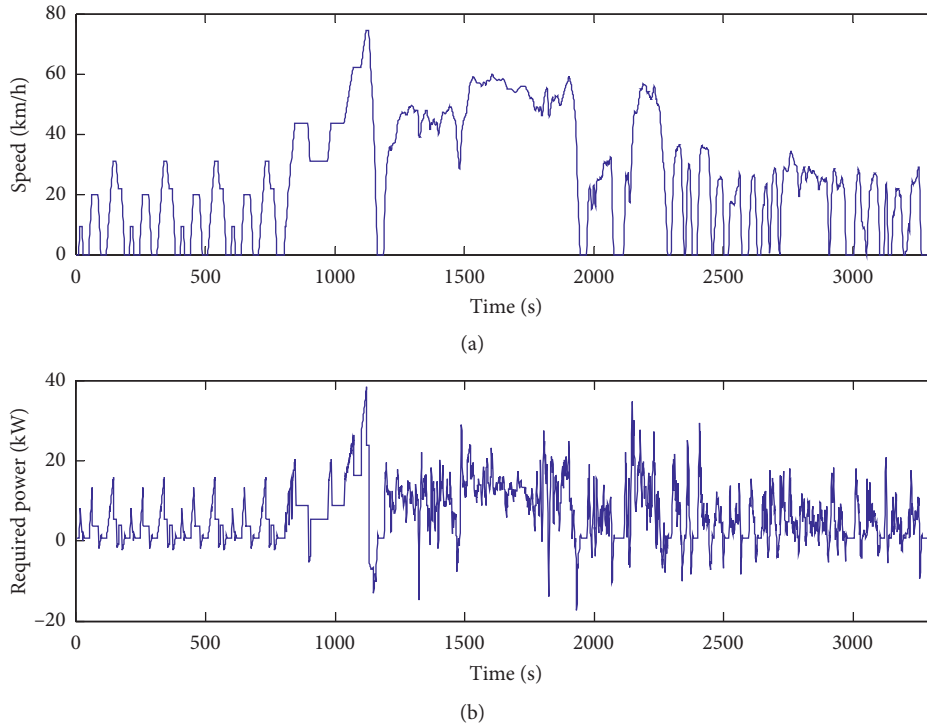


FIGURE 4: Vehicle speed and required power under combined drive cycle.

TABLE 1: Parameters of the vehicle model.

Parameter	Value
Vehicle mass (kg)	1113
Gravity constant, $g$ ( $m/s^2$ )	9.8
Rolling resistance coefficient	0.6
Aerodynamic drag coefficient	0.3
Vehicle frontal area ( $m^2$ )	1.75
Air density ( $kg/m^3$ )	1.22
Fuel cell maximum net power (kW)	30
Fuel cell average efficiency (%)	56
Battery maximum output power (kW)	20
Battery maximum stored energy (kW h)	9.25
Battery initial SOC	0.7
Supercapacitor maximum output power (kW)	70
Supercapacitor maximum stored energy (Wh)	350
Supercapacitor initial SOC	0.7
Motor maximum power (kW)	75
Motor maximum speed (rpm)	6283
Motor average efficiency (%)	90

Furthermore, fuel cell efficiency is shown in Figure 8. According to Figure 8, the proposed EMS can achieve and make the fuel cell operating efficiency over 55% during the most of whole drive cycle. It can be concluded

that, with the proposed EMS, fuel cell system is controlled to operate in a high efficiency region, which can achieve good fuel economy by reducing hydrogen consumption.

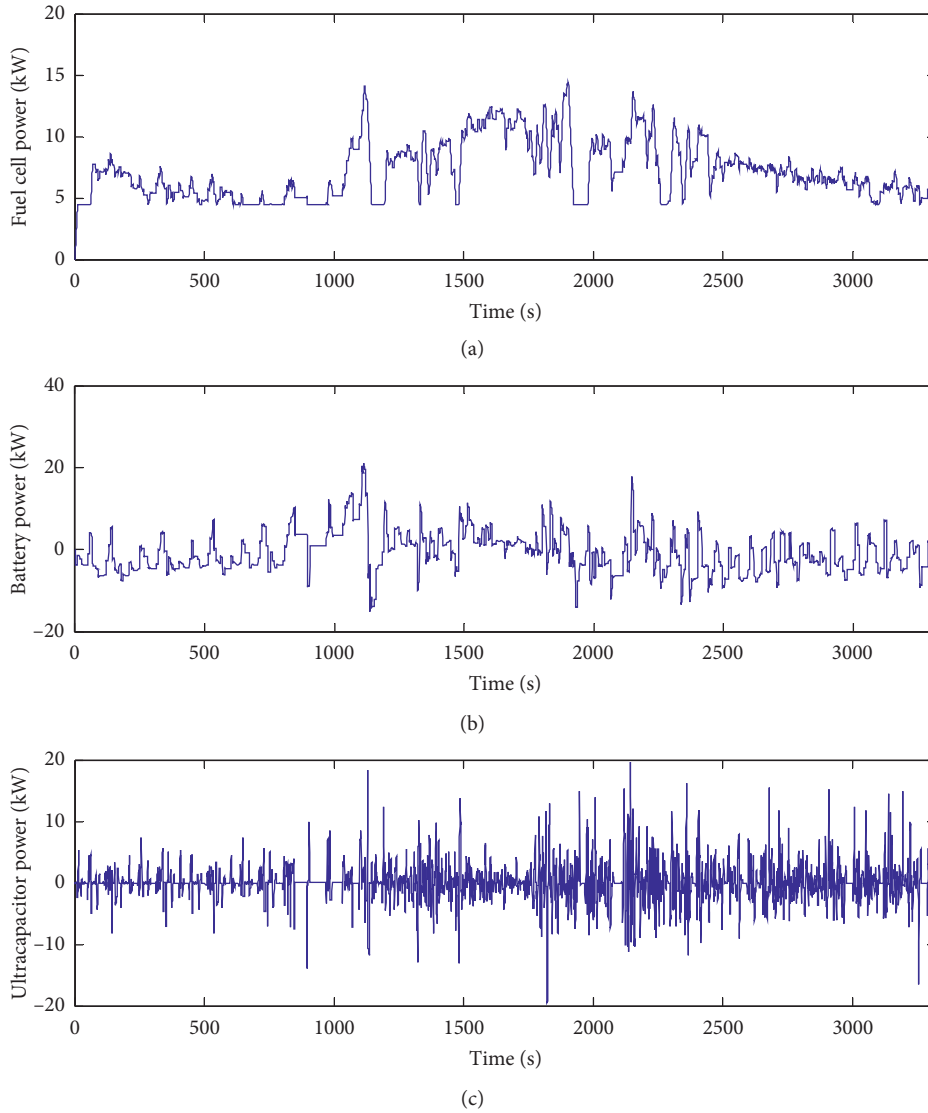


FIGURE 5: Power distribution of fuel cell, battery, and supercapacitor.

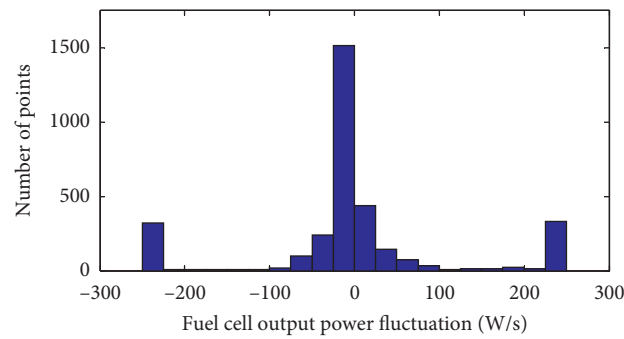


FIGURE 6: Fuel cell power fluctuation.

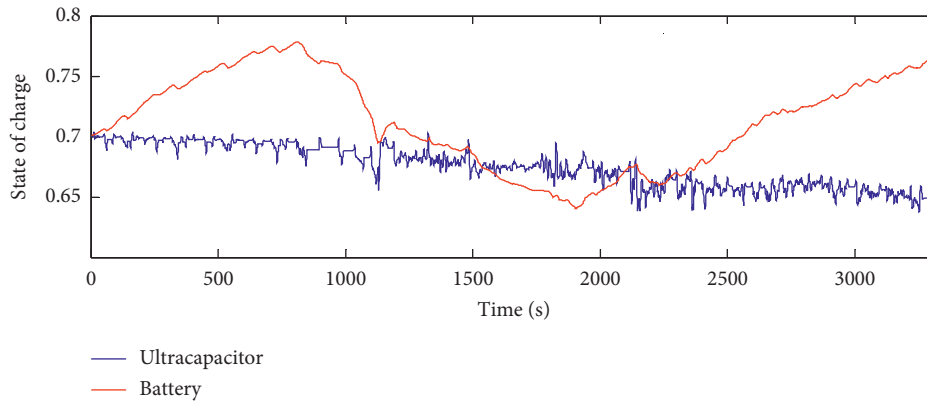


FIGURE 7: SOC of battery and supercapacitor.

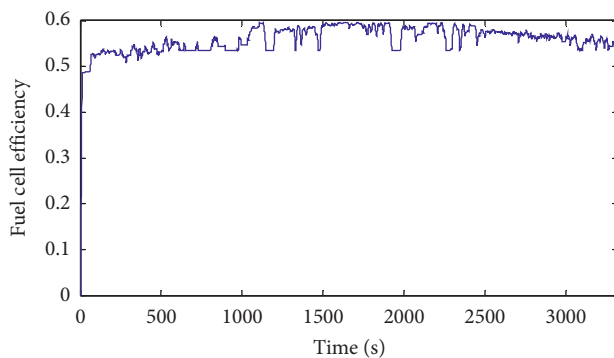


FIGURE 8: Fuel cell efficiency.

## 5. Conclusions

In this paper, energy management strategy using equivalent consumption minimization strategy is proposed for improving fuel cell efficiency and extending fuel cell lifespan. The proposed EMS separated required power into two components by WT. Supercapacitor is used to supply the high component of the required power to reduce the impact of load fluctuation on fuel cell and battery. The equivalent consumption minimization strategy is used to distribute the remaining low-frequency component power to fuel cell and battery for minimizing the hydrogen consumption. Simulation results show that the proposed EMS can effectively reduce fuel cell power fluctuation and limit it within  $\pm 250$  W/s, which is supposed to significantly extend fuel cell lifespan. Meanwhile, with the proposed EMS, fuel cell is guaranteed to operate in high efficiency ranges, which can achieve good fuel economy by reducing hydrogen consumption.

## Data Availability

The data used to support the findings of this study are included within the article.

## Conflicts of Interest

The authors declare that there are no conflicts of interest regarding the publication of this paper.

## Acknowledgments

This work was partially supported by the National Natural Science Foundation of China (Grant no. 61473115), Scientific and Technological Innovation Leaders in Central Plains (Grant no. 194200510012), Science, Technology Innovative Teams in University of Henan Province (Grant no. 18IRTSTHN011), Key Scientific Research Projects of Universities in Henan Province (Grant nos. 19A413007 and 20A120008), National Thirteen-Five Equipment Pre-Research Foundation of China (Grant nos. 1403120207 and 61402100203), Aeronautical Science Foundation of China (Grant no. 20185142003), and Scientific and Technological Project of Henan Province (Grant no. 202102310200).

## References

- [1] A. Flah and C. Mahmoudi, "Design and analysis of a novel power management approach, applied on a connected vehicle as V2V, V2B/I, and V2N," *International Journal of Energy Research*, vol. 43, no. 13, pp. 6869–6889, 2019.
- [2] X. Li, Q. Wang, M. Liu et al., "Cooperative wireless-powered NOMA relaying for B5G IoT networks with hardware impairments and channel estimation errors," *IEEE Internet of Things Journal*, vol. 1, 2020.
- [3] X. Li, H. Mengyan, Y. Liu, V. G. Menon, A. Paul, and Z. Ding, "I/Q imbalance aware nonlinear wireless-powered relaying of B5G networks: security and reliability analysis," *IEEE Transactions on Network Science and Engineering*, vol. 1, 2020.
- [4] M. S. Alam, B. Hyde, P. Duffy, and A. McNabola, "Analysing the Co-Benefits of transport fleet and fuel policies in reducing PM2.5 and CO<sub>2</sub> emissions," *Journal of Cleaner Production*, vol. 172, pp. 623–634, 2018.
- [5] K. V. Koteswararao, G. N. Srinivasulu, and V. Venkateswarlu, "A review on energy allocation of fuel cell/battery/ultracapacitor for hybrid electric vehicles," *International Journal of Energy Research*, vol. 42, no. 14, pp. 4263–4283, 2018.
- [6] H. Sun, Z. Fu, F. Tao, L. Zhu, and P. Si, "Data-driven reinforcement-learning-based hierarchical energy management strategy for fuel cell/battery/ultracapacitor hybrid electric vehicles," *Journal of Power Sources*, vol. 455, p. 227964, 2020.
- [7] Y. J. Wang, Z. D. Sun, and Z. H. Chen, "Energy management strategy for battery/supercapacitor/fuel cell hybrid source vehicles based on finite state machine," *Applied Energy*, vol. 254, 2019.

- [8] X. Li, M. Zhao, Y. Liu, L. Li, Z. Ding, and A. Nallanathan, "Secrecy analysis of ambient backscatter NOMA systems under I/Q imbalance," *IEEE Transactions on Vehicular Technology*, vol. 69, no. 10, p. 12286, 2020.
- [9] Y. Huang, H. Wang, A. Khajepour et al., "A review of power management strategies and component sizing methods for hybrid vehicles," *Renewable and Sustainable Energy Reviews*, vol. 96, pp. 132–144, 2018.
- [10] X. Li, J. Li, Y. Liu, Z. Ding, and A. Nallanathan, "Residual transceiver hardware impairments on cooperative NOMA networks," *IEEE Transactions on Wireless Communications*, vol. 19, no. 1, pp. 680–695, 2020.
- [11] Z. Fu, Z. Li, P. Si, and F. Tao, "A hierarchical energy management strategy for fuel cell/battery/supercapacitor hybrid electric vehicles," *International Journal of Hydrogen Energy*, vol. 44, no. 39, pp. 22146–22159, 2019.
- [12] B. Ji, Z. Chen, S. Chen et al., "Joint optimization for ambient backscatter communication system with energy harvesting for IoT," *Mechanical Systems and Signal Processing*, vol. 135, 2020.
- [13] X. Li, Q. Wang, Y. Liu, T. A. Tsiftsis, Z. Ding, and A. Nallanathan, "UAV-aided multi-way NOMA networks with residual hardware impairments," *IEEE Wireless Communications Letters*, vol. 9, no. 9, pp. 1538–1542, 2020.
- [14] Z. Chen, N. Guo, J. Shen, R. Xiao, and P. Dong, "A hierarchical energy management strategy for power-split plug-in hybrid electric vehicles considering velocity prediction," *IEEE Access*, vol. 6, no. 2, pp. 33261–33274, 2018.
- [15] Z. Z. Le, D. T. Qin, L. L. Hou et al., "An adaptive equivalent consumption minimization strategy for plug-in hybrid electric vehicles based on traffic information," *Energy*, vol. 190, 2020.
- [16] S. Zhang, R. Xiong, and F. Sun, "Model predictive control for power management in a plug-in hybrid electric vehicle with a hybrid energy storage system," *Applied Energy*, vol. 185, pp. 1654–1662, 2015.
- [17] Y. Huang, H. Wang, A. Khajepour, H. He, and J. Ji, "Model predictive control power management strategies for HEVs: a review," *Journal of Power Sources*, vol. 341, pp. 91–106, 2017.
- [18] J. Guo, H. He, and J. Peng, "A novel MPC-based adaptive energy management strategy in plug-in hybrid electric vehicles," *Energy*, vol. 175, pp. 378–392, 2019.
- [19] S. Zhang and R. Xiong, "Adaptive energy management of a plug-in hybrid electric vehicle based on driving pattern recognition and dynamic programming," *Applied Energy*, vol. 155, pp. 68–78, 2015.
- [20] Z. Fu, L. Zhu, F. Tao, P. Si, and L. Sun, "Optimization based energy management strategy for fuel cell/battery/ultracapacitor hybrid vehicle considering fuel economy and fuel cell lifespan," *International Journal of Hydrogen Energy*, vol. 45, no. 15, pp. 8875–8886, 2020.
- [21] A. Rezaei, J. B. Burl, B. Zhou, and M. Rezaei, "A new real-time optimal energy management strategy for parallel hybrid electric vehicles," *IEEE Transactions on Control Systems Technology*, vol. 27, no. 2, pp. 830–837, 2019.
- [22] W. Zhang, J. Li, L. Xu, and M. Ouyang, "Optimization for a fuel cell/battery/capacity tram with equivalent consumption minimization strategy," *Energy Conversion and Management*, vol. 134, pp. 59–69, 2017.
- [23] Z. Wang and X. Jiao, "Hierarchical model predictive control for hydraulic hybrid powertrain of a construction vehicle," *Applied Sciences*, vol. 10, no. 3, p. 745, 2020.
- [24] C. Wang, R. Xiong, H. He, Y. Zhang, and W. Shen, "Comparison of decomposition levels for wavelet transform based energy management in a plug-in hybrid electric vehicle," *Journal of Cleaner Production*, vol. 210, pp. 1085–1097, 2019.
- [25] Q. Zhang and G. Li, "A predictive energy management system for hybrid energy storage systems in electric vehicles," *Electrical Engineering*, vol. 101, no. 3, pp. 759–770, 2019.

## Research Article

# On Enhancing TCP to Deal with High Latency and Transmission Errors in Geostationary Satellite Network for 5G-IoT

Liang Zong <sup>1</sup>, Yong Bai,<sup>2</sup> Chenglin Zhao,<sup>1</sup> Gaofeng Luo,<sup>1</sup> Zeyu Zhang,<sup>3</sup>  
and Huawei Ma <sup>4,5</sup>

<sup>1</sup>College of Information Engineering, Shaoyang University, Shaoyang 422000, Hunan, China

<sup>2</sup>School of Information and Communication Engineering, Hainan University, Haikou 570228, Hainan, China

<sup>3</sup>School of Applied Sciences, Macao Polytechnic Institute, Macau 999078, China

<sup>4</sup>Institute of Data Science, City University of Macau, Macau 999078, China

<sup>5</sup>School of Information Technology, Beijing Institute of Technology, Beijing 519088, China

Correspondence should be addressed to Huawei Ma; [mkmhw@bitzh.edu.cn](mailto:mkmhw@bitzh.edu.cn)

Received 12 October 2020; Revised 6 November 2020; Accepted 26 November 2020; Published 9 December 2020

Academic Editor: Lingwei Xu

Copyright © 2020 Liang Zong et al. This is an open access article distributed under the Creative Commons Attribution License, which permits unrestricted use, distribution, and reproduction in any medium, provided the original work is properly cited.

The geostationary (GEO) satellite networks have two important influencing factors: high latency and transmission errors. Similarly, they will happen in the large-scale multihop network of the Internet of things (IoT), which will affect the application of 5G- (5th-generation mobile networks-) IoT. In this paper, we propose an enhanced TCP mechanism that increases the amount of data transferred in the slow start phase of TCP Hybla to mitigate the effect of long RTT and incorporates a refined mechanism of TCP Veno, which can distinguish packet loss between random and congestion. This scheme is evaluated and compared with NewReno, Hybla, and Veno by simulation, and the performance improvement of the proposed TCP scheme for GEO satellite network in the presence of random packet losses is demonstrated. At the same time, the enhanced TCP scheme can improve the transmission performance in the future 5G-IoT heterogeneous network with high delay and transmission .

## 1. Introduction

With the advent of the 5G era and the wide application of the IoT, satellite networks will play an increasingly important role as a cross-regional relay network [1]. The dominant transport layer protocol of Internet Transmission Control Protocol (TCP) provides reliable delivery of data streams with its intertwined flow control, congestion control, and error control functions. The original design of TCP protocol is used for terrestrial wired networks, and it has been proved to be very successful for supporting Internet data communications for decades. However, there are several factors that decrease the performance of the TCP over satellite networks [2–5]. Firstly, due to the ultralong distance of GEO satellite link, there will inevitably appear high delay phenomenon in data transmission. The high latency imposed by the long RTT (round-trip time) will delay the execution of TCP and affect its performance. For satellite links with long

RTTs, the bandwidth delay product (BDP) can be quite high, and TCP needs to keep the amount of packets “in flight” (i.e., sent but not yet acknowledged), which means that the TCP must be able to handle larger data in a single transfer window. Secondly, transmission errors can exist in satellite links due to some harmful effects (e.g., atmospheric conditions, jamming, and interference), and the resulting bit-error rates (BER) can be as low as  $10^{-7}$  on average and  $10^{-4}$  in the worst case, which are higher than typical terrestrial networks. In contrast with the packet loss caused by network congestion (due to router buffer overflow), the packet loss caused by transmission error is referred to as corruption loss, random loss, or error loss in the literature. Explicit congestion notification (ECN) [6] is a proposed addition to IP which allows routers to inform TCP senders about imminent congestion before the queue overflows. Other factors that may affect TCP performance include bandwidth asymmetry, variable RTTs, and intermittent connectivity.

With the above negative characteristics of satellite networks, improving TCP throughput over satellite links is a hot area of research [5]. The enhancements for TCP over satellite networks can be classified into three categories: lower-level approaches, end-to-end approaches, and performance-enhancing proxies (PEP). Two lower-level approaches are path maximum transmission unit (MTU) discovery and forward error correction (FEC). Path MTU discovery is conducted at the data link layer. In the end-to-end approach, only the sender and receiver are involved in flow control and congestion control. The MUT and FEC are employed in the TCP variants (Tahoe, Reno, and NewReno) [7, 8]. Several proposals show the enhanced performance to make the slow start less time-consuming, including using a large initial value of  $cwnd$  [9, 10] and turning off the mechanism of delayed ACKs. Another TCP enhancement is employing selective acknowledgments (SACKs) [11].

Since the geostationary (GEO) satellite networks have two important influencing factors, high latency and transmission errors, it is essential to focus on the satellite network with long RTT and high BER. In recent years, some algorithms have been proposed to solve the congestion control problem in satellite networks, such as TCP Hybla [12, 13], Vegas [14], Veno [15], and Westwood [16]. Aided by the normalized RTT, the update rules of  $cwnd$  in the actual congestion control algorithms are replaced to achieve the same transmission rate as the reference connection even over longer RTT connections.

The PEP approaches require some changes in the network, mainly on intermediate gateways. TCP connections may be split in the total network and different transport protocols can be employed on the split connections. TCP-Spoofing and TCP-Splitting are two such PEP solutions [17, 18]. In addition, Dubois et al. proposed some architecture elements for PEPs mechanisms considering mobility scenarios for satellite networks [19]. Pirovano and Garcia summarized and analyzed the common solutions of TCP over satellite and evaluated the scheme of splitting TCP connections [20]. Although promising, the PEP approaches intrinsically infringe the end-to-end semantics of TCP, which presents several disadvantages on deployment, security, and privacy issues.

In this paper, we present a scheme for the GEO satellite network that can distinguish packet loss between random corruption and congestion loss. Our proposal combines the benefits of Hybla (for dealing with long RTT) and Veno (for dealing with random errors). In the scheme, the new rules of  $cwnd$  of TCP Hybla are still used in the slow start and congestion avoidance phases to mitigate the effect of long RTT.

The satellite communication network has been an important part of the 5G-IoTs and Internet infrastructure. Whether it is the satellite-based NB-IOT (Narrow Band Internet of Things) network or the ground-based 5G-IoT network, both realize the interconnection of everything and expand the scope of 5G-IoT connection by expanding the connection mode of the Internet of things. This enables 5G-IoT communication technology to cover all scenarios, especially in cross-regional situations. Therefore, improving

the transmission performance of the satellite network is essential to improve the cross-regional 5G-IoT performance.

Section 2 of the paper gives an overview of related TCP variants. In Section 3, our proposed enhanced TCP mechanisms are presented. The performance evaluation of our proposal by simulation is conducted and discussed in Section 4. Finally, conclusions are drawn in Section 5.

## 2. Overview of Related TCP Variants

### 2.1. TCP Tahoe and NewReno

**2.1.1. TCP Tahoe.** The implementation of TCP Tahoe [7] for congestion control is divided into three steps: slow start, congestion avoidance, and loss recovery algorithm. The sender performs Additive Increase of the congestion window ( $cwnd$ ) in the initial phase of TCP connection. In the first slow start (SS) phase,  $cwnd$  increases from one or two initial values of the maximum segment size (MSS).

The increase of  $cwnd$  is exponential in the SS phase, and TCP slows down the increase of  $cwnd$  in the CA phase. TCP assumes that congestion exists when it detects a packet loss. The loss of packets can be detected via the timeout of the retransmission timeout (RTO) timer. Furthermore, Tahoe incorporates a so-called fast retransmit mechanism, in which the sender infers that a packet has been lost if three or more duplicate ACKs (DU-PACKs) are received successively. When the event of packet loss has been decided, the sender performs Multiplicative Decrease of  $cwnd$ :  $cwnd$  is reset to one, and  $ssthresh$  is set to half the current size of the congestion window. Then, TCP enters the SS phase. In summary, the update rules of  $cwnd$  and  $ssthresh$  of Tahoe are given as follows:

- (1) New Ack received:
  - if ( $cwnd < ssthresh$ )//SS phase
    - set  $cwnd = cwnd + 1$ ;
  - else//CA phase
    - set  $cwnd = cwnd + 1/cwnd$ ;
- (2) Packet loss detected (RTO timeout or three DUPACKs received):
  - set  $ssthresh = cwnd/2$ ;  $cwnd = 1$ ;
  - enter SS phase.

**2.1.2. TCP NewReno.** In TCP Reno [7], DUPACKs indicate that the data is still transmitting. If three DUPACKs are received, Reno is half the  $cwnd$  (instead of setting it to 1 MSS like Tahoe), set  $ssthresh$  to the new  $cwnd$ , and enter a phase called fast recovery. It avoids slow transmission of retransmitted data. In the fast recovery phase, TCP Reno retransmits the lost packet and waits for the information of the ACK before entering the congestion avoidance. In summary, the update rules of  $cwnd$  and  $ssthresh$  during Reno's fast recovery after three DUPACKs received are given as follows:

- After three DUPACKs were received:
  - set  $ssthresh = cwnd/2$ ;

```

    cwnd = ssthresh + 3;
    enter CA phase;
    cwnd = cwnd + 1 for each additional DUPACK.

```

If multiple packets are lost, the sender will receive the data acknowledgement from the receiver for retransmission (the fast retransmission algorithm has been entered at this time). In partial acknowledgement, TCP will cause the sender to exit and recover quickly. At this time, the sender must wait for the timeout. This directly leads to transmission performance degradation. TCP NewReno [8] handles this situation well and avoids going to the slow start.

**2.2. TCP Hybla.** TCP Hybla [12, 13] aims to eliminate the impact of long RTT caused by high delay ground line or satellite wireless link. It is modified by dynamic analysis of congestion window to reduce the performance dependence on RTT. Firstly, the normalized round-trip time  $\rho$  is defined and the round-trip time of the reference connection is  $RTT_0$ .

$$\rho = \frac{RTT}{RTT_0}. \quad (1)$$

The normalized round-trip time is helpful to maintain the high performance of TCP in the case of long delay. TCP Hybla's update window is as follows:

$$W_{i+1} = \begin{cases} W_i + 2^\rho - 1, & \text{SS phase,} \\ W_i + \frac{\rho^2}{W_i}, & \text{CA phase,} \end{cases} \quad (2)$$

where  $W_i$  is the update of the congestion window when the sender of TCP connection receives the  $i$ th ack. TCP Hybla also adopts some measures to improve transmission performance, such as forcing SACK strategy, using timestamp [21], using hoes channel bandwidth estimation [22, 23], and implementing packet spacing technology [24]. In theoretical simulation and practical tests, TCP Hybla has been greatly improved compared with the traditional TCP.

**2.3. TCP Veno.** TCP Veno [15] is an improved scheme of traditional TCP for solving the problem of high bit error rate in wireless network environment. It uses a mechanism similar to Vegas [14]. TCP Veno judges the state of the network by calculating the backlog of datagrams in the network. If the size of the backlog datagram is  $N$ , then

$$N = \text{Actual} \times (\text{RTT} - \text{BaseRTT}). \quad (3)$$

In practical application,  $\text{actual} = \text{cwnd}/\text{RTT}$ ,  $\text{expected} = \text{cwnd}/\text{BaseRTT}$ , and  $\text{cwnd}$  is the size of the congestion window. Thus,  $N$  is also as follows:

$$N = (\text{Expected} - \text{Actual}) \times \text{BaseRTT}. \quad (4)$$

TCP Veno takes the size of  $N$  as the basis to judge whether the network is congested or not and sets a threshold value  $\beta$ . When  $N$  exceeds  $\beta$ , it indicates that the data packets in the link are seriously overstocked, and the connection is in

the congestion state. If packet loss occurs at this time, the control mechanism similar to Reno is adopted; when  $N$  is less than  $\beta$ , TCP Veno sets a threshold value of  $\beta$  even if the sender detects the packet loss, the connection is normal, the packet loss is determined to be caused by other reasons, and a congestion control algorithm different from Reno is adopted.

TCP Veno also uses two stages to achieve high performance for congestion control. In the congestion avoidance phase, when the packet loss is not caused by congestion,  $\text{cwnd}$  is increased by 1 for each new acknowledgement. When the packet loss is detected to be caused by congestion,  $\text{cwnd}$  is increased by 1 for every two new acknowledgments. In fast retransmission and fast recovery, when receiving 3 or more repeated acknowledgments, if  $N < \beta$ , it is considered that the network is not congested enough, the packet loss is determined as immediate packet loss, the congestion threshold is set to  $4 * \text{cwnd}/5$ ,  $\text{cwnd} = \text{ssthresh} + 3$ , and the lost packets are retransmitted; if  $N > \beta$ , the network is considered to be congested, the congestion threshold is set to  $\text{cwnd}/2$ , and  $\text{cwnd} = \text{ssthresh} + 3$  is set to retransmit the lost packets.

### 3. Proposal of Enhanced TCP Mechanisms

According to the TCP performance test of Hybla and Veno, the former can deal with the low efficiency caused by long delay, while the latter can deal with the problem of high bit error rate in wireless communication. To make full use of their advantages on processing TCP scheme, this paper proposes an enhanced TCP scheme to adapt to the problems of long RTT and high bit error rate in satellite networks.

**3.1. Congestion Window in the Slow Start.** In the TCP Hybla, we first modify the value of  $RTT_0$ . The original  $RTT_0$  value is set to 25 ms. Considering that the value of round-trip delay in the satellite network is relatively large, generally the delay is 550 ms in GEO satellite network. For the congestion window in TCP Hybla, this will make the value of congestion window in the slow start phase become too large, which will affect its performance. Therefore, the original value of  $RTT_0$  can be appropriately increased. The references considered set the value of  $RTT_0$  to 70 ms [25, 26], and the value is set to 75 ms in the enhanced scheme. This mainly considers that the transmission control protocol will bring certain delays when dealing with real congestion. After the update  $RTT_0$  is reset, the original update scheme is still maintained for the congestion window update.

Under the above congestion window update rules, the enhanced scheme refines the window update. In the traditional TCP, the size of the slow start congestion window needs to be compared with the threshold value. In the proposed scheme, the different congestion windows are set according to the comparison of congestion window and threshold as follows:

```

    if (cwnd < ssthresh)//SS phase
    {

```

```

    if (cwnd ≤ ssthresh/4) && (flightsize < rwnd/4)//sub-
phase 1
        set cwnd = 2 * Wi + 1
    if (ssthresh/4 < cwnd < 3 * ssthresh/4) && (rwnd/4
flightsize < 3 * rwnd/4)//su-phase 2
        set cwnd = W + 1
    if (cwnd ≤ 3 * ssthresh/4)/(flightsize > 3 * rwnd/4)//
sub-phase 3
        set cwnd = W + 1/2
}

```

The above three subphases are divided according to four factors:  $cwnd$ ,  $ssthresh$ ,  $rwnd$  (receiver advertisement window), and  $flightsize$  (the total number of unacknowledged bytes in the network). From the first subphase, it can be seen that the value of congestion window is a relatively small value, while the values of  $rwnd$  and  $flightsize$  indicate that the amount of data transmitted in the network connection is at a low value. At this time, the amount of data transmission can be increased and the utilization efficiency of the link can be improved.

In subphase 2, with the update of congestion window, its value will gradually increase. When the congestion window is in the middle of the slow start threshold, the state of the receiving data in the long delay link cannot be determined. Therefore, the value of  $flightsize$  is added to judge the state of the received data. If the value of  $flightsize$  is in the middle of  $rwnd$ , it indicates that the network state may be in a relatively stable state. The size of the congestion window keeps increasing to the TCP Hybla settings.

In the last subphase, the value of congestion window is close to the threshold size of the slow start, or the value of the  $flightsize$  is close to the value of  $rwnd$ . The enhanced scheme judges that there may be a lot of backlogs in the network. To avoid data loss caused by data backlog, the added value of congestion window can be appropriately reduced.

In the slow start phase of the proposed scheme, we fully consider the influence of different variables ( $cwnd$ ,  $flightsize$ ,  $ssthresh$ , and  $rwnd$ ) on the congestion window. The value of congestion window is refined to better adapt to the different states.

**3.2. Congestion Window in the Fast Recovery.** Traditional TCP considers the data loss caused by timeout as congestion in the network, which is correct for the network with the stable wired links. For the satellite network of the wireless links, we must distinguish the real cause of data loss: the loss caused by the congestion or the random loss caused by the wireless link. The difference of data loss in TCP Veno is not suitable for the satellite network.

In the enhanced TCP scheme, the congestion window is adopted as follows:

```

if (N < β1)//random loss is most likely to have occurred
    set ssthresh = 4 * cwnd/5;
else if (β1 ≤ N < β2)//not certain which kind of loss
occurred

```

```

    set ssthresh = 3 * cwnd/5;
else set ssthresh = 2 * cwnd/5;//congestion loss is most
likely to have occurred

```

In the above scheme,  $\beta_1$  and  $\beta_2$  are set to 3 and 6, respectively. Considering that the data loss of satellite network is still caused by congestion loss and random loss, the enhanced TCP scheme refines the value of congestion window, and the size of  $N$  is an important basis for network congestion judgment. Different values of  $N$  represent the network congestion status, and the smaller  $N$  value indicates that the network congestion situation is relatively slight and the value of the congestion window can take a larger value. On the contrary, the backlog value of the network is high and congestion may be serious. At this time, the value of congestion window is smaller. In the fast recovery phase, different size of the congestion window value is given for different congestion conditions, which is conducive to adjust the amount of data transmitted by TCP in time and make full use of the link of satellite network.

## 4. Simulation Results and Discussions

The enhanced TCP scheme compares the performance of various TCPs through the simulation. The simulation topology is shown in Figure 1. The server is connected with the client through the ground gateway and satellite network. The simulation parameters are shown in Table 1.

**4.1. Performance in the Presence of Random Losses.** In the first simulation scenario, the buffer size of the gateway is set large enough to prevent congestion loss during file downloading. The throughput and response time are two important indexes to evaluate network performance. The response time is the time from sending a request to completing the response. Throughput is the ability to process tasks per unit time. Its unit is usually bit/sec or MB/sec. It takes system resources as the object. Therefore, the performance of the system directly affects the (theoretical) limit value of throughput. Generally, the shorter the average response time is, the greater the system throughput is. The longer the average response time is, the smaller the system throughput is. When the BERs change from  $10^{-9}$  to  $10^{-5}$ , Figure 2 shows the response time of four TCPs (TCP NewReno, Veno, Hybla, and proposed scheme). The response time increased with the increase of BER. In the low BER range, the performances of the four TCP schemes are similar. When BER increases, the response time increases sharply, and the proposed scheme is clearly better than the other three TCP schemes.

The wireless link of high-altitude satellite communication is easy to be interfered, such as ground interference, space interference, natural interference, and man-made interference, especially in the open satellite communication system, and the transparent transponder is more vulnerable to malicious interference. When BER is  $10^{-5}$ , the response times of our proposed scheme and Hybla are significantly lower than those of NewReno and Veno, and the response time of our proposed scheme is slightly lower than that of Hybla. Hence, the response time of our proposed scheme is



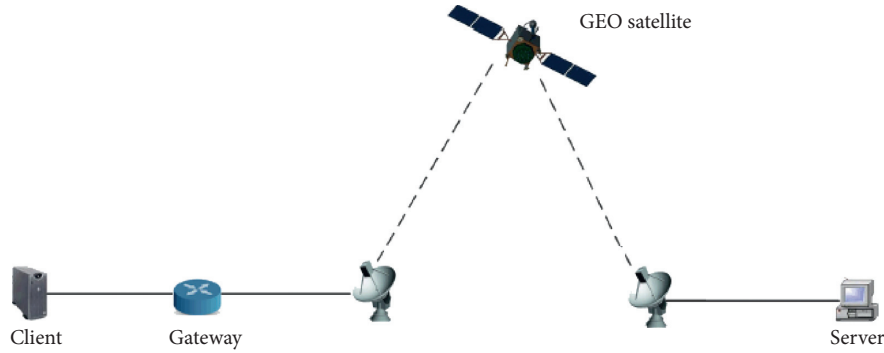


FIGURE 1: Network model.

TABLE 1: Simulation parameters.

Parameters	Value
Link rate of the server gateway	10 Mb/s
Uplink data rate	256 kb/s
Downlink data rate	2048 kb/s
One-way propagation delay	250 ms

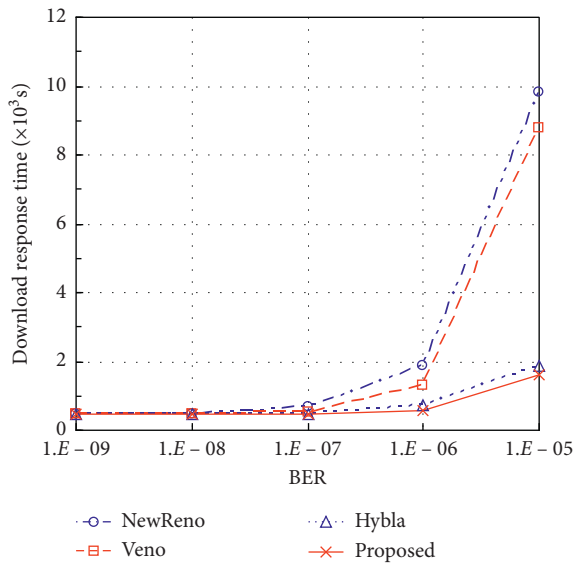


FIGURE 2: Response time for only random loss.

the lowest among the four TCP variants when there are random losses in the network. Figure 3 shows the satellite downlink throughput of four TCP variants versus BERs from  $10^{-9}$  to  $10^{-5}$ . It can be observed that the downlink throughput of the satellite network decreases with the increase of BER. When the BER changes from  $10^{-9}$  to  $10^{-7}$ , our proposed scheme exhibits comparable throughput to Hybla. The throughput rapidly decreases when the BER changes from  $10^{-7}$  to  $10^{-5}$ . With high BERs ( $10^{-7}$  to  $10^{-5}$ ), the throughput of our proposed scheme is slightly higher than that of Hybla and greatly higher than that of NewReno and Veno. From the simulation results, our proposed scheme can improve the throughput of GEO satellite links in the high BER range ( $10^{-6}$  to  $10^{-5}$ ).

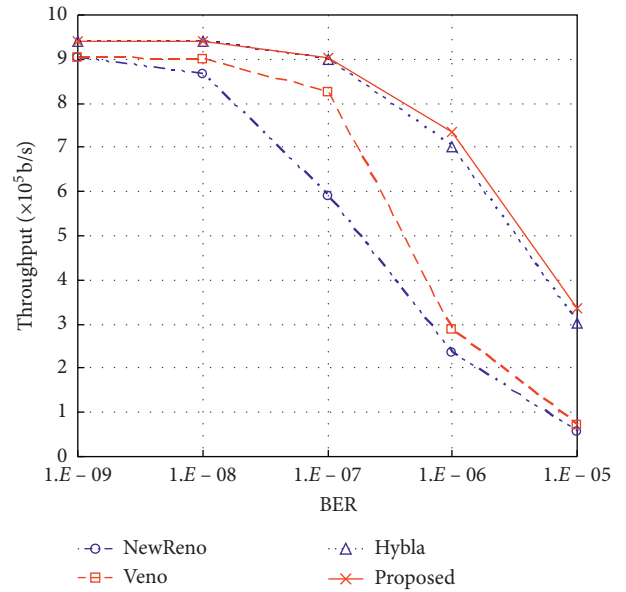


FIGURE 3: Throughput in the presence of random losses.

**4.2. Performance in the Presence of Both Random and Congestion Losses.** In the second simulation scenario, the buffer size of the gateway is set smaller (37.5 k bytes) such that congestion loss can happen during file downloading. When the BERs change from  $10^{-9}$  to  $10^{-5}$ , Figure 4 shows the response time of four TCPs (TCP NewReno, Veno, Hybla, and proposed scheme). Similarly, the response time increases with the increase of BER. In the low BER range, the performances of the four TCP schemes are also similar. When BER increases, the proposed scheme shows some advantages over the other three TCP schemes.

The response time of Veno is lower than that of NewReno if the BER is  $10^{-5}$ . The time of Hybla is the longest, and the response time achieved by our proposed scheme is shortest among the four TCPs. At higher BERs, the large packet losses are mainly due to the random losses. It turns out that Hybla cannot effectively reduce the response time for both random and congestion losses. On the other hand, our proposed scheme can effectively improve TCP performance in the presence of both random and congestion

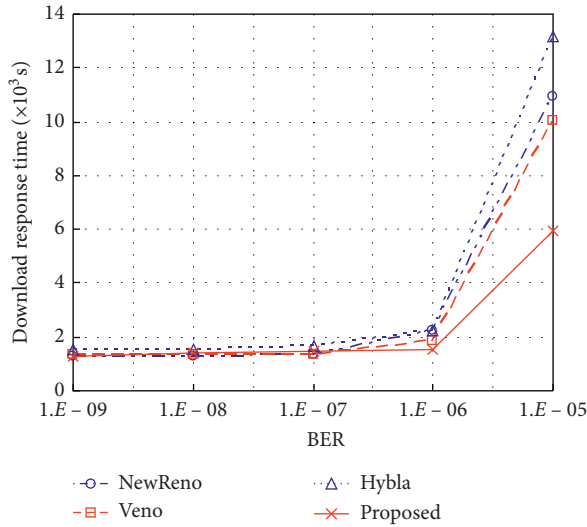


FIGURE 4: Response time for both random and congestion losses.

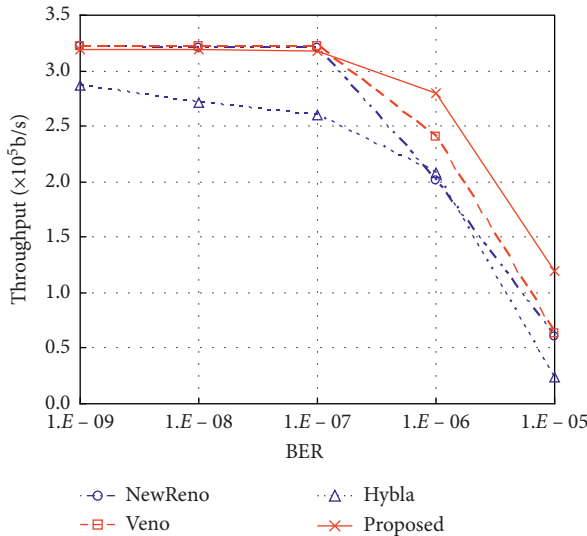


FIGURE 5: Throughput for both random and congestion losses.

losses. Figure 5 shows the satellite downlink throughput of the four TCPs versus BERs from  $10^{-9}$  to  $10^{-5}$ . It can be observed that the downlink throughput of the satellite network decreases with the increase of BER. When the BER changes from  $10^{-9}$  to  $10^{-5}$ , the throughput of Hybla is lower than that of the other three TCP variants. With higher BERs, the satellite link throughput of our proposed scheme exhibits the best performance among the four TCP variants. The above simulation results demonstrate that our proposed scheme can achieve smaller downloading time and higher throughput in the presence of both random and congestion losses. It inherently demonstrates that our proposed scheme updates the congestion window in more appropriate ways than NewReno, Hybla, and Veno. In the presence of both random and condensation losses when the BER is  $10^{-5}$ , the throughput of the proposed scheme is 1.96 times, 1.88 times, and 5.09 times higher than TCP Reno, Veno, and Hybla, respectively.

## 5. Conclusion

Although there have been many studies for improving TCP performance on GEO satellite networks, there are few studies on TCP solutions that can handle both long RTT and high BER. This paper focuses on these two aspects, combining the advantages of TCP Hybla in dealing with long RTT and TCP Veno's good performance in dealing with high BER in wireless networks to deal with satellite networks and refining the congestion window.

In our proposed scheme, the congestion window update equations of Hybla are still employed in the slow start and congestion avoidance phases to mitigate the effect of long RTT. Our proposed scheme enhances Hybla by modifying the setting of  $RTT_0$  (RTT of the reference connection) and allowing the congestion window to increase adaptively in the slow start phase corresponding to different networking conditions. Furthermore, our proposed scheme refines Veno's algorithm in fast recovery with multilevel differentiation for distinguishing different data losses. In the simulation test, the enhanced TCP scheme proposed in this paper can cope with random data loss and congestion data loss better than the other three schemes. The networking scenarios in the presence of only random packet loss and in the presence of both random and congestion losses are considered. The simulation results demonstrate that our proposed scheme exhibits better performance in the two networking scenarios compared with the other three TCP variants. The disadvantage of the proposed scheme is that the performance improvement is not very good at low BER, and there is no obvious advantage in throughput and response time. Finally, it needs to point out that our proposed scheme is an end-to-end approach for improving TCP performance over GEO satellite networks, where only the mechanisms of the TCP sender need to be modified, and the end-to-end semantics of TCP can be maintained, which has great value for large-scale practical applications, especially for the communication service providers and users who need to save communication costs [27].

## Data Availability

The data used to support the findings of this study are available from the corresponding author upon request.

## Conflicts of Interest

The authors declare that there are no conflicts of interest regarding the publication of this paper.

## Acknowledgments

This work was supported by the Hunan Provincial Natural Science Foundation (Grant no. 2020JJ40509), the Scientific Research Fund of Hunan Provincial Education Department (Grants nos. 19B512, 19A446, and 18B420), and the National Natural Science Foundation of China and Macau Science and Technology Development Joint Fund (Grants nos. 61961160706 and 0066/2019/AFJ).

## References

- [1] W. Zhang, G. Yang, F. Jiang et al., "Licklider transmission protocol for GEO-relayed space internetworking," *Wireless Networks*, vol. 25, no. 7, pp. 3747–3757, 2019.
- [2] J. Liu, Z. Han, and W. Li, "Performance analysis of TCP new Reno over satellite DVB-RCS2 random access links," *IEEE Transactions on Wireless Communications*, vol. 19, no. 1, pp. 435–446, 2019.
- [3] T. R. Henderson and R. H. Katz, "Transport protocols for Internet-compatible satellite networks," *IEEE Journal on Selected Areas in Communications*, vol. 17, no. 2, pp. 326–344, 1999.
- [4] M. Allman, D. Glover, and L. Sanchez, "Enhancing TCP over satellite links using standard mechanisms," RFC 2488, 1999.
- [5] M. Allman, S. Dawkins, D. Glover et al., "Ongoing TCP research related to satellites," RFC 2760, 2000.
- [6] K. Ramakrishnan and S. Floyd, "A proposal to add explicit congestion notification (ECN) to IP," IETF RFC 2481, 1999.
- [7] M. Allman and W. Stevens, "TCP congestion control," IETF RFC 2581, 1999.
- [8] S. Floyd and T. Henderson, "The NewReno Modification to TCP's fast recovery algorithm," IETF RFC 2582, 1999.
- [9] S. Floyd, T. Henderson, and C. Partridge, "Increasing TCP's initial window," IETF RFC 2414, 1998.
- [10] I. Biswas, "An investigation on TCP large initial window," *International Journal of Satellite Communications and Networking*, vol. 31, no. 3, pp. 111–121, 2013.
- [11] M. Mathis, J. Mahdavi, S. Floyd, and A. Romanow, "TCP selective acknowledgment options," IETF RFC 2018, 1996.
- [12] C. Caini and R. Firrincieli, "TCP Hybla: a TCP enhancement for heterogeneous networks," *International Journal of Satellite Communications and Networking*, vol. 22, no. 5, pp. 547–566, 2004.
- [13] C. Caini and R. Firrincieli, "End-to-end TCP enhancements performance on satellite links," in *Proceedings of the 11th IEEE Symposium on Computers and Communications*, pp. 1031–1036, Cagliari, Italy, June 2006.
- [14] L. S. Brakmo and L. L. Peterson, "TCP Vegas: end to end congestion avoidance on a global internet," *IEEE Journal on Selected Areas in Communications*, vol. 13, no. 8, pp. 1465–1480, 1995.
- [15] P. C. Fu and S. C. Liew, "TCP Veno: TCP enhancement for transmission over wireless access networks," *IEEE Journal on Selected Areas in Communications*, vol. 21, no. 2, pp. 216–228, 2003.
- [16] C. Casetti, M. Gerla, S. Mascolo, M. Y. Sanadidi, and R. Wang, "TCP Westwood: endto-end congestion control for wired/wireless networks," *Wireless Networks*, vol. 8, no. 5, pp. 467–479, 2002.
- [17] M. Luglio, M. Y. Sanadidi, M. Gerla, and J. Stepanek, "On-board satellite "split TCP" proxy," *IEEE Journal on Selected Areas in Communications*, vol. 22, no. 2, pp. 362–370, 2004.
- [18] E. Rendon-Morales, J. Mata-Diaz, J. Alins, J. L. Munoz, and O. Esparza, "Cross-layer architecture for TCP splitting in the return channel over satellite networks," in *Proceedings of the IEEE 6th International Symposium on Wireless Communication Systems*, pp. 225–229, Tuscany, Italy, 2009.
- [19] E. Dubois, J. Fasson, C. Donny, and E. Chaput, "Enhancing TCP based communications in mobile satellite scenarios: TCP PEPs issues and solutions," in *Proceedings of the IEEE 5th Advanced Satellite Multimedia Systems Conference (Asma) and the 11th Signal Processing for Space Communications Workshop (SpSC)*, pp. 476–483, Cagliari, Italy, June 2010.
- [20] A. Pirovano and F. Garcia, "A new survey on improving TCP performances over geostationary satellite link," *Network & Communication Technologies*, vol. 2, no. 1, pp. 1–18, 2013.
- [21] V. Paxson and M. Allman, "Computing tcp's retransmission timer," IETF RFC 2988, 2000.
- [22] J. C. Hoe, "Improving the start-up behavior of a congestion control scheme for TCP," *ACM SIGCOMM Computer Communication Review*, vol. 26, no. 4, pp. 270–280, 1996.
- [23] L. Xu, H. Wang, and T. A. Gulliver, "Outage probability performance analysis and prediction for mobile IoV networks based on ICS-BP neural network," *IEEE Internet of Things Journal*, p. 1, 2020.
- [24] C. Caini and R. Firrincieli, "Packet spreading techniques to avoid bursty traffic in satellite TCP connections," in *Proceedings of the IEEE 59th Vehicular Technology Conference. VTC 2004-Spring (IEEE Cat. No.04CH37514)*, pp. 2906–2910, Ottawa, Canada, May 2004.
- [25] M. K. Park, M. S. Shin, D. G. Oh, B. C. Kim, and J. Y. Lee, "TCP Hybla+: Making TCP More Robust against Packet Loss in Satellite Networks," in *Proceedings of the International Conference on Computational Science and Its Applications ICCSA2011*, pp. 424–435, Santander, Spain, June 2011.
- [26] H. Wang, L. Xu, Z. Yan, and T. A. Gulliver, "Low complexity MIMO-FBMC sparse channel parameter estimation for industrial big data communications," *IEEE Transactions on Industrial Informatics*, p. 1, 2020.
- [27] J. Vankka, "Performance of satellite gateway over geostationary satellite links," in *Proceedings of the 2013 IEEE Military Communications Conference*, pp. 289–292, San Diego, CA, USA, November 2013.

## Research Article

# On the Detection of a Non-Cooperative Beam Signal Based on Wireless Sensor Networks

Guofeng Wei <sup>1</sup>, Bangning Zhang <sup>1</sup>, Guoru Ding <sup>1</sup>, Bing Zhao <sup>1</sup>, Kefeng Guo <sup>2</sup>,  
and Daoxing Guo <sup>1</sup>

<sup>1</sup>College of Communications Engineering, Army Engineering University, Nanjing 210007, China

<sup>2</sup>School of Space Information, Space Engineering University, Beijing 101407, China

Correspondence should be addressed to Daoxing Guo; xyzgfg@sina.com

Received 8 September 2020; Revised 16 September 2020; Accepted 28 September 2020; Published 19 October 2020

Academic Editor: Xingwang Li

Copyright © 2020 Guofeng Wei et al. This is an open access article distributed under the Creative Commons Attribution License, which permits unrestricted use, distribution, and reproduction in any medium, provided the original work is properly cited.

With the extensive research of multiantenna technology, beamforming (BF) will play an important role in the future communication systems due to its high transmission gain and satisfying directivity. If we can detect the non-cooperative beams, it is of great significance in counter reconnaissance, beam tracking, and spectrum sensing of multiantenna transmitters. This paper investigates the wireless sensor networks (WSNs), which is used to detect the unknown non-cooperative beam signal. In order to perceive the presence of beam signals without the prior information, we first derive the detection probability based on the sensors' received signal strength (RSS). Then, based on the strong directivity of the beam signal, we propose an improved “ $k$  rank” fusion algorithm by jointly exploiting the energy detection (ED) information and location information of the sensors. Finally, the beam detection performance of different fusion algorithms is compared in simulation, and we find that our proposed algorithm showed better detection probability and lower error probability. The simulation results verify the correctness and effectiveness of the proposed algorithm.

## 1. Introduction

**1.1. Background and Motivation.** The sixth generation (6G) mobile communication system puts forward some higher requirements for the system capacity, transmission rate, and security [1–4]. Beamforming technology uses spatial gain to meet the needs of increasing system capacity which has become a major trend, focusing limited energy on a specific direction for transmission [5, 6]. It has been widely studied in recent years for different technologies: millimeter wave (mmWave) [6–8], massive multiple-input multiple-output (MIMO) [9], nonorthogonal multiple access (NOMA) [10, 11], satellite communication [12], vehicular communication [13], device-to-device networks (D2D) [14, 15], etc.

Millimeter wave communication is considered a promising 5G network technology. The frequency of 30–300 GHz is a new area of cellular communication, which provides a larger bandwidth and gains further benefits through beamforming and spatial multiplexing of

multielement antenna arrays [7]. Massive MIMO is a new and technically challenging system, and its key feature is to communicate a large number of base station antennas with users through beamforming technology [9]. Through using QAM-64 signals, the massive MIMO millimeter wave transceiver based on beamforming can achieve a stable 5.3 Gb/s throughput for a single user in a fast-moving environment [16]. In vehicular communication, beamforming technology is combined with millimeter wave to support the massive automotive sensing [13]. In radar applications, large radio arrays are used for beamforming to obtain enhanced radar performance [17]. The authors also investigated the application of these arrays from an energy and cost-effective perspective to promote new applications [9, 18]. Besides the above applications, beamforming is often used in the detection, directional communication [19–21], smart surface antenna [22], and covert communication [23].

However, the focus of most research is to combine the beamforming with millimeter wave, massive MIMO, and

other technologies to increase transmission capacity and reduce interference. Motivated by this fact, if we can detect multiantenna beam signal by WSNs that will bring the following benefits, first, it can better serve the spectrum sensing of secondary users for multiantenna primary users in cognitive radio [24]. Then, by detecting unknown beam signals, we can protect important targets from being discovered. Also, detecting the beam signal and obtaining as much beam information as possible is very significant for multiantenna beam tracking [15, 25].

*1.2. Related Work.* Wireless sensor network uses a large number of miniature sensor computing nodes to conduct real-time monitoring collaboratively through a self-organizing network, perceiving and collecting information about various environments or detection signal [26]. In recent years, with the rapid development of wireless communication technology and electronic device technology, the development and wide application of low-cost, low-power, and multifunctional wireless sensors have become possible. WSNs have been used in battlefield monitoring, environmental perception, search and rescue [26, 27], etc.

Beamforming, also known as spatial filtering, is a signal processing technique that shows potentials to significantly raise user throughput, enhance spectral and energy efficiencies, and increase the capacity of mobile networks in the mmWave frequency bands with massive antenna arrays [6, 28]. Many scholars have conducted research and application of beamforming technology. For instance, Zhang [29] introduced the progress and advantages of beamforming technology. Xu et al. [30] proposed a beamforming scheme to enhance the wireless information transmission of terrestrial cellular networks and satellite networks. A fast beam alignment algorithm was investigated for mmWave communications in [31]. Liu [32] applied beamforming technology to cognitive radio cooperative spectrum detection which had better detection performance. The author studied the application of beamforming in the sharing of millimeter wave spectrum between satellites and high-level platform networks and how to better design beams under incomplete channel state information [12]. The author studied the resource allocation design in the cellular mass Internet of Things (IoT) based on NOMA and coordinated the originally harmful cochannel interference in mass access through spatial beamforming [10, 33]. Yu et al. [34] studied the impact analysis of directional antenna arrays on millimeter wave network coverage.

It can be seen from the above that multiantenna will be more used in future communications, and beamforming technology will play an important role in future communications. However, these research results are all about how to improve the capacity and rate of communication through beamforming technology. At the same time, the authors considered the distributed detection problem, that is, the sensor transmits its local decision through a fully known wireless channel in [35]. The problem of distributed event detection under Byzantine attacks is considered in [36]. The theoretical performance analysis of detection fusion based

on conditional dependence and independent local decision-making is derived in [37]. The distributed detection of WSNs under multiple receiving antennas fading channels is studied in [38]. However, there is little research on how to perceive a beamforming signal. In accordance with the fact that non-cooperative beam signal has the characteristics that the sensors do not work without its beam coverage and lack the priori information. Unlike the previous research on detecting omnidirectional signals [39–41], it is difficult to detect the narrow and directional beam by the single sensor with the previous detection method, so we propose a non-cooperative beam signal detection scheme based on WSNs.

*1.3. Contributions.* The main contributions of this paper are summarized as follows:

- (i) We construct an unknown non-cooperative beam signal perception scenario which detects the beam signals lacking the prior knowledge by deploying a large number of sensors to form a network.
- (ii) Based on the general ED framework, we derive the detection probability expression under the given false alarm probability and propose a “ $k$  rank” fusion algorithm by jointly exploiting the ED information and location information of the sensors.
- (iii) To verify the detection performance of the proposed algorithm in the beam scene, we provide some simulation results to demonstrate the effectiveness of the algorithm. In addition, we discuss the impact of different parameters on the detection performance.

The rest of this paper is organized as follows. In Section 2, the system model is presented and energy detection probability is derived based on the received signal strength of the sensor. In Section 3, we have a brief introduction to the fusion rules. We propose an improved “ $k$  rank” algorithm based on distance selection in Section 4. Simulation results and analysis are provided in Section 5. Finally, we conclude the paper in Section 6.

*1.4. Notations.* For the sake of convenience, we use lower-case and upper-case bold letters represent vectors and matrices, respectively. The key notations used herein are summarized as in Table 1.

## 2. System Model

We consider a system model where WSNs are used to perceive the non-cooperative beam signal, as shown in Figure 1. Suppose an unknown multiantenna transmitter (equipped with  $m$  antennas) transmits a plane static beam signal through the beamforming technology. A wireless sensor network is composed of  $N$  uniformly distributed sensors where  $J$  sensors are within the coverage of the beam signal. The sensor is usually a miniature embedded system that has the ability to perceive physical environment data and process data, but its processing power, storage power,

TABLE 1: Notations throughout this paper.

Notation	Explanation
$P(\cdot)$	The probability
$P(\cdot \cdot)$	Conditional probability density function
$Q(\cdot)$	Generalized Marcum Q function
$\emptyset$	Empty set
$E\{\cdot\}$	Expectation operator
$\exp\{\cdot\}$	Exponential function
$\ \cdot\ $	Euclidean norm
$\mathbb{C}^{m \times n}$	Complex space of $m \times n$
$\mathcal{CN}(0, \sigma_v^2)$	Complex Gaussian distribution with mean 0 and variance $\sigma_v^2$

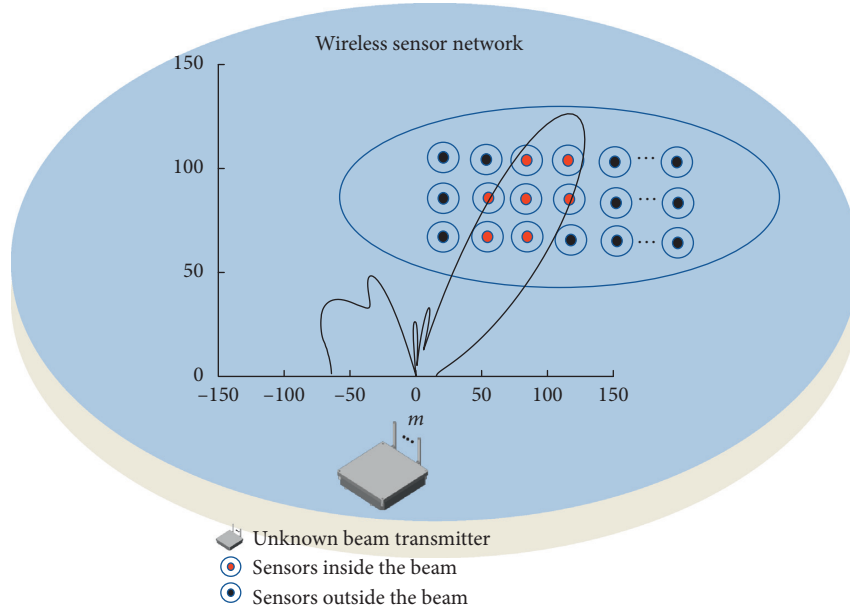


FIGURE 1: The detection system model of a non-cooperative beam signal based on WSNs.

and communication capabilities are relatively limited. We assume that the fusion center (FC) knows the position information of the sensors by exchanging information.

The received signal strength of  $i$ -th sensor can be characterized by the following beam signal propagation model:

$$p_i = P_{tx} g_i \left( \frac{4\pi d_i f}{c} \right)^{-\alpha_n}, \quad (1)$$

where  $g_i$  refers to the combined beamforming gain for the link between the  $i$ -th sensor and unknown multi-antenna transmitter,  $P_{tx}$  is the transmit power of unknown multi-antenna transmitter,  $\alpha_n \geq 2$  is power decay coefficient,  $c$  is the speed of light, and  $d_i$  is the distance between the  $i$ -th sensor and unknown multi-antenna transmitter.

According to the signal whether it is in the beam coverage or not, the received signal is

$$\begin{cases} y_{\text{inside}} = H_{\text{inside}} \mathbf{x} + v, \\ y_{\text{outside}} = H_{\text{outside}} \mathbf{x} + v, \end{cases} \quad (2)$$

where  $\mathbf{x} \in \mathbb{C}^{m \times 1}$  is the signal emitted by the radiation source and signal variance is  $\sigma_x^2$ ,  $H_{\text{inside}} \in \mathbb{C}^{m \times 1}$  and  $H_{\text{outside}} \in \mathbb{C}^{m \times 1}$  are the channel matrix of the beam source ( $m$  antennas) with the sensor in the beam and not in the beam, respectively; the beam signal  $\mathbf{x}$  is represented as

$$\mathbf{x} = \mathbf{w}u, \quad (3)$$

where  $\mathbf{w} \in \mathbb{C}^{m \times 1}$  is the beam excursion vector and satisfies  $\|\mathbf{w}\|^2 \leq P_{tx}$  and  $u$  is the coded signal.

A binary hypothetical model at  $i$ -th sensor is modeled as

$$y_i(n) = \begin{cases} v(n), & H_0, \\ Hx(n) + v(n), & H_1, \end{cases} \quad (4)$$

where  $n = 1, \dots, N_s$ ,  $N_s$  is the number of samples,  $H$  is the channel matrix, and assume that the transmitted signal passes through additive white Gaussian noise (AWGN) channels, so  $v(n) \in \mathcal{CN}(0, \sigma_v^2)$ .

For non-cooperative beam signals, the energy detection algorithm [42] can be conveniently detected without the prior information. It compares the energy value of the received signal at the sensor in a period with a preset threshold

to judge whether the target signal exists [43]. When the number of signal samples collected during each sampling period is large enough, according to the central limit theorem, the test statistics is approximately normal distribution. The signal energy value distribution of  $i$ -th sensor in sampling periods  $T$  is expressed as

$$Y_{i,T} = \begin{cases} \mathcal{N}\left(V_0, \frac{V_0^2}{N_s}\right), & H_0, \\ \mathcal{N}\left(p_{i,T} + V_0, \frac{(p_{i,T} + V_0)^2}{N_s}\right), & H_1, \end{cases} \quad (5)$$

where  $p_{i,T}$  is the signal strength received by the  $i$ -sensor, given by the formula (1), and  $V_0$  is the noise power.

Then, the detection probability  $P_{d,i}$  and the false alarm probability  $P_{f,i}$  can be expressed as

$$\begin{cases} P_{d,i} = P(Y_i \geq \gamma_i H_1) = Q\left(\frac{\gamma - (p_{i,T} + \sigma_v^2)}{\sqrt{(p_{i,T} + \sigma_v^2)^2 / N_s}}\right), \\ P_{f,i} = P(Y_i \geq \gamma_i H_0) = Q\left(\frac{\gamma - \sigma_0^2}{\sqrt{\sigma_0^4 / N_s}}\right), \end{cases} \quad (6)$$

where  $Q(x) = 1/\sqrt{2\pi} \int_x^\infty e^{-(y^2/2)} dy$  is the Generalized Marcum  $Q$  function.

Under the given constant false alarm probability  $P_{f,i}$ , the energy detection threshold  $\gamma$  can be obtained as

$$\gamma = \sigma_v^2 \left(1 + \sqrt{1/N_s} Q^{-1}(P_{f,i})\right). \quad (7)$$

So, the detection probability  $P_{d,i}$  can be expressed as

$$P_{d,i} = P(Y_i \geq \gamma_i H_1) = Q\left(\frac{\sqrt{1/N_s} Q^{-1}(P_{f,i}) - p_{i,T}}{\sqrt{(p_{i,T} + \sigma_v^2)^2 / N_s}}\right). \quad (8)$$

### 3. Fusion Rules of Wireless Sensor Networks

The fusion rules in wireless sensor networks is also called multisensor data fusion technology, which optimizes and merges the sensing data of multiple sensors to obtain more accurate and complete predictions or judgments than single sensor data. There are two main signal processing methods in wireless sensor networks.

The first is that all signals are transmitted to the central processor for processing. There must be no signal delay or signal delay tolerance during the transmission process. Because of the large amount of information to be processed, the bandwidth requirements are relatively high. The second signal processing method is distributed signal processing, that is, the preprocessing of the signal can be completed in the sensor, and only the decision result of the sensor needs to be submitted to the fusion center for fusion. In this way, it requires the least amount of data communication and its requirements for transmission bandwidth are also the

lowest. In addition, because the result of FC comes from the optimal synthesis of preliminary judgments of multiple nodes, it has little dependence on a single sensor and the processing cost of the FC is very low. The system has strong anti-interference ability and excellent flexibility in data processing.

Since the data result fusion is a fusion technology for specific decision-making problems, it is generally used to directly obtain the decision-making results of the current problem, so the performance of the fusion algorithm will directly affect the final detection performance. As shown in Figure 2, the sensor submits the quantified judgment result of energy detection to the fusion center and only cares about the signal whether exist, so what is presented here is a binary 0 or 1. The schematic of fusion center receiving perception results is shown as Figure 3.

Fusion rules can be divided into ‘‘AND’’ fusion, ‘‘OR’’ fusion, and ‘‘ $k$  rank’’ fusion.

‘‘AND’’ fusion: when the judgment result of all sensors is that the signal exists, the final judgment of the fusion center is that the signal exists. As long as one sensor determines that the signal does not exist, the final result of the fusion center is that the signal does not exist. The advantage of the cooperative sensing algorithm based on the ‘‘AND’’ fusion criterion is that the final false alarm probability is very low compared to single sensor perception, but the price is to reduce the detection probability.

‘‘OR’’ fusion: as long as a sensor judges that the signal exists, it can be considered that the signal exists. Only when all the sensors determine that the signal does not exist, the fusion center can finally determine that the signal does not exist. The cooperative sensing algorithm based on the ‘‘OR’’ fusion criterion has a higher detection probability than single-sensor sensing, because in this method it can be considered that the signal exists as long as there is a sensor to determine the existence of the primary user, and the judgment conditions are relatively loose. But its shortcomings are also obvious, that is, the probability of false alarms will be very high.

‘‘ $k$  rank’’ fusion: the fusion center setting a decision threshold  $k$ , if there are at least  $k$  sensors in the  $N$  sensors, the fusion center can determine the signal existence. Otherwise, the fusion center will determine that the signal does not exist. It can be seen that compared to the other two fusion rules, ‘‘ $k$  rank’’ fusion has a better application space.

### 4. Proposed ‘‘K Rank’’ Algorithm Based on Distance Selection

After the fusion center receives the information from the sensors, it will make a fusion decision according to some criteria. ‘‘ $k$  rank’’ fusion rule is a fusion decision based on the perception results sent by each sensor, that is, when at least  $k$  sensors of the  $N$  sensors detect the presence of the signal, the signal is judged to exist. According to the ‘‘ $k$  rank’’ fusion rule, the global detection probability  $P_d$  and global false alarm probability  $P_f$  of the final judgment result can be expressed as

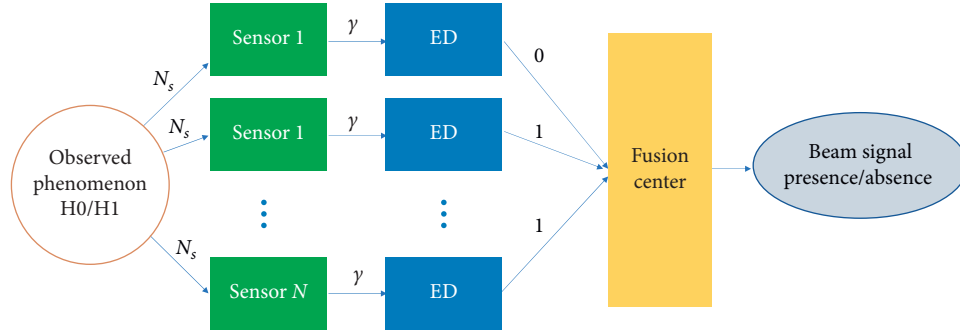


FIGURE 2: Fusion rules of wireless sensor networks.

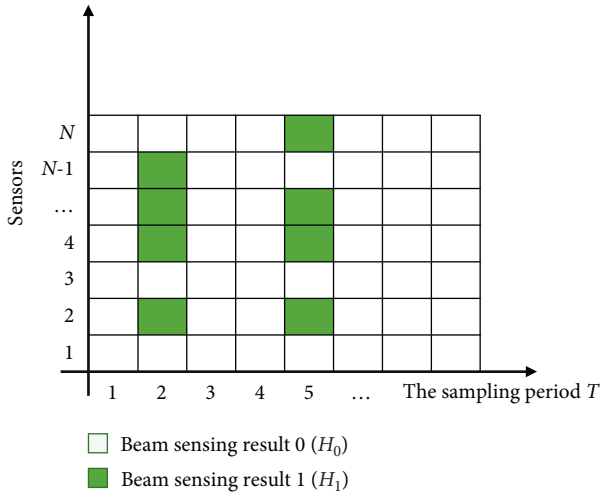


FIGURE 3: Schematic diagram of fusion center receiving perception results.

$$\begin{cases} P_f = \sum_{k=K}^N \left[ C_N^k \times P_{f,i}^k \times (1 - P_{f,i})^{N-k} \right] \\ P_d = \sum_{k=K}^N \left[ C_N^k \times P_{d,i}^k \times (1 - P_{d,i})^{N-k} \right]. \end{cases} \quad (9)$$

When  $k=1$ ,  $k=N$ , the “ $k$  rank” fusion rule is transformed into “OR” fusion rule and “AND” fusion rule. According to the research of M. Schwartz [44], the optimal  $k$  of  $N$  sensors is approximately  $k = 1.5\sqrt{N}$ . In addition, there is a half-voting algorithm  $k=N/2$  that is more commonly used.

In order to describe the detection performance of the sensor network better, we introduce the error probability to represent the perceived performance of the system. The error probability mainly consists of two parts: one is the probability which means there is a signal but the result is judged to be absent. The other is the probability which means there is no signal but the result is judged to be a signal. It is expressed specifically as

$$P_e = p(H_0) * P_d + p(H_1) * P_f. \quad (10)$$

According to the understanding of the “ $k$  rank” algorithm in beam signal perception scenario, we find that only sensors within and around the beam coverage contribute the most to the detection performance of WSNs, while sensors that are not within the beam coverage or far away from the beam sensing area have a limited contribution. If we directly apply the “ $k$  rank” fusion algorithm to make detection decisions based on all sensors ( $N$ ), it will definitely affect the detection performance. Therefore, aiming at the sensing characteristics of the beam signal, a “ $k$  rank” fusion algorithm based on distance selection is proposed in order to find the optimal  $N_{opt}$ .

We assume that the position information  $d_{i,j}$  of each sensor is known by exchanging information with the fusion center, and the distance between any two sensors ( $i$ -th sensor and  $j$ -th sensor) is

$$d_{i,j} = \sqrt{(d_i(x) - d_j(x))^2 + (d_i(y) - d_j(y))^2}. \quad (11)$$

We construct a neighbor node library of by finding the nearest neighbor node of  $i$ -th sensor;  $D_{near}$  is expressed as

$$D_{near}(i) = \{\text{sensors of } \min(d_{i,j})\} \quad (12)$$

We construct a sensing node library of the  $i$ -th sensor which greater than the detection threshold;  $D_{sensing}$  is expressed as

$$D_{sensing}(i) = \{\text{sensors of } P(Y_i \geq \gamma_i | H_1)\}. \quad (13)$$

Because the directionality of the beam signal is very obvious, in order to determine the sensors that detect the signal are concentrated in the beam signal, rather than scattered randomly distributed, we compare the smallest distance between sensors in the sensing node library  $D_{sensing}$  and the smallest distance in the sensor distance library  $D_{near}$ . The distance information should satisfy

$$d_{i,j} \text{ min of } D_{sensing} \leq d_{i \text{ min of } D_{near}}. \quad (14)$$

The main steps are summarized as follows: first, calculating the proximity point of each sensor to form the nearest library  $D_{near}$ . Second, finding the sensor with the perception result  $H_1$ , and putting the sensor with its neighbor library node together into the sensing library  $D_{sensing}$ . Finally, using



**Input:**  $P_{f,i}, P_{d,i}, N, J, \gamma_i$  and  $d_i(x, y)$ .  
**Initialize:**  $J = 0, D_{\text{sensing}} = \{\emptyset\}$ .  
 Calculate the proximity point of each sensor to form the nearest library  $D_{\text{near}}$  via formula (12).  
 Calculate the detection statistics of  $i$ -th sensor  $Y(i)$  via formula (5).  
 Energy detection: in order to find the sensor that detected the signal.  
**IF**  $Y(i) > \gamma_i$   
      $J = J + 1$   
**End**  
 Distance selection: to judge whether the sensors that perceive information are together.  
**IF**  $d_{ij \min} \text{ of } D_{\text{sensing}} < = d_{i \min} \text{ of } D_{\text{near}}$   
 Proposed the improved “ $k$  rank” fusion criterion algorithm.  
**For**  $i = 1, 2, \dots, J$  **do**  
     Update  $D_{\text{sensing}}$  via  $D_{\text{near}}$  of  $i$ -th sensor.  
**End For**  
 $N_{\text{opt}}$  = number of sensors in  $D_{\text{sensing}}$   
 Calculate the probability of  $P_d$  via formula (15).  
**Output:**  $N_{\text{opt}}, P_d$ .

ALGORITHM 1:  $k$  of  $N_{\text{opt}}$  fusion algorithm based on distance selection.

$N_{\text{opt}}$  that is the number of sensors in  $D_{\text{sensing}}$ , instead of the original  $N$  for “ $k$  rank” fusion. So the  $k$  of  $N_{\text{opt}}$  fusion is

$$\begin{cases} P_f = \sum_{k=K}^{N_{\text{opt}}} \left[ C_{N_{\text{opt}}}^k \times P_{f,i}^k \times (1 - P_{f,i})^{N_{\text{opt}}-k} \right], \\ P_d = \sum_{k=K}^{N_{\text{opt}}} \left[ C_{N_{\text{opt}}}^k \times P_{d,i}^k \times (1 - P_{d,i})^{N_{\text{opt}}-k} \right]. \end{cases} \quad (15)$$

The specific algorithm is shown in Algorithm 1.

## 5. Simulation Results

This section provides simulation results of the beam signal perception to evaluate the detection performance of the proposed algorithm. The simulation parameter [45] settings are shown in Table 2.

Figures 4 and 5 examine the beam pattern information of non-cooperative beam ( $0^\circ - 180^\circ$ ). Linear array ( $m = 8$  antennas) forms a beam signal pointing in  $45^\circ$  direction, beam excursion vector  $w = [0.593 + 0.805i, 0.282 - 0.959i, -0.934 + 0.357i, 0.850 + 0.527i, 0.850 - 0.527i, -0.934 - 0.357i, -0.734 + 0.679i, 0.985 + 0.173i]$ . Beamforming technology performs signal processing by weighting and combining the signals transmitted by the multiantenna array elements. By designing different weighting factors for the multichannel signals transmitted by multiple antennas and performing signal processing, the effective output of the source signal is improved, which can effectively reduce the interference between users and suppress the influence of noise and obtain the desired signal, thereby improving system performance. It can be seen from Figure 4 that the maximum gain of the beam signal is 18 dB. In Figure 5, it can be seen more intuitively that the main lobe direction of the beam is  $45^\circ$  and the space distribution between the beam side lobe and the main lobe can be displayed more concretely, which is more conducive to our understanding of beam signals. For convenience, we only show  $0-180^\circ$  here.

TABLE 2: Simulation parameters.

Parameters	Value
Center frequency	$f_c = 28\text{GHz}$
Beam transmit power	$P_{\text{tx}} = 30\text{dBm}$
Number of antennas	$m = 8$
Antenna spacing	$d = \lambda/2$
Beam pointing angle	$\theta = 45^\circ$
Beam width	$\text{Bw} = 17.8^\circ$
Beam maximum gain	$G = 18\text{dBi}$
Number of sensors	$N = 144$
Sensor sensing radius	$r = 5\text{m}$

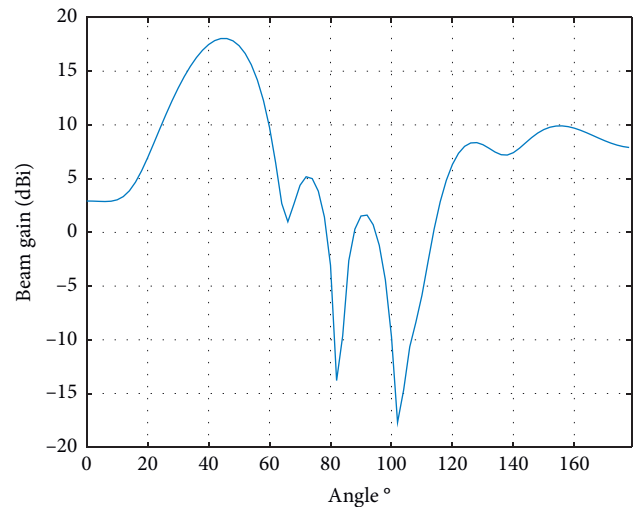


FIGURE 4: Antenna pattern of unknown noncooperative beam.

Since the beam source does not have any priori information for the sensor network, it is difficult to detect the beam signal. With the number of antennas increasing, the beam will become a narrower directional signal, which will bring great challenges to our beam sensing algorithm.

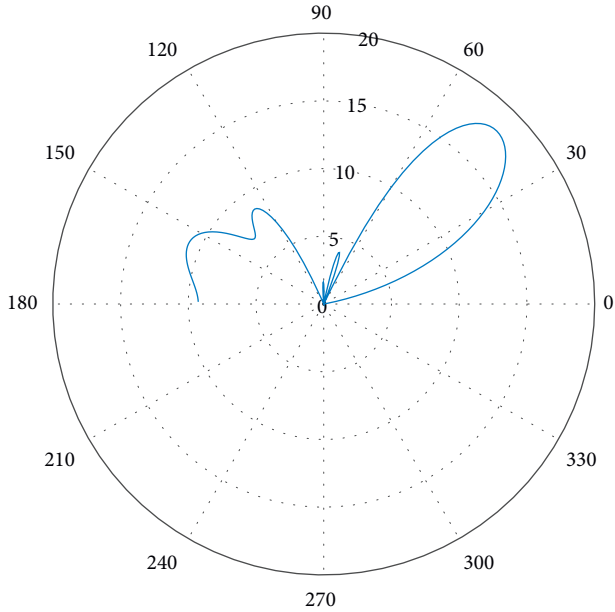


FIGURE 5: Polar antenna pattern of unknown noncooperative beam.

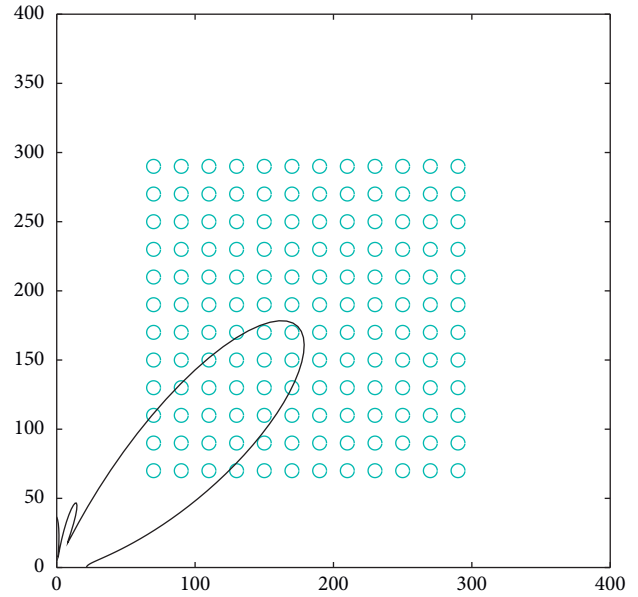


FIGURE 6: Schematic diagram of non-cooperative beam in 45°.

The simulation scene is shown in Figure 6; we deploy a  $12 \times 12$  uniform sensor network to detect the coverage area, set the sensing range of each sensor to 5m, and deploy an unknown signal source 60 m away from the sensor network in advance. It can be seen that the size of the sensor coverage area depends not only on the number of sensors but also on the sensing range of the sensor itself. In addition, due to the limited energy of the sensor, the sensing range is very limited.

Figures 7 and 8 are the plane and three-dimensional schematic diagrams of the signal receiving intensity of the sensor network, respectively. Since the sensor network lacks prior information for non-cooperative signals, it can only be detected and judged by the strength of the received signal. For the convenience of presentation, the signal receiving strength in the figure is not converted into db form ( $-70 \text{ dbm} \sim -38 \text{ dbm}$ ). It can be seen from Figure 7 that in a sensor network, when a beam signal is detected, the signal receiving strength of the sensor in a certain area will increase in detail, and the signal strength will gradually decrease with fading. The three-dimensional histogram in Figure 8 clearly shows the characteristics of the received signal strength of the sensor network when the directional beam signal is fading. On the other hand, it can be seen that due to the influence of sensor noise, it is very likely to affect the global detection probability.

Figure 9 shows the detection performance of the energy detection under different SNR ( $-20 \text{ dB} \sim 5 \text{ dB}$ ) and the number of samples  $N_s$  (64, 512, 2048) at  $i$ -th sensor. From Figure 9, we can obtain that the detection performance of  $i$ -th sensor increases with the increase of the SNR. The reason is that when the SNR increases, the signal strength of the beam also increases, and the noise is relatively small, so the sensor can better distinguish the signal of the beam, and the detection probability also increases. It also can be seen that

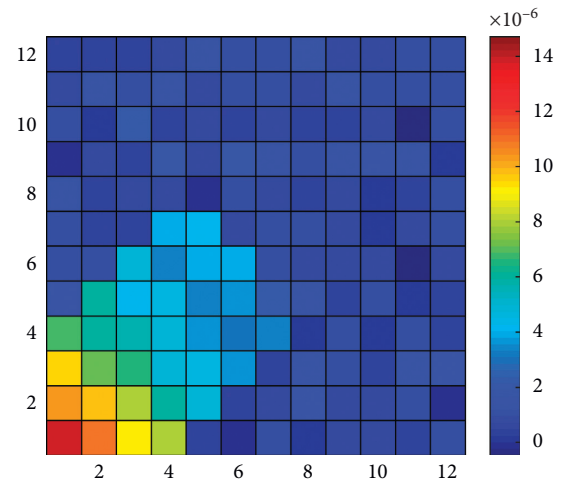


FIGURE 7: Schematic diagram of sensor network sensing beam signal strength (2D).

when  $N_s$  increases, the detection performance of the  $i$ -th sensor will be enhanced, and it can still maintain a high detection performance under a low SNR ( $-10 \text{ dB} \sim -5 \text{ dB}$ ). When the SNR is constant, the more the sampling points of the sensor, the higher the detection probability. This is because increasing the number of sampling points can increase the observation data of the detection signal and the increase in the observation data can make the sensor's judgment more accurate and improve the detection probability. The simulation result accords with the formula (8). In the actual environment, due to channel fading, sensors closer to the beam radiation source will have better channel conditions. Therefore, we can improve the detection performance of  $i$ -th sensor by improving channel quality and increasing the number of samples.

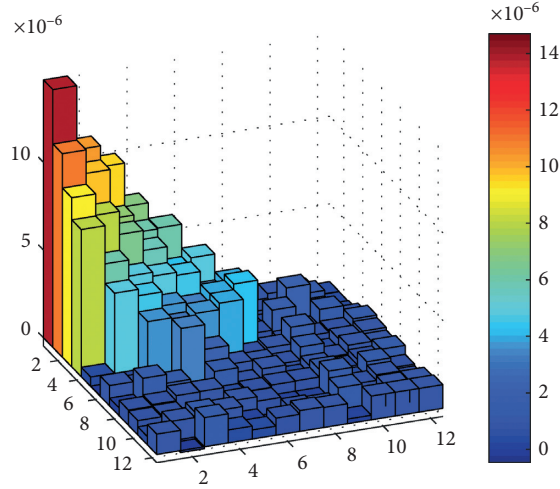


FIGURE 8: Schematic diagram of sensor network sensing beam signal strength (3D).

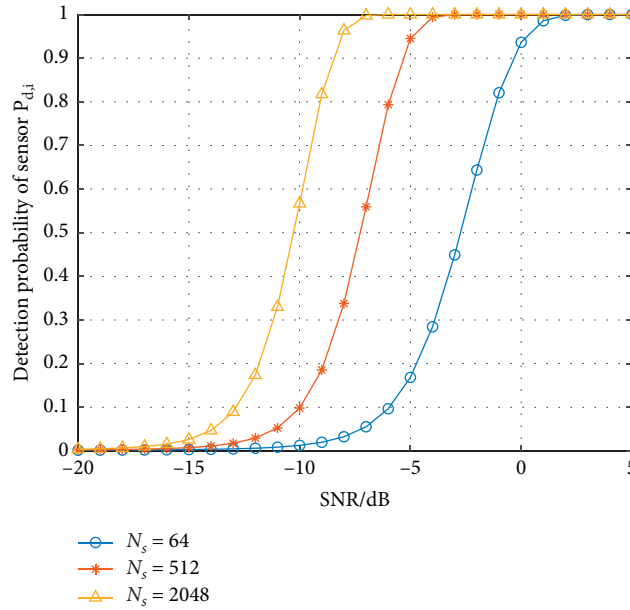


FIGURE 9: Energy detection performance under different SNR and  $N_s$ .

Figure 10 shows the detection performance of the energy detection under different  $P_f$ . As the false alarm probability increases, the detection probability below  $-5$  dB will increase. According to the formula (7), when the false alarm probability increases, the decision threshold is reduced, while detection probability will increase at this time. The simulation results also verify the correctness of the theoretical derivation.

Figure 11 plots the effect of different fusion algorithms on detection performance. It describes the change in detection performance when the detection probability of single sensor increases with different values of  $k$ . According to Algorithm 1, the simulation result is  $N_{\text{opt}} = 64$  when  $N = 144$ . It can be seen that the performance of “AND” fusion rule

and “OR” rule algorithms are the two extremes of the fusion algorithm. The overall detection probability increases when the single sensor detection probability is higher. The detection performance of our improved algorithm is improved over Schwartz algorithm by selecting  $N_{\text{opt}}$ . In half-voting algorithm, when the detection probability of a single sensor is greater than 0.5, the detection performance of the proposed algorithm is better.

In order to integrate the detection probability and false alarm probability and to better evaluate the detection performance of the network, Figure 12 illustrates error probability at different  $k$  values under formula (10) when  $p(H_0) = p(H_1) = 1/2$ . It can be noted that the proposed algorithm has a lower error probability. In the half-voting

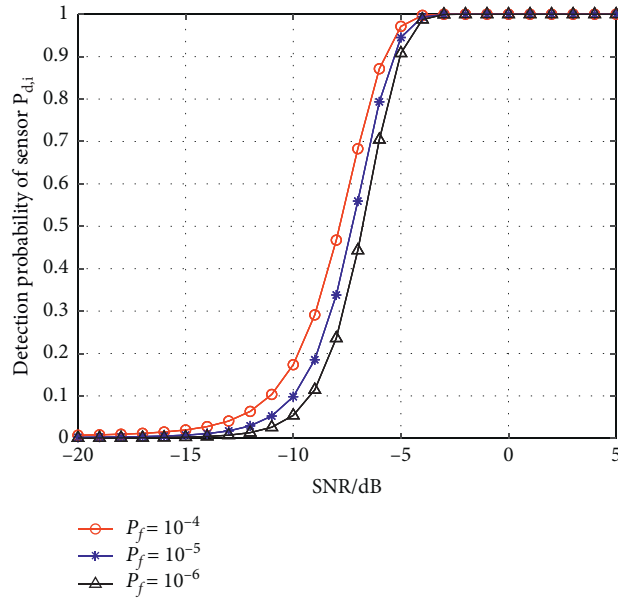


FIGURE 10: Energy detection performance under different SNR and  $P_f$ .

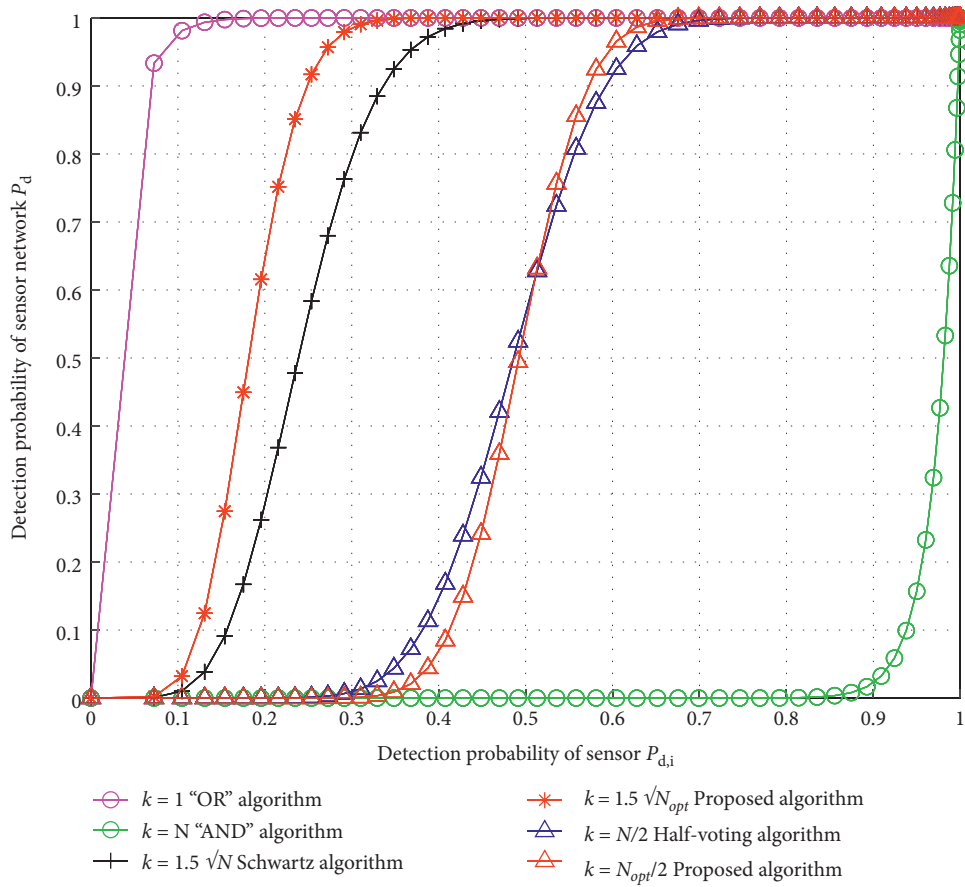


FIGURE 11: Detection probability comparison of different algorithms.

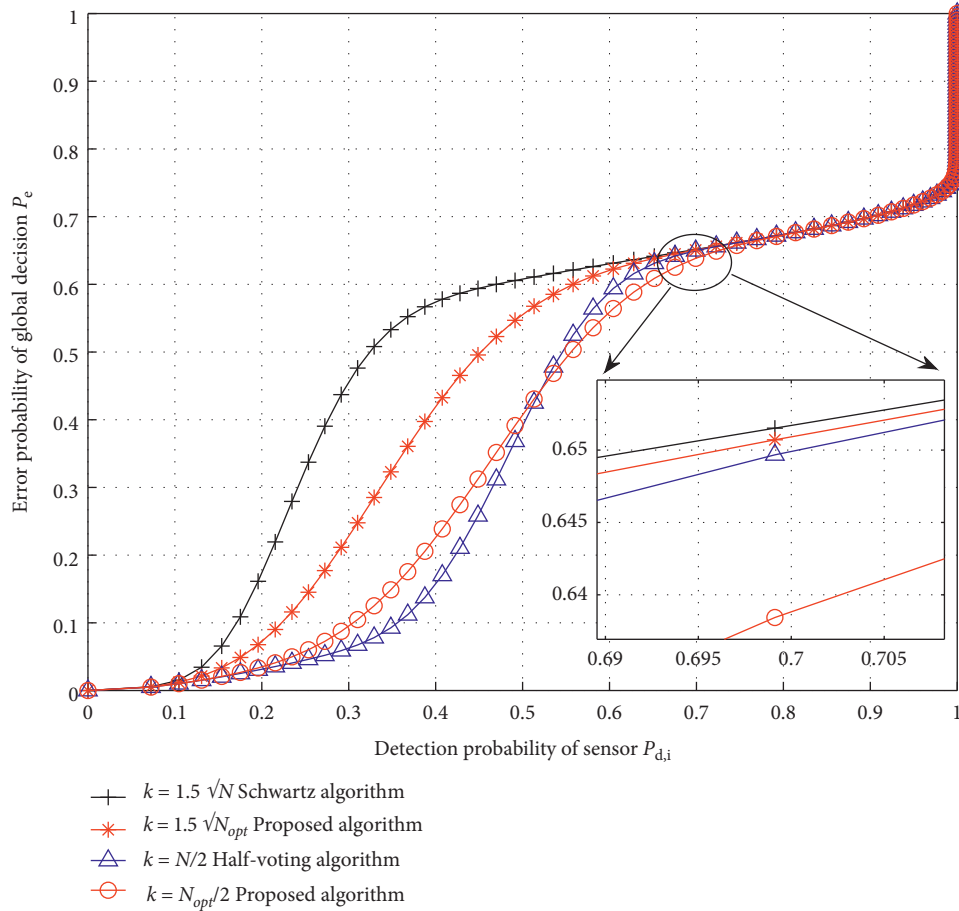


FIGURE 12: Error probability comparison of different algorithms.

algorithm, when the detection probability is less than 0.5, the error probability of the proposed algorithm is higher. Because according to Figure 11, the detection probability of the proposed algorithm is relatively low at this time. When the detection probability is greater than 0.5, the error probability of proposed algorithm is significantly lower than the half-voting algorithm. Because in our algorithm, a large number of low detection probability sensors that are not covered by the beam are reduced, making the decision-making of the entire network more reasonable.

## 6. Conclusions

In this paper, we mainly constructed a beam signal sensing scheme based on wireless sensor networks. According to the characteristics of beam information, First, we derived the detection probability expression under the given false alarm probability. Second, we improved the “ $k$  rank” fusion rule and selected  $N_{opt}$  based on the position information of the sensor. Finally, we provided some simulation results and gained the effectiveness of the algorithm. Through simulation analysis, we found some interesting findings in the energy detection, such as by improving the SNR and increasing the number of samples will improve the overall detection performance. Through comparison with different

fusion algorithms, our proposed algorithm showed better detection probability and lower error probability.

## Abbreviations

BF:	Beamforming
WSNs:	Wireless sensor networks
IoT:	Internet of Things
NOMA:	Nonorthogonal multiple access
D2D:	Device-to-device networks
mmWave:	Millimeter wave
RSS:	Received signal strength
6G:	The sixth generation
5G:	The fifth generation
QAM:	Quadrature amplitude modulation
MIMO:	Multiple-input multiple-output
FC:	Fusion center
AWGN:	Additive white Gaussian noise
ED:	Energy detection
SNR:	Signal to noise ratio.

## Data Availability

No data were used to support this study.

## Conflicts of Interest

The authors declare that they have no conflicts of interest regarding the publication of this article.

## Acknowledgments

This work was supported by the National Key R&D Program of China under Grant 2018YFB1801103, the National Natural Science Foundation of China (nos. 61871398, 61931011, and 62001517), the Natural Science Foundation for Distinguished Young Scholars of Jiangsu Province (no. BK20190030), and the Equipment Advanced Research Field Foundation (no. 61403120304).

## References

- [1] W. Saad, M. Bennis, and M. Chen, "A vision of 6G wireless systems: applications, trends, technologies, and open research problems," *IEEE Network*, vol. 34, no. 3, pp. 134–142, 2020.
- [2] W. Roh, J.-Y. Seol, J. Park et al., "Millimeter-wave beamforming as an enabling technology for 5G cellular communications: theoretical feasibility and prototype results," *IEEE Communications Magazine*, vol. 52, no. 2, pp. 106–113, 2014.
- [3] X. Li, H. Mengyan, Y. Liu, V. G. Menon, A. Paul, and Z. Ding, "I/Q imbalance aware nonlinear wireless-powered relaying of B5G networks: security and reliability analysis," *IEEE Transactions on Network Science and Engineering*, 1 page, 2020.
- [4] B. Li, Z. Fei, C. Zhou, and Y. Zhang, "Physical-layer security in space information networks: a survey," *IEEE Internet of Things Journal*, vol. 7, no. 1, pp. 33–52, 2020.
- [5] A. F. Molisch, V. V. Ratnam, S. Han et al., "Hybrid beamforming for massive MIMO: a survey," *IEEE Communications Magazine*, vol. 55, no. 9, pp. 134–141, 2017.
- [6] S. A. Busari, K. M. S. Huq, S. Mumtaz, L. Dai, and J. Rodriguez, "Millimeter-wave massive MIMO communication for future wireless systems: a survey," *IEEE Communications Surveys & Tutorials*, vol. 20, no. 2, pp. 836–869, 2018.
- [7] S. Rangan, T. S. Rappaport, and E. Erkip, "Millimeter-wave cellular wireless networks: potentials and challenges," *Proceedings of the IEEE*, vol. 102, no. 3, pp. 366–385, 2014.
- [8] M. S. Khan, S. J. Maeng, and Y. S. Cho, "Cell selection technique for Millimeter-Wave cellular systems with hybrid beamforming," *Sensors*, vol. 17, no. 6, pp. 1424–8220, 2017, <https://www.mdpi.com/1424-8220/17/6/1461>.
- [9] A. Puglielli, A. Townley, G. LaCaille et al., "Design of energy- and cost-efficient massive MIMO arrays," *Proceedings of the IEEE*, vol. 104, no. 3, pp. 586–606, 2016.
- [10] Q. Qi, X. Chen, and D. W. K. Ng, "Robust beamforming for NOMA-based cellular massive IoT with SWIPT," *IEEE Transactions on Signal Processing*, vol. 68, pp. 211–224, 2020.
- [11] X. Li, M. Zhao, Y. Liu, L. Li, Z. Ding, and A. Nallanathan, "Secrecy analysis of ambient backscatter NOMA systems under I/Q imbalance," *IEEE Transactions on Vehicular Technology*, p. 1, 2020.
- [12] Z. Lin, M. Lin, Y. Huang, T. d. Cola, and W.-P. Zhu, "Robust multi-objective beamforming for integrated satellite and high altitude platform network with imperfect channel state information," *IEEE Transactions on Signal Processing*, vol. 67, no. 24, pp. 6384–6396, 2019.
- [13] J. Choi, V. Va, N. Gonzalez-Prelcic, R. Daniels, C. R. Bhat, and R. W. Heath, "Millimeter-wave vehicular communication to support massive automotive sensing," *IEEE Communications Magazine*, vol. 54, no. 12, pp. 160–167, 2016.
- [14] N. Deng, M. Haenggi, and Y. Sun, "Millimeter-wave device-to-device networks with heterogeneous antenna arrays," *IEEE Transactions on Communications*, vol. 66, no. 9, pp. 4271–4285, 2018.
- [15] N. Deng, Y. Sun, and M. Haenggi, "Success probability of millimeter-wave D2D networks with heterogeneous antenna arrays," in *Proceedings of the 2018 IEEE Wireless Communications and Networking Conference*, pp. 1–5, Las Vegas, Nevada, USA, 2018.
- [16] B. Yang, Z. Yu, J. Lan, R. Zhang, J. Zhou, and W. Hong, "Digital beamforming-based massive MIMO transceiver for 5G millimeter-wave communications," *IEEE Transactions on Microwave Theory and Techniques*, vol. 66, no. 7, pp. 3403–3418, 2018.
- [17] F. C. Robey, S. Couetts, D. Weikle, J. C. McHarg, and K. Cuomo, "MIMO radar theory and experimental results," in *conference record of the thirty-eighth asilomar conference on signals Systems and Computers*, pp. 300–304, Pacific Grove, CA, USA, 2004.
- [18] J. Xu, L. Liu, and R. Zhang, "Multiuser MISO beamforming for simultaneous wireless information and power transfer," *IEEE Transactions on Signal Processing*, vol. 62, no. 18, pp. 4798–4810, 2014.
- [19] A. Merwaday, R. Vannithamby, M. M. Rashid, Yi Zhang, C. Chen, and X. Wu, "On the performance of directional communications in ultra-dense networks," in *Proceedings of the IEEE International Conference on Communications Workshops (ICC Workshops)*, pp. 522–527, Shanghai, China, 2017.
- [20] V. Raghavan, S. Subramanian, J. Cezanne, and A. Sampath, "Directional beamforming for millimeter-wave MIMO systems," in *Proceedings of the 2015 IEEE Global Communications Conference (GLOBECOM)*, pp. 1–7, San Diego, CA, USA, 2015.
- [21] B. Li, Z. Fei, Y. Zhang, and M. Guizani, "Secure UAV communication networks over 5G," *IEEE Wireless Communications*, vol. 26, no. 5, pp. 114–120, 2019.
- [22] S. Abeywickrama, R. Zhang, Q. Wu, and C. Yuen, "Intelligent reflecting surface: practical phase shift model and beamforming optimization," *IEEE Transactions on Communications*, vol. 1-1, 2020.
- [23] T. Zheng, H. Wang, D. W. K. Ng, and J. Yuan, "Multi-antenna covert communications in random wireless networks," *IEEE Transactions on Wireless Communications*, vol. 18, no. 3, pp. 1974–1987, 2019.
- [24] G. Ding, Q. Wu, F. Song, and J. Wang, "Spectrum sensing in opportunity-heterogeneous cognitive radio networks: non-cooperative case," in *Proceedings of the 2011 International Conference on Wireless Communications and Signal Processing (WCSP)*, pp. 1–5, Nanjing, China, 2011.
- [25] S. Haghghatshoar and G. Caire, "The Beam alignment problem in mmWave wireless networks," in *Proceedings of the 2016 50th Asilomar Conference on Signals, Systems and Computers*, pp. 741–745, Pacific Grove, CA, USA, November 2016.
- [26] G. Barriac, R. Mudumbai, and U. Madhow, "Distributed Beamforming for Information Transfer in Sensor Networks," in *Proceedings of the Third International Symposium on Information Processing in Sensor Networks*, pp. 81–88, New York, NY, April 2004.
- [27] P. Zhang, I. Nevat, G. W. Peters, G. Xiao, and H. Tan, "Event detection in wireless sensor networks in random spatial

- sensors deployments,” *IEEE Transactions on Signal Processing*, vol. 63, no. 22, pp. 6122–6135, 2015.
- [28] L. Zhang, H. Zhao, S. Hou et al., “A survey on 5G millimeter wave communications for UAV-assisted wireless networks,” *IEEE Access*, vol. 7, pp. 117460–117504, 2019.
- [29] R. Zhang, H. Zhang, and W. Xu, “Fast beam alignment algorithm for multi-user mmWave communications,” *Electronics Letters*, vol. 54, no. 25, pp. 1456–1458, 2018.
- [30] Q. Xu, C. Jiang, Y. Han, B. Wang, and K. J. R. Liu, “Waveforming: an overview with beamforming,” *IEEE Communications Surveys & Tutorials*, vol. 20, no. 1, pp. 132–149, 2018.
- [31] Z. Lin, M. Lin, J. Ouyang, W. Zhu, and S. Chatzinotas, “Beamforming for secure wireless information and power transfer in terrestrial networks coexisting with satellite networks,” *IEEE Signal Processing Letters*, vol. 25, no. 8, pp. 166–170, 2018.
- [32] H. Liu, J. Chen, G. Ding, T. A. Tsiftsis, and C. Rowell, “Antenna beamforming for energy harvesting in cognitive radio networks,” in *Proceedings of the 2016 IEEE MTT-S International Wireless Symposium (IWS)*, pp. 1–4, Shanghai, China, 2016.
- [33] M. Z. Hasan and H. Al-Rizzo, “Beamforming optimization in internet of things applications using robust swarm algorithm in conjunction with connectable and collaborative sensors,” *Sensors*, vol. 20, no. 7, 2020.
- [34] X. Yu, J. Zhang, M. Haenggi, and K. B. Letaief, “Coverage analysis for millimeter wave networks: the impact of directional antenna arrays,” *IEEE Journal on Selected Areas in Communications*, vol. 35, no. 7, pp. 1498–1512, 2017.
- [35] X. Zhang, H. V. Poor, and M. Chiang, “Optimal power allocation for distributed detection over MIMO channels in wireless sensor networks,” *IEEE Transactions on Signal Processing*, vol. 56, no. 9, pp. 4124–4140, 2008.
- [36] P. Zhang, J. Y. Koh, S. Lin, and I. Nevat, “Distributed event detection under byzantine attack in wireless sensor networks,” in *Proceedings of the IEEE Ninth International Conference on Intelligent Sensors, Sensor Networks and Information Processing (ISSNIP)*, Singapore, pp. 1–6, April 2014.
- [37] D. Ciuonzo, G. Romano, and P. Salvo Rossi, “Performance analysis and design of maximum ratio combining in hannel-aware MIMO decision fusion,” *IEEE Transactions on Wireless Communications*, vol. 12, no. 9, pp. 4716–4728, 2013.
- [38] I. Nevat, G. W. Peters, and I. B. Collings, “Distributed detection in sensor networks over fading channels with multiple antennas at the fusion centre,” *IEEE Transactions on Signal Processing*, vol. 62, no. 3, pp. 671–683, 2014.
- [39] M. Tavana, A. Rahmati, V. Shah-Mansouri, and B. Maham, “Cooperative sensing with joint energy and correlation detection in cognitive radio networks,” *IEEE Communications Letters*, vol. 21, no. 1, pp. 132–135, 2017.
- [40] S. Atapattu, C. Tellambura, and H. Jiang, “Energy detection based cooperative spectrum sensing in cognitive radio networks,” *IEEE Transactions on Wireless Communications*, vol. 10, no. 4, pp. 1232–1241, 2011.
- [41] Y. Liang, Y. Zeng, E. C. Y. Peh, and A. T. Hoang, “Sensing-throughput tradeoff for cognitive radio networks,” *IEEE Transactions on Wireless Communications*, vol. 7, no. 4, pp. 1326–1337, 2008.
- [42] H. Urkowitz, “Energy detection of unknown deterministic signals,” *Proceedings of the IEEE*, vol. 55, no. 4, pp. 23–31, 1967.
- [43] F. F. Digham, M. . Alouini, and M. K. Simon, “On the energy detection of unknown signals over fading channels,” *IEEE International Conference on Communications*, vol. 5, pp. 3575–3579, 2003.
- [44] M. Schwartz, “A coincidence procedure for signal detection,” *IEEE Transactions on Information Theory*, vol. 2, no. 4, pp. 135–139, 1956.
- [45] M. R. Akdeniz, Y. Liu, M. K. Samimi et al., “Millimeter wave channel modeling and cellular capacity evaluation,” *IEEE Journal on Selected Areas in Communications*, vol. 32, no. 6, pp. 164–179, 2014.

## Research Article

# Secrecy Analysis of Cognitive Radio Networks over Generalized Fading Channels

Jiangfeng Sun,<sup>1</sup> Zhisong Bie ,<sup>1</sup> Hongxia Bie,<sup>1</sup> Pengfei He,<sup>2</sup> and Machao Jin<sup>3</sup>

<sup>1</sup>The School of Information and Communication Engineering, Beijing University of Posts and Telecommunications, Beijing 100084, China

<sup>2</sup>The Institute of Science and Technology for Opto-electronic Information, Yantai University, Yantai Shandong 264005, China

<sup>3</sup>Department of Information and Communication, Shanxi Metallurgical Geotechnical Engineering Investigation Co., Ltd., Taiyuan, Shanxi 030002, China

Correspondence should be addressed to Zhisong Bie; zhisongbie@bupt.edu.cn

Received 24 July 2020; Revised 20 August 2020; Accepted 9 September 2020; Published 22 September 2020

Academic Editor: Lingwei Xu

Copyright © 2020 Jiangfeng Sun et al. This is an open access article distributed under the Creative Commons Attribution License, which permits unrestricted use, distribution, and reproduction in any medium, provided the original work is properly cited.

At present, the fifth generation (5G) communication networks are in the time of large-scale deployment principally because its characteristics consists of large bandwidth, fast response, and high stability. As a partner of 5G, the Internet of Things (IoT) involves billions of devices around the world, which can make the wireless communication environment more intelligent and convenient. However, the problem that cannot be ignored is the physical layer security of 5G-IoT networks. Based on this, we perform a security analysis of cognitive radio networks (CRN) for IoT, where the CRN is the single-input multiple-output (SIMO) model experiencing  $\kappa$ - $\mu$  shadowed fading with multiple eavesdroppers. To analyze the confidentiality of the system under consideration, we analyze the security performance for the considered IoT systems with the help of the derived secure outage probability (SOP) and probability of strictly positive secrecy capacity (SPSC). As a verification of the theoretical formula, Monte Carlo simulation is also provided. The results of great interest are the factors that can produce better security performance in high SNRs region which consist of smaller  $M$ , smaller  $k$ , and larger  $N$ , and larger  $\mu$ , smaller  $I_p$ , and smaller  $R_{th}$ .

## 1. Introduction

On the fifth generation (5G) networks, Internet of Things (IoT) technology makes the data exchange between people and things and objects and objects more rapid and intelligent [1]. However, the physical layer security (PLS) problem, that is, the confidential signals between IoT entities are easy to be intercepted and decoded by eavesdroppers [2]. Therefore, how to improve the confidentiality performance of IoT systems is an urgent issue to be solved. There are two methods to deal with this problem; the first is based on the encryption and decryption algorithm of the network layer and above, and the other is to improve the security capacity of the channel by using the characteristics of the fading channel. In recent years, the latter, namely, physical layer security, has gradually become a hot topic in security research. Based on the channel capacity theory [3] and the

classic Wyner's eavesdropping model [4], Wei et al. in [5] described the optimal power of artificial noise to ensure the best antieavesdropping ability in the wiretap networks experiencing Rayleigh fading. The PLS of nonorthogonal multiple access (NOMA) networks [6] and relaying 5G networks [7] with Rayleigh channels were developed. The authors in [8] studied the factors that affect the security capability of Wyner's model based on Rician channel, where analytical SOP were deduced and proved. The physical performance and security of nonideal IoT networks over Nakagami- $m$  fading channels were investigated through two important metrics, namely, outage probability (OP) and intercept probability (IP) [9].

Different from the channels described above, the universality of generalized channels, that can be equivalent to other fading channels, has recently received considerable attention. [10–16]. On the premise of fully considering the



actual unfavourable factors of the relaying wireless communication networks (WCNs) over Weibull channels, Li et al. [10] has completed the derivation of the exact formula of OP and the asymptote. The work in [11] developed the approximate expression of probability density function (PDF) and obtained the SOP analysis of the classical Wyner's systems over generalized- $K$  fading channels. Based on the proposed IoT relay networks, the authors of [12] explored the theoretical derivation and simulation analysis of OP and average symbol error probability (ASEP). In [13], when all the links in the wiretap networks suffered from  $\kappa$ - $\mu$  fading, Bhargav et al. derived the lower limit of SOP and the closed-form expression of SPSC. Under the condition of imperfect signal transmission, the authors in [14] obtained the theoretical formula of OP in considered model over  $\alpha$ - $\mu$  fading with two different scenarios. Referring to Wyner's classical wiretap model, Kong et al. derived and analyzed the SOP and the probability of nonzero secrecy capacity (PNZ) of Fox's H-Function [15] channels and Fisher-Snedecor  $F$  [16] channels, respectively.

Recently, security issues are very important for popular applications such as Internet of vehicles [17], neural networks [18], and big data [19]. As a developing strategy to solve the obstacles of spectrum scarcity and power allocation in IoT networks, CRN can significantly improve the transmission range and quality have gained great attention in recent literatures [20–26]. With the aid of artificial noise, the IP in the secondary network over Gaussian channel was investigated in [20]. The cooperation of multiple secondary users will further enhance the capacity of CRN; based on this, two different protocols were proposed, and achievable ergodic secrecy rate (ESR) was used to analyze the security performance of the considered system [21]. By employing a CRN network, which suffered from Rayleigh fading and had a legitimate receiver with multiple antennas, the authors of [22] provided the derivation of PNZ and SOP. In [23, 24], Lei et al. studied the security performance of CRNs undergoing Nakagami- $m$  fading and generalized- $K$  fading, respectively. The study of Zhang et al. [25] proposed a method to improve the security capacity of primary networks and secondary networks simultaneously and discussed the strategy of power allocation and band sharing. The authors in [26] studied the secrecy performance of nonorthogonal multiple access (NOMA) CRN over Nakagami- $m$  fading channels, in which connection outage probability (COP), SOP, and effective secrecy throughput (EST) were obtained in a unified form.

More recently, the  $\kappa$ - $\mu$  shadowed model was first introduced by Paris in [27], and it is a generalized fading channel, which can be simplified as Rayleigh, Rician shadowed, one-side Gaussian, Nakagami- $m$ , and  $\kappa$ - $\mu$  under suitable conditions. Moreover, the  $\kappa$ - $\mu$  shadowed fading can be applied to different systems including IoT links [28], satellite channels [29], and underwater links [30]. According to the proposed mobile communication model with  $\kappa$ - $\mu$  shadowed fading, the authors of [31] studied the transmission performance by analyzing OP and ergodic channel capacity (ECC). The statistical characteristics of different shadowed  $\kappa$ - $\mu$  fading were derived in [32], where

the closed-form PDF and cumulative distribution function (CDF) for envelope and signal-to-noise ratio (SNR) were obtained, respectively. The work in [33] investigated the outage performance of hexagonal network affected by  $\kappa$ - $\mu$  shadowed fading in term of analyzing the performance benchmark, namely, outage probability and rate. Sun et al. in [34] presented the derivation of SOP and SPSC for the systems over  $\kappa$ - $\mu$  shadowed distribution, in which legitimate users and eavesdroppers were both single antenna receivers. As continuations of [34], the security analyses of SIMO networks and decode-and-forward (DF) relaying networks were carried out in [35, 36].

So far, we have not discovered relative research based on CRN over  $\kappa$ - $\mu$  shadowed distribution in the open database, let alone the existence of multiple antennas and multi-eavesdroppers. Therefore, combined with the advantages of multiantenna technology [37, 38], this paper is explored. We first present a CRN for IoT, in which the subchannels undergo  $\kappa$ - $\mu$  shadowed fading. Then, we derive the mathematical expressions of SOP and SPSC under the condition of multiple eavesdroppers. Finally, Monte Carlo simulations are provided to compare with the mathematical analysis; moreover, some valuable conclusions are obtained. The work can provide theoretical basis for the security performance evaluation of WCNs (5G, Internet of vehicles, etc.).

The paper is arranged as follows; this section mainly introduces the background, related literatures, and motivation. In Section 2, we explain the CRN model for IoT over  $\kappa$ - $\mu$  shadowed fading channels, and the PDF and CDF of the channels with multiple eavesdropping terminals are also illustrated. SOP analysis is presented in Section 3. The theoretical derivation of SPSC is made in Section 4. Section 5 provides the numerical results and some interesting results. The conclusions of the paper appear in Section 6.

## 2. IOT System Model and Properties of Generalized Channels

*2.1. IOT System Model.* The work considers a four entities CRN model for IoT, as shown in Figure 1, where  $S$  is the data source of the secondary networks, while  $P$  is the sender of the primary networks, and  $D$  is the preset receiver, which uses multiple antennas ( $N_D$ ) to receive signals. There are many eavesdroppers ( $E_1, E_2, \dots, E_M$ ) equipped with multiple antennas ( $N_E$ ). The secondary network is composed of  $S$ ,  $D$ , and  $E$ . Underlay CRN makes spectrum sharing possible, but the cost is that the power of  $S$  will not affect the communication of the main networks.  $h_{SP}$  is interpreted as the channel coefficient of the link ( $S \rightarrow P$ ) and the channel coefficients of main link ( $S \rightarrow D$ ) and wiretap link ( $S \rightarrow E$ ) are  $\mathbf{h}_D$  and  $\mathbf{h}_E$ , respectively. It should be noted that  $\mathbf{h}_D$  and  $\mathbf{h}_E$  are vectors because of multiantenna reception at  $D$  and  $E$ . In our model, we consider passive eavesdropping scenarios, where  $S$  does not know the channel state information (CSI) of the wiretap link, but grasps the CSI of the main link.

$S$  will communicate with  $P$ ,  $D$ , and  $E$  in the considered IoT networks at the same time. Suppose the secret signal from  $S$  is  $x$ ; then, we have

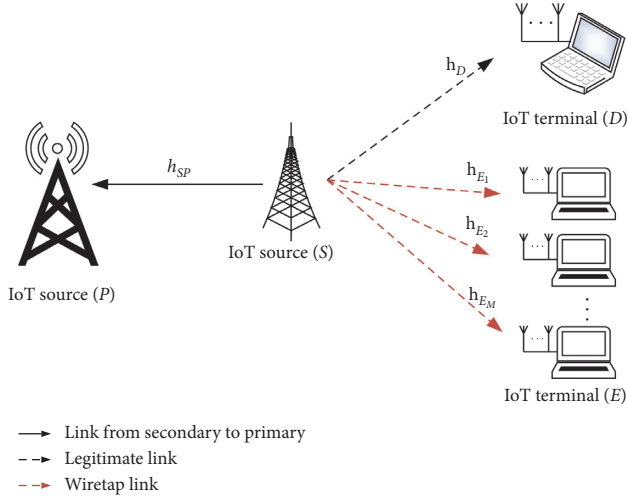


FIGURE 1: The CRN model for IoT.

$$\begin{aligned} y_{SP} &= \sqrt{P_S} h_{SP} x + z_{SP}, \\ \mathbf{y}_{SD} &= \sqrt{P_S} \mathbf{h}_D x + \mathbf{z}_D, \\ \mathbf{y}_{SE} &= \sqrt{P_S} \mathbf{h}_E x + \mathbf{z}_E, \end{aligned} \quad (1)$$

where  $P_S$  is the output power of  $S$ ,  $y_{SP}$  is the signal received by  $P$ ,  $z_{SP}$  is the complex white Gaussian noise on the link from  $S$  to  $P$ , the statistical expectation of  $z_{SP}$  is zero, and the standard deviation is  $\sigma$ .  $\mathbf{y}_{SD}$  and  $\mathbf{y}_{SE}$  represent the received signal matrices of  $D$  and  $E$ , while  $\mathbf{z}_D$  and  $\mathbf{z}_E$  denote noise matrices, and both standard deviations are  $\sigma$ .

**2.2. Properties of Generalized Channels.** The generalized channels considered in our IoT model is  $\kappa$ - $\mu$  shadowed fading channel. This section describes its statistical properties, mainly including the PDFs and CDFs for SNRs in link ( $S \rightarrow P$ ), link ( $S \rightarrow D$ ), and link ( $S \rightarrow E$ ). Relying on [27], the PDF for  $\kappa$ - $\mu$  shadowed variable can be expressed as

$$\begin{aligned} f(\gamma) &= \frac{\mu^\mu m^m (1+k)^\mu}{\Gamma(\mu) (\mu k + m)^m \Omega^\mu} e^{-\mu(1+k)\gamma/\Omega} \\ &\times \gamma^{\mu-1} {}_1F_1\left(m, \mu; \frac{\mu^2 k (1+k)\gamma}{(\mu k + m)\Omega}\right), \end{aligned} \quad (2)$$

where the parameters used to determine the  $\kappa$ - $\mu$  shadowed variable are  $k$ ,  $\mu$ , and  $m$ .  $\gamma$  and  $\Omega$  are described as the instantaneous SNR and average SNR on  $\kappa$ - $\mu$  shadowed fading channels,  $\Gamma(\cdot)$  denotes the Gamma function (equation (8.310.1) in [39]), and  ${}_1F_1(\cdot)$  is defined as confluent hypergeometric function (equation (9.14.1) in [39]), respectively.

According to (2) and [34], we can obtain the PDF and CDF for the SNR at the link from ( $S \rightarrow P$ ) as

$$f_s(\gamma) = (a_s)^{\mu_s} (b_s)^{m_s} \frac{1}{\Gamma(\mu_s)} \sum_{q=0}^{\infty} \frac{(m_s)_q}{(\mu_s)_q q!} \times \left( \frac{a_s k_s \mu_s}{b_s m_s} \right)^q \gamma^{\mu_s+q-1} e^{-a_s \gamma}, \quad (3)$$

$$\begin{aligned} F_s(\gamma) &= b_s^{-m_s} \frac{1}{\Gamma(\mu_s)} \sum_{q=0}^{\infty} \frac{(m_s)_q (k_s \mu_s / b_s m_s)^q}{(\mu_s)_q q!} \\ &\times (\mu_s + q - 1)! \left( 1 - e^{-a_s \gamma} \sum_{s=0}^{\mu_s+q-1} \frac{(a_s \gamma)^s}{s!} \right), \end{aligned} \quad (4)$$

where  $a_s = \mu_s (1 + k_s) / \Omega_s$ ,  $b_s = (\mu_s k_s + m_s) / m_s$ .  $s$  in the lower right corner indicates that the parameter belongs to the channel ( $S \rightarrow P$ ).

Because the expected receiver ( $D$ ) has  $N_D$  antennas and the maximum ratio combining (MRC) merging is adopted, the pdf for random variable (RV) at ( $S \rightarrow D$ ) can be formulated as [35]

$$\begin{aligned} f_D(\gamma) &= (N_D a_D)^{N_D \mu_D} \frac{b_D^{-N_D m_D}}{\Gamma(N_D \mu_D)} \sum_{q=0}^{\infty} \frac{(N_D m_D)_q}{(N_D \mu_D)_q q!} \\ &\times \left( \frac{N_D a_D k_D \mu_D}{b_D m_D} \right)^q \gamma^{N_D \mu_D + q - 1} e^{-N_D a_D \gamma}, \end{aligned} \quad (5)$$

where  $(x)_y$  means Pochhammer calculation [39]. From (4), we can deduce the CDF of RV at  $S \rightarrow D$  as

$$\begin{aligned} F_D(\gamma) &= b_D^{-N_D m_D} \frac{1}{\Gamma(N_D \mu_D)} \sum_{q=0}^{\infty} \frac{(N_D m_D)_q}{(N_D \mu_D)_q q!} \\ &\times \left( \frac{k_D \mu_D}{b_D m_D} \right)^q (N_D \mu_D + q - 1)! \\ &\times \left( 1 - e^{-N_D a_D \gamma} \sum_{s=0}^{N_D \mu_D + q - 1} \frac{(N_D a_D \gamma)^s}{s!} \right), \end{aligned} \quad (6)$$

for eavesdropping channel ( $S \rightarrow E$ ) with multiple eavesdroppers cooperation. Employing [35], we can obtain the PDF of the eavesdropping link as

$$\begin{aligned} f_E(\gamma) &= (N_E a_E)^{N_E \mu_E} \frac{b_E^{-N_E m_E}}{\Gamma(N_E \mu_E)} \times \sum_{q=0}^{\infty} \frac{(N_E m_E)_q}{M^{N_E \mu_E + q} (N_E \mu_E)_q q!} \\ &\times \left( \frac{N_E a_E k_E \mu_E}{b_E m_E} \right)^q \gamma^{N_E \mu_E + q - 1} e^{-N_E a_E \gamma / M}. \end{aligned} \quad (7)$$

### 3. SOP Analysis

For the IoT systems, we need clear benchmarks to measure its security performance [40]. For the passive eavesdropping scenario considered in our model, SOPs are very suitable criteria, which can be understood as the probability that the difference value between the instantaneous capacity of the

main link and the capacity of the eavesdropping link is less than a fixed threshold  $R_{\text{th}}$  [41], and SOP can be written as

$$\text{Sop} = P\{(C_D - C_E) \leq R_{\text{th}}\}, \quad (8)$$

where  $C_D - C_E$  is the difference value between the instantaneous capacity of  $S \rightarrow D$  and  $S \rightarrow E$ .

Two constraints that must be considered in underlay CRN are (i) the power of  $S$  cannot exceed the maximum power value ( $P_{\text{sm}}$ ) and (ii) the power of  $S$  should not exceed the threshold of anti-interference ability ( $I_P$ ) to the primary networks. Referring to (9) and [24], SOP in underlay CRN can be expressed as

$$\begin{aligned} \text{Sop} &= P\{(C_D - C_E) \leq R_{\text{th}}\} \\ &= P\{(C_D - C_E) \leq R_{\text{th}}, P_S = P_{\text{sm}}\} \\ &\quad + P\{(C_D - C_E) \leq R_{\text{th}}, P_S = \frac{I_P}{X}\} = P_1 + P_2, \end{aligned} \quad (9)$$

where  $X$  is the instantaneous SNR of the link of  $S \rightarrow P$ . Next, we will derive  $P_1$  and  $P_2$  in (9).

3.1. Calculation of  $P_1$ .  $P_1$  can be further written as

$$\begin{aligned} P_1 &= P\left\{(C_D - C_E) \leq R_{\text{th}}, X \leq \frac{I_P}{P_{\text{sm}}}\right\} \\ &= P\left\{\gamma_D \leq \theta\gamma_E + \frac{\theta - 1}{\varsigma}\right\} P\left\{X \leq \frac{I_P}{P_{\text{sm}}}\right\} = J_1 J_2, \end{aligned} \quad (10)$$

where  $\theta = e^{R_{\text{th}}}$  and  $\varsigma = P_{\text{sm}}/\sigma^2$ , and we obtain

$$J_1 = \int_0^\infty F_D\left(\theta\gamma_E + \frac{\theta - 1}{\varsigma}\right) f_E(\gamma_E) d\gamma_E. \quad (11)$$

Employing (6) and (7), we have

$$\begin{aligned} J_1 &= \Lambda_1 \int_0^\infty \left(1 - e^{-N_D a_D (\theta\gamma_E + (\theta - 1)/\alpha)}\right) \times \sum_{s=0}^{N_D \mu_D + q - 1} \frac{(N_D a_D (\theta\gamma_E + (\theta - 1)/\alpha))^s}{s!} \\ &\quad \times \gamma^{N_E \mu_E + p - 1} \exp\left(-\frac{N_E a_E \gamma_E}{M}\right) d\gamma_E, \end{aligned} \quad (12)$$

where

$$\begin{aligned} \Lambda_1 &= \frac{b_D^{-N_D \mu_D}}{\Gamma(N_D \mu_D)} \sum_{q=0}^\infty \frac{(N_D m_D)_q (k_D \mu_D / b_D m_D)^q}{(N_D \mu_D)_q q!} \\ &\quad \times (N_D \mu_D + q - 1)! (N_E a_E)^{N_E \mu_E} \\ &\quad \times \frac{b_E^{-N_E \mu_E}}{\Gamma(N_E \mu_E)} \sum_{p=0}^\infty \frac{(N_E m_E)_p (N_E a_E k_E \mu_E / b_E m_E)^p}{M^{N_E \mu_E + p} (N_E \mu_E)_p p!}, \end{aligned} \quad (13)$$

utilizing equation (1.111) in [39],

$$\left(\theta\gamma_E + \frac{\theta - 1}{\varsigma}\right)^s = \sum_{t_1=0}^s (t_1^s) \theta^{t_1} \gamma_E^{t_1} \left(\frac{\theta - 1}{\varsigma}\right)^{s-t_1}. \quad (14)$$

Then, making using of equation (3.381.4) in [39], after a more complex integral operation, we have

$$J_1 = \Lambda_1 \left( \Lambda_2 - e^{-N_D a_D (\theta - 1/\alpha)} \times \sum_{s=0}^{N_D \mu_D + q - 1} \frac{(N_D a_D)^s \sum_{t_1=0}^s (s/t_1) \theta^{t_1} (\theta - 1/\alpha)^{s-t_1}}{s!} \times \frac{\Gamma(N_E \mu_E + p + t_1)}{(N_D a_D \theta + N_E a_E / M)^{(N_E \mu_E + p + t_1)}} \right), \quad (15)$$

where

$$\Lambda_2 = \frac{\Gamma(N_E \mu_E + p)}{(N_E a_E / M)^{(N_E \mu_E + p)}}. \quad (16)$$

From (4),  $J_2$  is derived as

$$J_2 = P\left(X \leq \frac{I_P}{P_{\text{sm}}}\right) = \frac{b_s^{-m_s}}{\Gamma(\mu_s)} \sum_{q=0}^\infty \frac{(m_s)_q (k_s \mu_s / b_s m_s)^q (\mu_s + q - 1)!}{(\mu_s)_q q!} \times \left(1 - e^{-a_s (I_P / P_{\text{sm}})} \sum_{s=0}^{\mu_s + q - 1} \frac{(a_s I_P / P_{\text{sm}})^s}{s!}\right). \quad (17)$$

3.2. *Calculation of  $P_2$* . It can be seen from (9),  $P_2$  is stated as

$$P_2 = P\left\{C_D - C_E \leq R_{th}, P_S = \frac{I_P}{X}\right\}. \quad (18)$$

Referring to [22], we can rewrite  $P_2$  as

$$P_2 = \int_{I_P/P_{sm}}^{\infty} G(x) f_s(x) dx, \quad (19)$$

where

$$G(x) = \int_0^{\infty} F_D\left(\theta y + \frac{(\theta-1)x}{\xi}\right) f_E(y) dy. \quad (20)$$

In (20),  $\xi = I_P/\sigma^2$ . By means of (6) and (7),  $G(x)$  can be derived as

$$G(x) = \Lambda_1 \left( \Lambda_2 - e^{-N_D a_D (\theta-1)x/\xi} \Lambda_3 x^{s-t_2} \right), \quad (21)$$

where

$$\Lambda_3 = \frac{\Gamma(N_E \mu_E + p + t_2)}{(N_D a_D \theta + N_E a_E / M)^{(N_E \mu_E + p + t_2)}} \times \sum_{s=0}^{N_D \mu_D + q - 1} \frac{(N_D a_D)^s}{s!} \sum_{t_2=0}^s (t_2^s) \theta^{t_2} \left( \frac{\theta-1}{\xi} \right)^{s-t_2}. \quad (22)$$

Replacing  $G(x)$  in (19) with (21), then, after the integral is completed by using equation (3.351.2) in [39], we obtain the derivation of  $P_2$  as

$$P_2 = \Lambda_1 a_s^{\mu_s} b_s^{m_s} \frac{1}{\Gamma(\mu_s)} \sum_{q=0}^{\infty} \frac{(m_s)_q (a_s k_s \mu_s / b_s m_s)^q}{(\mu_s)_q q!} \times \Lambda_2 a_s^{-(\mu_s+q)} \Gamma\left(\mu_s + q, a_s \frac{I_P}{P_{max}}\right) - \Lambda_3 a_s^{-(s-t_2+\mu_s+q)} \Gamma\left(s - t_2 + \mu_s + q, \left(a_s + \frac{N_D a_D (\theta-1)}{\xi}\right) \frac{I_P}{P_{sm}}\right), \quad (23)$$

where  $\Gamma(a, b)$  is called the incomplete Gamma function (equation (8.350.2) in [39]).

According to (15), (17), (23), and (9), we finally deduce the theoretical analysis formula of SOP.

#### 4. SPSC Analysis

For passive eavesdropping scenarios, SPSC is often used to investigate the confidentiality of WCNs; therefore, we explore the SPSC of IoT networks in this section. According to the definition of SPSC in [41], we know that it can

understand the probability that the difference value of instantaneous capacity between main channel and eavesdropping channel is not less than zero, which can be formulated as

$$Sp_{sc} = 1 - P\{C_D - C_E \leq 0\} = 1 - \int_0^{\infty} F_D(\gamma_E) f_E(\gamma_E) d\gamma_E = 1 - \Xi. \quad (24)$$

For  $\Xi$  in (24), after replacing the integral term with (6) and (7), we can obtain

$$\Xi = \int_0^{\infty} \frac{b_D^{-N_D m_D}}{\Gamma(N_D \mu_D)} \sum_{q=0}^{\infty} \frac{(N_D m_D)_q}{(N_D \mu_D)_q q!} \times \left( \frac{k_D \mu_D}{b_D m_D} \right)^q (N_D \mu_D + q - 1)! \times \left( 1 - \sum_{s=0}^{N_D \mu_D + q - 1} \frac{e^{-N_D a_D \gamma} (N_D a_D \gamma)^s}{s!} \right) \times \frac{(N_E a_E)^{N_E \mu_E} b_E^{-N_E m_E}}{\Gamma(N_E \mu_E)} \sum_{p=0}^{\infty} \frac{(N_E m_E)_p}{M^{N_E \mu_E + p} (N_E \mu_E)_p p!} = \Lambda_1 \left( \Lambda_2 - \sum_{s=0}^{N_D \mu_D + q - 1} \frac{(N_D a_D)^s}{s!} \times \frac{\Gamma(N_E \mu_E + p + s)}{((N_E a_E / M) + N_D a_D)^{(N_E \mu_E + p + s)}} \right). \quad (25)$$

Finally, by employing (24), we can complete the proof of SPSC.

#### 5. Numerical Results

In this part, we perform the theoretical simulations of (9) and (24). As a verification of correctness, Monte Carlo simulations are also obtained for comparison with the analysis results. From all simulation diagrams (Figures 2–9), we can capture the following information. (i) All the analysis curves coincide well with the statistical simulation curves.

(ii) All simulation results change with abscissa, namely,  $\Omega_D$ , and the change trend indicates that a large  $\Omega_D$  can improve the security of IoT systems. Moreover, matlab simulations show that the convergence condition of the analytical expression including infinite series is that the upper limit of the cycle is 55 times.

Figures 2 and 3 indicate how the SOP and SPSC change with  $\Omega_D$  when  $M$  takes different values. From Figure 2, we can see that when  $\Omega_D$  is fixed, the value of SOP will rise along with the rise of  $M$ . In Figure 3, the increase of  $M$  will lead to the decrease of SPSC. Moreover, the distances between

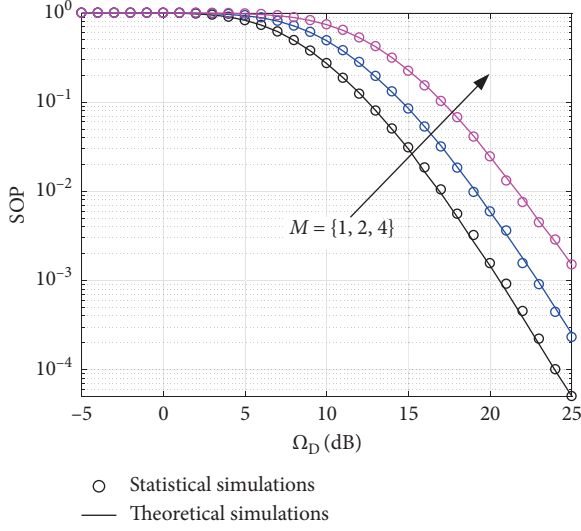


FIGURE 2: SOP versus  $\Omega_D$  with various ( $M$ ), where  $k_S = k_D = k_E = 2$ ,  $\mu_S = \mu_D = \mu_E = 2$ ,  $m_S = m_D = m_E = 1$ ,  $N_D = N_E = 2$ ,  $R_{th} = 0.1$ , and  $I_P = 0.1$ .

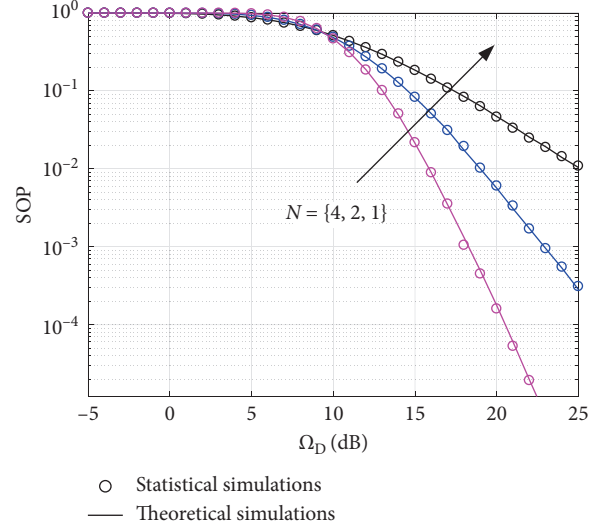


FIGURE 4: SOP versus  $\Omega_D$  with various ( $N$ ), where  $k_S = k_D = k_E = 2$ ,  $\mu_S = \mu_D = \mu_E = 2$ ,  $m_S = m_D = m_E = 1$ ,  $M = 2$ ,  $R_{th} = 0.1$ , and  $I_P = 0.1$ .

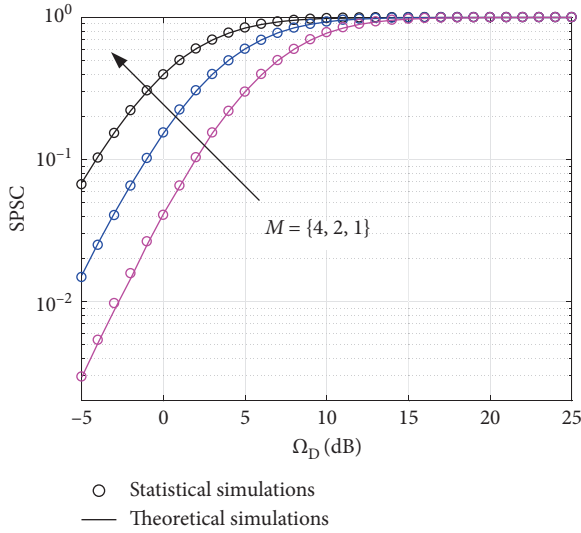


FIGURE 3: SPSC versus  $\Omega_D$  with various ( $M$ ), where  $k_S = k_D = k_E = 2$ ,  $\mu_S = \mu_D = \mu_E = 2$ ,  $m_S = m_D = m_E = 1$ ,  $N_D = N_E = 2$ ,  $R_{th} = 0.1$ , and  $I_P = 0.1$ .

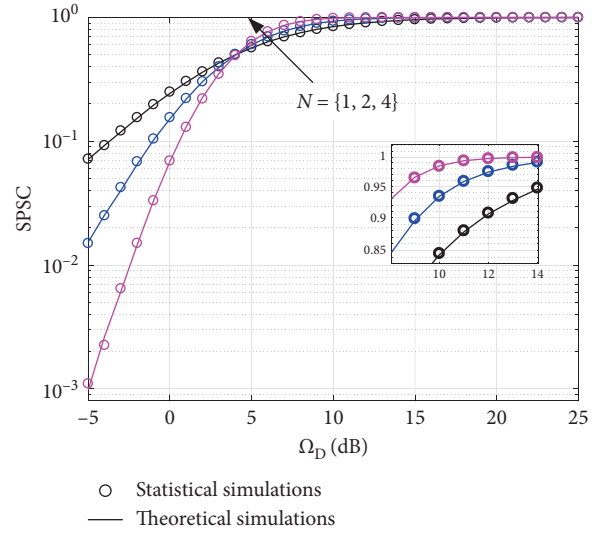


FIGURE 5: SPSC versus  $\Omega_D$  with various ( $N$ ), where  $k_S = k_D = k_E = 2$ ,  $\mu_S = \mu_D = \mu_E = 2$ ,  $m_S = m_D = m_E = 1$ ,  $M = 2$ ,  $R_{th} = 0.1$ , and  $I_P = 0.1$ .

curves represented by different  $M$  are larger. Therefore, we conclude that the increase of the number of eavesdroppers will significantly reduce the performance of IoT model.

The influence of the number of antennas on the safety performance is provided in Figures 4 and 5. We assume  $N_D = N_E = N$ . According to simulation curves, a valuable discovery is that when the value of abscissa is greater than 9 dB; the increase of antenna number, i.e.,  $N$ , will decrease the SOP and increase the SPSC. This means that, under the mechanism of high SNR, the security can be improved by increasing the number of receiving antennas. On the contrary, in the case of small SNR, the increase of the number of antennas will reduce the ability of security.

When the shape parameters  $k$  and  $\mu$  of the generalized channel change, the security analyses are shown in Figures 6 and 7. We suppose that  $k_S = k_D = k_E = k$  and  $\mu_S = \mu_D = \mu_E = \mu$ , where the subscript  $S$ ,  $D$ , and  $E$  indicate that the links are  $S \rightarrow P$ ,  $S \rightarrow D$ , and  $S \rightarrow E$ , respectively. Referring to Figures 6(a) and 7(a), we can see that the gradual increase of  $k$  causes the increase of SOP and the decrease of SPSC with  $\Omega_D \geq 7$  dB. However, the effect of increasing  $\mu$  on the IoT systems is opposite to that of  $k$  based on Figures 6(b) and 7(b).

$I_P$  means the threshold of anti-interference ability to the primary networks. Figure 8 describes its effect on SOP for IoT networks under consideration.  $R_{in}$  represents the

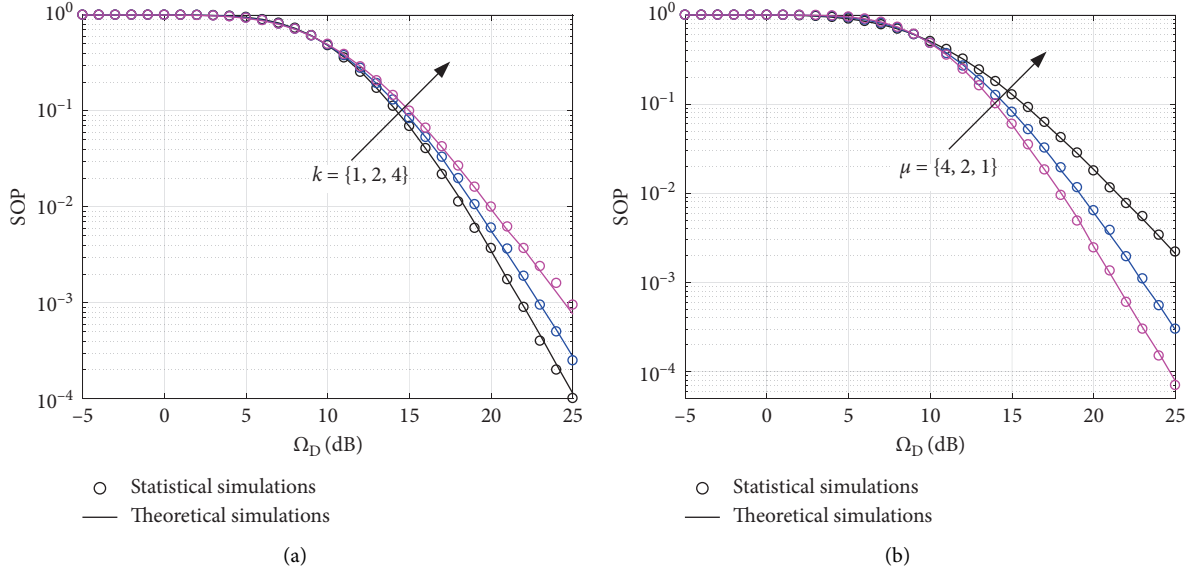


FIGURE 6: (a) SOP versus  $\Omega_D$  with various  $k$ , where  $\mu_S = \mu_D = \mu_E = 2$ ,  $m_S = m_D = m_E = 1$ ,  $N_D = N_E = 2$ ,  $M = 2$ ,  $R_{th} = 0.1$ , and  $I_P = 0.1$ . (b) SOP versus  $\Omega_D$  with various  $\mu$ , where  $k_S = k_D = k_E = 2$ ,  $m_S = m_D = m_E = 1$ ,  $N_D = N_E = 2$ ,  $M = 2$ ,  $R_{th} = 0.1$ , and  $I_P = 0.1$ .

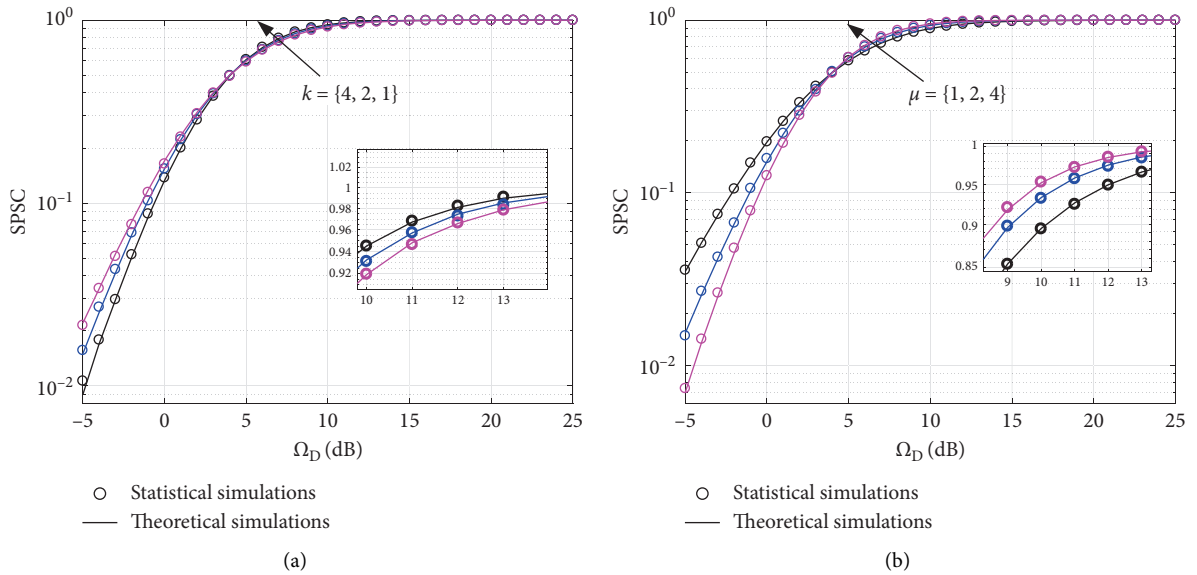


FIGURE 7: (a) SPSC versus  $\Omega_D$  with various  $k$  where  $\mu_S = \mu_D = \mu_E = 2$ ,  $m_S = m_D = m_E = 1$ ,  $N_D = N_E = 2$ ,  $M = 2$ ,  $R_{th} = 0.1$ , and  $I_P = 0.1$ . (b) SPSC versus  $\Omega_D$  with various  $\mu$ , where  $k_S = k_D = k_E = 2$ ,  $m_S = m_D = m_E = 1$ ,  $N_D = N_E = 2$ ,  $M = 2$ ,  $R_{th} = 0.1$ , and  $I_P = 0.1$ .

threshold value of security capacity interruption, the impact of its change on system performance is illustrated in Figure 9. When  $I_P$  changes from 5 dB to -7 dB, then to 15 dB and  $R_{th}$  from 0.1 dB to 0.5 dB and then to 1 dB, the change trend of SOP is gradually decreasing. Therefore, we can find that smaller  $I_P$  and smaller  $R_{th}$  will increase the probability of system security interruption. Moreover, it is interesting that the impact of  $I_P$  on security is more significant than that of  $R_{th}$ .

$m$  is also an important parameter of  $\kappa$ - $\mu$  shadowed distribution, which represents the degree of shadow fading. The simulation results show that when the high SNR is

established, the increase of  $m$  will improve the SPSC and reduce the SOP, but the difference between the curves is very small. In other words, the impact of  $m$  on the security performance is not obvious.

Good security performance requires as small as possible SOP and as large as possible SPSC. Through the above analysis of all simulations, we can obtain that larger  $M$ , larger  $k$ , and smaller  $N$  will worsen the security of the system when the SNR is large. Meanwhile, we also know that larger  $\mu$ , smaller  $I_P$ , and smaller  $R_{th}$  will enhance the security performance.

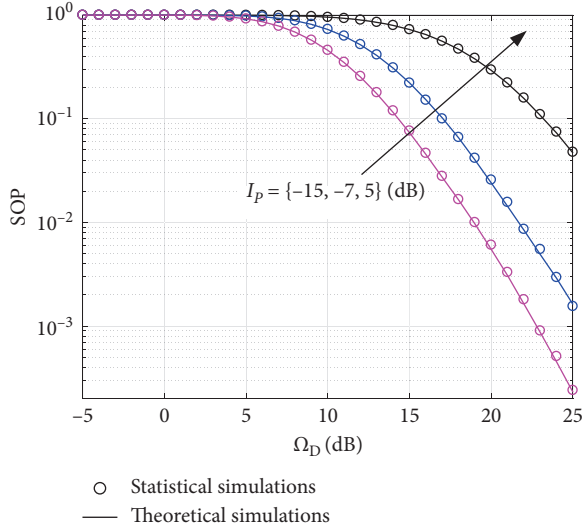


FIGURE 8: SOP versus  $\Omega_D$  with various  $I_p$ , where  $k_S = k_D = k_E = 2$ ,  $\mu_S = \mu_D = \mu_E = 2$ ,  $m_S = m_D = m_E = 1$ ,  $N_D = N_E = 2$ ,  $M = 2$ , and  $R_{th} = 0.1$ .

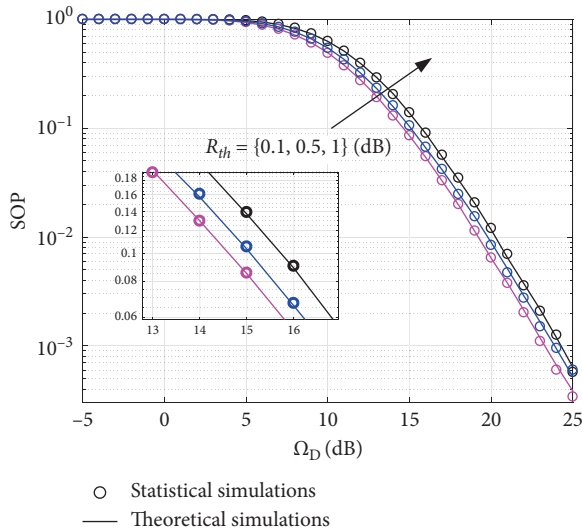


FIGURE 9: SOP versus  $\Omega_D$  with various  $R_{th}$ , where  $k_S = k_D = k_E = 2$ ,  $\mu_S = \mu_D = \mu_E = 2$ ,  $m_S = m_D = m_E = 1$ ,  $N_D = N_E = 2$ ,  $M = 2$ , and  $I_p = 0.1$ .

## 6. Conclusion

In this paper, we explore PHY layer security of Underlay CRNs for IoT networks over generalized fading channels on the basis of the derived SOP and SPSC. The CRN model with multiple antennas can be used in many different situations. The analytical formulas for SOP and SPSC are derived in a concise form. The accuracy of the analytical formulas is verified by Monte Carlo simulations. Moreover, we discuss the influence of the parameters including  $M$ ,  $N$ ,  $k$ ,  $\mu$ ,  $I_p$ , and  $R_{th}$  on the security of IoT networks.

## Data Availability

The data used to support the findings of this study are available from the corresponding author upon request.

## Conflicts of Interest

The authors declare that there are no conflicts of interest regarding the publication of this paper.

## Acknowledgments

This work was supported in part by the National Natural Science Foundation of China under Grant 41174158 and Ministry of Land and Resources P.R.C. Special Project in the Public Interest under Grant 201311195-04.

## References

- [1] G. A. Akpakwu, B. J. Silva, G. P. Hancke, and A. M. Abu-Mahfouz, "A survey on 5G networks for the Internet of things: communication technologies and challenges," *IEEE Access*, vol. 6, pp. 3619–3647, 2018.
- [2] M. Seliem, K. Elgazzar, and K. Khalil, "Towards privacy preserving IoT environments: a survey," *Wireless Communications And Mobile Computing*, vol. 2018, Article ID 1032761, 15 pages, 2018.
- [3] C. E. Shannon, "Communication theory of secrecy systems," *Bell System Technical Journal*, vol. 28, no. 4, pp. 656–715, 1949.
- [4] A. D. Wyner, "The wire-tap channel," *Bell System Technical Journal*, vol. 54, no. 8, pp. 1355–1387, 1975.
- [5] H. Wei, X. Hou, Y. Zhu, and D. Wang, "Security analysis for rayleigh fading channel by artificial noise," in *Proceedings of the 2014 Sixth International Conference On Wireless Communications And Signal Processing, WCSP*, Hefei, China, pp. 1–6, 2014.
- [6] X. Li, M. Zhao, Y. Liu, L. Li, Z. Ding et al., "Secrecy analysis of ambient backscatter NOMA systems under I/Q imbalance," *IEEE Transactions on Vehicular Technology*, p. 1, 2020.
- [7] X. Li, H. Mengyan, Y. Liu, V. G. Menon, A. Paul, and Z. Ding, "I/Q imbalance aware nonlinear wireless-powered relaying of b5g networks: security and reliability analysis," *IEEE Transactions on Network Science and Engineering*, Article ID 03902, 2006.
- [8] Y. Ai, L. Kong, and M. Cheffena, "Secrecy outage analysis of double shadowed Rician channels," *Electronics Letters*, vol. 55, no. 13, pp. 765–767, 2019.
- [9] X. Li, M. Huang, J. Li, Q. Yu, K. Rabie et al., "Secure analysis of multi-antenna cooperative networks with residual transceiver HIs and CEEs," *IET Communications*, vol. 13, no. 17, pp. 2649–2659, 2019.
- [10] X. Li, J. Li, and L. Li, "Performance analysis of impaired SWIPT NOMA relaying networks over imperfect Weibull channels," *IEEE Systems Journal*, vol. 14, no. 1, pp. 669–672, 2020.
- [11] H. Zhao, Y. Liu, A. Sultan-Salem, and M.-S. Alouini, "A simple evaluation for the secrecy outage probability over generalized-K fading channels," *IEEE Communications Letters*, vol. 23, no. 9, pp. 1479–1483, 2019.
- [12] A. Dziri, M. Terre, and N. Nasser, "Performance analysis of relay selection for iot networks over generalized k distribution," in *Proceedings of the 2019 15th International Wireless*

- Communications And Mobile Computing Conference (IWCMC)*, pp. 1411–1415, Tangier, Morocco, 2019.
- [13] N. Bhargav, S. L. Cotton, and D. E. Simmons, “Secrecy capacity analysis over  $\kappa$ - $\mu$  fading channels: theory and applications,” *IEEE Transactions on Communications*, vol. 64, no. 7, pp. 3011–3024, 2016.
  - [14] X. Li, J. Li, Y. Liu, Z. Ding, and A. Nallanathan, “Residual transceiver hardware impairments on cooperative NOMA networks,” *IEEE Transactions on Wireless Communications*, vol. 19, no. 1, pp. 680–695, 2020.
  - [15] L. Kong, G. Kaddoum, and H. Chergui, “On physical layer security over fox’s  $\mathcal{H}$ -function wiretap fading channels,” *IEEE Transactions on Vehicular Technology*, vol. 68, no. 7, pp. 6608–6621, 2019.
  - [16] L. Kong and G. Kaddoum, “On physical layer security over the Fisher-snedecor  $\mathcal{F}$  wiretap fading channels,” *IEEE Access*, vol. 6, pp. 39466–39472, 2018.
  - [17] L. Xu, X. Yu, H. Wang et al., “Physical layer security performance of mobile vehicular networks,” *Mobile Networks and Applications*, vol. 25, no. 2, pp. 643–649, 2020.
  - [18] L. Xu, J. Wang, H. Wang et al., “BP neural network-based ABEP performance prediction for mobile internet of things communication systems,” *Neural Computing And Applications*, 2019.
  - [19] H. Wang, L. Xu, Z. Yan, and T. A. Gulliver, “Low complexity MIMO-FBMC sparse channel parameter estimation for industrial big data communications,” *IEEE Transactions on Industrial Informatics*, vol. 2020, Article ID 2995598, 11 pages, 2020.
  - [20] P. Xie, M. Zhang, G. Zhang, R. Zheng et al., “On physical-layer security for primary system in underlay cognitive radio networks,” *IET Networks*, vol. 7, no. 2, pp. 68–73, 2018.
  - [21] M. Qin, S. Yang, H. Deng, and M. H. Lee, “Enhancing security of primary user in underlay cognitive radio networks with secondary user selection,” *IEEE Access*, vol. 6, pp. 32624–32636, 2018.
  - [22] H. Zhao, H. Liu, Y. Liu, C. Tang, and G. Pan, “Physical layer security of maximal ratio combining in underlay cognitive radio unit over rayleigh fading channels,” in *Proceedings of the 2015 IEEE International Conference On Communication Software And Networks, ICCSN*, Chengdu, China, pp. 201–205, 2015.
  - [23] H. Lei, H. Zhang, I. S. Ansari, C. Gao et al., “Secrecy outage performance for SIMO underlay cognitive radio systems with generalized selection combining over Nakagami-,” *IEEE Transactions on Vehicular Technology*, vol. 65, no. 12, pp. 10126–10132, 2016.
  - [24] H. Lei, H. Zhang, I. S. Ansari, G. Pan, and K. A. Qaraqe, “Secrecy outage analysis for SIMO underlay cognitive radio networks over generalized- $K$  fading channels,” *IEEE Signal Processing Letters*, vol. 23, no. 8, pp. 1106–1110, 2016.
  - [25] Y. Zhang, R. Lu, B. Cao, and Q. Zhang, “Cooperative jamming-based physical-layer security of cooperative cognitive radio networks: system model and enabling techniques,” *IET Communications*, vol. 13, no. 5, pp. 539–544, 2019.
  - [26] Z. Xiang, W. Yang, G. Pan, Y. Cai et al., “Physical layer security in cognitive radio inspired NOMA network,” *IEEE Journal of Selected Topics in Signal Processing*, vol. 13, no. 3, pp. 700–714, 2019.
  - [27] J. F. Paris, “Statistical characterization of  $\kappa$ - $\mu$  shadowed fading,” *IEEE Transactions on Vehicular Technology*, vol. 63, no. 2, pp. 518–526, 2014.
  - [28] L. Moreno-Pozas, F. J. Lopez-Martinez, S. L. Cotton, J. F. Paris, and E. Martos-Naya, “Comments on human body shadowing in cellular device-to-device communications: channel modelling using the shadowed  $\kappa$ - $\mu$  fading model,” *IEEE Journal on Selected Areas in Communications*, vol. 35, no. 2, pp. 517–520, 2017.
  - [29] M. K. Arti, “Beamforming and combining based scheme over  $\kappa$ - $\mu$  shadowed fading satellite channels,” *IET Communications*, vol. 10, no. 15, pp. 2001–2009, 2016.
  - [30] E. Illi, F. El Bouanani, and F. Ayoub, “Asymptotic analysis of underwater communication system subject to  $\kappa$ - $\mu$  shadowed fading channel,” in *Proceedings of the 2017 13th International Wireless Communications And Mobile Computing Conference, IWCMC*, Valencia, Spain, pp. 855–860, 2017.
  - [31] I. Singh and N. P. Singh, “Outage probability and ergodic channel capacity of underlay device-to-device communications over  $\kappa$ - $\mu$  shadowed fading channels,” *Wireless Networks*, vol. 26, no. 1, pp. 573–582, 2020.
  - [32] N. Simmons, C. R. N. Da Silva, S. L. Cotton, P. C. Sofotasios et al., “On shadowing the  $\kappa$ - $\mu$  fading model,” *IEEE Access*, vol. 2020, Article ID 3005527, 9 pages, 2020.
  - [33] S. Kumar and S. Kalyani, “Outage probability and rate for  $\kappa$ - $\mu$  shadowed fading in interference limited scenario,” *IEEE Transactions on Wireless Communications*, vol. 16, no. 12, pp. 8289–8304, 2017.
  - [34] J. Sun, X. Li, M. Huang, Y. Ding, J. Jin et al., “Performance analysis of physical layer security over  $\kappa$ - $\mu$  shadowed fading channels,” *IET Communications*, vol. 12, no. 8, pp. 970–975, 2018.
  - [35] J. Sun, H. Bie, X. Li, K. M. Rabie, and R. Kharel, “Average secrecy capacity of simo  $\kappa$ - $\mu$  shadowed fading channels with multiple eavesdroppers,” in *Proceedings of the 2020 IEEE Wireless Communications And Networking Conference (WCNC)*, pp. 1–6, Seoul, Korea, 2020.
  - [36] J. Sun, H. Bie, and X. Li, “Security performance analysis of SIMO relay systems over Composite Fading Channels,” *KSII Transactions on Internet and Information Systems*, vol. 14, no. 6, pp. 2649–2669, 2020.
  - [37] Z. Chu, Z. Zhu, M. Johnston, and S. Y. Le Goff, “Simultaneous wireless information power transfer for MISO secrecy channel,” *IEEE Transactions on Vehicular Technology*, vol. 65, no. 9, pp. 6913–6925, 2016.
  - [38] Z. Zhu, Z. Chu, F. Zhou, H. Niu, Z. Wang et al., “Secure beamforming designs for secrecy MIMO SWIPT systems,” *IEEE Wireless Communications Letters*, vol. 7, no. 3, pp. 424–427, 2018.
  - [39] I. S. Gradshteyn and I. M. Ryzhik, *Table of Integrals, Series, and Products*, Academic Press, Cambridge, MA, USA, 2007.
  - [40] N. Neshenko, E. Bou-Harb, J. Crichigno, G. Kaddoum, and N. Ghani, “Demystifying IoT security: an exhaustive survey on IoT vulnerabilities and a first empirical look on internet-scale IoT exploitations,” *IEEE Communications Surveys and Tutorials*, vol. 21, no. 3, pp. 2702–2733, 2019.
  - [41] M. Bloch, J. Barros, M. R. Rodrigues, and S. W. McLaughlin, “Wireless information-theoretic security,” *IEEE Transactions on Information Theory*, vol. 54, no. 6, pp. 2515–2534, 2008.